

1982

SOIL-STEEL STRUCTURES UNDER SHALLOW COVER.

HISHAM HUSSEIN. HAFEZ

University of Windsor

Follow this and additional works at: <http://scholar.uwindsor.ca/etd>

Recommended Citation

HAFEZ, HISHAM HUSSEIN., "SOIL-STEEL STRUCTURES UNDER SHALLOW COVER." (1982). *Electronic Theses and Dissertations*. Paper 3511.

This online database contains the full-text of PhD dissertations and Masters' theses of University of Windsor students from 1954 forward. These documents are made available for personal study and research purposes only, in accordance with the Canadian Copyright Act and the Creative Commons license—CC BY-NC-ND (Attribution, Non-Commercial, No Derivative Works). Under this license, works must always be attributed to the copyright holder (original author), cannot be used for any commercial purposes, and may not be altered. Any other use would require the permission of the copyright holder. Students may inquire about withdrawing their dissertation and/or thesis from this database. For additional inquiries, please contact the repository administrator via email (scholarship@uwindsor.ca) or by telephone at 519-253-3000ext. 3208.

CANADIAN THESES ON MICROFICHE

I.S.B.N.

THESES CANADIENNES SUR MICROFICHE



National Library of Canada
Collections Development Branch

Canadian Theses on
Microfiche Service

Ottawa, Canada
K1A 0N4

Bibliothèque nationale du Canada
Direction du développement des collections

Service des thèses canadiennes
sur microfiche

NOTICE

The quality of this microfiche is heavily dependent upon the quality of the original thesis submitted for microfilming. Every effort has been made to ensure the highest quality of reproduction possible.

If pages are missing, contact the university which granted the degree.

Some pages may have indistinct print especially if the original pages were typed with a poor typewriter ribbon or if the university sent us a poor photocopy.

Previously copyrighted materials (journal articles, published tests, etc.) are not filmed.

Reproduction in full or in part of this film is governed by the Canadian Copyright Act, R.S.C. 1970, c. C-30. Please read the authorization forms which accompany this thesis.

THIS DISSERTATION
HAS BEEN MICROFILMED
EXACTLY AS RECEIVED

AVIS

La qualité de cette microfiche dépend grandement de la qualité de la thèse soumise au microfilmage. Nous avons tout fait pour assurer une qualité supérieure de reproduction.

S'il manque des pages, veuillez communiquer avec l'université qui a conféré le grade.

La qualité d'impression de certaines pages peut laisser à désirer, surtout si les pages originales ont été dactylographiées à l'aide d'un ruban usé ou si l'université nous a fait parvenir une photocopie de mauvaise qualité.

Les documents qui font déjà l'objet d'un droit d'auteur (articles de revue, examens publiés, etc.) ne sont pas microfilmés.

La reproduction, même partielle, de ce microfilm est soumise à la Loi canadienne sur le droit d'auteur, SRC 1970, c. C-30. Veuillez prendre connaissance des formules d'autorisation qui accompagnent cette thèse.

LA THÈSE A ÉTÉ
MICROFILMÉE TELLE QUE
NOUS L'AVONS REÇUE

SOIL-STEEL STRUCTURES UNDER SHALLOW COVER

by

 Hisham Hussein Hafez

A Dissertation
submitted to the Faculty of Graduate Studies
through the Department of
Civil Engineering in Partial Fulfillment
of the requirements for the Degree of
Doctor of Philosophy at
The University of Windsor

Windsor, Ontario, Canada

1981



Hisham Hussein Hafez

770400

To Nahla, Dählia and Mona

ABSTRACT

Soil-steel structures are flexible conduits made of corrugated metal sheets and buried in a well compacted granular media. Classical methods of design for conventional sized flexible buried conduits are simple and not suitable for long span structures, especially under relatively shallow cover. Herein, the live load effect cannot be considered secondary as in the case of conduits under deep cover. Also, field experience has shown that failure of the structure could be initiated by soil failure. The present codes avoid the problems associated with shallow cover by requiring a minimum depth of cover. This requirement is empirical and does not differentiate between the different shapes of conduits.

A plane strain finite element analysis is developed and used to study long span soil-steel structures of different shapes under any depth of cover and loading condition with due consideration given to the soil state of stress. The structure wall is replaced by conventional beam elements. Soil is simulated by a combination of constant strain and linear strain compatible elements. Storage and time requirements for the numerical solution are kept to the lowest level without sacrificing the desired accuracy. Two-noded spring type interface elements are introduced between soil and culvert elements.

Nonlinear stress-dependent hyperbolic relationships are used to model the soil and shear behaviour of interface elements. Construction procedure is simulated by automatically generating the finite element mesh layer by layer and by including the effect of compaction in the incremental analyses. Live load is applied concentrically or eccentrically, in increments. Initiation and propagation of soil failure are detected based on a curved Mohr envelope, and applying a stress transfer technique.

A finite element program is developed on the basis of the foregoing analytical procedure to predict the state of stresses in the system due to dead and live loads, as well as the live load causing soil failure. The analytical results are compared with experimental results for live load tests conducted on existing long span soil-steel structures under shallow cover. The results of laboratory tests carried out until failure of soil are also compared with the analytically predicted values. Reasonable agreement is found in both cases.

An analytical study establishes the parameters governing soil failure above the conduit. These parameters include the depth of cover, magnitude and position of loading, and the size and geometric shape of the conduit.

ACKNOWLEDGEMENTS

The author is deeply grateful to Dr. G. Abdel-Sayed who kindly supervised this research, for his enlightening guidance, important suggestions and continuous encouragement throughout the preparation of this dissertation. The author also records his special thanks to the Civil Engineering Faculty members at The University of Windsor for their indirect inspiration through their valuable courses.

Thanks are due to the Computer Centre programming staff members for their help in running the computer programs developed in the course of this study.

The author extends his thanks to the Ontario Ministry of Transportation and Communications for providing Live Load Test Results, and to Mr. F. Kiss for his assistance in the laboratory test.

Special appreciation is extended to Mrs. Zeleney for typing the manuscript.

The author is grateful to the financial support provided by the National Research Council of Canada.

TABLE OF CONTENTS

ABSTRACT.	v
ACKNOWLEDGEMENTS.	vii
LIST OF ILLUSTRATIONS	xii
LIST OF TABLES.	xvii
NOMENCLATURE.	xviii
 CHAPTER	
I. INTRODUCTION.	1
1.1 General	1
1.2 Purpose of Research	4
II. LITERATURE REVIEW	6
2.1 General	6
2.2 Conventional Design Methods	6
2.2.1 Marston-Spangler Method.	7
2.2.2 Ring Compression Theory.	10
2.2.3 Buckling Considerations.	12
2.3 Soil-Structure Interaction Studies.	14
2.3.1 Arching.	15
2.3.2 Pressure Redistribution.	16
2.4 Recent Methods of Analysis.	17
2.4.1 Analytical Solutions	17
2.4.2 Numerical Solutions.	18
2.4.2.1 Spring Method	19
2.4.2.2 Finite Element Method	21
III. ANALYSIS PROCEDURE.	23
3.1 General	23
3.2 Finite Element Approach	24
3.3 Modelling Characteristics of the Finite Element	26
3.4 Finite Element Formulation.	29

3.5	Formulation of Soil Finite Elements	33
3.5.1	Constant Strain Triangular Element	34
3.5.2	Linear Strain Triangular Element	36
3.5.2	Compatible Linear Strain Quadrilateral Element	38
	3.5.3.1 Nine-Noded Quadrilateral Element	38
	3.5.3.2 Eight-Noded Quadrilateral Element	41
3.6	Soil Model	46
3.6.1	Time-Independent Stress-Strain Model	47
3.6.2	Hyperbolic Stress-Strain Model	50
3.6.3	Unloading and Reloading Modulus	55
3.6.4	Hyperbolic Volume Change Behaviour	56
3.7	Beam element for conduit Walls	58
3.8	Interface Finite Element	60
3.8.1	Available Interface Elements	60
3.8.2	Spring Type Interface Element	62
3.9	Interface Model	67
3.9.1	Unit Normal Stiffness at the Interface	67
3.9.2	Unit Tangential Stiffness at the Interface	69
3.10	Construction Simulation	72
3.10.1	Sequential Construction	73
3.10.2	Compaction Simulation	75
3.11	Iterative Procedure for Accurate Representation of Material Properties	78

3.11.1	Iteration for Soil Elements.	79
3.11.2	Iteration for Interface Elements.	80
3.12	Failure Consideration in Soil Elements	81
3.12.1	Soil Tension Failure	82
3.12.2	Soil Shear Failure	83
3.12.2.1	Curved Strength Envelope	83
3.12.2.2	Proposed Modifications	84
3.12.3	Stress Transfer Method	86
3.12.4	Determination of Failure Load.	87
3.13	Failure Consideration in Interface Elements.	88
3.13.1	Interface Tension Failure.	89
3.13.2	Interface Shear Failure.	90
3.14	Computer Program	91
3.14.1	Automatic Mesh Generation.	91
3.14.2	Moving Local Axes.	92
3.14.3	Automatic Initial Values for New Elements.	93
IV.	EXPERIMENTAL VERIFICATION.	94
4.1	General.	94
4.2	Live Load Field Tests.	95
4.2.1	Details of Soil-Steel Structures Tested Under Shallow Cover.	95
4.2.2	Instrumentation.	96
4.2.3	Testing Procedure.	98
4.2.4	Preparation of Test Results.	101
4.2.5	Comparison of Experimental and and Analytical Results.	106
4.2.5.1	Axial Thrusts.	106
4.2.5.2	Bending Moments.	109
4.2.5.3	Relative Vertical Deflections.	111
4.3	Soil Failure Laboratory Tests.	111

4.3.1	Details of the Tested Soil- Steel Structure.	111
4.3.2	Instrumentation and Set-Up.	112
4.3.3	Testing Procedure and Observations	113
4.3.4	Experimental and Analytical Results.	114
V.	Stability of Soil Cover	117
5.1	General	117
5.2	Effect of Height of Cover	118
5.3	Effect of Conduit Size.	120
5.4	Effect of Conduit Shape	121
5.5	Effect of Eccentricity of an Axle Load.	122
VI.	Conclusions and Recommendations	123
6.1	Conclusions	123
6.2	Recommendation for Future Research.	125
APPENDIX A	Stiffness Matrices for Finite Elements.	197
APPENDIX B	Flow Chart.	239
APPENDIX C	Tables.	246
BIBLIOGRAPHY.	252
VITAE AUCTORIS.	268

LIST OF ILLUSTRATIONS

Figure		Page
1.1	Soil-Steel bridge structure.	128
1.2	Common shapes for long span flexible conduits	129
2.1	Pressure distribution assumed in the Marston-Spangler Method.	130
2.2	Pressure distribution assumed in Ring Compression Theory for circular cross- sections	131
2.3	Pressure distribution assumed in Ring Compression Theory for non-circular cross-sections	132
2.4	Actual and simulated loading and structural system considering a frame on spring supports	133
3.1	Finite element mesh for a circular conduit using triangular elements only	134
3.2	Finite element mesh for a circular conduit using triangular and quadrilateral elements	135
3.3	Finite element mesh for a circular conduit under extremely shallow cover.	136
3.4	Finite element mesh for an elliptical shape conduit.	137
3.5	Finite elements around the conduit	138
3.6	Constant strain triangular element	139
3.7	Linear strain triangular element	140
3.8	Nine-noded linear strain quadrilateral element.	141
3.9	Eight-noded linear strain quadrilateral element.	142

Figure		Page
3.10a	Hyperbolic stress-strain relationship.	143
3.10b	Transformed hyperbolic stress-strain relationship	143
3.11	Variation of initial tangent modulus	144
3.12	Mohr-Coulomb strength parameters	145
3.13	Unloading-reloading modulus.	146
3.14a	Hyperbolic axial strain-radial strain relationship	147
3.14b	Transformed hyperbolic axial strain-radial strain relationship.	147
3.15	Variation of initial Poisson's Ratio	148
3.16	Beam element	149
3.17	One dimensional interface element.	150
3.18	Spring type interface element.	151
3.19	Stress-deformation curves for the interface element	152
3.20	Transformed hyperbolic shear stress-shear deformation relationship	153
3.21	Variation of initial unit tangential stiffness.	154
3.22	Nonlinear analysis using incremental technique.	155
3.23	Shear failure consideration in soil elements	156
3.24	Failure lines under the effect of increasingly applied live loads.	157
3.25	Interpolation to determine fractional increment for failure loads.	158

Figure		Page
4.1	Details of the White Ash Creek soil- steel structure.	159
4.2	Details of the Adelaide Creek soil- steel structure.	160
4.3	Typical strain gauge positions at one location	161
4.4	Instrumented locations at the Central cross-section of White Ash Creek structure.	162
4.5	Instrumented locations at the Central cross- section of Adelaide Creek structure.	163
4.6	Details of one of the testing vehicles	164
4.7	Rear tandem positions during testing	165
4.8	Different vehicle lanes during testing	166
4.9	Experimental and analytical live load thrust in White Ash Creek due to Load Level 2, Lane 4 and Position 1	167
4.10	Experimental and analytical live load thrust in White Ash Creek due to Load Level 2, Lane 8, Position 1.	168
4.11	Experimental and analytical live load thrust in White Ash Creek due to Load Level 2, Lane 4, Position 2.	169
4.12	Experimental and analytical live load thrust in White Ash Creek due to Load Level 2, Lane 8, Position 2.	170
4.13	Experimental and analytical live load thrust in Adelaide Creek due to Load Level 2, Lane 4, Position 1.	171
4.14	Experimental and analytical live load thrust in Adelaide Creek due to Load Level 2, Lane 8, Position 1.	172

Figure		Page
4.15	Experimental and analytical live load thrust in Adelaide Creek due to Load Level 2, Lane 4, Position 2	173
4.16	Experimental and analytical live load thrust in Adelaide Creek due to Load Level 2, Lane 8, Position 2	174
4.17	Live load pressure distribution in White Ash Creek due to Load Level 2, Lane 4, Position 1	175
4.18	Live load pressure distribution in White Ash Creek due to Load Level 2, Lane 8, Position 1	176
4.19	Live load pressure distribution in White Ash Creek due to Load Level 2, Lane 4, Position 2	177
4.20	Live load pressure distribution in White Ash Creek due to Load Level 2, Lane 8, Position 2	178
4.21	Live load pressure distribution in Adelaide Creek due to Load Level 2, Lane 4, Position 1	179
4.22	Live load pressure distribution in Adelaide Creek due to Load Level 2, Lane 8, Position 1	180
4.23	Live load pressure distribution in Adelaide Creek due to Load Level 2, Lane 4, Position 2	181
4.24	Live Load pressure distribution in Adelaide Creek due to Load Level 2, Lane 8, Position 2	182
4.25	Experimental and analytical live load moment in Adelaide Creek due to Load Level 2, Lane 4, Position 1	183
4.26	Experimental and analytical live load moment in Adelaide Creek due to Load Level 2, Lane 8, Position 1	184

Figure		Page
4.27	Experimental and analytical live load moment in Adelaide Creek due to Load Level 2, Lane 4, Position 2.	185
4.28	Experimental and analytical live load moment in Adelaide Creek due to load Level 2, Lane 8, Position 2.	186
4.29	Experimental Set	187
4.30	Dial Gauge Locations on Loading Beams.	188
4.31	Load-Deflection curves for the first cycle of loading in Test 1	189
4.32	Load-Deflection curves for two cycles of loading in Test 1	190
4.33	Load-Deflection curves for laboratory Test No. 2	191
5.1	Effect of height of cover on soil failure under centric axle load.	192
5.2	Effect of height of cover on soil failure under multi-axle truck loading	193
5.3	Effect of conduit size on soil failure under centric axle load.	194
5.4	Effect of conduit size on soil failure under multi-axle truck loading	195
5.5	Effect of eccentricity of an axle load	196

LIST OF TABLES

Table		Page
C.1	Comparison between analytical results using method 1 and method 2 for representing live load.	247
C.2	Analytical and Measured Relative Vertical Displacements at Crown of the Tested Conduits (in inches).	249
C.3	Measured Displacements at Dial Gauge Locations G1 to G9 in Test No. 1. (in inches x 10 ⁻³).	250
C.4	Measured Displacements at Dial Gauge Locations G1 to G9 in Test No. 2 (In inches x 10 ⁻³).	251

NOMENCLATURE

A	cross-sectional area per unit of the conduit wall
A_t	area of triangular element
a	parameter for the hyperbolic model
b	parameter for the hyperbolic model
c	cohesion
d	parameter for the hyperbolic volume change
d_c	depth of corrugation
E	modulus of elasticity of the conduit wall material
E^*	modulus of soil reaction
E_e	equivalent modulus of elasticity for beam element
E_i	initial tangent modulus
E_t	tangent modulus
E_{ur}	unloading-reloading modulus
e	eccentricity of applied load
F	reduction in initial Poisson's ratio for a ten-fold increase in confining pressure
f_b	buckling stress
f_y	yield stress
G	value of initial Poisson's ratio at one atmospheric confining pressure
h	height of cover above crown
\bar{h}	average cover height

I	cross-section moment of inertia per unit length of conduit
K_I	dimensionless stiffness number for interface model
K_S	modulus number for soil model
K_{si}	initial unit shear stiffness for interface element
K_{sr}	reduced unit shear stiffness for interface element
K_{ur}	unloading-reloading modulus number
k	a factor for buckling calculation
k_1	constant in the Iowa deflection formula
k_s	unit tangential stiffness
k_n	unit normal stiffness
L	length of beam element
L	length of interface corresponding to one interface element
M	moment per unit length of conduit
m	modulus exponent for soil model
n	total number of positions
n	number of the position of the load
n_s	stiffness exponent for interface model
P	soil pressure on the conduit
P_a	standard axle load of 32 kips
P_b	soil pressure on bottom of conduit
P_c	vertical pressure at crown of conduit
P_d	first method for representing concentrated loads
$P_{d'}$	second method for representing concentrated loads

P_f	centrix axle load causing failure in soil above conduit
$P_{f'}$	heavy rear axle load for a truck loading causing failure in soil
P_h	soil pressure on haunches of conduit
P_i	force acting in the direction of spring number i
P_n	normal force
P_s	tangential force
P_{si}	soil pressure on side of conduit
P_t	soil pressure on top of conduit
p_a	atmospheric pressure
P_l	equivalent live load pressure
R	radius of circular conduit
R'	radius of curvature
R_b	bottom radius for conduit
R_f	failure ratio parameter for soil
R_h	haunch radius for conduit
R_s	side radius for conduit
R_{sf}	failure ratio parameter for interface
R_t	top radius for conduit
r	radius of gyration of the conduit wall
S	span of the conduit cross-section
S_l	stress level in soil, or fraction of soil strength mobilized
S_s	shear stress level in interface element
\bar{s}	surface of a body

T thrust in conduit wall
 T temperature
 t finite elements thickness taken as unity
 t time
 U_s strain energy
 u displacement in the x-direction
 V volume of a body
 v displacement in the y-direction
 w water content
 X, Y global cartizian coordinates
 x anisotropy
 x, y local cartizian coordinates
 α angle measured from the crown of the conduit
 α_i coefficients of the displacement functions
 β a reduction factor accounting for the depth of cover of soil
 γ unit weight of soil
 γ_w unit weight of water
 γ_{xy} shear strain
 δ relative displacement between two nodes
 δ_n relative normal stiffness
 δ_s relative tangential stiffness

ϵ	strain
ϵ'	strain gauge reading under the effect of live load
ϵ_a	axial strain
ϵ_c	strain of the crest of corrugation in conduit wall
ϵ_f	final strain gauge reading
ϵ_o	initial strain gauge reading
ϵ_r	radial strain
ϵ_v	strain at the valley of corrugation
ϵ_x	strain in the x-direction
ϵ_y	strain in the y-direction
ϵ_{vo}	volumetric strain
ϕ	the angle of internal friction
ϕ'	the angle of friction between soil and steel
ϕ_o	angle internal friction for a confining pressure equal to the atmospheric pressure
θ	angle between local coordinates and local coordinates
$\Delta\phi$	reduction in ϕ corresponding to a ten-fold increase in confining pressure
μ	coefficient of friction
ν	Poisson's ratio
ν_i	initial Poisson's ratio
σ	stress
σ_1	major principal stress
σ_3	minor principal stress
σ_{1f}	major principal stress at failure
σ_{3f}	minor principal stress at failure
σ_{1fb}	major principal stress before considering failure

σ_{3fb}	minor principal stress before considering failure
σ_{1i}	major principal stress at the start of an incremental analysis
σ_{3i}	minor principal stress at the start of an incremental analysis
σ_n	average normal stress at interface element
σ_x	stress in the x-direction
σ_y	stress in the y-direction
$\sigma_1 - \sigma_3$	stress difference
$(\sigma_1 - \sigma_3)_f$	stress difference at failure
$(\sigma_1 - \sigma_3)_{ult}$	ultimate stress difference
τ_f	average shear stress at failure for interface element
τ_s	average shear stress in interface element
τ_{ult}	ultimate shear stress in interface element
τ_{xy}	shear stress
λ	a factor for the calculation of k
λ	rotation
Π_p	total potential energy
$\{\alpha\}$	vector of interpolation coefficients
$\{\delta\}$	relative displacement vector
$\{\epsilon\}$	strain vector
$\{\sigma\}$	stress vector
$\{q\}$	nodal displacements vector
$\{q\}_n$	nodal displacements vector for the nine-noded quadrilateral element

$\{q_a\}$	vector of exterior nodal displacements for the nine-noded quadrilateral element
$\{q_b\}$	vector of interior nodal displacements for the nine-noded quadrilateral element
$\{P\}_n$	vector of nodal forces for the nine-noded quadrilateral element
$\{P_a\}$	vector of exterior noded forces for the nine-noded quadrilateral element
$\{P_b\}$	vector of interior nodal forces for the nine-noded quadrilateral element
$\{P_a^*\}$	vector of equivalent nodal forces for the eight-noded quadrilateral element
$\{P\}$	force vector for interface element
$\{s\}$	vector defined in Equation 3.24
$\{u\}$	displacements vector
$\{\bar{x}\}$	body forces vector
$[\Phi]$	interpolation matrix
$[\Phi_s]$	interpolation matrix evaluated along the surface of the element
$[A]$	matrix containing nodal co-ordinates terms
$[B]$	matrix relating strain vector to vector of interpolation coefficients
$[D]$	modulus matrix, or constitutive matrix, or elasticity matrix
$[E]$	matrix relating relative displacement vector to nodal displacement vector for interface element
$[k]$	global element stiffness matrix

$[k_e]$	local element stiffness matrix
$[k]_c$	global stiffness matrix for constant strain triangular element
$[k_e]_l$	local stiffness matrix for linear strain triangular element
$[k_e]_b$	local stiffness matrix for beam element
$[k_e]_i$	local stiffness matrix for interface element
$[k]_n$	local stiffness matrix for the nine-noded quadrilateral element
$[k_{aa}]$,	submatrices of the element stiffness matrix for the nine-noded quadrilateral element defined in Equation 3.15
$[k_{ab}]$,	
$[k_{bb}]$	
$[k_{aa}^*]$	element stiffness matrix for the eight-noded quadrilateral element
$[k_D]$	diagonal material property matrix for interface element
$[r]$	matrix defined in Equation 3.23
$[T]$	transformation matrix
$[T]_e$	transformation matrix for linear strain triangular element
$[T]_b$	transformation matrix for beam element
$[\bar{T}]$	surface traction vector
$[T]_q$	Transformation matrix for eight-noded quadrilateral element

CHAPTER I

INTRODUCTION

1.1 General

Underground conduits have been used for many years as sewers or drainage structures in highway, railway and municipal applications. In the last two decades, their use has been extended to act as bridge substitutes. Currently, they are constructed in North America with increasing frequency as highway and railroad bridges, tunnels and highway underpasses; an example is shown in Fig. 1.1 This development was accompanied by a steady increase in size of installed conduits (144, 158). Spans as large as 52 ft. have been successfully constructed and have performed satisfactorily.

These buried flexible conduits are being built using corrugated metal sheets and constructed so as to induce beneficial interaction between the conduit walls and the surrounding soil. The soil acts as an integral part of the structural system. The conduit is referred to as long span soil-steel structure or long span corrugated metal buried structure, if its span exceeds 25 ft.

Long span soil-steel structures came to be regarded as economical alternatives to conventional short span bridges

because of ease and speed of the design and construction (71). Construction of conventional bridges is labour intensive and much of this labor is highly skilled. Major capital plant equipments, such as cranes and the like, are required and the conventional bridge components are usually made of high grade material. In contrast, the major component in soil-steel structures is soil which is widely available and one of the lowest cost building material. Furthermore, the high performance of earth moving equipment makes the construction of flexible buried conduits highly productive and economical. The cost of maintaining diversions and detours is reduced because of the very fast construction. Normal pavement and shoulders over the structure eliminate problems such as bridge deck deterioration (145).

A report by the United States Federal Highway Administration estimates that using these low cost bridges result in savings of 30% over other conventional short span bridges. Similar savings are reported in Canada (34), while the Australian experience found the cost of soil-steel, bridges to be typically one third that of the conventional bridges (64). Value analysis by a product designer (152) concludes that most conventional overpass structures do not represent optimum designs. Alternative design using flexible

metal arches and culverts were favored when considering all governing parameters. These parameters are the economy in design, fabrication, construction, maintenance, appearance and safety features.

The most common shapes for long span flexible conduits are shown in Fig. 1.2. These structures may be large diameter circular pipes, vertical or horizontal ellipses, low or high profile arches, pipe arches or inverted pear conduits.

The conduit walls are usually made of cold formed corrugated plates. The pitch of corrugation is of the order of 6 in. with a depth of 1.5 in. to 2 in.. The plates are corrugated, punched and then galvanized and curved. They are usually shipped unassembled and bolted together at the site. The steel thickness of the plates ranges from 0.109 in. to 0.375 in. (32).

Granular materials are generally recommended for bedding and backfill which should be well compacted (144). Such materials do not exhibit much change in their physical and engineering properties once they are constructed. Environmental factors such as moisture changes do not affect these properties to the same degree as they affect those of cohesive soils.

The design of most flexible soil-steel structures has mainly relied upon observed behaviour of similar systems,

empirical formulae, and simple theories. These conventional methods of design; as well as modern methods, such as the finite element method, are critically reviewed in Chapter II.

1.2 Purpose of Research

Experience in the field has shown that failure of a soil-steel structure could be initiated by shear or tension failure in soil (109). The Code writers (1, 124) avoided such problems by specifying a minimum depth of cover of one sixth of the structure span. This requirement is empirical and does not differentiate between different shapes of conduits. In addition, a literature survey of available methods to analyze soil-culvert systems shows that the main concern is the determination of stresses in the culvert walls with no mention of the state of stresses in the soil media.

Available analyses of soil-steel structures have other shortcomings. Some important aspects of the problem, such as compaction and consideration of local failure in soil, are neglected in spite of their effects on the behaviour of the soil-structure system. Moreover, complete fixation at the interface between soil and culvert walls is often assumed for simplicity.

This research is motivated by the need for an in-depth study to investigate the actual performance of large con-

duits under shallow cover. Furthermore, it is necessary to examine the parameters governing the lower limits for the height of cover as dictated by soil failure above the conduit.

In order to achieve these goals, it is essential to develop a new computer program for the analysis of soil-structure systems under any depth of cover. The program avoids the previously mentioned shortcomings by:

1. considering not only the state of stresses in the culvert walls, but also that in the soil media as a criteria to study the relationship between depth of cover and permissible live loads,
2. being valid for both symmetrical and unsymmetrical loading conditions, and
3. considering compaction, soil failure and probability of slip between structure walls and soil.

CHAPTER II

LITERATURE REVIEW

2.1 General

Many years of field experience have resulted in simplified theories and empirical formulae for the design of conventional buried flexible structures. These widely used classical methods were generally confirmed by field observations of small sized circular pipes built under usual field conditions (10, 37, 114, 115). They are briefly reviewed in this chapter. Then, the summary of a considerable amount of research work to study the interaction between soil and flexible culverts is outlined. Finally, modern methods, which have been applied recently to analyze flexible conduits in a more rational way, are discussed.

2.2 Conventional Design Methods

In traditional methods of design, soil structure interaction is not properly represented. However, they are briefly summarized here in order to provide an appreciation of past thinking which eventually led to the more refined techniques.

Basically, design of most flexible culverts has relied

upon three criteria: a deflection criterion, a wall compression criterion, and a wall buckling criterion. The deflection criterion is based on a deflection calculated by the Iowa deflection formula in which a stress distribution suggested by Marston and Spangler is assumed. The wall and seam compression criterion depends on a design compression force obtained from the ring compression theory as proposed by White and Lager. The wall buckling criterion follows the studies conducted by many researchers such as Booy, Watkins, Meyerhoff, Luscher and Abdel-Sayed.

2.2.1 Marston-Spangler Method

The Marston-Spangler approach (111, 147, 148) was basically developed for small diameter circular conduits. It is comprised of Marston's estimation of effective vertical load acting on the conduit and Spangler's assumption for the load distribution around it. At the top and bottom of the conduit, the vertical soil pressure is assumed uniform; and at the sides a parabolic horizontal pressure with a maximum at mid-height is considered.

As shown in Fig. 2.1, the vertical pressure is distributed over the pipe diameter and the horizontal pressure over the arc length subtending a 100° angle at the centre. The intensity of the effective uniform pressure is assumed to be equal to the weight of a sliding vertical soil column above the crown of the conduit plus or minus the shearing

resistance on the sides of the soil column. The sign and magnitude of the shearing resistance are in part dependent on the relative stiffness of the pipe to stiffness of the soil. The maximum horizontal pressure at the ends of the horizontal diameter of the conduit is assumed to be directly proportional to the horizontal deflection of the sides. Where a uniform soil support is provided by proper compaction of the soil envelope and with the height of cover exceeding the diameter, the maximum horizontal pressure on the sides is up to 35 percent greater than the vertical pressure on the top of the structure.

According to the assumed pressure distribution, the circumferential thrust is a function of the radius of the circular cross-section of the conduit, R , and the intensity of the vertical pressure at the crown, P_c . It varies from a minimum of a $0.7 P_c R$ at the top and bottom of the conduit and $P_c R$ at the sides, to a maximum of about $1.1 P_c R$ at the haunches. The corresponding circumferential moment in the wall varies from about $0.02 P_c R^2$ at the top, sides and bottom, to about $-0.02 P_c R^2$ at the haunches (116, 147).

The radial deflection under the assumed loading consists of a downward movement of the top and outward movements of the sides of the conduit. The maximum horizontal deflection d , is given by:

$$d = \frac{k_1 P_c R^4}{EI + 0.061 E' R^3} \quad (2.1)$$

where,

E = modulus of elasticity of the conduit wall material in psi,

I = moment of inertia per unit length of cross-section of conduit in in.⁴/in.,

E' = modulus of soil reaction, and

k₁ = constant, its value depending on the bedding angle and deflection lag factor.

Spangler concluded from his experimental investigation (147) that, if the vertical diameter of a circular flexible conduit decreases by about 20% from the initial diameter, the pipe is in a state of incipient collapse. Additional vertical load on the pipe causes failure due to reversal curvature or snap-through buckling. It became customary, then, to refer to failure conditions in flexible pipe as 20% decrease in vertical diameter. It was also observed that the decrease in vertical diameter is almost equal to the increase in the horizontal diameter and is obtained from Equation 2.1. Design is achieved by adjusting the in-plane bending stiffness of the conduit to limit deflection to 5 percent or less of the diameter.

2.2.2 Ring Compression Theory

White and Layer (157) suggested that, once a flexible conduit has been installed in a compacted backfill capable of taking reaction pressures, it can be analyzed as a thin ring in compression. The theory was developed on the assumption that the non-uniform soil pressure distribution around the conduit proposed by Marston-Spangler Theory has little effect on the magnitude and distribution of the circumferential thrust. Thus, it simplified the complex loading condition by neglecting the effect of any soil friction forces and assuming a uniform pressure distribution. This assumption is considered valid for flexible circular conduits with cover heights exceeding one-eighth of the conduit diameter. The uniform pressure, P_c , is taken as the over-burden pressure plus any distributed live load, P_1 , including impact at the top of the conduit:

$$P_c = \gamma h' + P_1 \quad (2.2)$$

where,

γ = unit weight of fill,

h' = average height of cover above structure, and

P_1 = the equivalent live load pressure.

For cover heights exceeding the diameter of the conduit, the minimum cover height, h , at the top of the structure

may be used instead of the average height h in Equation 2.2. The average and minimum cover heights are shown in Fig. 2.2.

According to the theory the circumferential thrust in the conduit wall is given by:

$$T = P_c \left(\frac{S}{2} \right) \quad (2.3)$$

where,

S = span of the conduit cross-section.

In the wall of a non-circular conduit, the radial soil pressure is considered to vary in such a way that the circumferential thrust in the wall remains constant throughout the circumference. Hence, the soil pressure on the structure at any point may be written as:

$$P = \frac{T}{R} \quad (2.4)$$

where,

R = radius of curvature at the point under consideration.

The soil pressure, being inversely proportional to the radius of curvature, is maximum at the point of minimum radius, as for example, at the haunches of a pipe arch. The distribution of soil pressure according to the ring compression theory for two conduits of different shapes

as shown in Fig. 2.3. For any of these shapes, design is achieved by supplying sufficient conduit wall area such that the thrust stress is safely below the wall strength.

2.2.3 Buckling Considerations

Booy (19) suggested that the conduit wall can, in some cases, fail by instability before deformations become large enough to cause collapse. In order to check the conduit walls against buckling, he proposed applying the buckling formula of an elastically supported beam (151) which results in the following equation:

$$f_b = \frac{2}{A} \sqrt{\frac{EIE^*}{R}} \quad (2.5)$$

where,

f_b = buckling stress, and

A = cross-sectional area per unit length of the conduit wall.

Meyerhof and Baikie (113) and Luscher (108) suggested similar equations for calculating the buckling stresses of flexible pipes buried in soil with a high coefficient of subgrade reaction.

Watkins (153) considered a modification of the buckling stress for a pipe under hydrostatic pressure to account for the friction in actual soil around the conduit. Based on Watkin's equation, and the studies of Glock and Kloeppel, Abdel Sayed (2) suggested the following formula

which considers the relative stiffness of the soil with respect to the rigidity of the conduit wall, as well as the effect of shallow cover:

$$f_b = \frac{3E\beta}{(k'R/r)^2} \quad (2.6)$$

where,

r = radius of gyration of the conduit wall, and

β = a reduction factor accounting for the depth of cover.

The value of β is equal to 1.0 if the depth of cover is greater than twice the radius of curvature of the conduit, at the crown; for other cases, its value is given by:

$$\beta = [h/2R]^{0.5} \quad (2.7)$$

The value of factor k , which depends upon the relative stiffness of the conduit wall with respect to the adjacent soil, is given by:

$$k = \lambda \left[\frac{EI}{E'R^3} \right]^{0.25} \quad (2.8)$$

The value of the λ is equal to 1.22 for the wall in the sides and bottom where it displaces towards the soil.

For the upper zone, where the wall is subject to active pressures and tangential movement has considerable effect on the buckling stress of the wall, λ is given by:

$$\lambda = 1.22 \left[1.0 + 2 \left(\frac{EI}{E^3 R^3} \right)^{0.25} \right] \quad (2.9)$$

Inelastic buckling is considered to start when f_b equals half the yield stress f_y of the wall material. A parabolic equation is assumed for the transition zone between full yielding ($\frac{kR}{r} = 0$) and the elastic zone at $f_y/2$. This results in the following equation for buckling:

$$f_b = f_y - \frac{f_y^2}{12E\beta} \left(\frac{kR}{r} \right)^2 \quad (2.10)$$

where k and β have the same values as those for buckling in the elastic zone.

Design, based on the buckling criterion is achieved by selecting the wall thickness so that it is capable of carrying the thrust with an adequate factor of safety against buckling stress.

2.3 Soil-Structure Interaction Studies

Extensive research work followed the pioneering work done at Iowa State University by Marston and Spangler. The aim was to study the interaction between flexible tubular structures and the surrounding soil. These studies confirmed the importance of two aspects of the interaction which are described by Luscher and Hoeg (106, 107) as arching and pressure redistribution. Their conclusions are based on their own experimental

and theoretical studies as well as the work of others.

2.3.1 Arching

Arching (121) is the phenomenon by which the vertical load on the flexible conduit is reduced or increased as it deflects in the vertical direction. Positive arching is a favourable condition wherein a portion of the overburden load is diverted around the pipe in a compression arch of soil. Hoeg (78) found that the vertical pressure on the tops of flexible tubes is sand decreased to about 70% of the overburden pressure as the flexibility of the tubes increased. Allgood and Ciani (11) found that the reduction in the vertical load on tubes embedded in sand due to arching would depend on the degree of compaction of the sand. For a height of cover of about one diameter, the average reduction was 30% when tube was buried in dense sand, and it was only about 10% when sand around the tube was loose. Similarly, Howard (79), and Howard and Selander (80) found that the pressure at the crown of flexible pipes they tested were always less than the overburden pressure.

However, it may not always be possible to count on a load reduction due to arching. Davis and Bacher (36) found that the load on a flexible culvert beneath a 170 ft. deep fill was greater than the overburden pressure.

This unfavourable "negative arching" indicated that a pipe might draw load in excess of the soil weight above it. Consequently, it can be seen that there exists a case of "neutral arching" where load on a flexible pipe is equal to the actual weights above it.

2.3.2 Pressure Redistribution

The second important aspect of the interaction between flexible conduits and soil is pressure redistribution affected by the conduit flexibility. It is the action by which the pressure on the side of the conduit is increased above the vertical pressure. As the structure is loaded vertically and deflects under the loading, the sides of the structure push into adjacent soil and the side pressure increases. The uniform hydrostatic pressure assumed by White and Layer does not really exist. Hoeg (78) found that the side pressure on thin metal tubes buried in sand increased with increasing flexibility of the tubes up to a certain point. As the flexibility of the tubes increased beyond this point, the vertical pressure did not decrease further but remained equal to about 90% of the overburden pressure. Similar results were reported by Howard (79) and Howard and Selander (80) for model tests on plastic pipes in both cohesionless and cohesive soils. Selig (141, 142) and Selig and Calabrese (143) concluded that the

sequence of construction operations could play an important part in determining the magnitudes and distributions of loads on a buried flexible culvert. They also found that loads on a structure might be controlled to some extent through the use of temporary internal bracing during construction.

2.4 Recent Methods of Analysis

In recent methods of analysis, the load distribution around the pipe, or at least part of it, is not assumed, but is determined in the course of the solution. Solution techniques may further be classified as analytical or numerical. Analytical approaches use classical theory of elasticity and shell theory to obtain what is termed an "exact" solution. Numerical methods depend on approximating techniques, such as finite differences or finite elements.

2.4.1 Analytical Solutions

Analytical solutions for flexible conduits embedded in soil have been discussed by Savin (138), Burns and Richard (23), Burns (24) and Hoeg (77). Savin investigated the stress state around a composite liner of a hole in an infinite elastic isotropic plate subjected to a system of external forces. Burns' solution is a closed form one and is quite convenient to use. According to Burns, a circular pipe having a depth of soil cover of more than 1.5 times

the pipe diameter can be analyzed by assuming it an elastic thin cylindrical shell encased in an isotropic, linearly elastic medium of infinite extent subject to a surface overpressure. Even though this theory has several simplifying assumptions, it is capable of either neglecting or taking into account the friction at the soil conduit interface.

Several investigators (35, 87) have proposed design methods based on Burn's solution. To determine culvert behaviour, the developed equations in cartesian coordinates were converted to graphical form. Curves were drawn to indicate relationships between deformation, bending moment and circumferential thrust parameters and a soil culvert stiffness parameter.

Hoeg generated a plane strain solution, similar to Burn's solution, in polar coordinates.

2.4.2 Numerical Solutions

Many of the restrictions and approximations necessary in applying to practice the solutions obtained from elastic theory, are no longer required when numerical techniques are used in conjunction with an electronic computer. The numerical approaches to analyze soil-culvert structures may be further grouped under two headings. The first represents the soil system as a set of springs whose

response is designed to simulate that of the soil. The second approach deals with the soil medium as a continuum, and the soil-conduit system is analyzed by the finite element method.

2.4.2.1 Spring Method

The spring method (48, 90, 149) is considered a step forward compared to the Spangler and White methods, since it assumes only the distribution of the active live load while the soil reaction is obtained in the course of the analysis. This method was suggested by Drawsky in the United States and applied by Kloeppel and Glock in Germany.

Drawsky (48) proposed a mathematical model based on replacing the conduit by a segmented ring surrounded by a system of radial springs instead of soil. The actual complex problem of determining the response of the soil-conduit system to an applied load is solved to any desired accuracy by an iterative numerical procedure. A wide variety of situations may be handled using this approach such as various culvert shapes and variation in soil moduli.

Kloeppel and Glock (90) suggested the use of a basically similar method as Drawsky, but with improvements. Their method consisted of replacing a unit length of the conduit wall by a partially supported two-dimensional polygon as shown in Fig. 2.4. The soil is replaced by

discrete springs which are capable of sustaining only compression. The frame is loaded by a radial pressure, which is in the form of a sine wave with the maximum intensity, P_c , at the crown, which is calculated as follows:

$$P_c = \gamma h + P_1 \quad (\text{for } P_1 < \gamma h) \quad (2.11)$$

$$P_c = 1.1 (\gamma h + P_1) \quad (\text{for } P_1 > \gamma h) \quad (2.12)$$

The 10 percent increase for structures with shallow depths of cover accounts for the effect of load concentration due to traffic loads. The radial pressure at $\alpha = 90^\circ$ is recommended to be $0.5 P_c$ when the depth of cover is more than the span of the conduit; and equal to zero for shallower covers. The polygon is then treated as a statically indeterminate structure. However, the accuracy of this approach is deterred by the lack of information concerning the evaluation of the rigidity of the springs. The stiffness of springs is equal to the coefficient of soil reaction times the spring spacing.

At the present time, constant values for the coefficient of soil reaction are assigned (81, 82). No consideration is being given to the stress dependent behaviour of soil. The friction between the conduit wall and soil can be accounted for through an over-simplified approach in which the spring supports act at an angle from the radial direction, $\tan^{-1} \mu$,

where μ is the coefficient of friction. Furthermore an iterative process, in which springs subjected to tensile forces are eliminated, is required to determine the zone of passive soil pressures and the corresponding internal forces.

2.4.2.2 Finite Element Method

Because of its flexibility the finite element method is most adaptable for the analysis of buried conduit problem. The method was applied by modelling the soil and culvert walls by an assemblage of finite elements in a two-dimensional plane-strain problem. Therefore, it is assumed that there is no variation of force effects in the longitudinal direction of the conduit (57, 84), which is an assumption inherent to all other methods mentioned earlier.

Earlier applications of the method to a flexible culvert problem were performed by Brown (22) who developed a finite element program for flexible culverts under high fill. This was followed by several finite element investigations reported by Allgood and Takahashi (13), Kirkland and Walker (89), Abel, Mark, and Richards (4), and Nataraja (119). More sophisticated finite element programs have been developed recently. The most general of these is CANDE (Culvert Analysis and Design) developed

by Katona, Smith, Odello, and Allgood (84, 85, 86).

CANDE program uses either the elasticity solution of Burns (24) with nonlinear modifications or the finite element method. A wide variety of conduit wall materials such as corrugated steel or reinforced concrete may be handled automatically. The finite element formulation in CANDE is based on an extended Hardin nonlinear soil model (73). However, the program has several drawbacks.

A minimum height of soil cover of 1.25 the average diameter, measured from the spring line, is imposed. Compaction is not treated and sequential construction simulation is not accurately enough considered.

Other important finite element programs were developed by Duncan (55, 56, 57, 58). These programs are based on the hyperbolic stress-strain relationship for the soil. Compaction of soil layers is not considered. Complete fixation between soil and conduit is assumed. Representation of live loads is based on the Boussinesq elastic theory although its application in the presence of the culvert opening is doubtful.

CHAPTER III

ANALYSIS PROCEDURE

3.1 General

The capabilities and limitations of the finite element approach as an effective method for the analysis of underground flexible culverts are investigated. The characteristics and features of the method used in the analysis are summarized.

Constant strain triangular elements, as well as linear strain quadrilateral elements are used to simulate the soil media in the finite element mesh. A nonlinear stress-strain relationship is assumed for soil elements. Beam elements are employed as culvert wall. A two-noded interface element is formulated. It simulates possible behaviour at the common interface between culvert wall and soil such as sliding or separation. Nonlinearity of the load deformation relationship of the interface elements is taken into account.

Important aspects of the construction process simulation are described. The procedure includes both incremental analysis for each layer of soil added to the system and compaction effects. Some iteration processes are applied to improve the theoretical results obtained from the finite element analysis. Failure considerations for

soil elements, as well as interface elements, are presented. Finally, the computer program developed to carry out the computations involved in the analysis is briefly described.

3.2 Finite Element Approach

A direct application of the classical theories of continuum mechanics to analyze a buried flexible structural plate conduit problem is virtually impossible. The complexities involved in determining stress distribution, displacement pattern or failure zones throughout the soil media and culvert walls are beyond the capacity of such theories.

The only logical analytical approach able to incorporate most of the aspects of a soil-steel structure system with a minimum of over-simplifying idealizations is the finite element method. In addition, it is known that this immensely powerful numerical analysis possesses many important features that make it of great potential in solving interaction problems. It has considerable flexibility in assigning and modifying the different material properties for individual soil and interface elements. Hence it is possible to simulate nonlinear behaviour in a realistic manner, to account for different types of soil and to represent nonuniform structural stiffness.

The consistency of finite elements in dealing with different types of soil structure problems allows a reliable comparison between buried structural plate conduits with different shapes and varying height of cover. It allows complicated boundary shapes to be accommodated. In addition, by changing the geometry of the finite element mesh, it is possible to simulate placement of fill in layers around the structure and follow the varying structural geometry that accompanies actual construction sequences. Finally, its results offer a complete picture of the stress distribution and deformation in the entire media. The ring compression forces and bending moments in the culvert wall are also obtained throughout construction and under applied external loads.

It should be noticed that the finite element method is an approximate analytical tool. Its accuracy depends on the mesh size and on the type of element used as the basic unit of the mesh. The information derived from the analytical results is heavily influenced by correctly including most of the major aspects of the problem during idealization. As more of these influences are taken into account in the analytical model, the accuracy, as well as the storage requirement, computational time and effort, increases.

Bearing these important factors in mind, the finite element approach is realistically applied to analyze and study the interaction between flexible culvert structures and surrounding soil. The features of the analytical model are described in the following section.

3.3 Modelling Characteristics of the Finite Element

The first step in a finite element analysis consists of replacing the actual soil structure system by a system of finite elements or subregions interconnected at a finite number of nodal points. This idealization results in a finite element mesh which simulates the presence of the soil mass and the structure. A complete idealization needs to be three-dimensional in space to take into account any varying condition along the axis of the culvert such as external loads. The time dimension may also be included to follow the load history effects. However, the computational requirements essential to incorporate the important aspects of the problem make it virtually impossible to undertake static three-dimensional finite element analysis. Therefore, a plane-strain condition is assumed for the cross-section under consideration. The thickness of all finite elements taken as unity is kept constant throughout the analysis to account for the study of a cross-section instead of the three dimensional analysis.

Figures 3.1 to 3.4 show some typical meshes that are generated throughout this study to analyze different situations encountered in soil-steel structures. Fig. 3.5 is an enlargement of the elements around the structure. In these meshes conduit walls are replaced by conventional plane frame elements and soil media is discretized into membrane elements.

The mesh in Fig. 3.1 is developed for the analysis of circular culvert structures under shallow cover. It contains only constant strain triangular elements to simulate soil media. These simple elements reduce the computational effort appreciably compared to higher order elements. Resulting stresses in the conduit walls are reasonable compared to experimental results. However, they do not convey a clear and dependable picture of the state of stress in the soil around the upper half of the culvert where possibilities of failure do exist. The mesh in Fig. 3.2 is also used to analyze shallow cover circular culvert structures. It contains constant strain triangular elements as basic soil elements up to the spring lines of the culvert. Above the spring lines linear strain quadrilateral elements are used to replace the soil around the culvert. These higher order elements are much superior to basic elements in regions of high stress gradient. They are also essential to follow the

start and propagation of failure in soil under the effect of heavy loads. They result in a more accurate solution for the stresses and strains in the culvert walls.

To study the soil-steel structure system under extremely shallow cover, the mesh in Fig. 3.3 can be used. Constant strain triangular elements and linear strain quadrilateral elements are used, however, the top layer consists of only one element in the vertical direction above the crown instead of three. In this case, the height to width ratio of the element is improved. Dependable results are obtained compared to misleading ones as in the case of using three elements in the vertical direction above the crown with a height to width ratio less than $1/3$.

To extend the study to common shapes other than circular, a mesh similar to that in Fig. 3.4 is used. In this mesh, the span and height of culvert, in addition to the different radii of curvature, are needed to generate an elliptical shape pipe.

A standard displacement method of analysis yield the nodal point displacements and the internal stresses in the culvert walls and in the soil during construction as well as under the effect of external loads.

3.4 Finite Element Formulation

The formulation procedures of the finite element method can be based on direct approach, variational principles and other methods such as the method of weighted residuals. The use of variational principles permits generalization of the finite element, provides physical insights and is convenient in formulating the equations of the different types of elements used in this study. The variational principle of minimum potential energy in which displacements are adopted as primary unknowns is outlined below.

For each type of elements, a displacement function that uniquely describes the state of displacement at all points within the element is chosen. The assumed function must contain one unknown for each degree of freedom encountered in the element. Usually a polynomial form for the displacement in terms of generalized coordinates is defined as follows:

$$\{u\} = [\Phi] \{a\} \quad (3.1)$$

where,

$\{u\}$ = is a vector of displacements at any point;

$\{a\}$ = is a vector of coefficients for the assumed interpolation function; and

$[\Phi]$ = is the interpolation matrix which, in case of a polynomial, contains terms in x and y .

Substituting the displacements and coordinates of the nodes of the element into Equation 3.1, yields:

$$\{q\} = [A] \{\alpha\} \quad (3.2)$$

where,

$\{q\}$ = vector of nodal displacements, and

$[A]$ = matrix containing nodal coordinates terms.

The vector of unknown coefficients $\{\alpha\}$ may be eliminated by combining Equations 3.1 and 3.2; and the vector of displacements is obtained in terms of nodal displacements as:

$$\{u\} = [\Phi] [A^{-1}] \{q\} \quad (3.3)$$

where,

$[A^{-1}]$ = inverse of $[A]$.

Applying the strain-displacement relationships to Equation 3.3, the strain at any point within the element may be written as:

$$\{\epsilon\} = [B] [A^{-1}] \{q\} \quad (3.4)$$

where,

$\{\epsilon\}$ = strain vector, and

$[B]$ = matrix obtained by differentiating $[\Phi]$.

From the theory of elasticity, the stresses may be related to strain by the elasticity matrix as follows:

$$\{\sigma\} = [D]\{\epsilon\} \quad (3.5)$$

where,

[D], sometimes called the modulus matrix, contains the elastic properties of the element such as its modulus of elasticity E and Poisson's ratio ν .

The total potential energy of the element represents the sum of the internal strain energy and the potential energy of the loads acting on the element. In turn, the potential energy of loads, is the negative sum of the work done by surface loads and by body forces. Thus the element total potential energy can be expressed in matrix form as:

$$\Pi_p = \frac{1}{2} \int_V \{\epsilon\}^T \{\sigma\} dV - \int_V \{u\}^T \{\bar{x}\} dV - \int_{\bar{s}} \{u\}^T \{\bar{T}\} d\bar{s} \quad (3.6)$$

where,

Π_p = total potential energy,

$\{\bar{x}\}$ = body forces vector,

$\{\bar{T}\}$ = surface traction vector,

\bar{s} = surface of the element,

V = volume of the element, and

$\{\ }^T$ = transpose of the vector.

Substituting Equations 3.3 through 3.5 into Equation

3.6 yield

$$\begin{aligned} \Pi_p = & \int_V \{q\}^T [A^{-1}]^T [B]^T [D] [B] [A^{-1}] \{q\} dV \\ & - \int_V \{q\}^T [A^{-1}]^T [\phi] \bar{T}(\bar{x}) dV \\ & - \int_S \{q\}^T [A^{-1}]^T [\phi_s] \bar{T} dS \end{aligned} \quad (3.7)$$

where,

$[\phi_s] = [\phi]$, evaluated along surface points only.

Equation (3.7) represents a scalar function of the discretized unknown nodal displacements $\{q\}$. The total potential energy of a system of finite elements is the algebraic summation of the total potential energy of individual elements. It has a stationary value when equilibrium is achieved. Taking the variation of Equation 3.7 with respect to displacements, and equating the result to zero, the element stiffness matrix can be obtained as:

$$[k_e] = \int [A^{-1}]^T [B]^T [D] [B] [A^{-1}] dV \quad (3.8)$$

It is much easier to derive the element stiffness matrix with respect to convenient local coordinates instead of global coordinates. In this case, a standard transformation matrix is used to transfer in the local stiffness matrix into the global system as follows:

$$[k] = [T]^T [k_e] [T] \quad (3.9)$$

where,

[k] = element stiffness matrix with respect to the global coordinate system, and

[T] = transformation matrix containing direction cosines of the local axes with respect to the global axes.

Finally the total global stiffness matrix of the structural system is obtained by an automatic algebraic assemblage of individual element stiffness matrices in global coordinates.

3.5 Formulation of Soil Finite Elements

Available finite element programs use either constant strain elements or non-compatible linear strain elements to represent soil. In this study, a combination of constant strain triangular elements and compatible linear strain quadrilateral elements is employed. Where stress variation is not rapid, constant strain elements are used for their simplicity. Around the upper half of the culvert, where rapid variation in stresses occurs under the effect of live loads, linear strain elements are used for their accuracy. These soil finite elements are briefly formulated in the following sections.

3.5.1 Constant Strain Triangular Element

Figure 3.6 shows a triangular finite element having three corner nodes in global co-ordinates. Since each node has two degrees of freedom, the linear interpolation functions for displacements at any point are expressed in terms of six unknowns. These displacements, which satisfy element boundary compatibility, are assumed as:

$$u = \alpha_1 + \alpha_2 x + \alpha_3 y \quad (3.10a)$$

$$v = \alpha_4 + \alpha_5 x + \alpha_6 y \quad (3.10b)$$

where,

u = displacement in the x-direction,

v = displacement in the y-direction, and

α_i = coefficients of the displacement functions.

Equations 3.10 may be written in a matrix form as in Equation 3.1. Using the nodal displacements and coordinates, matrix [A] defined in Equation 3.2 is obtained. The strain displacement relationships for a two-dimensional element are given by:

$$\epsilon_x = \frac{\partial u}{\partial x} \quad (3.11a)$$

$$\epsilon_y = \frac{\partial v}{\partial y} \quad (3.11b)$$

$$\gamma_{xy} = \frac{\partial u}{\partial y} + \frac{\partial v}{\partial x} \quad (3.11c)$$

where,

ϵ_x = strain in the x-direction

ϵ_y = strain in the y-direction, and

γ_{xy} = shear strain

Differentiating the matrix expression for the displacement vector yields matrix [B] defined in Equation 3.4. Since the assumed displacements are linear, the coefficients of the [B] matrix are constant and reflect the state of constant strain in the element.

For plane strain condition, the following relationships exist between stresses and strains:

$$\sigma_x = \frac{E}{(1+\nu)(1-2\nu)} [(1-\nu)\epsilon_x + \nu\epsilon_y] \quad (3.12a)$$

$$\sigma_y = \frac{E}{(1+\nu)(1-2\nu)} [\nu\epsilon_x + (1-\nu)\epsilon_y] \quad (3.12b)$$

$$\tau_{xy} = \frac{E}{2(1+\nu)} \gamma_{xy} \quad (3.12c)$$

where,

σ_x = stress in the x-direction

σ_y = stress in the y-direction, and

τ_{xy} = shear stress

Writing Equations 3.12 in a matrix form, the modulus matrix [D] is obtained. By substituting the matrices [A], [B] and [D] into Equation 3.8, and performing the integration over the volume of the element, the element stiffness matrix is generated. It should be noted that since a unit thickness is assumed in plane strain analysis, the integration in Equation 3.8 is performed over the area of the element.

The element stiffness matrix is developed directly with respect to the global axes shown in Fig. 3.5. Therefore, no transformation matrix, as suggested in Equation 3.9, is needed. The details of matrices [A], [B] and [D] are given in Appendix (A).

3.5.2 Linear Strain Triangular Element

The formulation of linear strain triangular element is based on complete quadratic polynomials to describe displacements in the x and y directions. The assumed displacement functions, for any point in the element, are expressed as:

$$u = \alpha_1 + \alpha_2 x + \alpha_3 y + \alpha_4 x^2 + \alpha_5 y^2 + \alpha_6 xy \quad (3.13a)$$

$$v = \alpha_7 + \alpha_8 x + \alpha_9 y + \alpha_{10} x^2 + \alpha_{11} y^2 + \alpha_{12} xy \quad (3.13b)$$

Six nodal points, each having two degrees of freedom, are needed to determine the twelve constants in Equations

3.13. It is convenient to locate interior nodes at mid-points of the sides of the triangle in addition to exterior nodes at the corners as shown in Fig. 3.7. Convenient local axes are chosen such that the point of origin coincides with a corner nodal point, assigned number 1, and the x-axis extends along the base. The use of such local axes greatly facilitates the derivation of the element stiffness matrix. Assuming the numbering system shown in Fig. 3.7, only three nodal coordinate values are sufficient to fully define the position of the six nodal points, namely, x_2 , x_3 , and y_3 .

Matrix [A], which relates the nodal displacements vector { δ } to the vector of interpolation coefficients { α } is obtained by substituting nodal displacements into Equations 3.13. Details of [A], as well as its inverse $[A]^{-1}$, are given in Appendix A.

The strain-displacement relationships and stress-strain equations for a plane strain condition are given in Equations 3.11 and 3.12. These equations yield the same matrix [D] as that obtained for a constant strain triangular element. However, the resulting matrix [B] contains linear elements, obtained by differentiating quadratic quantities assumed in the displacement interpolation functions. Therefore, the state of strain is varying linearly within the boundaries of the six-noded

triangular element.

Finally, the derived matrices $[A^{-1}]$, $[B]$ and $[D]$ are substituted into Equation 3.8. The integration over the volume of the element is replaced by an integration over the triangular area since the constant thickness of the element is unity. Details of matrix $[B]$, the resulting local element stiffness matrix, and the orthogonal transformation matrix $[T]$ are included in Appendix A.

3.5.3. Compatible Linear Strain Quadrilateral

Element

The formulated linear strain triangular element is not explicitly included in the finite element mesh. It is used as a basis to derive the stiffness matrix of a linear strain quadrilateral element. The purpose of the quadrilateral element is to provide the advantages of a linear strain triangular element in addition to appreciable savings in the storage and computational requirements of the developed computer program discussed later on. These advantages are more noticeable by using an eight-noded quadrilateral element which is handled through the derivation of the stiffness matrix of a nine-noded element.

3.5.3.1 Nine-Noded Quadrilateral Element

Figure 3.8 shows a quadrilateral element which has

four corner nodes, four mid-side nodes, and one interior node at the centre of one of the diagonals. Convenient local axes which facilitate the derivation of the elements stiffness matrix are chosen as shown in the figure. The point of origin coincides with a corner nodal point which is assigned number 1. The x-axis lies along the diagonal containing the interior node and divides the element into two triangular regions.

The node numbering system for the quadrilateral element is shown outside the element. For derivation purposes, the six nodes forming the upper triangle are internally numbered as shown inside its boundary. The internal numbering system is identical to that of the formulated linear strain triangular element. Therefore, by assuming complete quadratic displacement functions for any point within the upper triangle, as given by Equation 3.13, its local stiffness matrix becomes identical to that of the triangular element.

The lower six-noded triangle may be treated as an inverted linear strain triangle by satisfying two conditions. First, the six-nodal points should be numbered locally as shown inside the boundary of the lower triangle in Figure 3.8. The numbering system in this case is clockwise compared to the counter-clockwise numbering of the linear strain triangular element. Second, the same

complete quadratic displacement functions adopted within the upper triangle are valid within the lower triangle with respect to the same local axes.

Because of the inverted situation of the linear strain lower triangle, its local stiffness matrix is not identical to that of the upper region. Since the chosen numbering systems of the triangles are such that both triangles have a common base lying along the local x-axis, the need for a rotational transformation matrix to relate their local stiffness is eliminated. Only some sign changes in the upper local stiffness matrix are required to obtain the stiffness matrix for the lower region. The changes reflect the geometric properties of the triangle affected by being inverted. To illustrate the changes, consider the three coordinate values that define completely the six nodes of the triangular shape which are x_2 , x_3 and y_3 . Since the sign of x_2 , which geometrically means the base of the triangle, is not affected by inversion, it does not need change. Similarly, the sign of x_3 remains the same whether the triangle is inverted or not. However, y_3 indicates the height of the triangle which is positive for the upper triangle. Thus, the sign of y_3 of the lower triangle should be changed when substituted in the stiffness matrix expressions. In addition, some elements of the stiffness matrix should

also change sign to keep consistent sign convention for the force-displacement relationships. These are the elements relating an x-displacement to a y-force or a y-displacement to an x-force. Mathematically, this is done by multiplying all the elements of the matrix by $(-1)^{i+j}$ where 'i' is the row number and 'j' is the column number of the element in the stiffness matrix.

The total stiffness matrix of the quadrilateral element is obtained by combining the stiffness matrices of the upper and lower triangular regions. Corresponding expressions relating common degrees of freedom to common nodal forces are added algebraically. The details of the final stiffness matrix with respect to local axes are given in Appendix A. It consists of eighteen rows and eighteen columns.

3.5.3.2 Eight-Noded Quadrilateral Element

It is possible to reduce the number of degrees of freedom of the nine-noded quadrilateral element to sixteen by eliminating the internal node as shown in Figure 3.9. A condensation technique (65) is applicable since the interior degrees of freedom are not common with other finite elements. The reduction in size of the element stiffness matrix results not only in an overall reduced number of degrees of freedom at the assembled level, but

also in an efficient storage scheme of the assembled total stiffness matrix. This is due to a reduction in the band width. Therefore, the peripheral processing time is reduced.

There are two approaches to perform condensation, a direct approach and an approach that employs the concept of a coordinate transformation. The direct approach is illustrated below and applied to eliminate the internal node of the quadrilateral element and its degrees of freedom.

The original stiffness matrix of the nine-noded quadrilateral element relates eighteen degrees of freedom, the nodal displacements, to corresponding nodal forces as follows:

$$[k]_n \{q\}_n = \{P\}_n \quad (3.14)$$

where,

$[k]_n$ = nine-noded quadrilateral element stiffness matrix

$\{q\}_n$ = vector of nodal displacement for the element,

and $\{P\}_n$ = vector of nodal forces for the element.

The matrix $[k]_n$ in Equation 3.14 may be partitioned into four sub-matrices relating four sub-vectors as shown in Equation 3.15.

$$\begin{bmatrix} k_{aa} & k_{ab} \\ k_{ab}^T & k_{bb} \end{bmatrix} \begin{Bmatrix} q_a \\ q_b \end{Bmatrix} = \begin{Bmatrix} P_a \\ P_b \end{Bmatrix} \quad (3.15)$$

where,

$[k_{aa}]$ = sub matrix relating the sixteen exterior displacement degrees of freedom $\{q_a\}$ to corresponding forces acting at the exterior nodes, $\{P_a\}$,

$[k_{ab}]$ = sub matrix relating the two interior degrees of freedom at node 9, $\{q_b\}$, to the sixteen exterior nodal forces $\{P_a\}$, and

$[k_{bb}]$ = two by two submatrix relating the interior nodal displacements $\{q_b\}$ to corresponding interior forces $\{P_b\}$.

Only $\{q_a\}$ consists of degrees of freedom common with other elements, therefore they are not to be condensed out. In order to eliminate the internal degrees of freedom $\{q_b\}$, first the lower partition is solved to yield:

$$[k_{ab}]^T \{q_a\} + [k_{bb}] \{q_b\} = \{P_b\} \quad (3.16)$$

Rearranging Equation 3.16, an expression for $\{q_b\}$ is obtained as follows:

$$\{q_b\} = [k_{bb}]^{-1} \{P_b\} - [k_{bb}]^{-1} [k_{ab}]^T \{q_a\} \quad (3.17)$$

Similarly the upper partition is expanded and written as:

$$[k_{aa}] \{q_a\} + [k_{ab}] \{q_b\} = \{P_a\} \quad (3.18)$$

Substituting for the internal degrees of freedom from Equation 3.17, Equation 3.18 becomes:

$$\begin{aligned}
& [k_{aa}]\{q_a\} + [k_{ab}][k_{bb}]^{-1}\{P_b\} \\
& - [k_{ab}^T][k_{bb}]^{-1}[k_{ab}]\{q_a\} \\
& = \{P_a\}
\end{aligned} \tag{3.19}$$

The condensed element equations may be written in the form:

$$[k_{aa}^*]\{q_a\} = \{P_a^*\} \tag{3.20}$$

where $[k_{aa}^*]$ is the required eight noded quadrilateral element stiffness matrix given by:

$$[k_{aa}^*] = [k_{aa}] - [k_{ab}][k_{bb}]^{-1}[k_{ab}]^T \tag{3.21}$$

and $\{P_a^*\}$ is the vector of equivalent nodal forces calculated as:

$$\{P_a^*\} = \{P_q\} - [k_{ab}][k_{bb}]^{-1}\{P_b\} \tag{3.22}$$

It should be mentioned that the inversion of $[k_{bb}]$ in Equations 3.21 and 3.22 is a formal one and may be avoided. Consequently, the number of matrix multiplications required to get the condensed stiffness matrix and equivalent nodal forces is reduced. This efficient method of calculation is achieved by using the following simple technique. Each matrix multiplication involving

the inverse of $[k_{bb}]$ is replaced by one unknown matrix. In other words, the following relations are assumed:

$$[k_{bb}]^{-1}[k_{ab}]^T = [r] \quad (3.23)$$

and

$$[k_{bb}]^{-1}\{P_b\} = \{s\} \quad (3.24)$$

where,

$[r]$ = an unknown matrix, and

$\{s\}$ = an unknown vector.

Applying the basic definition of the inverse of a matrix it is clear that:

$$[k_{bb}][r] = [k_{ab}]^T \quad (3.25)$$

and

$$[k_{bb}]\{s\} = \{P_b\} \quad (3.26)$$

A standard linear equations solution (112) is used to evaluate $[r]$ and $\{s\}$ directly from Equations 3.25 and 3.26.

Combining Equations 3.21, 3.22, 3.23 and 3.24, the required condensed element stiffness matrix and equivalent nodal forces are expressed in simple forms as follows:

$$[k_{aa}^*] = [k_{aa}] - [k_{ab}][r] \quad (3.27)$$

and

$$\{P_a^*\} = \{P_a\} - [k_{ab}]\{s\} \quad (3.28)$$

where $[k_{aa}^*]$ is the element stiffness matrix in local coordinates. The corresponding transformation matrix is given in Appendix A. The condensed global element stiffness matrix is obtained by substituting these matrices into Equation 3.9.

3.6 Soil Model

In general, the mechanical properties of soil are complex. The soil state of stress is a function of different variables and may be expressed as:

$$\sigma = F(\epsilon(t^), T^ (t^), w(t^), x (t^), \dots t^)$$

(3.29)

where,

$\epsilon(t^)$ = strain conditions,

$T^ (t^)$ = temperature effect,

$w(t^)$ = the moisture content,

$x^ (t^)$ = anisotropy, and

$t^$ = time.

In addition, soil variability in the ground poses another challenge to accurately model real soil by any unique stress-strain relationship. Therefore, soil models include only important variables in the domain of interest, while unessential variables are excluded. For cohesionless soil, which is used around steel culverts, it is possible

to discard for example, time effects.

3.6.1 Time-Independent Stress-Strain Models

Principal time-independent stress-strain relationships used in soil-mechanics may be classified into three broad groups: linear elastic models, nonlinear or variable modulus models and elastoplastic models.

Elastic isotropic models are fully defined by only two independent parameters. No complicated programming or large computational effort is involved in a linear elastic solution. These models may give an insight to the behaviour of soil in some cases, however, the results are unreliable in most cases. Bilinear elastic models assume initial values for the independent parameters until the stresses reach a yield value after which their values are reduced. Such models offer only marginal improvements.

Nonlinear modulus models express the independent soil properties as mathematical functions of stress or strain or both. Early developed stress-strain mathematical models were based on idealizing the geometric shape of particles by assuming regular spheres arranged in hexagonal (162) or other forms of packing (50, 105). These attempts were followed by nonlinear idealizations based on experimental stress-strain curves of actual soil specimens.

There are two major differences among the variable modulus models. Firstly, the mathematical function and to define the stress-strain relationship is assumed to be one of the following: a parabola, a hyperbola, a polynomial or a spline. Secondly, the method is set up to define either a secant or a tangential modulus. All these models, however, illustrate the same trend: the stiffness of soil is increased with the increase of confining pressure, as well as, with the decrease in shear strain. The details of the variable modulus models may be obtained from References 21, 31, 39, 40, 44, 45, 47, 51, 73, 88, 93, 94, 134, 135 and 160.

Elasto-plastic models relate the rate of stress to the rate of strain. They require a yield criterion, a hardening rule, and a flow rule. The first requirement is fulfilled by specifying a yield surface which is a function of stress or stress invariants. If the state of stress lies within the yield surface, the stress-strain law is assumed to be elastic. Plastic strains are superimposed on the elastic if the state of stress reaches the yield surface and attempts to cross it. In this case, the yield surface changes and strain hardening occurs. The hardening rule redefines the yield criterion after plastic deformation and is usually a function of plastic work and stress level. The third requirement

is achieved by assuming a plastic potential, the gradient of which relates the plastic strain rate to the plastic stress rate. The flow rule is associative, if the plastic potential is assumed to be equal to the yield surface function, otherwise it is said to be non-associative. The different elastoplastic models assume different yield surfaces, hardening rules or flow rules. Some of these models are referenced in 99, 126, 129, 130, 137, 139, 156, and 164.

Theoretically, elastoplastic models should simulate constitutive laws for soil better than variable modulus models. Abrupt increases in stiffness upon unloading are automatically taken into account. However, on the negative side, some of the models do not consider frictional contribution to shear strength of soil such as the non-frictional models. Frictional models with associated flow rules seem to predict unreasonably large dilatational strains. In addition, elastoplastic models are generally difficult to correlate with laboratory test data, which means that it is relatively difficult to determine their parameters.

On the other hand, the reasonable past success of the elasticity theory in soil mechanics lends some justification for its use in the soil steel structure problem. In particular, the use of an elastic solution is probably more appropriate for compacted sand than for many other soils to which it is commonly applied. Furthermore, the variable

modulus models have the ability to closely approximate experimental data. Hence, the parameters of these models are determined with relative ease. Adding their relative computational simplicity to these advantages, variable modulus models become more attractive to use.

The hyperbolic soil model is found to be the most suitable to simulate soil behaviour around culverts in this study. Its parameters, which are easily obtained from triaxial tests, have physical meaning. It is relatively easy to program in a finite element analysis. It has been widely and successfully used. In addition, typical reliable parameter values for different types of soil under different loading conditions have been completed and classified.

3.6.2 Hyperbolic Stress Strain Model

The hyperbolic stress-strain relationship is originally attributed to Kondner and Kondner and Zelasko (93, 94, 95). They showed that, for soil loaded under constant radial stress in a conventional triaxial compression test, the plot of principal stress difference versus axial strain can be approximated by a rectangular hyperbola with a high degree of accuracy. The shape of the proposed hyperbola is controlled by the initial slope and the asymptotic value of the stress

difference as shown in Fig. 3.10a. The hyperbolic curve can be represented by an equation relating the principal stress difference to the axial strain, as follows:

$$(\sigma_1 - \sigma_3) = \frac{\epsilon_a}{a + b\epsilon_a} \quad (3.30)$$

where,

σ_1 = major principal stress,

σ_3 = minor principal stress,

ϵ_a = axial strain, and

a and b = parameters whose values depend on the sand tested and the confining pressure.

Both 'a' and 'b' may be determined experimentally. Physically 'a' meaning can be visualized as for 'a' to be equal to the reciprocal of the initial tangent modulus E_i , and 'b' is equal to the reciprocal of the asymptotic value of stress difference, called the ultimate stress difference, $(\sigma_1 - \sigma_3)_{ult}$. Using transformed axes as shown in Fig. 3.10b, Equation 3.30 is simplified to a linear form written as:

$$\frac{\epsilon_a}{(\sigma_1 - \sigma_3)} = \frac{1}{E_i} + \frac{1}{(\sigma_1 - \sigma_3)_{ult}} \epsilon_a \quad (3.31)$$

where,

$\frac{1}{E_i}$ is the intercept of the resulting straight line, and

$\frac{1}{(\sigma_1 - \sigma_3)_{ult}}$ is the slope of the line.

It should be mentioned that Hansen (72) suggested other complicated hyperbolic forms, such as:

$$(\sigma_1 - \sigma_3) = \sqrt{\frac{\epsilon_a}{a + b\epsilon_a}} \quad (3.32)$$

and

$$(\sigma_1 - \sigma_3) = \frac{\sqrt{\epsilon_a}}{a + b\epsilon_a} \quad (3.33)$$

However, because Equations 3.32 and 3.33 cannot be simplified or transformed to linear forms, they were not pursued by other researchers.

The value of the two parameters in Equation 3.31 can be obtained by plotting the experimental data in the transformed form and determining the best straight line fit for it.

The described stress-strain model is stress-dependent for all soils, except fully saturated soils tested under unconsolidated undrained conditions. An increase in confining pressure results in a steeper stress-strain curve and a higher strength. Both the value of E_i and $(\sigma_1 - \sigma_3)_{ult}$ increase if σ_3 is increased. An empirical relationship between the initial tangent modulus and confining pressure has been suggested by Janbu (83). Based on his experimental work, the stress-dependent initial tangent modulus is expressed as:

$$E_i = K_s p_a \left(\frac{\sigma_3}{p_a} \right)^m \quad (3.34)$$

where,

K_s = an experimental parameter called the modulus number,

m = an experimental parameter called the modulus exponent, and

p_a = the atmospheric pressure.

Both K_s and m , which are dimensionless numbers, may be determined by plotting the experimental values of $\frac{E_i}{p_a}$ versus $\frac{\sigma_3}{p_a}$ for a series of tests on a log scale, and fitting a straight line to the data. Fig. 3.11 shows the straight line representation of Equation 3.34. The atmospheric pressure in Equation 3.34 is introduced to keep the parameters K_s and m unchanged when using different systems of units, as long as the units of p_a are the same as that of E_i and σ_3 .

The compressive strength, or the stress difference at failure, $(\sigma_1 - \sigma_3)_f$, may be expressed in terms of the confining pressure, σ_3 , using the familiar Mohr-Coulomb failure criterion, as follows (160):

$$(\sigma_1 - \sigma_3)_f = \frac{2\sigma_3 \sin \phi + 2c \cos \phi}{1 - \sin \phi} \quad (3.35)$$

where ϕ and c are the Mohr-Coulomb strength parameters

shown in Fig. 3.12. ϕ is the angle of internal friction, and c is the cohesion intercept.

Duncan et al. (51) contributed to the development of a convenient expression for the tangent modulus based on the foregoing relationships. They related the stress difference at failure to the asymptotic stress difference through the use of a failure ratio parameter, R_f , as follows:

$$(\sigma_1 - \sigma_3)_f = R_f (\sigma_1 - \sigma_3)_{ult} \quad (3.36)$$

where the failure ratio R_f is always smaller than unity, and varies between 0.5 and 0.9 for most soils.

For a constant minor principal stress, σ_3 , the tangent modulus E_t can be expressed as:

$$E_t = \frac{\partial}{\partial \epsilon_a} (\sigma_1 - \sigma_3) \quad (3.37)$$

An expression for the tangent modulus value may be obtained by carrying out the following three steps. First, Equation 3.30 is differentiated with respect to ϵ_a . Second, ϵ_a is eliminated from the result of differentiation by using its value from Equation 3.31. Finally, Equations 3.34, 3.35 and 3.36 are substituted into the resulting expression. The following equation for the tangent modulus results:

$$E_t = \left[1 - \frac{R_f(\sigma_1 - \sigma_3)(1 - \sin\phi)}{2\sigma_3 \sin\phi + 2c \cos\phi} \right] K_s p_a \left(\frac{\sigma_3}{p_a} \right)^m \quad (3.38)$$

The five parameters in Equation 3.38, R_f , ϕ , c , K_s and m , may be directly evaluated on the basis of data obtained from standard triaxial tests. The values of these hyperbolic parameters have also been compiled for a wide range of soil types and testing conditions in several reports (98, 160).

Parameter values used in this research are obtained from published properties for soils for which the stress-strain data are considered to be of the highest quality and the greatest dependability.

3.6.3 Unloading and Reloading Modulus

It has been reported by many researchers (62, 74, 75, 91, 98, 160) that primary loading strains for soil are only partially recoverable upon unloading. If soil is reloaded, it behaves nearly elastically. Fig. 3.13 shows the stress strain curve for a soil specimen in a triaxial test during primary loading, unloading at some stage during the test, and reloading. During unloading, the stress-strain curve is steeper than the initial tangent for primary loading. During reloading, the slope of the curve is almost as steep as the unloading curve.

Experimental work by Duncan and Chang (51) has shown that it is reasonably accurate to approximate the behaviour during unloading and reloading as a linear and elastic behaviour, thus ignoring any hysteresis effects. One value for the modulus, E_{ur} , may be used for both unloading and reloading. It is represented by an equation similar to Equation 3.34 as follows:

$$E_{ur} = K_{ur} p_a \left(\frac{\sigma_3}{p_a} \right)^m \quad (3.39)$$

where E_{ur} is the unloading-reloading modulus value, and K_{ur} is unloading-reloading modulus number.

The value of the exponent 'm' in Equation 3.39, which is a measure of the effect of confining pressure, is practically equal to the 'm' value during primary loading. However, the value of K_{ur} , which is always greater than the value of K_s , may vary between 1.2 K_s for stiff soil such as dense sands and 3 K_s for soft soils like loose sands (160)..

3.6.4 Hyperbolic Volume Change Behaviour

To represent the mechanical behaviour of any material, at least two independent stress-strain coefficients are required. Wong and Duncan (160) have determined a nonlinear expression for tangent Poisson's ratio by analyzing the volume changes which occur during a

triaxial test. The volumetric strain in a triaxial test is given by:

$$\epsilon_{vo} = \epsilon_a + 2\epsilon_r \quad (3.40)$$

where ϵ_r is the radial strain.

Fig. 3.14a illustrates the variation of ϵ_a with ϵ_r . The resulting curve may be reasonably approximated by a hyperbolic equation of the form:

$$\epsilon_a = \frac{-\epsilon_r}{v_i - d^* \epsilon_r} \quad (3.41)$$

where v_i is the initial Poisson's ratio; d^* is an experimental parameter representing the change in the value of Poisson's ratio with radial strain.

The hyperbolic equation may be transformed into a linear equation represented in Fig. 3.14b and given by:

$$-\frac{\epsilon_r}{\epsilon_a} = v_i - d^* \epsilon_r \quad (3.42)$$

For most soils, except saturated soils under undrained conditions, v_i decreases with the increase in confining pressure as shown in Fig. 3.15. This relation is expressed by the following equation:

$$v_i = G-F \log_{10} \left(\frac{\sigma_3}{p_a} \right) \quad (3.43)$$

where,

G = value of v_i at one atmosphere confining pressure,

and

F = the reduction in v_i for a ten-fold increase in σ_3 .

By differentiating equation 3.41 with respect to ϵ_r , eliminating the strain using Equations 3.30, 3.34, 3.35 and 3.36, and substituting Equation 3.43 into the result, the tangent Poisson's ratio may be written in terms of stresses as follows:

$$v_t = \frac{G - F \log \left(\frac{\sigma_3}{p_a} \right)}{\left[1 - \frac{d^2 (\sigma_1 - \sigma_3)}{k_s p_a \left(\frac{\sigma_3}{p_a} \right)^m \left[1 - \frac{R_f (\sigma_1 - \sigma_3) (1 - \sin \phi)}{2 \sigma_3 \sin \phi + 2 c \cos \phi} \right]} \right]^2} \quad (3.44)$$

3.7 Beam Finite Element for Conduit Walls

Because no buckling analysis is involved in this study, curved finite elements are not necessary to represent conduit walls. The straight beam elements are adequate, provided that a sufficient number of elements are used to approximate the curved shape of the cross-section. The element is defined by two nodes, each having three degrees of freedom as shown in Fig. 3.16.

The beam has constant properties along its longitudinal axis. The displacement interpolation functions of the beam element with respect to local coordinates are given by the following expressions:

$$u = \alpha_1 + \alpha_2 x \quad (3.45a)$$

$$v = \alpha_3 + \alpha_4 x + \alpha_5 x^2 + \alpha_6 x^3 \quad (3.45b)$$

$$\lambda = \frac{dv}{dx} \quad (3.45c)$$

where λ is the rotation; and the coefficients α_1 to α_6 are given by:

$$\alpha_1 = u_1 \quad (3.46)$$

$$\alpha_2 = \frac{u_2 - u_1}{L} \quad (3.47)$$

$$\alpha_3 = v_1 \quad (3.48)$$

$$\alpha_4 = \lambda_1 \quad (3.49)$$

$$\alpha_5 = \frac{1}{L^2} (3v_2 - 3v_1 - 2L\lambda_1 - L\lambda_2) \quad (3.50)$$

$$\alpha_6 = \frac{1}{L^3} (2v_1 - 2v_2 + L\lambda_1 + L\lambda_2) \quad (3.51)$$

where L is the length of the beam element.

The local stiffness matrix of the beam element and its transformation matrix are given in Appendix A.

3.8 Interface Finite Element

In the conventional finite element analysis, the common nodes at the contact surface between two materials undergo displacements which are the same for the two materials. Therefore, possible relative movements between the two materials under certain cases of loading are not accounted for. In order to overcome this deficiency, caused by using the same node for both materials, an interface finite element is introduced between different materials. The element is designed to handle the interface behaviour, and allow for independent displacements of the two materials in contact. This is basically done by assigning a different nodal point number on each side of the interface.

3.8.1 Available Interface Elements

Interface conditions in a finite element formulation may be treated by using either the method of constraints or the method of stiffness. The first method is based on constraint equations to model interfaces (25, 30). A complete finite element formulation using the method of constraints for soil-culvert system is given by Katona et al. (84). This method requires a larger stiffness matrix, more computer time than the method of stiffness, and an iteration technique, which does not always

converge.

The method of stiffness is basically a simple concept in which an element across the interface with different normal and tangential stiffnesses is used. The concept of adding a linkage element stiffness to the local stiffness matrix was developed by Ngo and Scordellis (120) in the course of the analysis of reinforced concrete beams. Goodman (69) developed a one-dimensional finite element to represent the interface behaviour for the jointed rock. In his formulation, the interface, between two adjacent locations at a distance L apart, is represented by one element having two pairs of nodes as shown in Fig. 3.17. Ellison (61) used a linear interface element for symmetric loading on a pile-soil system. Ghaboussi, et al. (66) presented a different approach to develop a one-dimensional interface finite element by using relative displacements between opposing sides of the slip surface as degrees of freedom. Although the linear interface element has been used successfully in retaining wall applications (27), its application in culverts and other curved surfaces between different materials causes several problems. At common nodes between consecutive interface elements, there is a considerable difference between resulting stresses calculated in each element.

Contradicting results are usually obtained if failure occurs in an element while inclined neighbouring elements are still working. Iterations necessary to treat such failure may be unsuccessful.

3.8.2 Spring Type Interface Element

A simple interface finite element is used here to reflect the state of normal and shearing stresses between the soil media and the conduit wall in a consistent manner.

While the spring type interface element represents a length along which the two materials are in contact, it actually has no physical dimension. Only its mechanical properties are of importance. Therefore, it can be placed between the conduit and soil without disturbing their geometry. The element can be conceptually thought of as consisting of two sets of springs: one in the tangential direction to the surface of the conduit wall and one in the normal direction.

The spring type interface element has only two nodes as shown in Fig. 3.18. Initially, the two nodal points of the interface occupy the same position when no stress exists between the two materials. The local coordinates originate at the element location itself, and the 'x' axis is oriented in the direction tangential

to the surface at the interface. The strain energy stored in a system of springs is known to be equal to the work done by internal forces in each spring during its deformation. The strain energy of the interface element, U_s , may be written as:

$$U_s = \frac{1}{2} \sum \delta_i P_i \quad (3.52)$$

where,

δ_i = the relative displacement between the two nodes of the element in the direction of spring number 'i' and

P_i = the force in the same direction.

In matrix notation, Equation 3.52 may be rewritten as:

$$U_s = \frac{1}{2} \{\delta\}^T \{P\} \quad (3.53)$$

in which

$$\{\delta\} = \begin{Bmatrix} u_2 - u_1 \\ v_2 - v_1 \end{Bmatrix} \quad (3.54)$$

$$\{P\} = \begin{Bmatrix} P_s \\ P_n \end{Bmatrix} \quad (3.55)$$

where,

u_2 = tangential displacement of the top node.

u_1 = tangential displacement of the bottom node,

v_2 = normal displacement of the top node,

v_1 = normal displacement of the bottom node,

P_s = tangential force, and

P_n = normal force

The force vector is related to the relative displacement vector through a matrix of spring stiffnesses as follows:

$$\{P\} = [k_D]\{\delta\} \quad (3.56)$$

in which $[k_D]$ is a diagonal material property matrix given by:

$$[k_D] = L \begin{bmatrix} k_s & 0 \\ 0 & k_n \end{bmatrix} \quad (3.57)$$

where,

k_s = unit tangential stiffness for the element,

k_n = unit normal stiffness, and

L = length along the interface corresponding to the element.

The variables k_s and k_n are determined experimentally as explained in Section 3.9.

Substituting Equation 3.56 into Equation 3.53 yields:

$$U_s = \frac{1}{2} \{\delta\}^T [k_D] \{\delta\} \quad (3.58)$$

The relative displacement vector $\{\delta\}$ is related to the nodal displacement vector $\{q\}$ as follows:

$$\{\delta\} = [E]\{q\} \quad (3.59)$$

in which;

$$\{q\}^T = \{u_1 \ v_1 \ u_2 \ v_2\} \quad (3.60)$$

and

$$[E] = \begin{bmatrix} -1 & 0 & 1 & 0 \\ 0 & -1 & 0 & 1 \end{bmatrix} \quad (3.61)$$

Substituting Equation 3.59 into 3.58, yields the strain energy, in terms of the nodal displacement vector as follows:

$$U_s = \frac{1}{2} \{q\}^T [E]^T [k_D] [E] \{q\} \quad (3.62)$$

Comparing Equation 3.62 with the strain energy expression in Equation 3.7, the element stiffness matrix of the interface finite element, with respect to its local coordinates may be written as:

$$[k_{e_i}] = [E]^T [k_D] [E] \quad (3.63)$$

which yields

$$[k_e] = L \begin{bmatrix} k_s & 0 & -k_s & 0 \\ 0 & k_n & 0 & -k_n \\ -k_s & 0 & k_s & 0 \\ 0 & -k_n & 0 & k_n \end{bmatrix} \quad (3.64)$$

The following transformation matrix is used to transform the local element stiffness matrix, given by Equation 3.64, to a global matrix:

$$[T] = \begin{bmatrix} \cos\theta & \sin\theta & 0 & 0 \\ -\sin\theta & \cos\theta & 0 & 0 \\ 0 & 0 & \cos\theta & \sin\theta \\ 0 & 0 & -\sin\theta & \cos\theta \end{bmatrix} \quad (3.65)$$

where θ is the angle of inclination of the local coordinates with respect to the global coordinates.

Under the effect of loads applied to the soil-stress structure, the nodes of the interface element, initially at the same position, are displaced. The average interface stresses can be directly obtained, in terms of relative displacements, as follows:

$$\sigma_n = k_n (v_2 - v_1) \quad (3.66)$$

$$\tau_s = k_s (u_2 - u_1) \quad (3.67)$$

where,

σ_n = average normal stress, and

τ_s = average shear stress.

3.9 Interface Model

The value of the interface unit normal stiffness, k_n , is expected to increase with an increase in the normal compressive stress, and to diminish to zero once tension is developed. The assigned values of k_n used in this study are discussed in Section 3.9.1. On the other hand, the unit shear stiffness, k_s , is expected to increase with an increase in the compressive normal stress, as well as with a decrease in the shear stress level. Herein, the variation of the interface shear stiffness with the acting normal and shear stress is assumed to be nonlinear. The mathematical formulation of this nonlinear conduct of the interface finite element in shear is given in Section 3.9.2.

3.9.1 Unit Normal Stiffness at the Interface

Equation 3.66 suggests that the unit normal stiffness k_n , may be obtained from a direct shear box test on composite specimens. Each specimen consists partly of granular soil similar to that used in the soil-steel structure system, and partly of structural galvanized steel. When a normal stress is applied, the specimen shortens. The total measured deformation in the normal direction may be regarded as a summation of three distinct deformations. These are: elastic shortening

of the structural steel, the deformation of the granular soil, and the interface normal deformation. If the interface deformation is calculated for several applied normal stresses, the results may be plotted on a graph as shown in Fig. 3.19. For working stresses, the normal stress deformation curve would be a straight line indicating that the unit normal stiffness is constant.

In the absence of accurate test data, the normal stiffness may be assigned a very large value to prevent significant overlap between the two materials. A value in the order of 10^6 lb/in³ reflects a very small interference between the two nodes in the normal direction under the effect of an acting compressive stress. Physically, this means that the soil and structure wall are almost rigidly connected in the normal direction when the two materials are pressed against each other. The validity of this assumption has been checked during the study. It has been found that a large change in the assigned value of the unit normal stiffness would almost yield the same state of stresses at the end of a finite element analysis. Only the relative displacements between the two nodes of each interface element in the normal direction have been affected.

It is obvious that no tension stress can exist

at the interface between the soil and conduit wall. Therefore, the value of the unit normal stiffness is adjusted to zero if a tensile stress exists in the normal direction of the interface element. Physically, this implies that the two nodes of the element are not connected to each other. Therefore, an analysis based on this assumption yields a separation between the two materials and a state of no stress at the interface element location.

3.9.2 Unit Tangential Stiffness at the Interface

Figure 3.19 also shows the expected shear stress-shear deformation curve for a direct shear box test on a composite specimen under constant normal stress. The slope of the curve is a measure of the unit tangential stiffness, k_s , is not constant as in the case of unit normal stiffness. It is a function of the acting normal and shear stress as well as the angle of friction between the soil and structural steel wall. Clough and Duncan (27) have shown that the nonlinear shear stress-displacement relationship may be represented by a hyperbola of the form:

$$\tau_s = \frac{\delta_s}{a + b\delta_s} \quad (3.68)$$

where δ_s is the interface shear displacement, and 'a' and 'b' are empirical coefficients determined experimentally.

As shown in Fig. 3.20, the stress displacement rela-

relationship, given by Equation 3.68, may be transformed to another set of axes, on which hyperbolae plot as straight lines. The transformed straight line equation is written in the following form:

$$\frac{\delta_s}{\tau_s} = a + b\delta_s \quad (3.69)$$

Consequently, coefficient 'a' becomes the intercept of the best fit straight line for the experimental values of δ_s/τ_s plotted against values of δ_s . The slope of the straight line on the transformed graph yields coefficient 'b'. The physical meaning of the hyperbolic coefficient 'a' may be clarified by observing Equation 3.68 when the shear displacement δ_s approaches zero. In this case, the initial unit shear stiffness, k_{si} , which is equal to $\frac{\tau_s}{\delta_s}$, approaches $\frac{1}{a}$. As the shear displacement approaches infinity, the shear stress in Equation 3.68 approaches $\frac{1}{b}$. Therefore, 'b' is the reciprocal of the asymptotic value of shear stress denoted by τ_{ult} . Since the shear strength at failure is reached before the shear stress-displacement curve becomes asymptotic, the failure shear, τ_f , is assumed to be related to the ultimate shear through the following equation:

$$\tau_f = R_{sf} \tau_{ult} \quad (3.70)$$

where R_{sf} is the failure ratio which is always smaller than unity.

The shear strength is directly proportional to the

acting normal stress. The constant of proportionality is the coefficient of friction between the soil and the wall material. The strength characteristics may be expressed as follows:

$$\tau_f = \sigma_n \tan \phi \quad (3.71)$$

where ϕ is the angle of friction between soil and conduit wall.

The initial shear stiffness, k_{si} , can be related to the normal stress acting on the interface according to an equation of the general form suggested by Janbu (83):

$$K'_{si} = K_I \gamma_w \left(\frac{\sigma_n}{p_a} \right)^{n_s} \quad (3.72)$$

where,

K'_{si} = dimensionless stiffness number,

n_s = stiffness exponent, and

γ_w = unit weight of water expressed in the same units as K'_{si} .

As shown in Fig. 21, K_I and n_s are determined experimentally by plotting $\log \left(\frac{K'_{si}}{\gamma_w} \right)$ versus $\log \left(\frac{\sigma_n}{p_a} \right)$, as obtained from the results of a series of shear box tests in which the acting normal stress varies. The intercept of the best fit straight line gives $\log (K_I)$, and the slope of the line yields n_s .

Substituting Equations 3.70 through 3.72 into Equation 3.68 yields:

$$\tau_s = \frac{\delta_s}{\frac{1}{K_I \gamma_w \left(\frac{\sigma_n}{p_a} \right)^{n_s}} + \frac{R_{sf} \delta_s}{\sigma_n \tan \phi}} \quad (3.73)$$

By definition, the unit shear stiffness is the slope of the tangent to the shear stress-displacement curve. It may be obtained by differentiating Equation 3.73 with respect to δ_s . Substituting the shear displacement from Equation 3.69 into the expression resulting from differentiation yields the following relationship for the unit shear stiffness:

$$k_s = K_I \gamma_w \left(\frac{\sigma_n}{p_a} \right)^{n_s} \left(1 - \frac{R_{sf} \tau_s}{\sigma_n \tan \phi} \right)^2 \quad (3.74)$$

The four parameters K_I , n_s , R_{sf} and ϕ appearing in the nonlinear equation for shear stiffness can be obtained from shear box tests on composite specimens.

3.10 Construction Simulation

As first pointed out by Terzaghi (150), the sequence of construction has a significant influence on earth pressures and structural behaviour. The effect of construction on long span corrugated metal conduits is even more pronounced because of their flexibility. Thus, it is essential that a reliable analytical technique has the capability to simulate anticipated construction processes. Furthermore, the construction simulation in available finite element applications is not complete because it also neglects compaction

simulation. Therefore, it is worthwhile to explain how these two important aspects of construction have been dealt with in the analysis.

3.10.1 Sequential Construction

Goodman and Brown (68) were the first to propose an incremental procedure to calculate dead load stresses. An analogous incremental analysis procedure, which takes into account nonlinearity, is used in this research. Each finite element mesh used in analyzing a soil-structure system, (Figs. 3.1 to 3.4), is broken into a series of small construction increments or layers. One layer at a time is added to the system and its effects on existing layers are analyzed. Placement of the layer is simulated by applying nodal forces that represent the weight of the added layer. The weight of a constant strain triangular element is distributed equally between its three nodes. For linear strain triangles, the weight of the element is equally distributed between its three mid-side nodes, as determined by equating the work done by the two systems of loads. The equivalent nodal forces for a linear strain quadrilateral element under its own weight are obtained by adding the equivalent nodal forces of its two linear strain triangles. Then, a condensation technique (65) is used to distribute the internal nodal forces between the

eight nodes of the element.

Each element in the layer being placed is assigned preliminary stresses consistent with the overburden pressure at its center. These assigned stresses are used to calculate the element tangent modulus and Poisson's ratio according to the nonlinear hyperbolic model. Then, a finite element analysis of the existing mesh, including the new layer under its own weight, is carried out. The resulting incremental displacements and stresses are added to the previously accumulated displacements and stresses for existing nodes and elements to yield the final values after constructing the new layer. For the new layer, the nodal points at the top are assigned zero displacements. This means that the positions of the top nodes immediately after placement of the layer are taken as the reference positions for measuring movements due to subsequent loading. The preliminary assigned stresses to the newly placed elements are replaced by the resulting incremental stresses at the end of the analysis. The final state of stress in each soil or interface element establishes the conditions for the next incremental analysis.

A new layer is then added and the procedure is repeated until the placement of fill above the crown of the steel structure is complete.

Since the weight of the steel structure is relatively small when compared to the weight of the soil elements it can be neglected. In general, during the first phase of construction where backfilling is completed to the crown of the steel structure, the nonlinearities are more pronounced than those of the second phase where soil layers are added above the crown level. The varying geometry which accompanies the incremental analysis in both phases is taken into account by allowing the finite element mesh to be modified as explained in Section 3.14.2.

3.10.2 Compaction Simulation

Accounts of the soil-steel structure behaviour during construction indicate that the specific degree of compactive effort in regions adjacent to the conduit is strongly reflected in the system response. Therefore, the compaction process also requires simulation. This is done by assuming a specified surface load to be acting along the top of the most recently added incremental layer during the sequential construction simulation. The value of this uniformly distributed surface load depends on the type and weight of compaction equipment to be used on site. Equivalent nodal forces that produce

the same work done by the assumed surface load are applied in the incremental analysis. In the case where constant strain triangular elements have bases along the top of soil, the equivalent nodal forces are obtained directly by dividing the total surface load on the top of the element equally between the two top nodes. Whereas, in the case of linear strain quadrilateral elements, an unequal distribution of the total surface load, between its three top nodes, results from energy consideration. The equivalent compaction force on each corner node is one sixth of the total element surface load. The intermediate node attracts two thirds of the load.

The incremental finite element analysis is performed under the effect of both the body weight loads of the new added layer, mentioned in Section 3.10.1, and the surface compaction load on the top layer. Resulting incremental stresses and displacements are added to existing stresses and displacements before the addition of the new layer to the system. The stresses and displacements of the new layer are treated as described in the previous section. Next, the material properties for soil and interface elements are updated according to the nonlinear relationships.

In order to complete the compaction simulation, the assumed surface loads must be removed. This removal cor-

responds to the compaction equipment leaving the area after compacting the added layer of soil. If another layer of soil is to be added to the system during construction simulation, the removed compaction loads are simultaneously applied. In other words, each compacted layer is subject to the effect of releasing the previously applied compaction loads during the following incremental analysis. Therefore, during an intermediate incremental finite element analysis that simulates the construction process, the acting nodal forces result from the algebraic summation of three components. The first component is due to the weight of the newly added layer and acts at all the nodes of the elements in the layer. The second component acts at the top surface nodes only, and represents compaction loads on the new layer. The third component of the nodal forces acts at the bottom surface nodes only, simulating removal of the compaction loads which were applied earlier on the lower layer.

Although the specified compaction loads on top of the added layer are removed during the simulation of the newest layer, their effect in densifying the soil is locked in the finite elements. This results from changes in both the elemental properties and geometry already being accounted for prior to removal of the

forces. Stiffer soil properties will result causing less deformation during unloading than loading. This simulates actual field compaction.

3.11 Iterative Procedure for Accurate Representation of Material Properties

A nonlinear finite element analysis employing an incremental technique usually starts with assigning initial values to define element properties. Next, analysis under incremental loading is performed. Finally, the resulting stresses are used to determine new element properties. These new properties constitute the initial conditions for the following incremental step.

The application of this traditional method of analysis leads to an increasing divergence between the piecewise linear element properties used in the incremental analysis and the assumed nonlinear properties for the element. A simplified clarification is presented in Fig. 3.22. The smooth curve shows the nonlinear stress-strain relationship that is followed in the course of successive incremental analyses. During each incremental finite element analysis, element properties remain constant. Therefore, the stress-strain path, during the first step, would follow the straight direction 'oa`' instead of the curved direction 'oa'. This

leads to a deviation between the actual and computed strains and stresses in elements. This deviation will be further amplified in the following incremental analysis as the stress-strain path follows 'ab`' instead of 'ab', and so on.

In this study, each incremental analysis is coupled with an iterative procedure to bring the piecewise linear stress-strain path much closer to the smooth curve. The details of the procedure are given below for soil and interface elements.

3.11.1 Iteration for Soil Elements

To improve soil properties representation during the incremental finite element analyses, the following iterative procedure is used:

- i. Under a certain loading condition, the incremental analysis starts on the basis of initial element properties, for example, the initial tangent of the nonlinear curve shown in Fig. 3.22. The stress-strain path would follow the straight line 'oa`'.

- ii. At the end of the analysis, the resulting stresses are used to calculate final element properties as given by Equations 3.38 and 3.44.

- iii. The initial and final properties are averaged, and the analysis is repeated for the same loading con-

dition using the average properties. The stress-strain path changes to 'oa' where 'a' is much closer to the nonlinear path 'oa'.

iv. The stress-strain path may be improved by repeating the iteration: i.e., final stresses and properties are calculated at the end of the first iteration, these properties are averaged with the initial properties to yield new properties that will be used in the repeated analysis.

v. At the end of the iterative procedure, the final stresses will be used to calculate the initial properties in the subsequent incremental analysis.

This procedure of iteratively refining the presentation of the soil elements yields results that are closer to the actual behaviour of soil-steel structures.

3.11.2 Iteration for Interface Elements

The value of unit tangential stiffness for an interface element at each increment is obtained by following the iterative procedure outlined below:

i. Under the effect of a certain loading condition, the initial properties for the interface element are used in a primary analysis, and corresponding normal and tangential stresses are determined for the element.

ii. The resulting stresses in the element are substi-

tuted into Equation 3.74 to calculate the corresponding unit tangential stiffness. The average tangential stiffness is then calculated.

iii. The finite element analysis is repeated under the same loading condition, using the average unit tangential stiffness. The resulting stresses are more accurate than those obtained at the end of the first iteration.

iv. A further improvement may be obtained by repeating the analysis using a modified average tangential stiffness.

v. At the end of the iteration, the final normal and tangential stresses are used to calculate the corresponding unit tangential stiffness. This new value is used as the initial stiffness for the interface element in the next incremental analysis.

3.12 Failure Consideration in Soil Elements

In the course of the incremental finite element analyses, tension or shear failure may occur in some soil elements. Tension failure is associated with a state of no pressure, and a possibility of migration of some soil particles to fill any gap that may develop. Shear failure is associated with a relative movement between soil particles along a plane

of shear. The analytical steps taken to consider these two types of failure are summarized below. Their effect on the state of stress in neighbouring elements is taken into account through a stress transfer technique (76, 163) described in Section 3.12.3.

3.12.1 Soil Tension Failure

At the end of each incremental analysis, the principal stresses in each element are calculated. It is known that for cohesionless soil, the presence of tension cannot be a realistic state of stress. The strength envelope passes through the origin of the shear-normal stress diagram, and lies totally in the compression zone. Therefore, if a tensile stress is detected in a soil element, the element is considered to have failed and cannot sustain any stresses.

In order to reduce the stresses in the finite element to zero, without violating equilibrium, a stress transfer technique (Section 3.12.3) is used. At the end of this process, the stresses in the element dissipate to neighbouring elements. Because the remaining stresses in the element become almost zero, the apparent tangent modulus given by Equation 3.38 reduces to zero. However, another assigned initial tangent modulus of the element under consideration is computed using a value of σ_3 equal

to 0.1 of the atmospheric pressure. This is used for the failing element in the following incremental analysis. It should be mentioned that the idea of using a minimum value for the stiffness of a soil finite element is not new (44, 45, 58). Similarly, the initial value of Poisson's ratio for the element to be used in the following incremental analysis is assumed to be equal to 0.49. The use of the suggested material properties for an element in tension failure leads to two possibilities during the following incremental analysis. The element may attract compressive stresses under the effect of incremental loading, and the analysis continues or the element may remain in tension. The stress transfer technique is reapplied. If several elements along a line indicate the development of tensile stresses during consecutive loading increments then local failure in the soil is assumed to have occurred and a failure load is calculated according to Section 3.12.4.

3.12.2 Soil Shear Failure

3.12.2.1 Curved Strength Envelope

Shear failure occurs in an element if its maximum shear stress exceeds the soil strength (Equation 3.35). For cohesionless soil, the cohesion intercept 'c' is equal to zero. If the angle of internal friction ' ϕ '

is constant the Mohr failure envelope becomes a straight line as shown by the dotted line in Fig. 3.23. However, it is known that the Mohr envelope is curved to some extent, and the wider the range of pressures involved, the greater the curvature. To represent this curvature analytically, the value of ϕ is assumed to vary with the confining pressure ' σ_3 '. In this case, ' ϕ ' is determined experimentally by enveloping each triaxial test circle of stress by a straight line starting at the origin. Wong and Duncan (160) have found that values of ϕ determined by this method decrease in proportion with the logarithm of the confining pressure. The equation representing this variation may be written as:

$$\phi = \phi_0 - \Delta\phi \log_{10} \left(\frac{\sigma_3}{p_a} \right) \quad (3.75)$$

where, ϕ_0 is the angle of internal friction for a confining pressure equal to the atmospheric pressure, and $\Delta\phi$ is the reduction in ϕ corresponding to a 10-fold increase in σ_3 .

3.12.2.2 Proposed Modifications

If at the end of an incremental analysis, a soil element fails in shear, the graphical representation of the state of stress will intersect the strength envelope as shown in Fig. 3.23. The stresses in the element subject to

failure are reduced from σ_{1fb} and σ_{3fb} to σ_{1f} and σ_{3f} respectively. This reduction is achieved by using the stress transfer technique where σ_{1f} and σ_{3f} are determined on the basis of the initial principal stresses σ_{1i} and σ_{3i} . During the incremental loading, the rate of change in the minor principal stress is assumed proportional to the rate of change in the major principal stress. This assumption can be expressed as follows:

$$\frac{\sigma_{3f} - \sigma_{3i}}{\sigma_{1f} - \sigma_{1i}} = \frac{\sigma_{3fb} - \sigma_{3i}}{\sigma_{1fb} - \sigma_{1i}} \quad (3.76)$$

Both Equations 3.35 and 3.76 deal with the principal stress at failure. They are used to determine the limits within which the principal stresses are kept during the stress transfer process.

The element properties used initially during the following incremental analysis cannot be obtained from Equations 3.38 and 3.44 because they yield zero tangent modulus and infinite Poisson's ratio. Instead, the modulus is calculated on the basis of a stress level equal to 0.95 of the stress level at failure, and Poisson's ratio is not allowed to exceed 0.49. If during the following incremental analyses, the shear failure still exists in the element or propagates to

neighbouring elements along a line, local failure is assumed to occur and the failure load is determined as explained in Section 3.12.4.

3.12.3 Stress Transfer Method

Following Zienkiewicz et al. (1963), the stress transfer method, used in this study to keep stresses in an element within limits without disturbing equilibrium, is summarized in the following steps:

- i. The equivalent nodal forces required to change the stresses in a certain element are evaluated.
- ii. Equal and opposite pairs of nodal forces are imagined to act at the element nodes. This will not disturb equilibrium.
- iii. One set of the forces vanishes when the stresses are reduced to the desired level.
- iv. The other set of nodal forces is applied as an external loading to the system. The analysis is carried out using the same properties for each element used in the incremental analysis. The resulting stresses and displacements are added to the corresponding stresses and displacements calculated at failure.
- v. The final stresses obtained in step 3 may indicate failure once again in the soil element

However, the deviation between the limiting state of stress, σ_{1f} and σ_{3f} , and the new state of stress will be considerably less than in the first case. This deviation is transferred into equivalent nodal forces and the procedure is repeated until the deviation from the limiting state of stress becomes negligible.

Local failure is assumed if the stresses in the element do not converge to the limiting values or if other neighbouring elements fail under the effect of the equivalent nodal forces.

3.13.4 Determination of Failure Load

Stability analysis of soil cover is performed by applying live load in equal increments. The continuously increasing applied load eventually leads to the start and propagation of failure along lines extending between the upper part of the structure walls and the surface of the soil. An example of a failure pattern under a centric concentrated load is shown in Fig. 3.24. A number is assigned to each of the soil elements that have failed. This number represents the number of live load increment at which failure has been initiated and continued to exist in the element. The linear arrangement of soil

elements that have failed represents planes of shear failure. In this example, increment No. 3 of the live load causes shear failure in the soil elements to extend along a full line. Therefore, failure is assumed to occur between increment No. 2 and increment No. 3. The exact value of the total live load that causes failure is determined graphically according to the state of stress in the last element to fail. A range of two increments before failure and two after is considered.

For each of these increments, the fraction of strength mobilized, or the stress level S , is calculated as follows:

$$S_{\ell} = \frac{\sigma_1 - \sigma_3}{(\sigma_1 - \sigma_3)_f} \quad (3.77)$$

Substituting Equation 3.35 into Equation 3.77, yields:

$$S_{\ell} = \frac{(\sigma_1 - \sigma_3)(1 - \sin \phi)}{2\sigma_3 \sin \phi + 2c \cos \phi} \quad (3.78)$$

Before failure, S_{ℓ} is less than 1, and after failure it exceeds 1. The four calculated values of S_{ℓ} are then plotted on a stress level-load graph as shown in Fig. 3.25. The failure load corresponds to a value of S_{ℓ} equal to 1.

3.13 Failure Consideration in Interface Elements

During the incremental analyses of a soil-steel structure system, the interface elements indicate the

shearing and normal stresses existing between the soil and structure. If an interface element is subjected to tensile stresses at the end of an incremental analysis, a tension failure must be considered to represent the actual no-tension behaviour at the interface. If the shear stresses at an interface element, subjected to compressive normal stresses, exceed the allowable limits, then shear failure will occur.

3.13.1 Interface Tension Failure

The soil and conduit walls are not bonded, thus no tension stress can exist between the two materials. If, under certain loading condition, a tensile stress develops in an interface element, the incremental analysis is repeated after changing the element properties. Both the unit normal and unit tangential stiffness, are assigned a value of zero for the above element. The zero tangential stiffness reflects the fact that no shear stress can exist in the absence of a normal stress. The results of the repeated analysis demonstrates that a complete separation between the two nodes of the failing interface elements will occur. The corresponding shear and normal stress at the location under consideration will be zero.

In the following incremental analysis, the initial,

conditions for the element, after failure are:

- i. The two nodes of the element are assumed to be coinciding,
- ii. the total normal and shearing stresses are set to zero,
- iii. the unit normal stiffness is assigned its original value, and
- iv. the unit tangential stiffness is assumed equal to the last value prior to failure.

If the results at the end of the incremental analysis show compressive stresses, the analysis will continue.

3.13.2 Interface Shear Failure

During an incremental analysis, shear failure occurs at an interface element if its resulting shear stress exceeds the shear strength given by Equation 3.71. If failure takes place, the unit tangential stiffness of the element is reduced and the incremental analysis is repeated. A larger relative displacement between the two nodes of the element occurs in the tangential direction. The reduction factor is taken inversely proportional to the shear stress level defined as:

$$S_s = \frac{\tau}{\tau_F} \quad (3.79)$$

Substituting Equation 3.71 into Equation 3.79, the reduced unit tangential stiffness becomes:

$$k_{sr} = k_s \times \frac{\sigma_n \tan \phi}{\tau_s} \quad (3.80)$$

Repeated analysis yields a smaller value of shear stress. If it still exceeds the limit given by Equation 3.71, the unit tangential stiffness is reduced once again according to Equation 3.80. This procedure is repeated until shear failure is eliminated.

3.14 Computer Program

A computer program was developed to handle the mathematical computations for the incremental analyses described in this chapter. The main features of the program are briefly discussed in the following sections.

3.14.1 Automatic Mesh Generation

Providing the mesh data required by the finite element program on cards requires time, effort and a large number of data cards. The average mesh contains 285 nodes, 556 degrees of freedom, 30 beam elements, 30 interface elements, 38 quadrilateral elements and 186 triangular elements.

In order to simplify the use of the program, a scheme for an automatic generation of the incrementally

constructed finite element meshes is developed. The mesh data is generated from a minimum number of geometric parameters such as height and span of the conduit, height of cover and number of lifts.

Unlike other programs (55, 56, and 84) this program uses a numbering system for the nodes that leads to a minimum band width. This considerably reduces the computing time.

Eccentric loads are analyzed by generating a full mesh extending a length of six times the span of the conduit. The variables involved in the automatic mesh generation are handled with relative ease. The number of layers below or above the conduit and height of cover are determined by the user. Locations of external applied loads may be given either by their nodal positions or by their coordinates.

3.14.2 Moving Local Axes

At the end of each incremental analysis, geometrical changes are taken into account. Nodal coordinates are updated by adding the incremental global displacements to the coordinates at the start of the incremental analysis. Therefore, local coordinates and areas of triangular and quadrilateral elements are modified according to the new nodal coordinates. This incremental up-

dating process compensates for nonlinearity due to large deformations of the soil-steel structure.

3.14.3 Automatic Initial Values for New Elements

During construction simulation, a new layer of soil is added to the mesh and the modified system is analyzed. The incremental analysis is carried out after assigning initial material properties. For soil elements, the height at the centroid of the element is automatically calculated and used to get the vertical and horizontal stresses. These values are substituted into Equations 3.38 and 3.44 to define the initial element properties. As previously mentioned in Section 3.11.1, these properties will be modified after the first iteration. Similarly, whenever contact between the culvert walls and the new layer occurs, a new interface element is inserted between the nodal points that are in contact. The depth of soil at the interface location is used to get approximate shear and normal stresses. The calculated unit shear stiffness is used in the initial analysis, and its value is modified after iteration according to Section 3.11.2.

CHAPTER IV

EXPERIMENTAL VERIFICATION

4.1 General

In order to verify the analytical formulation and the developed computer program, the experimental results of a series of live load tests conducted by the Ontario Ministry of Transportation and Communications on existing soil-steel structures with shallow depths of cover are used.

The details of two of the tested structures are first described. This is followed by a brief summary of the instrumentation and test procedure. Finally, a comparison between the analytically calculated and the measured static load responses of the conduit wall for each structure is presented.

A laboratory scale test was also carried out to verify the analytical prediction of load causing failure in soil. A brief description of laboratory instruments used in the test, procedure and results is given at the end of the Chapter.

4.2 Live Load Field Tests

Several existing long span flexible culverts were tested in Ontario (17) in order to measure thrusts and moments in their walls due to live loads. Two of these culverts can be classified as soil-steel structures under shallow cover. The details of these two structures are given below since their experimental results are later compared to theoretical values obtained from the developed computer program.

4.2.1 Details of Soil-Steel Structures Tested Under Shallow Cover

The two flexible culverts tested under shallow cover are the White Ash Creek and the Adelaide Creek culverts. They have different cross-sectional shapes; however, their height of cover to span ratios are less than 1/5, which is considered fairly shallow.

The first culvert, the White Ash Creek soil-steel structure is located on Highway 21 in Thamesville. Its details are given in Fig. 4.1. It is a Westeel Rosco k-D plate pipe. Its metal wall is composed of 6 in. x 2 in. corrugated plate with a thickness of 0.184 in. Its cross-section is circular with a diameter of 25 ft. The soil cover ranges between 3 ft. and 4 ft. 1 in. which is considered to be extremely shallow in comparison to its span. The conduit is free from any special features such as

transverse ribs, etc. Backfill is reported to be of well compacted, good quality, granular material.

The second tested structure is the Adelaide Creek soil-steel structure, which is located on Highway 22. This, too, is a Westeel Rosco k-D plate pipe; however, it is of horizontally elliptical cross-section having three radii as shown in Fig. 4.2. The span of the structure is 23 ft. 10 in. and the rise is 13 ft. 5 in. The structure has a fairly shallow cover, ranging between 4 ft. 1 in. and 4 ft. 4 in. As in the case of White Ash Creek, the conduit wall is composed of 0.184 in. thick plates of 6 in. x 2 in. corrugation profile. No special features are present and backfill is of well compacted good quality granular material.

4.2.2 Instrumentation

Strains in culvert walls were monitored by means of temperature-compensated uniaxial electrical resistance gauges installed on the inside of the culvert. At every location, three gauges were installed. Positions of gauges at a typical location are shown in Fig. 4.3. It should be noted that while it was possible to install a gauge at the crest and another one at the valley of the corrugations, the middle gauge could not always be fixed at the exact center of the corrugated metal. Gauges were

installed at six different locations in the central cross-section of White Ash Creek structure. For the Adelaide Creek structure, nine locations were instrumented at its central cross section. Positions of the instrumented locations on the central cross-section of each structure are shown in Figs. 4.4 and 4.5.

Displacement transducers were used to measure vertical deflection of the crown and relative horizontal movements of spring lines at each instrumented cross-section under the effect of applied live loads.

The strain gauges and displacement transducers were connected to a computer based data acquisition system. It had the ability to instantaneously read the output of all the gauges and transducers, keep it in a memory, and then write the results through a printer.

Two testing vehicles were used to apply the live load. Their axle weights were regulated by means of concrete blocks. For each vehicle, two levels of weights were used. Load level No. 2 has heavier weights on the rear axles than for load level No. 1. The axle spacings and weights of one of the testing vehicles are shown in Fig. 4.6. The other testing vehicle has the same dimensions and very similar weights.

4.2.3 Testing Procedure

Preparation of the site for testing started by determining a transverse center line on the highway directly above the crown of the buried structure. This was done using ordinary surveying procedure. After marking clearly this main transverse line, seven parallel lines were drawn 5 ft. apart on one side of the center line. These transverse lines indicated the positions at which the centroid of the rear two axles of the testing vehicle or vehicles would be located during testing. Fig. 4.7 shows the positions of the transverse lines, referred to as rear tandem positions, as they are numbered in each test.

In the longitudinal or highway direction, the center line of the highway was located in the same vertical plane containing the cross-section of the soil-steel structure that was instrumented. To study the load dispersion in the longitudinal direction of the structure, six lines that are parallel to the longitudinal center line of the highway were marked. Each of these longitudinal lines including the center line constituted a lane along which the testing vehicle would travel, the longitudinal center line of the vehicle being in the same vertical plane as the longitudinal line. The distances between these lanes and their numbering system are shown in Fig. 4.8. In addition to the seven lanes along which a single testing

vehicle travelled, Fig. 4.8 shows what is referred to as lane number 8. It is designated to indicate that two testing vehicles travelled parallel to each other in the same direction symmetrically about the instrumented cross-section, one at line number 2 and the other at line number 6. It may be mentioned here that since the study of the live load dispersion in the longitudinal direction of the soil steel structure is beyond the scope of this research, only lane number 4 and lane number 8 are of interest and are analyzed using the theoretical formulation and finite element mesh mentioned in Chapter III. Hence, only the experimental results corresponding to these two lanes will be presented and discussed.

Before each static test, readings of all instruments were taken without live load on the structure. Heavy concrete blocks of known weight were mounted in position on one testing vehicle. The operation of mounting the concrete blocks was completed away from the soil steel structure location.

With the weights of each axle of the testing truck known, the vehicle moved slowly towards the site. A guide had to direct the driver to travel exactly along lane number 1. At position number 1, the vehicle was stopped and the computer based data acquisition system produced the readings of all the strain gauges and

displacement transducers in the instrumented cross-section of the culvert. Then, the vehicle had to move slowly in the same lane until the next stop at position number 2, 5 ft. from position number 1; and the reading procedure and printing was repeated.

This sequence was repeated until the output of the eight positions in lane number one were recorded. Then, the testing vehicle moved away from the site, and a final set of readings of all strain gauges and displacement transducers were recorded without any load in the lane or on the structure.

Then, for each of the lanes number 2 to number 7, the same procedure was repeated where an initial and a final set of readings, without load on the structure, in addition to readings for the testing vehicle at each position in the lane under consideration, were recorded.

At the same time, the second testing vehicle was loaded with concrete blocks away from the site of the structure to yield approximately the same axle weights as the first testing vehicle. The final step in the test started by taking instrument readings without load on the structure. Then the two vehicles moved as one unit to different positions along what is termed lane number 8. Each time, a set of readings for the gauges and transducers was recorded. A last record of the readings was taken

after clearing the site from the moving vehicles.

After finishing this first round of testing on the soil-steel structure, the number of concrete blocks on each vehicle was increased and a second round of testing was carried out for the new live load level.

4.2.4 Preparation of Test Results

The M.T.C. provided the recorded test outputs and the writer had to interpret the strain readings and calculate thrusts and moments in each structure wall under different loading conditions. The following steps have been done to prepare results for presentation.

First, the strain at each uniaxial electrical resistance gauge position due to live load effect was calculated taking into account the possible gauge readings drift. The drift in gauge readings was detected by comparing the reading recorded before starting the loading in a certain lane to the reading taken after the testing truck left the lane away from the site. In most cases, these two readings were not the same, the difference being a few microstrains.

To eliminate the effect of this drift, it was distributed equally according to the number of loading conditions between the two readings. Hence, the strain at a certain location due to a given live load was calculated as:

$$\epsilon = \epsilon' - \frac{\epsilon_o(n+1-n') + \epsilon_f(n')}{n+1} \quad (4.1)$$

where,

ϵ' = strain gauge reading under the effect of live load,

ϵ_o = initial reading before the live load entered the lane under consideration,

ϵ_f = final reading after the live load left the lane,

n' = number of the position of the load, and

n = total number of positions.

Second, the calculated strains of the three electrical resistance gauges installed at a certain location in the cross-section of the soil-steel structure are considered. The thrust and moment are calculated using only two strains: that at the crest, and that at the valley of the corrugations. The middle gauge strain is used only as a control to check that the variation between the top and bottom gauge strains is approximately linear, since it was not possible to fix it exactly in position.

The thrust at a location is given by:

$$T = \frac{EA}{2}(\epsilon_c + \epsilon_v) \quad (4.2)$$

where,

ϵ_c = strain calculated at the crest of the corrugation at the location where the thrust T per unit

length of the culvert wall is measured, and ϵ_v = strain calculated at the valley of the corrugation.

The moment per unit length of the culvert wall is calculated as follows:

$$M = \frac{EI}{d_c} (\epsilon_c - \epsilon_v) \quad (4.3)$$

where, d_c = depth of corrugation which is 2 in. in the case of the White Ash Creek and Adelaide Creek structures.

Using the structural notations, positive strain means tensile strain, the thrust given by Equation 4.2 is tension when its sign is positive. Positive moment given by Equation 4.3 causes tension at the extreme fibers on the inside of the structure.

Modulus of elasticity of steel is assumed to be 29,000 ksi and Poisson's ratio 0.3. The two structures are made up of 0.184 in. thick plates. The moment of inertia of this plate was taken to be 0.108 in. 4/in. and its cross-sectional area to be 0.228 in²/in.

The measured structure wall thrusts and moments are presented below and compared with analytical results computed using the developed computer program.

In general, the two-dimensional plane-strain analysis involves an inherent assumption regarding live loads. It does not consider the variation of their effects in the third dimension, i.e., it deals only with line loads. However, the structures under consideration have been tested under axle loads which disperse through soil both longitudinally and transversely. A realistic simulation of a concentrated live load in the two-dimensional analysis of the transverse direction should account for a dispersion in the longitudinal direction at a slope of two vertically to one horizontally (124).

Two methods of representing the applied axle loads in the plane strain finite-element analysis are compared. In the first method, the intensity of an axle load is obtained by dividing the load value by the axle width. The full intensity is applied in position at the top surface of the soil mesh; and a corresponding part of the applied load intensity is assumed to be acting in an upward direction at the bottom of each layer below the position of the axle load. These upward forces account for the dispersion in the longitudinal direction by representing the parts of the load supported by neighbouring two-dimensional slices at different depths.

The second method accounts for the longitudinal dispersion first, then a line load equivalent to the dispersed

load is directly applied in the two-dimensional finite element mesh. In this simplified method, the intensity of the loading at the level of the crown of the conduit, after dispersion at an angle of two to one in the third dimension, is applied as a surface line load.

In a preliminary investigation, the White Ash Creek and the Adelaide Creek Structures are analyzed under the effect of one testing vehicle load having the rear tandem in a concentric position with the centre-line of the cross-section of the conduit. For each structure, the live load is represented according to the first method and the thrust and moment results in the different beam elements simulating the structure walls are shown in Table C.1. The first method is denoted by P_d . The results obtained by representing the live load according to the second method, denoted by P_d' , are also summarized in the table. A comparison between the two methods indicates that the difference between the resulting thrusts or moments does not exceed 5%. The second method is on the conservative side. Based on these comparisons, the live axle load is represented throughout this study according to the second simplified method.

4.2.5 Comparison of Experimental and Analytical Results

Experimentally obtained thrusts and moments in the central cross-sections of White Ash and Adelaide Creek structures under the effect of live loads are compared with analytical results. Two positions are considered for each conduit: Position 1, in which the rear tandem load is concentric with the conduit centre line, and Position 2, in which the eccentricity of the rear tandem load is 5 ft. Only Load Level 2 results are presented since its larger response has the same trend as that of Load Level 1.

The analytical results are based on incremental analysis in which the following properties for dense sand are assumed (160): $K_s = 3100$, $R_f = 0.92$, $m = 0.52$, $\phi_o = 45^\circ$, $\Delta\phi = 3^\circ$, $G = 0.34$, $F = 0.12$, $d^* = 75.9$ and $\gamma = 0.069 \text{ lb/in}^3$. The nonlinear behaviour of the interface elements is reflected by using the following experimental parameters (110): $K_I = 43070$, $R_{sf} = 0.834$, $n_s = 0.6$, and $\phi^* = 23^\circ$.

4.2.5.1 Axial Thrusts

Live load thrusts, due to one and two vehicle loads in Position 1 over White Ash Creek structure, are shown in Figs. 4.9 and 4.10. The conduit wall thrusts computed

from measured strains, and those obtained by the proposed finite element analysis are plotted.

In general, good agreement is found between the analytical and experimental results. It may also be noticed that the analytical results are closer to the measured responses for the case of Lane 8 when compared to those for Lane 4. This is attributed to the fact that two vehicles beside each other cause the applied loads on corresponding axles to be closer to the line load assumed in the finite element analysis.

Both experimental and analytical results show that the live load thrust is far from being uniform around the conduit as assumed in the ring compression theory. The thrust is maximum at the haunches of the upper half of the conduit. It diminishes quickly in the lower half because of the effect of dispersion of the applied surface loading.

The effect of loading eccentricity for circular soil-steel structures is noticed in Figs. 4.11 and 4.12. In these figures, the analytical thrust distributions due to truck loads in Position 2 over White Ash Creek culvert are compared to experimental values. The eccentricity of the nearest axle load to the centre line of the conduit cross-section is 2 ft, and that of the centroid of the rear tandem load is 5 ft.

Reasonable agreement is also noticed between

thrusts as computed from measured strains at the six strain gauge locations and the corresponding thrusts obtained analytically by the finite element method. Few points show experimental results which are slightly higher than the corresponding analytical values. However, these points are located in the zone of low thrust level.

Compared to the centric situation, the maximum thrust occurs at the haunch of the upper quarter on the side of applied loads, and is slightly shifted towards the load side. There is also a similar shift for the thrust distribution on the other side of the conduit. Maximum thrust is slightly lower than that of the centric case. For the lower half of the conduit, thrust values are much smaller on the side away from the load than on the load side. On the load side, thrust is larger than that in the lower half for the centric case.

Figures 4.13 to 4.16 show experimental and analytical live load thrusts for Adelaide Creek soil-steel structure for the same loading level, position and lane as in White Ash Creek. In general, the same remarks mentioned for White Ash Creek structure remain valid for Adelaide Creek structure. The value of maximum thrust that governs soil-steel structure design occurs in Position 1 under concentric load.

The pressure between the conduit walls and the soil is not directly measured during testing. However, by neglecting the moment effects, it is possible to estimate the experimental pressure at a certain location by dividing the measured thrust by the radius of curvature of the structure at the location according to Equation 2.4.

The experimental and analytical live load pressure as obtained by dividing the thrust values by the corresponding radius are shown in Figs. 4.17 to 4.24. On the same figures, the radial soil pressure is shown as calculated around the structure according to Boussinesq equations (132). The Boussinesq's pressure is obtained by assuming each case of loading to act on the surface of a semi-infinite elastic media having Poisson's ration of 0.3.

For all the cases considered Boussinesq's solution yields a maximum stress which is larger than the analytical or experimental results. The presence of the conduit changes the pressure distribution considerably. The pressure is reduced around the crown area because of the arching effect, while it is increased at the spring lines due to the passive resistance of the soil.

4.2.5.2 Bending Moment

Moment values measured at the six gauge locations in

the White Ash Creek structure are negligible. Analytical moments are larger, with a maximum at the crown where no measurements are taken.

The Adelaide Creek experimental moments computed from recorded strains are plotted in Fig. 4.25 for Lane 4 and Position 1, in Fig. 4.26 for Lane 8 and Position 1, in Fig. 4.27 for Lane 4 and Position 2, and in Fig. 4.28 for Lane 8 and Position 2.

On the same figures, the corresponding analytically obtained moments are given. It should be noticed that the plotted values of moment are not large. The maximum observed moment corresponds to a maximum fiber stress of only 930 psi. For live loads in Position 1, Figs. 4.25 and 4.26, the maximum negative moment, which causes tension on the outside fibers, occurs at the haunches of the top portion of the conduit. The maximum positive moment occurs at the crown zone. Maximum analytical values are in a reasonable agreement with the maximum experimental moment values.

Moment distribution due to eccentric live loads in Position 2, Figs. 4.27 and 4.28, is similar in shape to for the centric case with a shift towards the load side. Experimental moments are not in full agreement with corresponding moments obtained by finite element analysis.

However, maximum positive and negative values in both cases are comparable.

A final remark concerning the lower portion of the conduit is valid for both concentric and eccentric loads. Moments are negligible in magnitude as in the case of thrusts.

4.2.5.3 Relative Vertical Deflections

A comparison between measured relative vertical deflection, between the crown and bottom line of White Ash and Adelaide Creek structures, and analytical values is shown in Table C.2. Analytical values of deflections are larger than experimental values. In general, measured deflections seem to be unreliable since they incorporate relative displacements of small magnitude which are measured by transducers connected by very long flexible wires.

4.3 Soil Failure Laboratory Tests

A full scale failure test of a soil-steel structure is very difficult to conduct. The alternative is to conduct tests on small scale flexible culverts in the laboratory until failure of soil or conduit is noticed. The details of these tests are briefly presented in the following sections and results are compared with analytically predicted failure load.

4.3.1 Details of the Tested Soil-Steel Structure

Two tests are conducted on a soil-steel structure

model, built by Ekhande (60), under shallow cover. Fig. 4.29 shows the model lying in an open top rectangular box 12' long, 5'1" wide, and 6' high. The box is made of 3/4 in. thick plywood and 1/2 in. thick plexiglass. The soil used in the box is clean, dry sand from Lake Erie. The soil bed is 12 in. deep, laid in two layers. On the sides of the structure, the soil was placed in four equal layers. Thereafter, one layer of soil having a depth of 5 in. is placed over the crown of the conduit. Each of these layers is compacted manually leading to a soil density of 119 pcf.

The conduit is 31" in diameter, 3/16" thick, 60" long, and is made of an aluminum alloy 6061-T-6 plate having a modulus of elasticity of 10×10^6 psi, a Poisson's ratio of 0.33, and a yield stress of 40 ksi. The conduit ends are wrapped with foam rubber to seal the gaps between the ends and the box wall. This sealing does not obstruct the free movement of the conduit at the ends.

4.3.2 Instrumentation and Set-Up

A hydraulic jack is used to apply load on the soil. The load is distributed along a line directly above the crown through an I-beam 58 inches long as shown in Fig. 4.30. The width of the base of the I-beam is 4 inches.

A flat Universal load Cell is placed between the

hydraulic jack and the loading I-beam to measure the magnitude of the applied load. The maximum capacity of the load cell is 10 kips. A portable strain indicator, with which the load cell has been calibrated, is used to take readings of the cell.

Six dial gauges are installed along the beam line as shown in Figure 4.30. The one inch range dial gauges are used to measure the deflection of the I-beam during loading. Three more dial gauges are placed inside the conduit to take measurements of the vertical deflection along the crown line.

Installed electrical resistance strain gauges are used to monitor the strains at several positions along the conduit wall. A multichannel automatic digital strain indicator is connected to the strain gauges to record their readings during loading.

4.3.3 Testing Procedure and Observations

Two tests are conducted until failure of soil is noticed. Each test starts by zeroing the dial and strain gauge readings. In the first test, load is applied through the I-beam, directly resting on soil in increments. At the end of each increment, the dial gauges reading are taken, and the strains are recorded by the automatic strain indicator. After a maximum value of applied load is reached,

the measured load cell reading begins to decrease in spite of the continuous hydraulic supply. This is accompanied by an increase in deflections along the I-Beam as measured by the dial gauges. Loading is then released and dial and strain readings are recorded. Reloading is applied in increments, and readings of dial and strain gauges are taken. Test 1 ends when continuous visual and measured deflections of the I-Beam is first noticed and continues to increase in spite of load decrease. Upon unloading, full elastic deflection of the conduit is recovered.

In the second test, a 10.5 inches wide wood plate is inserted between the I-Beam and the soil to test failure of soil under a more distributed load. Testing procedure is similar to that of the first test. However, when soil failure occurs, a wedge of soil is trapped underneath the wide plate, and almost all the deflection of the beam is transmitted to the crown level. The test is stopped when large deflection of the crown of the conduit is noticed.

4.3.4 Experimental and Analytical Results

The measured displacements in Test 1 and Test 2 are given in Tables C.3 and C.4. The curves for load versus average displacement of the loading frame and load versus average deflection of the crown of the conduit are shown in Figs. 4.31 to 4.33. The first load cycle for Test 1, Fig. 3.31,

reveals that measured deflections are almost linear. The deflection at the surface of soil is almost twice that of the conduit.

At the maximum applied load, 2.5 kips, measured strains indicate that the stresses in the conduit are still in the elastic range. The drop in loading is accompanied by a large displacement of the top surface of the soil and a small deflection of the crown. Upon releasing the applied load, the conduit wall recovers completely its original shape as shown in Fig. 4.32. This is another indication that stresses, during the first cycle of loading, are in the elastic zone. However, a permanent measured displacement of the top surface of the soil of about 0.3 in. remains. The only possible cause for such soil displacement is soil failure.

The second load cycle shows the post failure behaviour. Maximum applied load is less than in the first cycle. Deflection of the conduit crown, however, is identical to the crown deflection during the first loading.

(Figure 4.33 shows the experimental results of Test 2. There is no apparent failure load as in the case of Test 1. However, the rate of increase in measured deflections at the crown and the loading frame levels are rapid after the applied load exceeds 3 kips. At the start of

the increase in rate of deflection, measured strains indicate that all the stresses in the conduit wall are well below the yield point. Therefore, the only explanation for the rapid rate of increase is soil failure. The deflection of the conduit crown is increased because, after soil failure, a wedge of soil below the wide piece of wood is trapped and is transmitting the load directly to the conduit.

An analytical study of the tested conduit, carried out prior to the testing, is based on the same interface properties mentioned in Section 4.2.5 and the following soil properties (160): $K_s = 1200$, $R_f = 0.85$, $m = 0.48$, $\phi_o = 45^\circ$, $\Delta\phi = 7^\circ$, $G = 0.5$, $F = 0.23$, $d = 11.7$. The resulting failure load is 3.22 kips, which is in a reasonable agreement with test results.

CHAPTER V

STABILITY OF SOIL COVER

5.1 General

The proposed finite element analysis and the corresponding computer program are confirmed by the experimental verification outlined in Chapter IV. The analytical procedure is also capable of determining the stress conditions in the soil and the possible soil failure in the conduit cover, as described in Section 3.11.4. This capability is also confirmed by the laboratory tests presented previously.

This chapter is directed to the study of the parameters governing the soil failure above the conduit due to live loads. Several soil-steel structures are examined using the developed computer program. For each case, construction sequence is simulated to yield the state of stresses in the system, as well as the soil elements properties, before the application of live load. Thereafter, live load is applied in increments and analysis is carried out until a complete line of failure is detected through the soil.

Four parameters are included in this study. These are: height of cover, size of conduit, shape of conduit,

and eccentricity of loading. Each parameter is varied while the others are kept constant. In general, stability of soil is considered under two different cases of loading: a) one centric axle load, and b) multi-axle truck loading. The centric load is simulated by one nodal force applied on top of soil directly above the crown of the structure. The multi-axle truck loading consists of five-point loads such that the distances between consecutive loads are as shown in Fig. 4.6. The intensities of consecutive point loads are proportional to the corresponding axle loads of the truck.

For all the cases considered, the nonlinear properties for the granular material around the structure are considered the same as those used in the analysis of the live load tests. The type and size of structure walls considered are galvanized steel 2x6 corrugated sheets, with a thickness of 0.184 inches.

5.2 Effect of Height of Cover

Several structures under varying height of cover are analyzed. Each structure has a span of 300 inches and a height of cover between 24 and 96 inches. Three different shapes for the conduit are considered: a circular cross-section, a horizontal and a vertical el-

liptical cross-section. Their height to span ratio is 1, 0.6 and 1.6 respectively.

The final results are presented in Figs. 5.1 and 5.2. Fig. 5.1 relates the ratio of height of cover to span $\frac{h}{s}$, to the ratio of the centric axle load causing soil failure to a standard axle load of 32 kips $\frac{P_f}{P_a}$. Fig. 5.2 relates $\frac{h}{s}$, to the ratio of the rear loading in multi-axle condition to the standard axle load $\frac{P_f}{P_a}$. Each of the three shapes show the same trend, i.e., an increase in the height of cover above the structure leads to an increase in the expected value of applied load causing soil failure.

In general, the rate of increase in P_f increases with the soil cover height. This trend is expected because of the combined effect of load dispersion and increased failure resistance of soil with the increase in depth. For the truck loading and circular shape an apparent increase is observed in the load causing soil failure, when the ratio of height to span decreases below 1/6. This may be due to the effect of eccentricity of the two rear axles of the truck relative to the soil cover depth.

5.3 Effect of Conduit Size

One of the important parameters that affects soil failure above conduits is their size. Under a depth of cover of 48 inches, several soil-steel structures of different sizes and shapes are analyzed.

The conduit span was varied between 150 and 450 inches. Horizontal and vertical elliptic shapes, as well as circular shapes are considered. The rise to span ratio for horizontal elliptic shapes is constant and equals to 0.6, and for vertical elliptic shapes 1.6. For each case, failure in soil is detected under the relative loads shown in Figs. 5.3 and 5.4. For each of the three shapes under consideration, increasing the span while height of cover is constant causes a decrease in the value of applied load which results in soil failure. This conclusion is consistent with the conclusion drawn by varying the height of cover while span is constant. However, for the circular shape under truck load, the span increase is associated with a decrease of the failure multi-axle loading, except when the span to height ratio is above 7. For the vertical elliptic shape, soil failure occurs under smaller truck loads when the span to height of cover ratio increases above 5. Below 5, smaller truck loads also cause failure in soil. The only explanation that may be given for this

behaviour is the effect of eccentricity of load, which increases the possibility of soil failure within certain limits.

5.4 Effect of Conduit Shape

The cross-sectional shape of a soil-steel structure has a considerable effect on failure of soil above the structure. Any set of graphs in Figs. 5.1 to 5.4 reveals that the load causing failure in soil is much higher for a vertical elliptic shape conduit than for a horizontal elliptic shape conduit of equal span and height of cover. Failure in soil above a circular conduit occurs under an intermediate value of applied loads. This may be attributed to the sensitivity of each shape to deform under applied load when surrounded by compacted granular material. The horizontal elliptical cross-section is more susceptible to vertical deformation of the portion around the crown under the effect of applied live load than the circular cross-section. This negatively affects the shear stresses in soil and the failure load. On the other hand, a vertical elliptical cross-section is stiffer than the circular cross-section when it comes to vertical deformations around the crown area. Thus, the soil above it appears to be stronger because it can sustain more load without failure in comparison with the circular cross-section.

5.5 Effect of Eccentricity of an Axle Load

Typical effect of eccentricity of one axle load applied over a circular conduit, with 300 inch span and 48 inch height of cover, is shown in Fig. 5.5. The graph provides the analytically obtained relationship between the ratio of eccentricity to half span, $\frac{2e}{S}$, and the ratio of $\frac{P_f}{P_a}$. As the eccentricity increases from zero to a certain limit, the failure load decreases gradually. If the eccentricity of the applied axle load increases beyond that limit, the increase in the amount of load required to induce failure becomes considerable.

This behaviour may explain the previously presented results for soil failure under testing truck load, which seem to be opposite to the general conclusions drawn for the case of single axle load. For example, in Fig. 5.4, the curve for vertical elliptic structures shows a decrease in failure loads in spite of span decrease because the eccentricity of the rear axle causes a decrease in the value of failure loads compared to the case of concentric loads.

CHAPTER VI

CONCLUSIONS AND RECOMMENDATIONS

6.1 Conclusions

The main objective of the present thesis is to study the behaviour of soil-steel structures under shallow cover and the parameters governing soil failure above the structure. A finite element analysis, using linear strain compatible elements and two-noded interface elements is used. The important aspects of the interaction and construction simulations are accounted for. Analytical results are compared and found to be in agreement with field tests under truck loads and with laboratory tests under line loads causing soil failure. The influence of several parameters on soil failure above the conduit is demonstrated.

The following conclusions may be drawn out of the present study:

1. The finite element method is capable of incorporating most of the nonlinear interaction aspects of a soil-steel structure with a minimum of over-simplifying idealizations.

2. A compatible eight-noded linear strain quadri-

lateral element offers important savings in time and storage requirements over linear strain triangular elements, while maintaining the same accuracy.

3. The proposed two-noded interface element considers the possibility of slip and separation between soil and conduit wall much better than available linear interface elements and requires less computational efforts

4. The hyperbolic nonlinear soil and interface models are accurate enough to represent soil and interface behaviour.

5. Compaction simulation is important in a soil-steel structure finite element analysis. It affects the stress distribution around the structure.

6. Failure in soil or interface elements may be considered using simplified procedures instead of complicated plasticity approaches.

7. Under the effect of symmetrical live loads about the centre line of a conduit cross-section, maximum thrust and negative moment occur at the haunches of the upper half of the steel structure. Maximum analytical positive moment occurs at the crown.

8. Stresses in the bottom third of the structure due to surface live loads are negligible.

9. As eccentricity of live loads increases above half the span, internal forces in structure walls decrease considerably.

10. In general, an increase in height of soil cover leads to an increase in the value of applied loads which cause failure of soil above a conduit.

11. In general, under a constant cover, an increase in conduit size is associated with a decrease in load resulting in soil failure.

12. Vertical elliptic conduit shapes can support more load before soil failure than circular conduit shapes. Horizontal elliptic shapes can support much less loads before soil failure than the other two shapes.

13. Small eccentricity of axle loading leads to a reduction in the value of soil failure load, compared to that of centric loading, up to a limit. However, beyond the limit, any additional eccentricity is accompanied with an increase in the value of failure load.

6.2 Recommendations for Future Research

The analytical approach used in this study is limited to the investigation of static live load effects on initiation of failure in soil. Future research may be extended to cover the following areas:

1. Transient dynamic load responses and their effect on initiation of soil failure should be studied.
2. An elastoplastic analysis could be used to examine post failure stress distribution under higher loads.

3. The effect of special features associated with the construction of soil steel structures such as tie rods, thrust beams, and relieving slabs, should be studied.

4. The use of reinforced earth in construction may be considered in the future.

5. The interaction of local or general buckling of the conduit with soil failure should be examined.

ILLUSTRATIONS

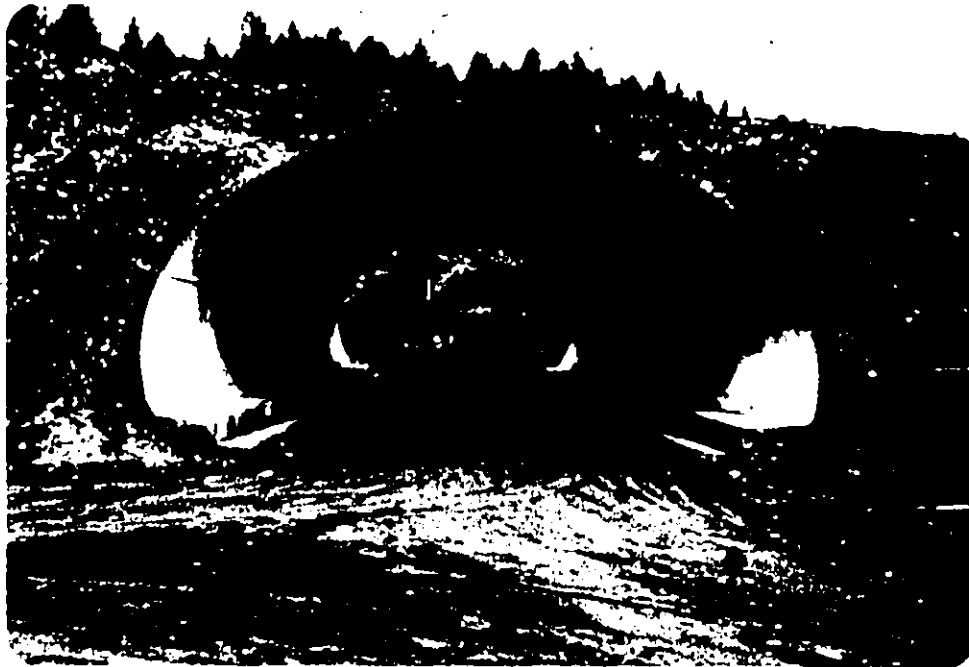
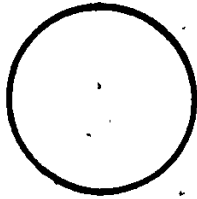
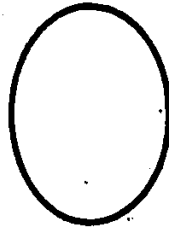


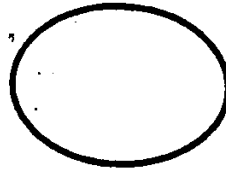
Fig. 1.1. Soil-Steel bridge structure.



Round



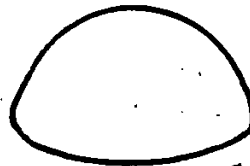
Vertical Ellipse



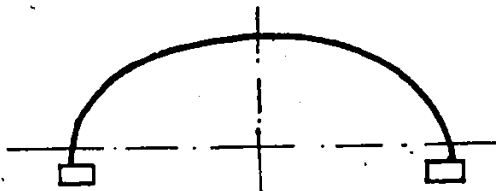
Horizontal Ellipse



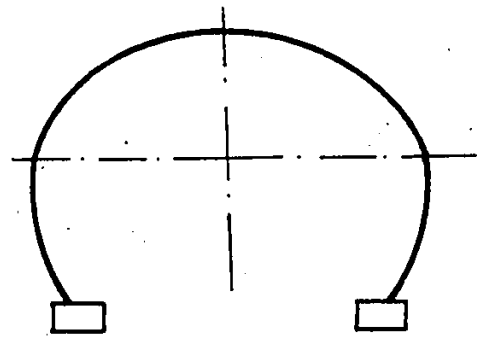
Arch



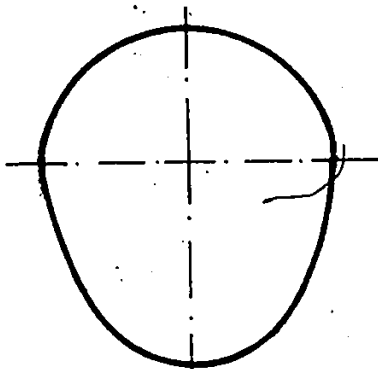
Pipe Arch



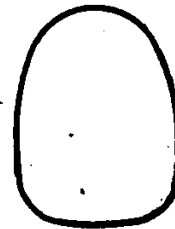
Low Profile Arch



High Profile Arch



Inverted Pear



Underpass

Fig. 1.2. Common shapes for long span flexible conduits.

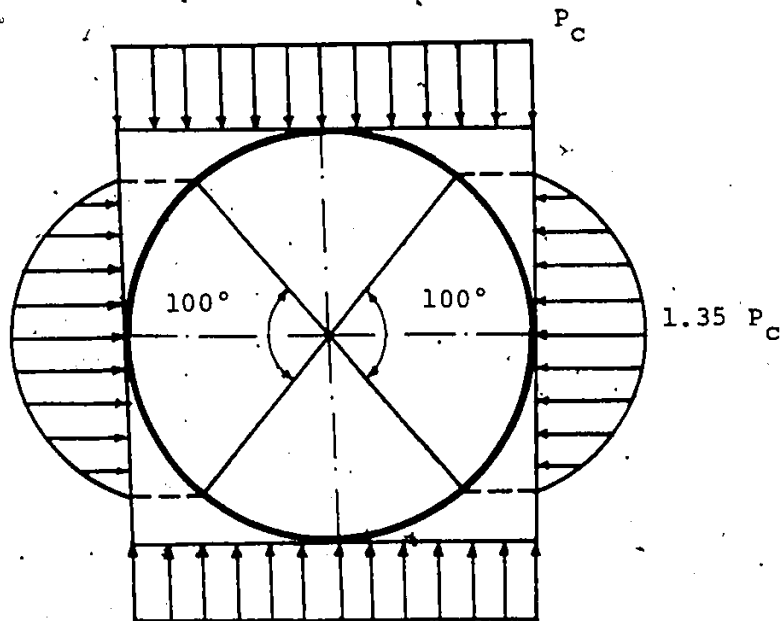


Fig. 2.1. Pressure distribution assumed in the Marston-Spangler Method.

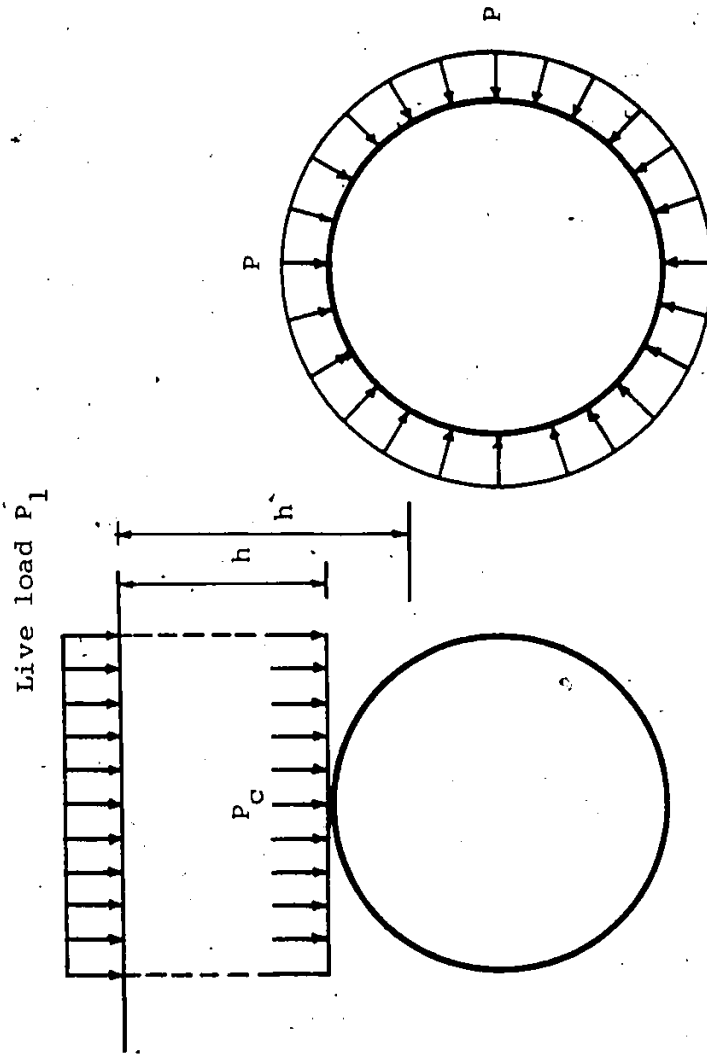


Fig. 2.2. Pressure distribution assumed in Ring Compression Theory for circular cross-sections.

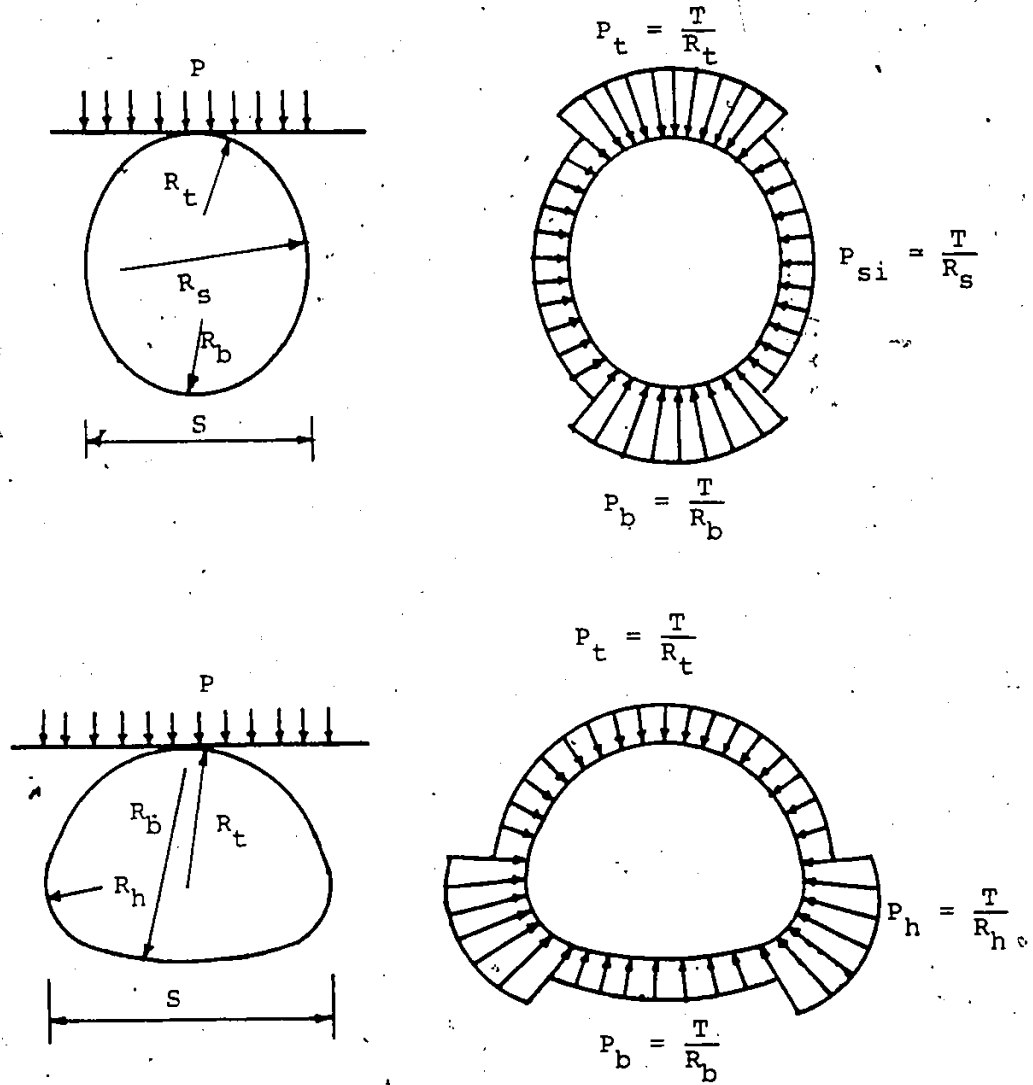


Fig. 2.3. Pressure distribution assumed in Ring Compression Theory for non-circular cross-sections.

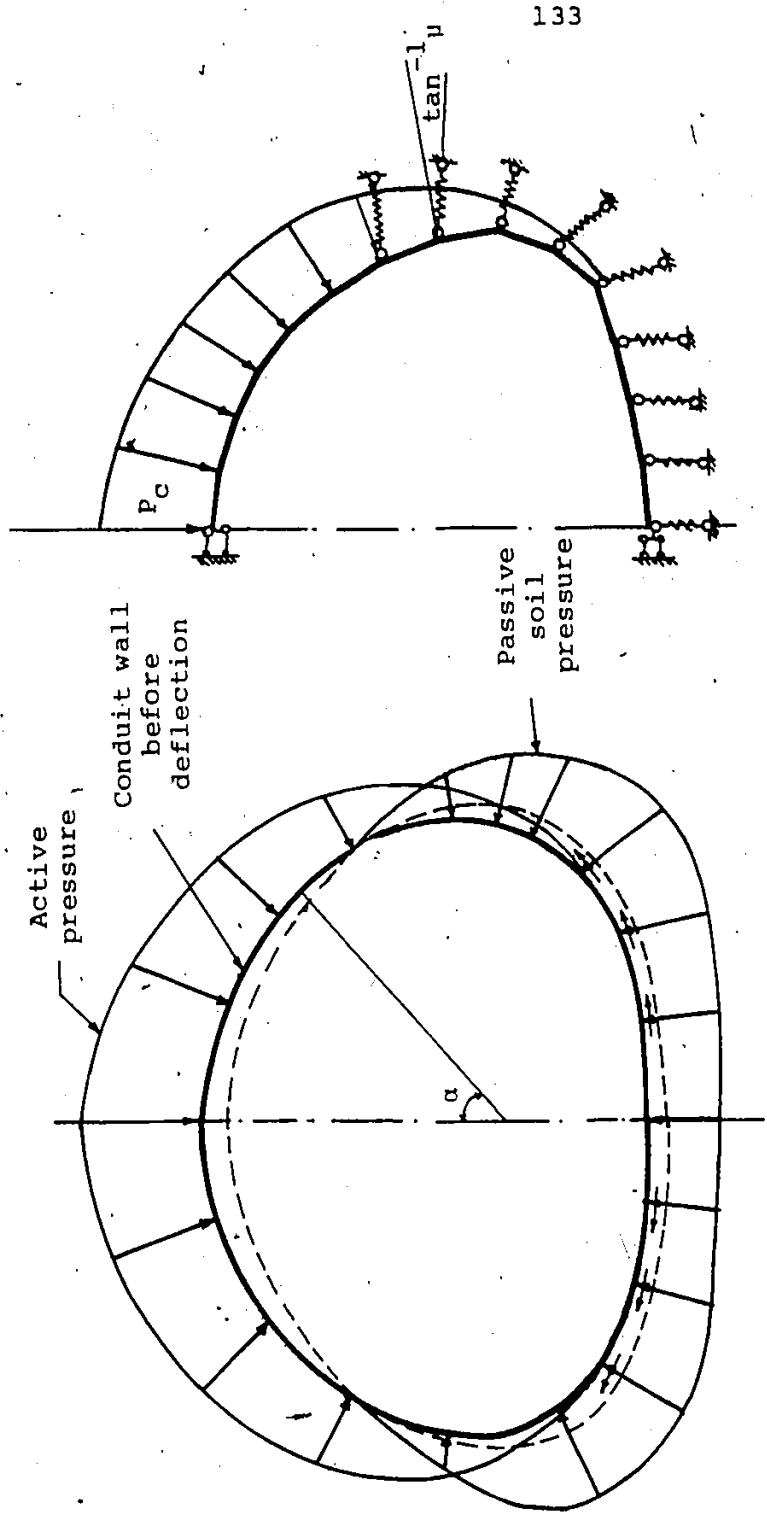


Fig. 2.4. Actual and simulated loading and structural system considering a frame on spring supports.

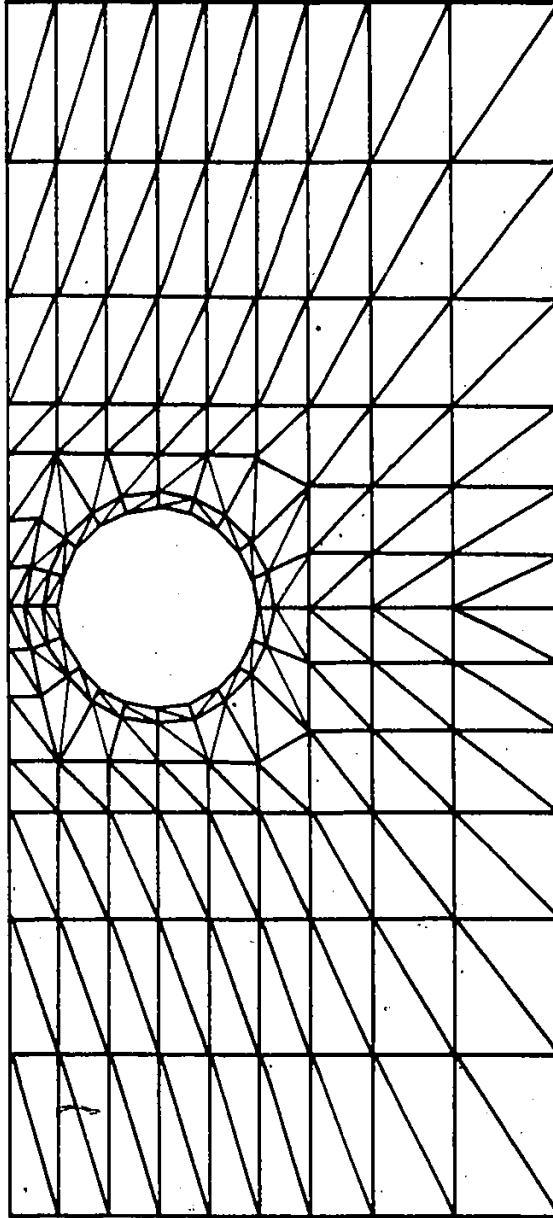


Fig. 3.1. Finite element mesh for a circular conduit using triangular elements only.

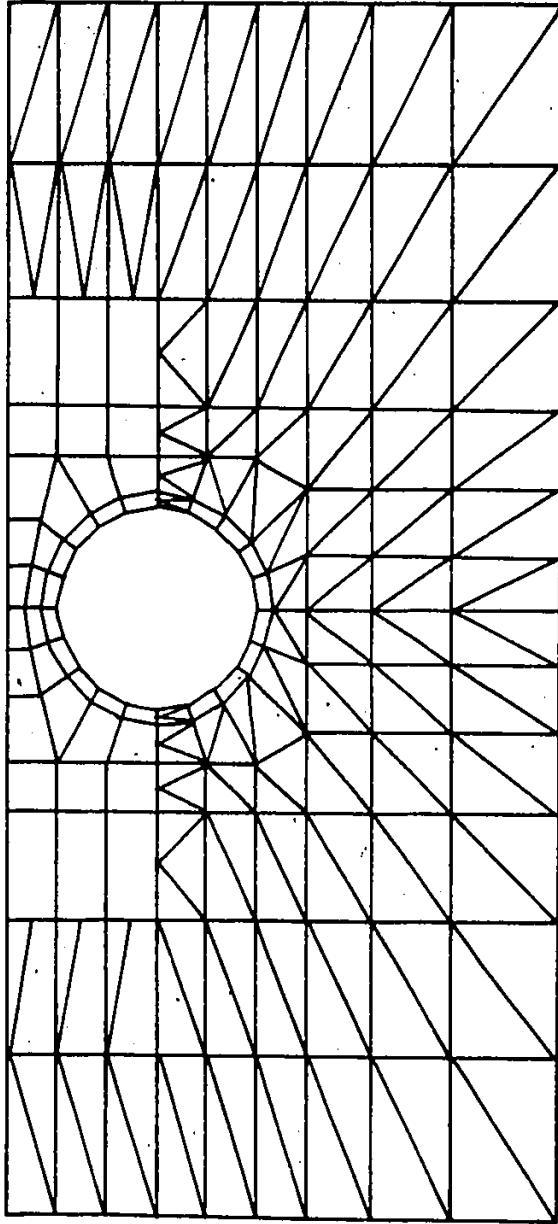


Fig. 3.2. Finite element mesh for a circular conduit using triangular and quadrilateral elements.

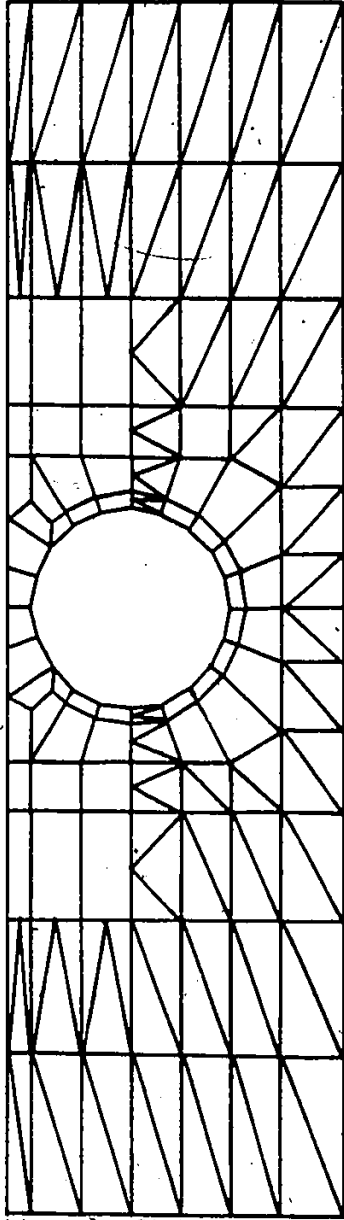


Fig. 3.3. Finite element mesh for a circular conduit under extremely shallow cover.

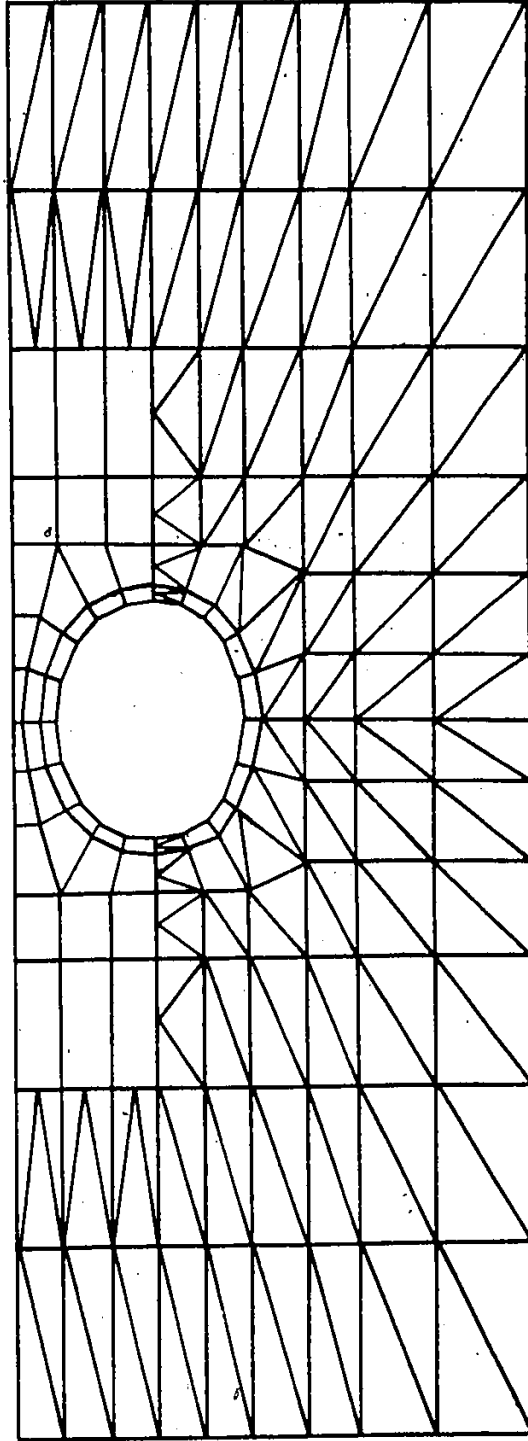


Fig. 3.4. Finite element mesh for an elliptical shape conduit.

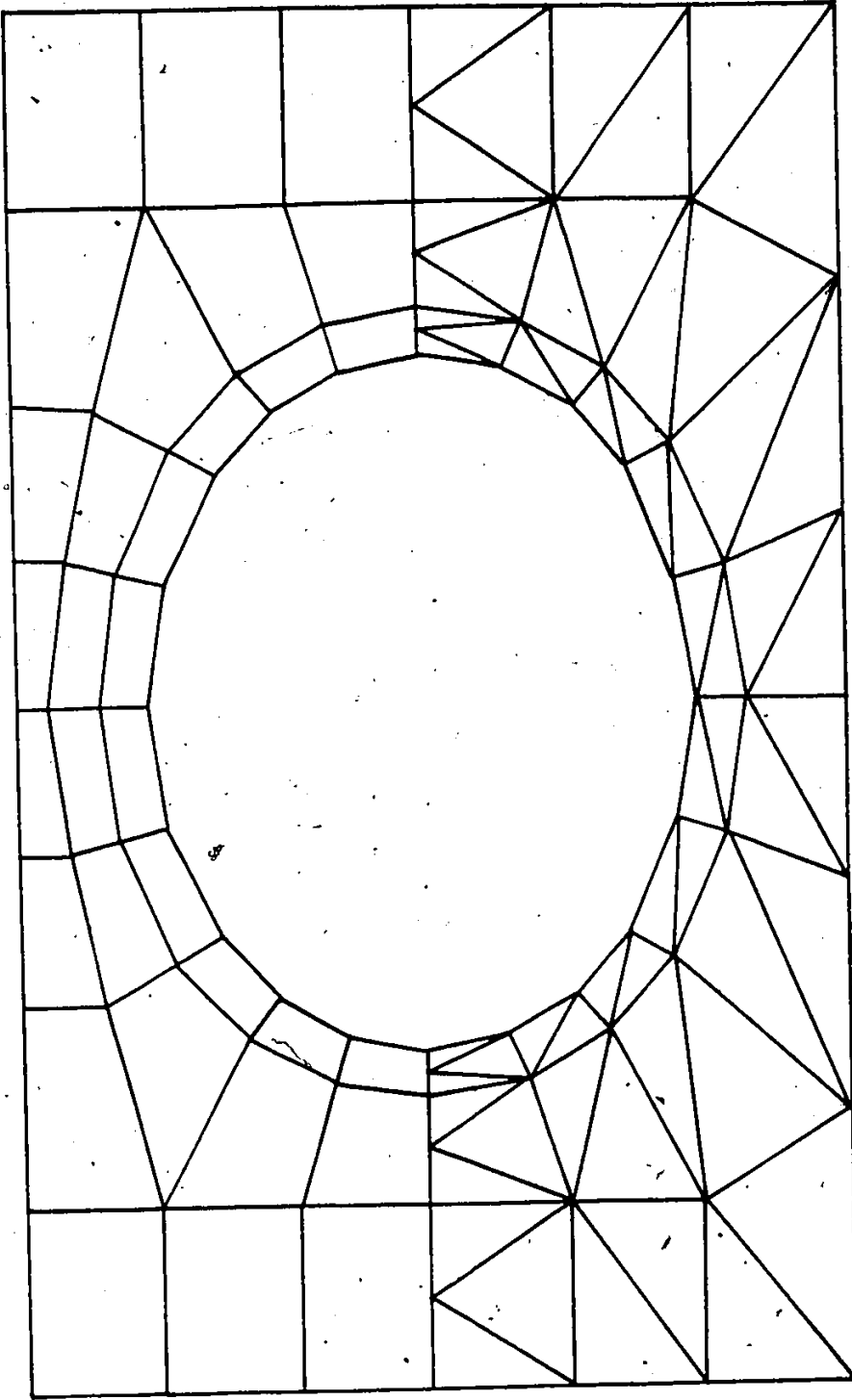


Fig. 3.5. Finite elements around the conduit.

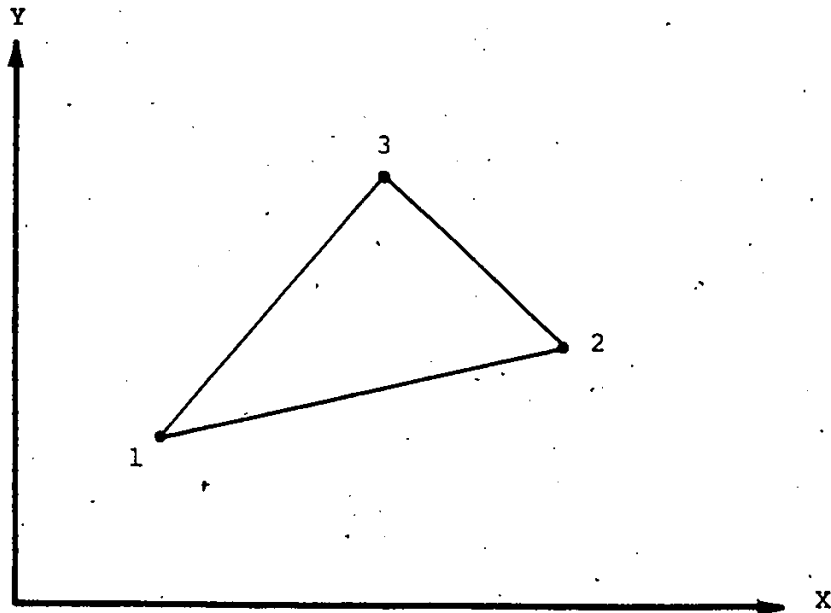


Fig. 3.6. Constant strain triangular element.

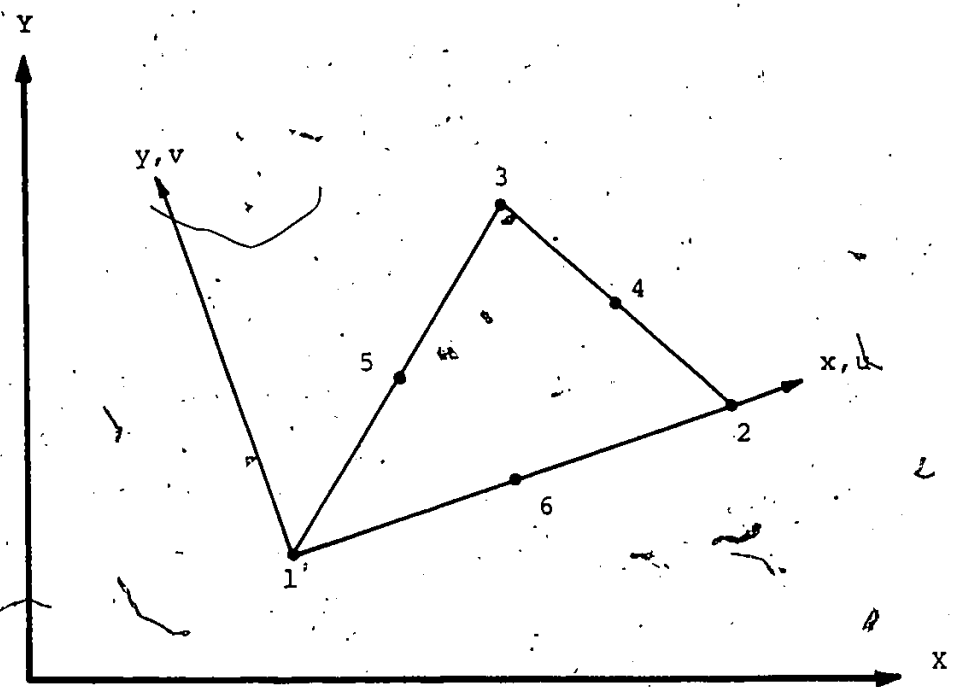


Fig. 3.7. Linear strain triangular element.

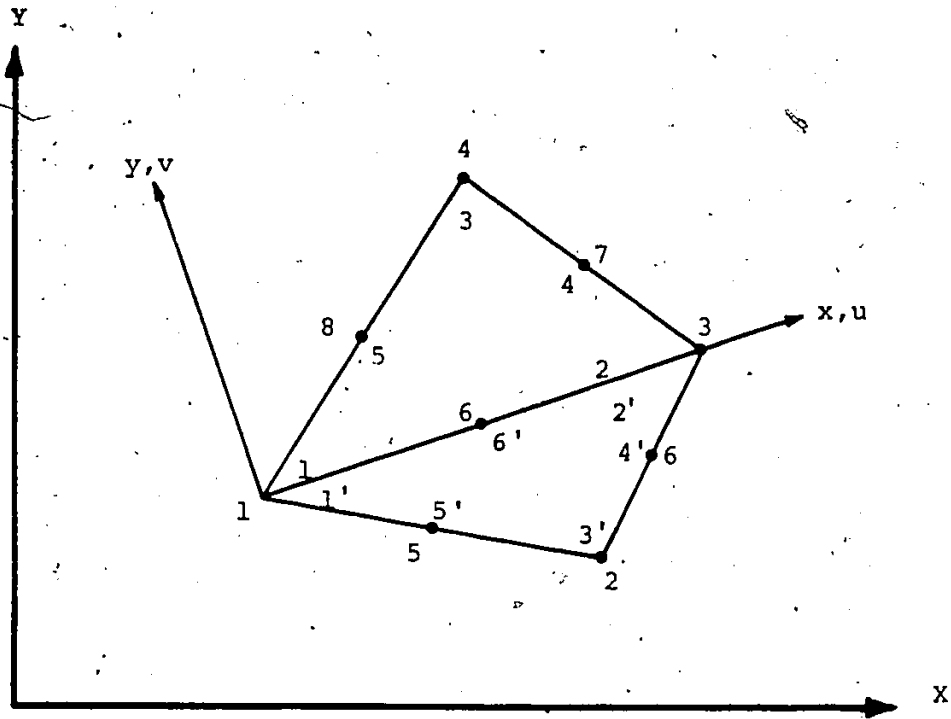


Fig. 3.8. Nine-noded linear strain quadrilateral element

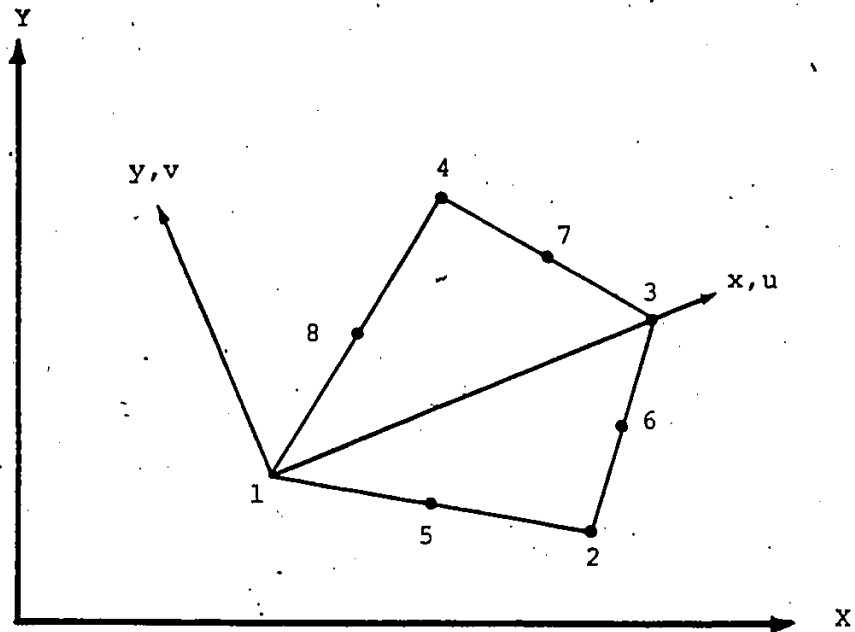


Fig. 3.9. Eight-noded linear strain quadrilateral element.

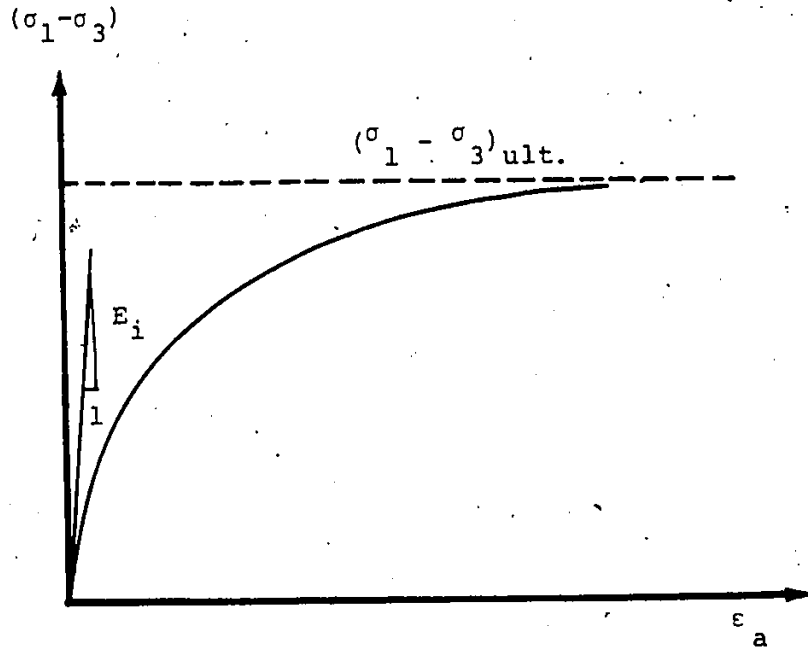


Fig. 3.10a. Hyperbolic stress strain relationship.

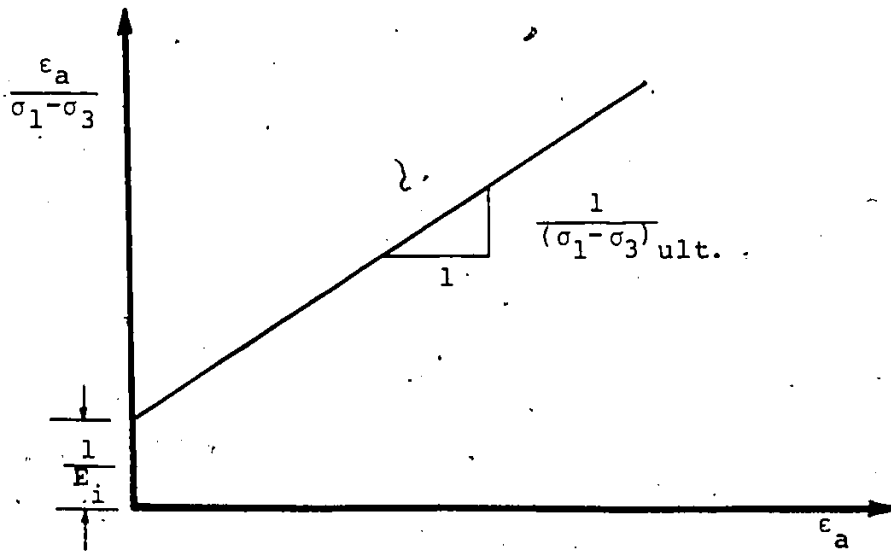


Fig. 3.10b. Transformed hyperbolic stress-strain relationship.

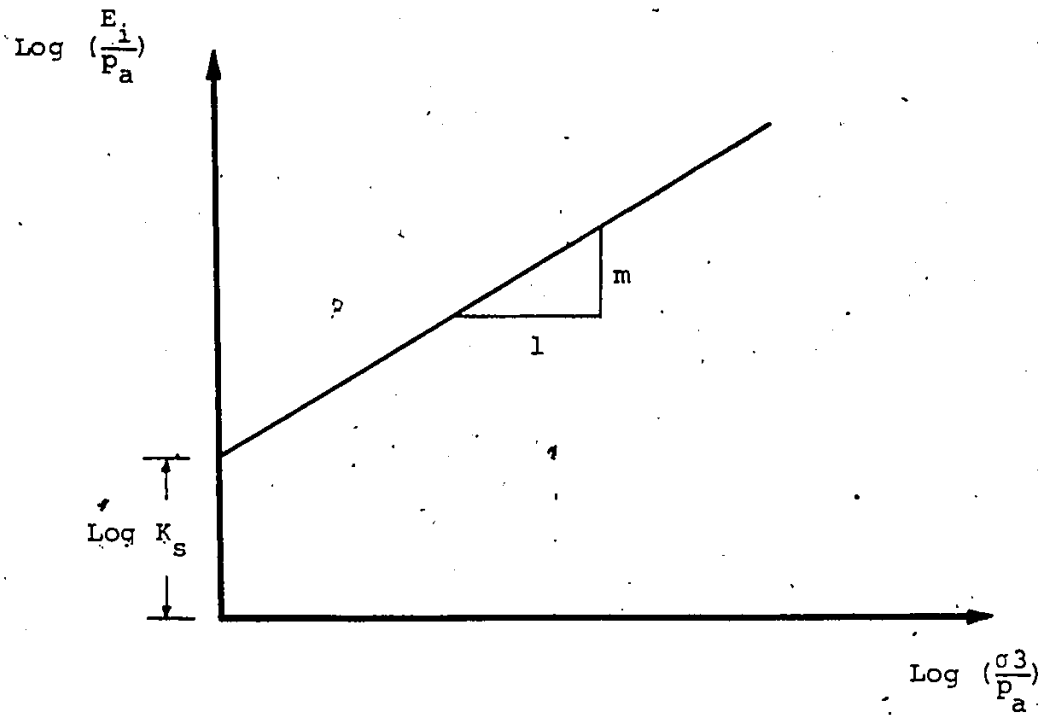


Fig. 3.11 Variation of initial tangent modulus.

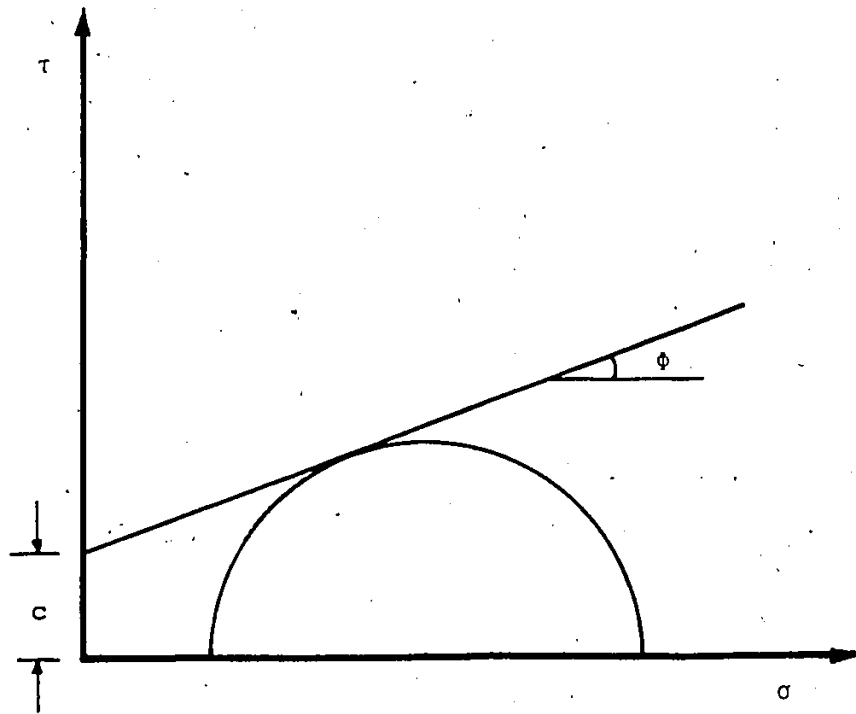


Fig. 3.12. Mohr-Coulomb strength parameters.

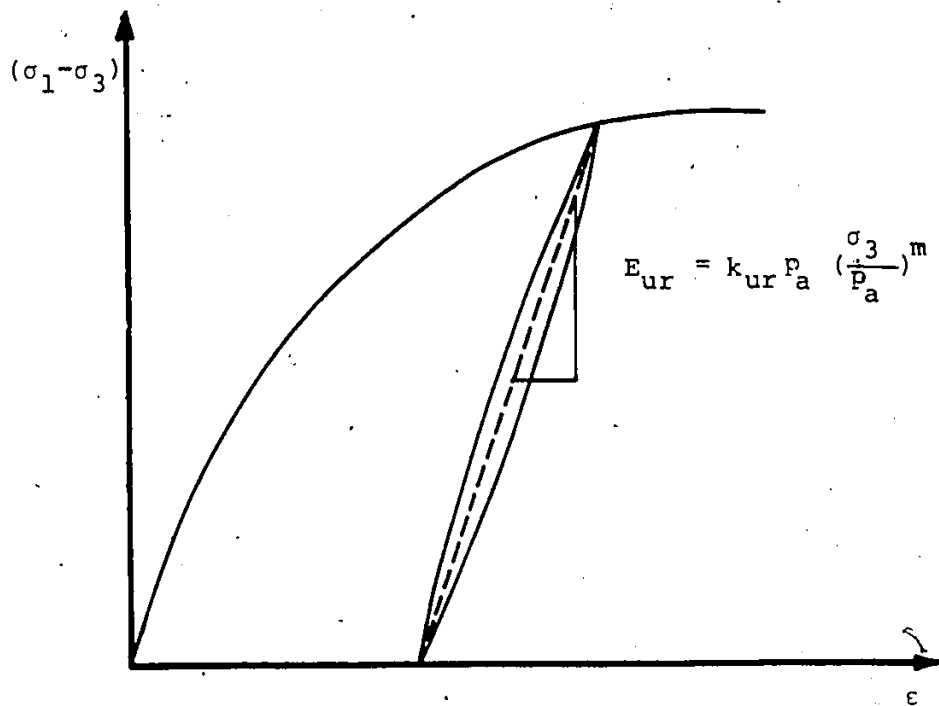


Fig. 3.13. Unloading-reloading modulus.

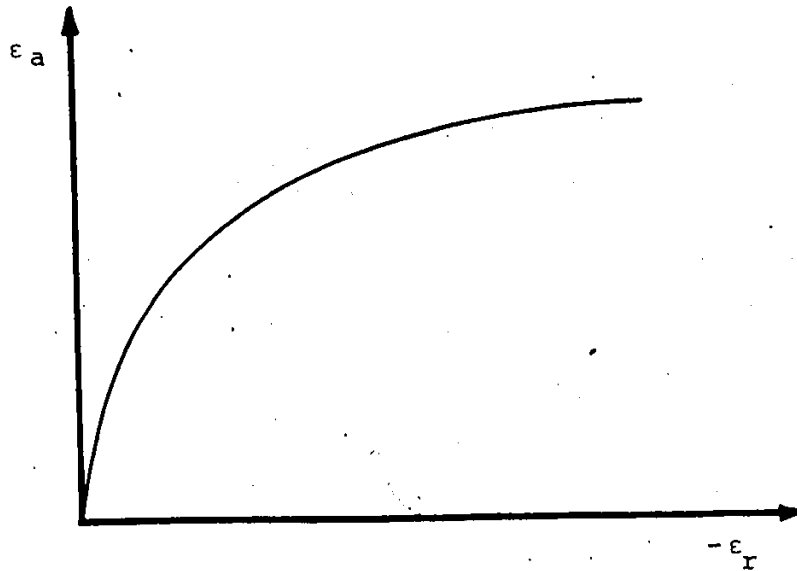


Fig. 3.14a. Hyperbolic axial strain-radial strain relationship.

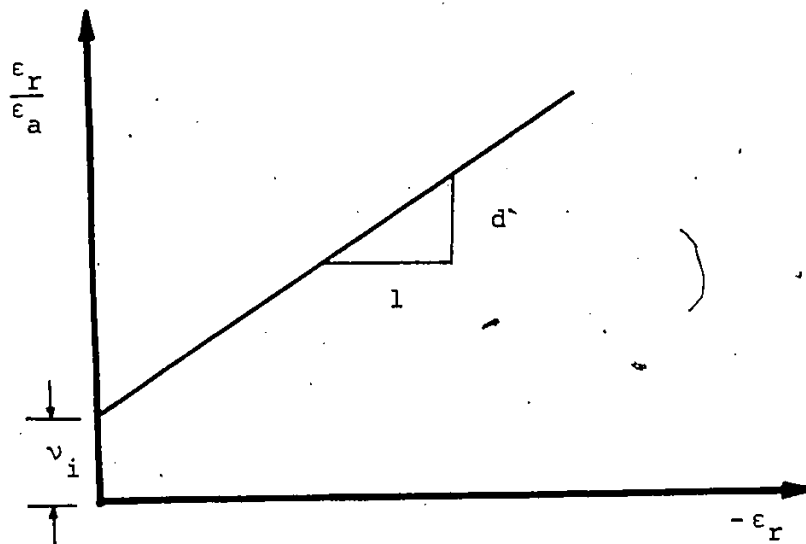


Fig. 3.14b. Transformed hyperbolic axial strain-radial strain relationship.

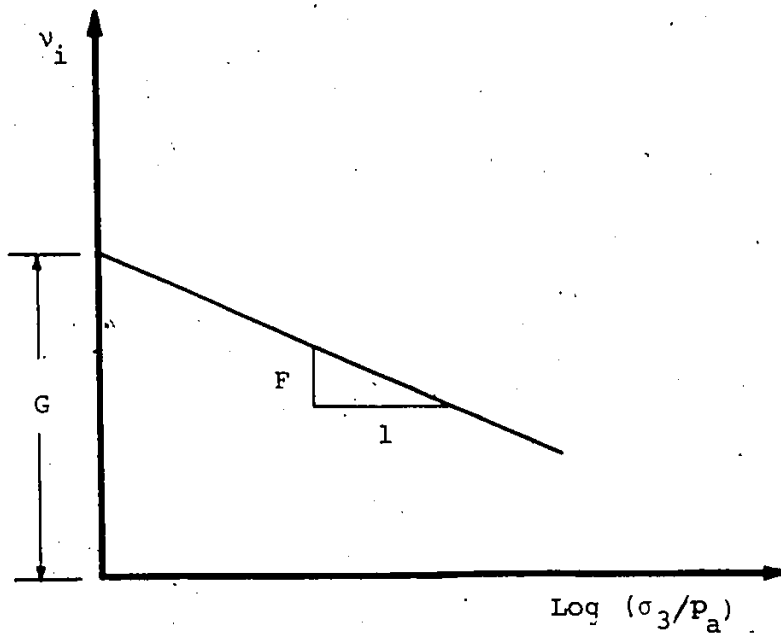


Fig. 3.15. Variation of initial Poisson's Ratio.

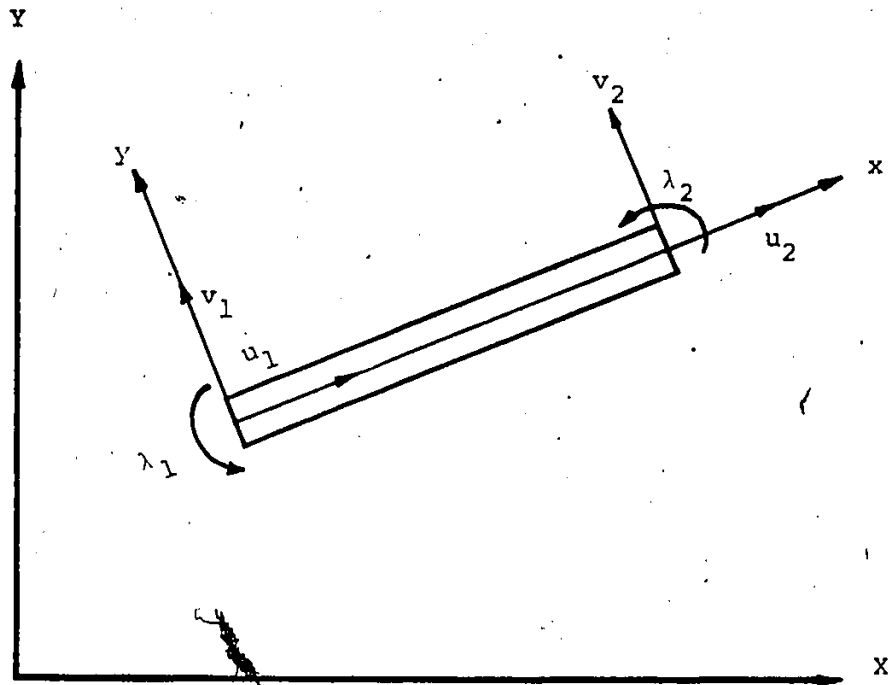


Fig. 3.16. Beam element.

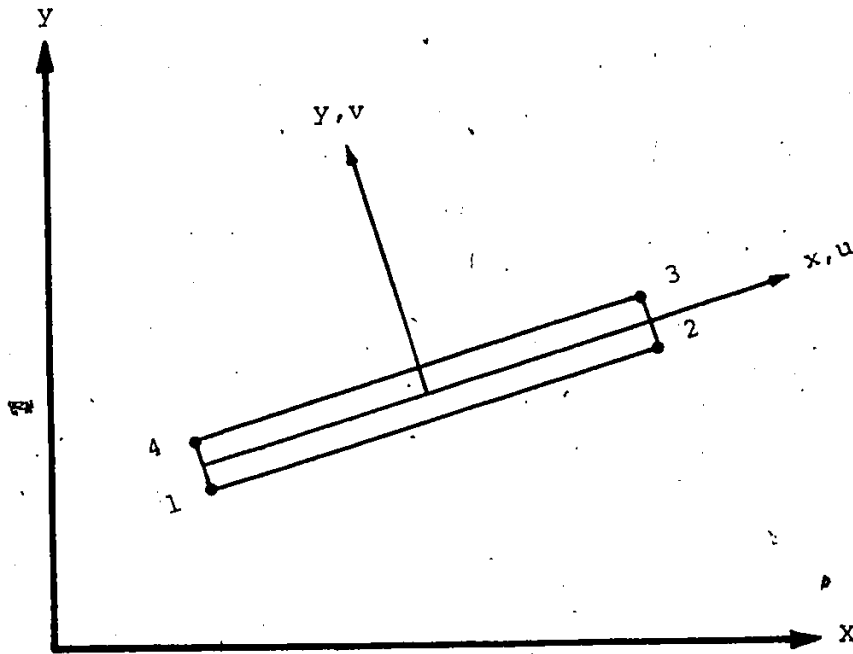


Fig. 3.17. One dimensional interface element.

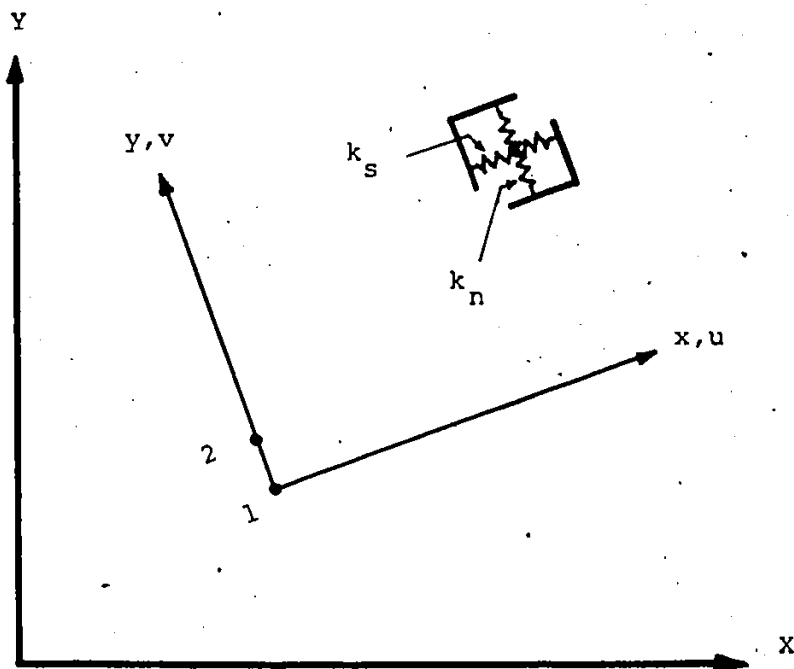


Fig. 3.18. Spring type interface element.

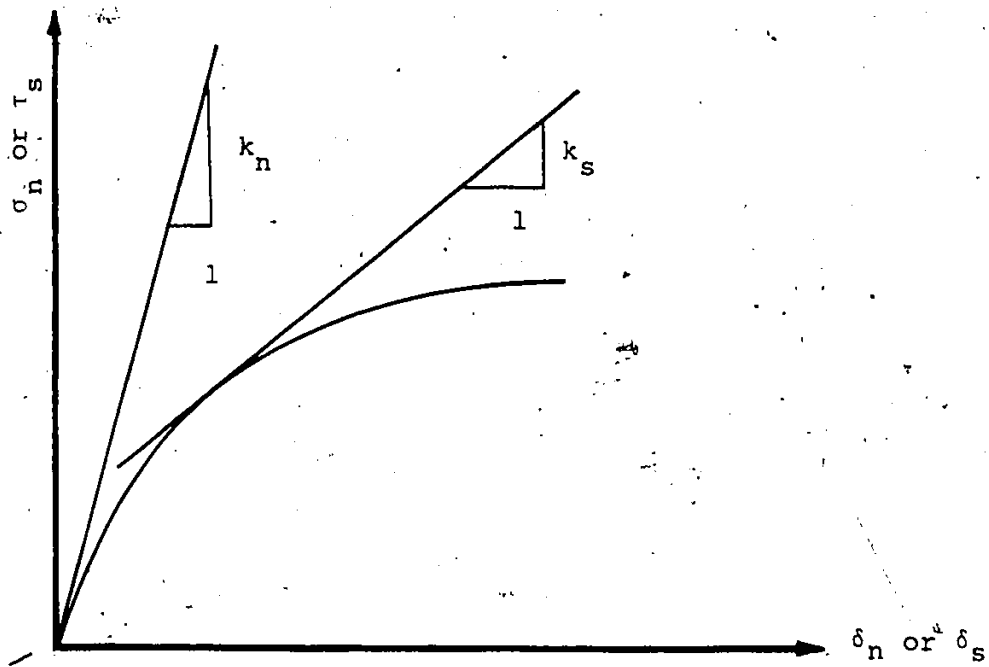


Fig. 3.19. Stress deformation curves for the interface element.

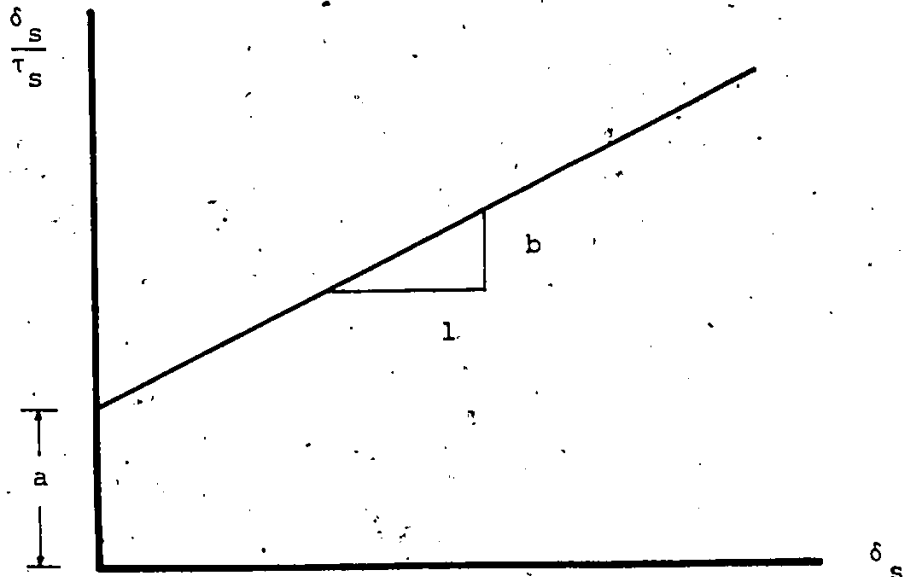


Fig. 3.20. Transformed hyperbolic shear stress - shear deformation relationship.

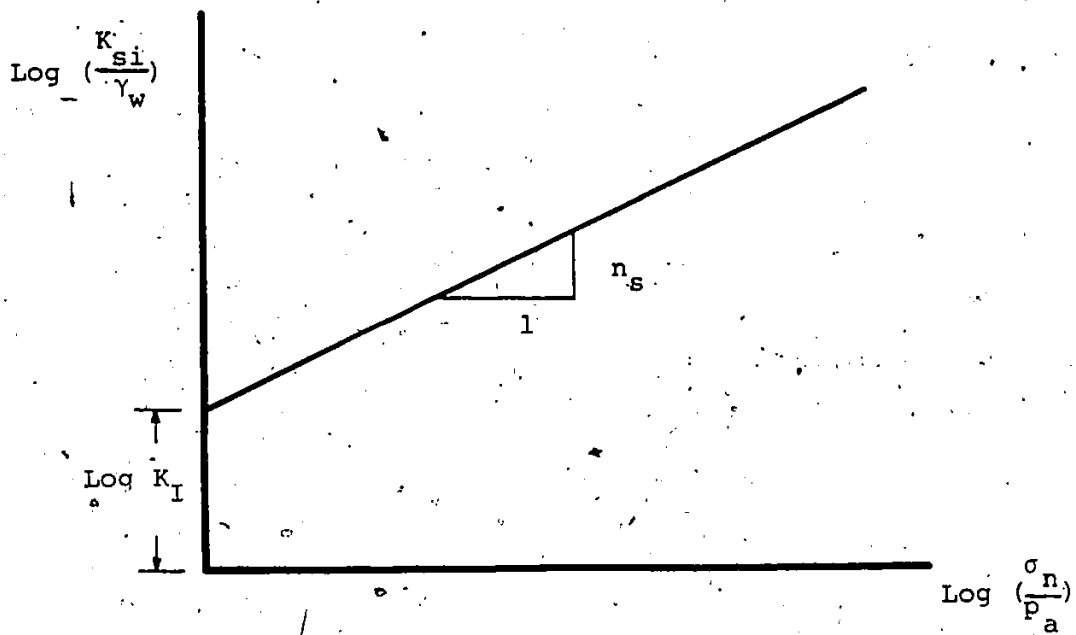


Fig. 3.21. Variation of initial unit tangential stiffness.

Stress

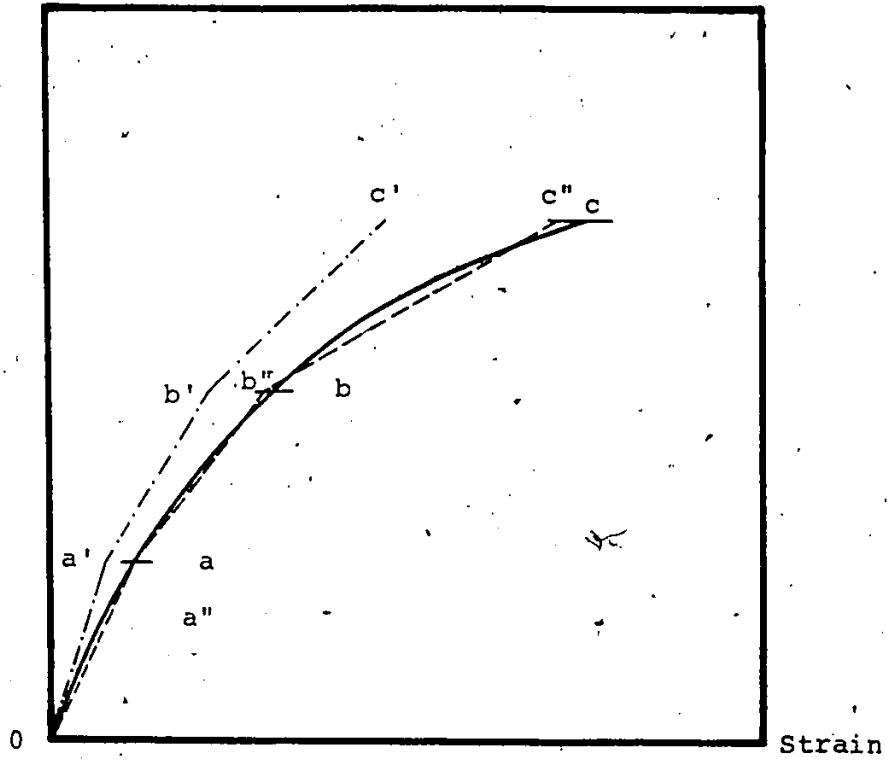


Fig. 3.22. Nonlinear analysis using incremental technique.

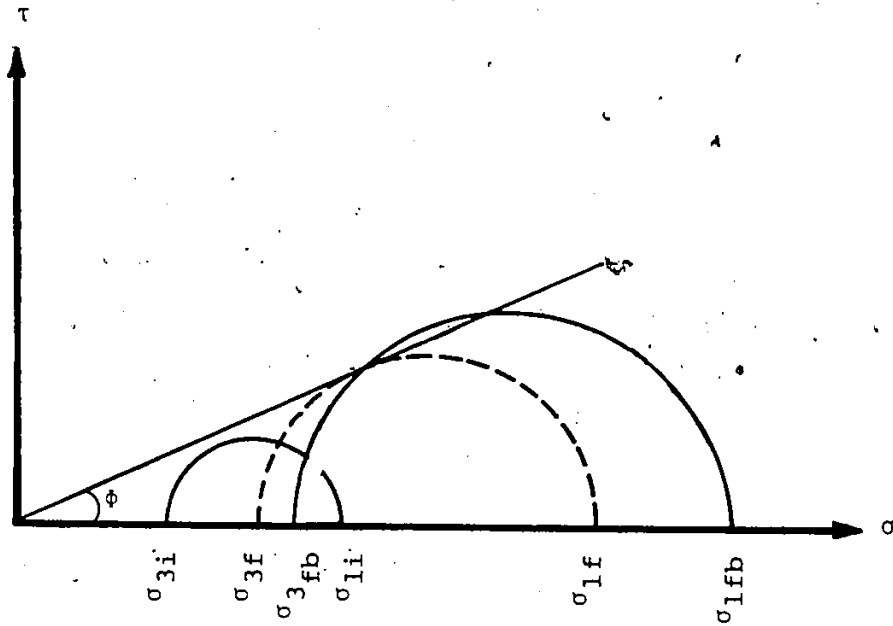


Fig. 3.23. Shear failure consideration in soil element.

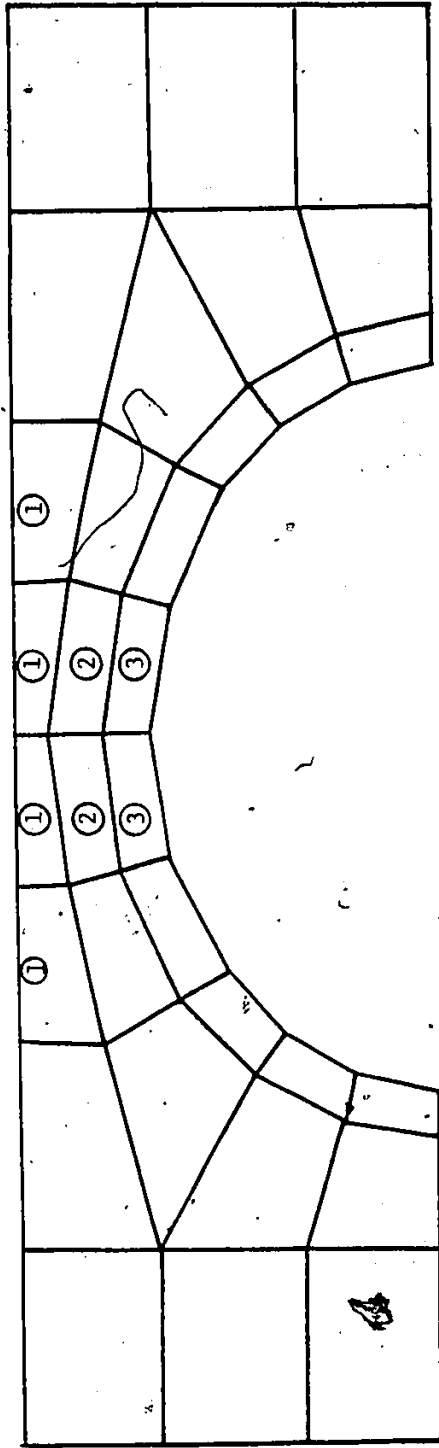


Fig. 3.24. Failure lines under the effect of increasingly applied live loads.

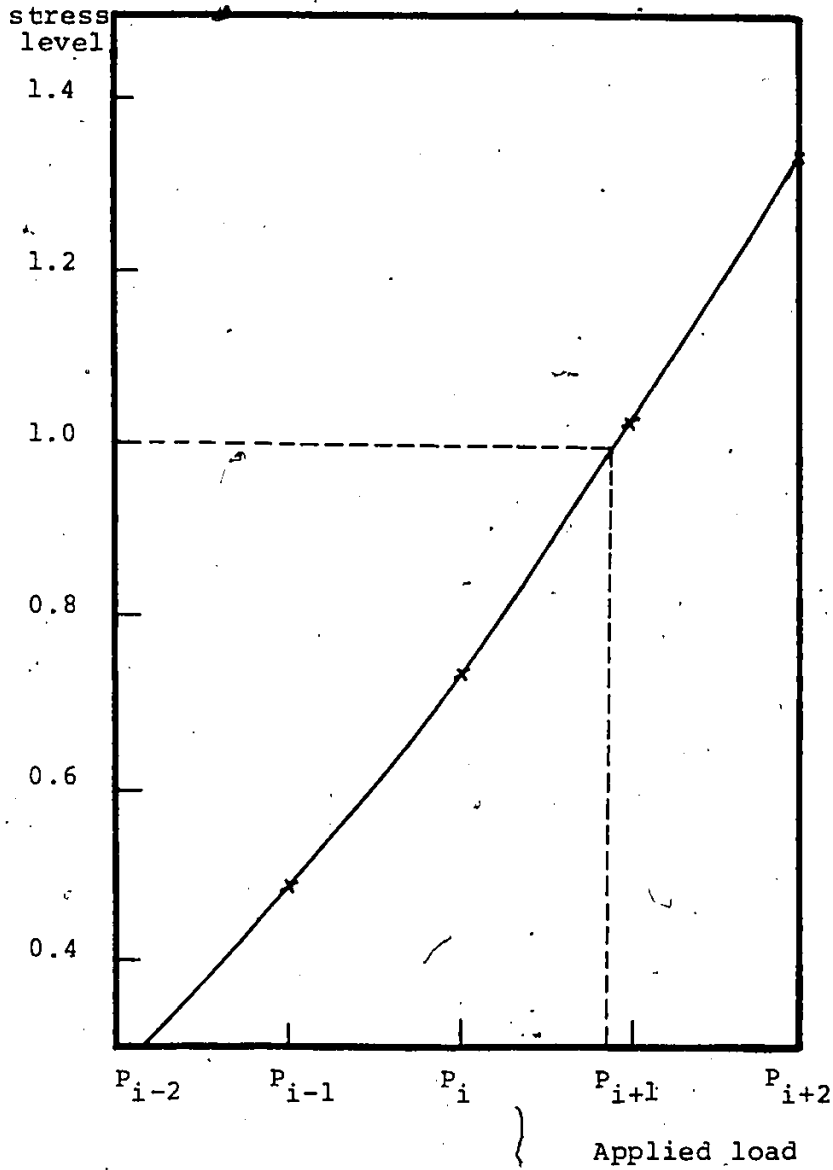


Fig. 3.25 Interpolation to determine fractional increment for failure loads

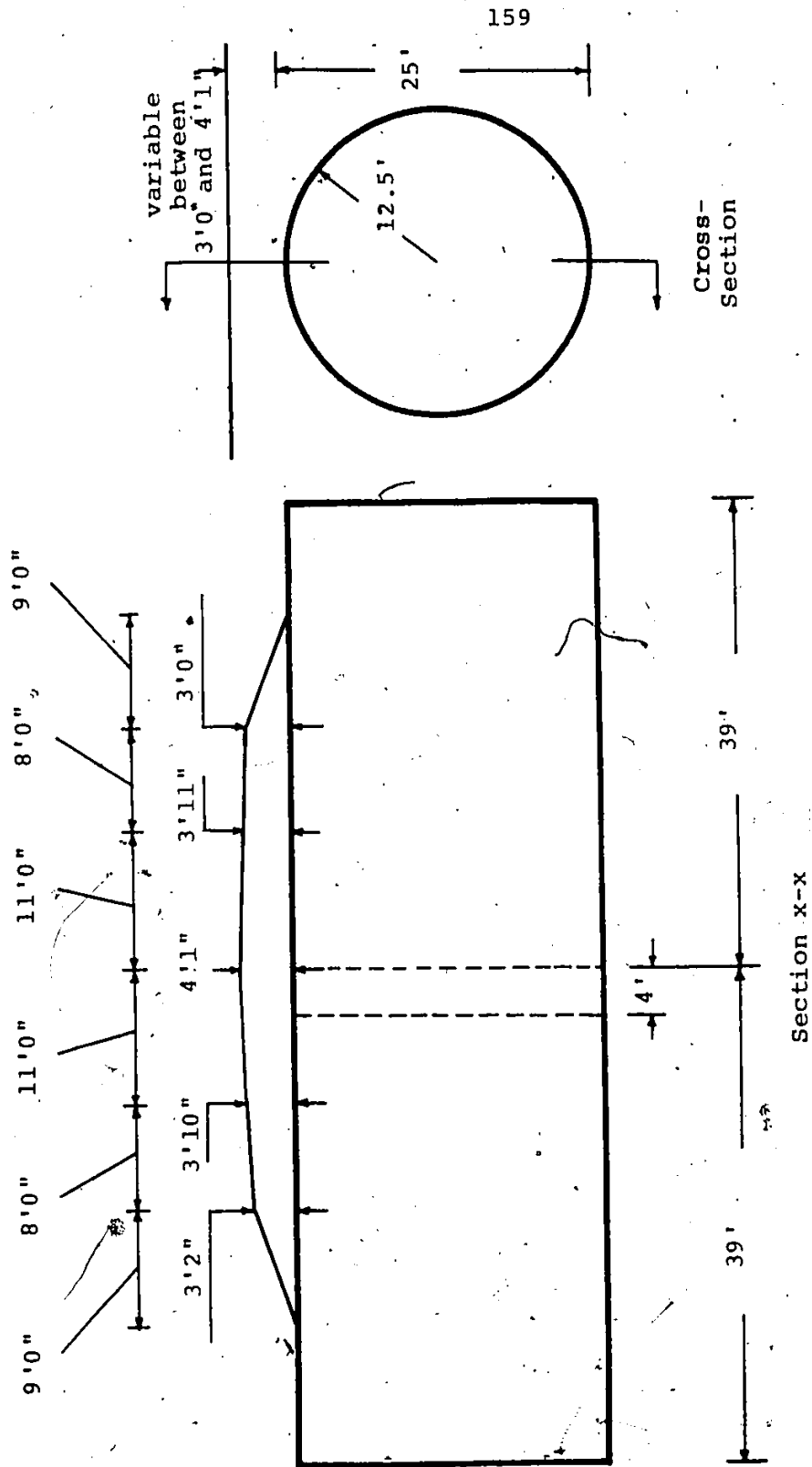


Fig. 4.1 Details of White Ash Creek soil-steel structure.

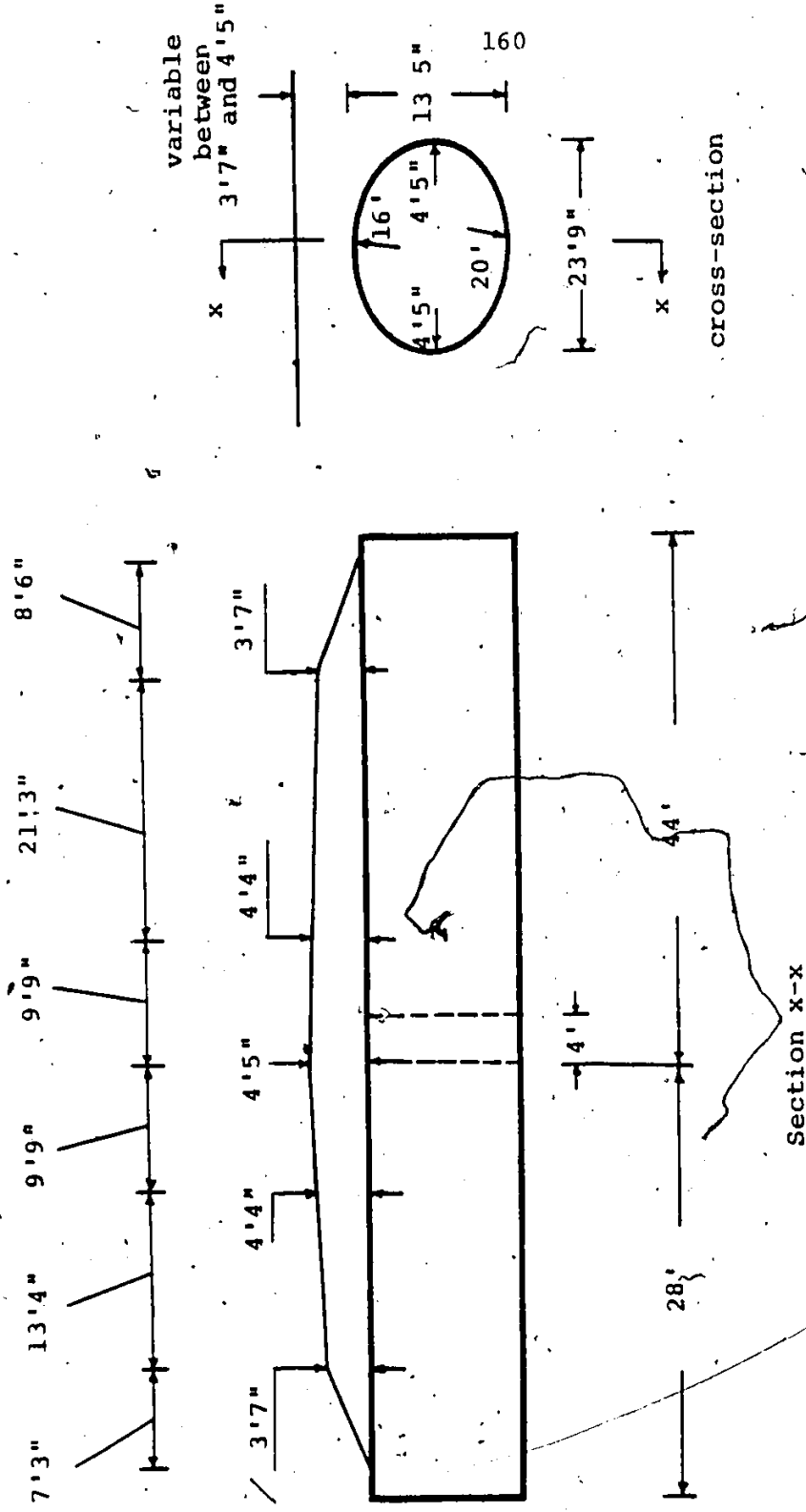


Fig. 4.2. Details of Adelaide Creek soil-steel structure.

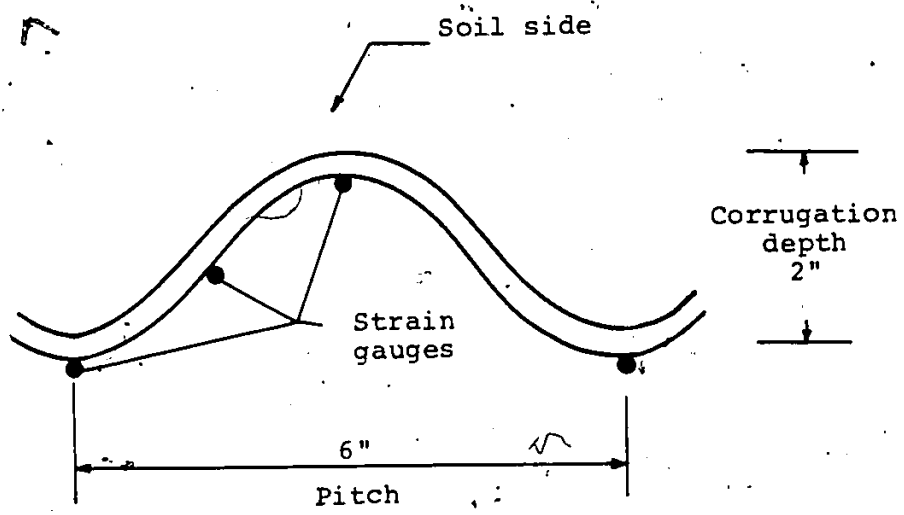
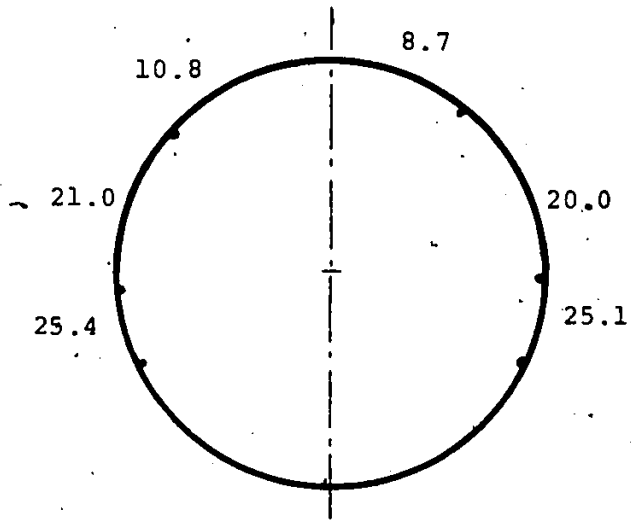
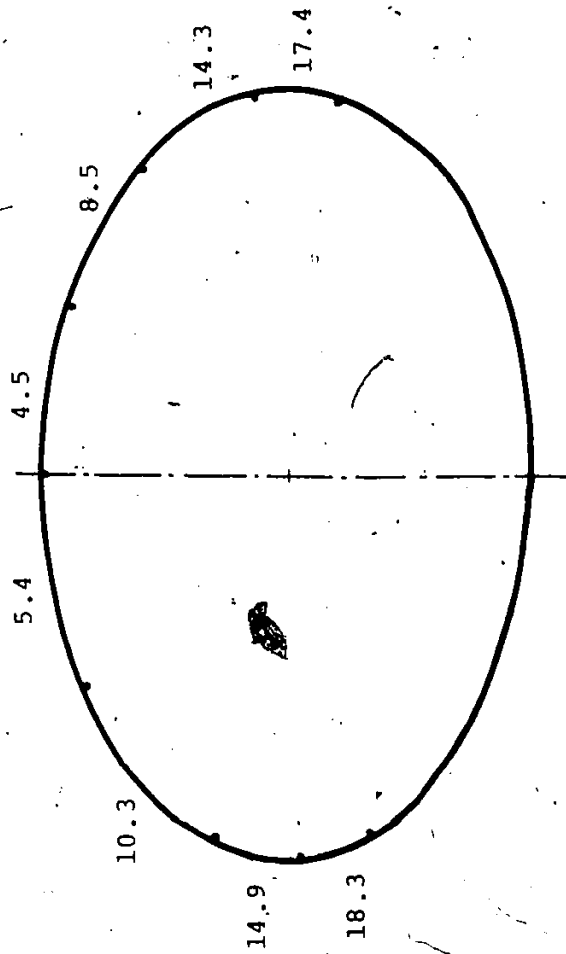


Fig. 4.3. Typical strain gauge positions at one location.



Distance to gauge location from
top C/L. (in feet).

Fig. 4.4. Instrumented locations at
the Central cross-section of
White Ash Creek structure.



Distance to gauge location from top C/L. (in feet).

Fig. 4.5. Instrumented locations at the Central cross-section of Adelaide Creek structure.

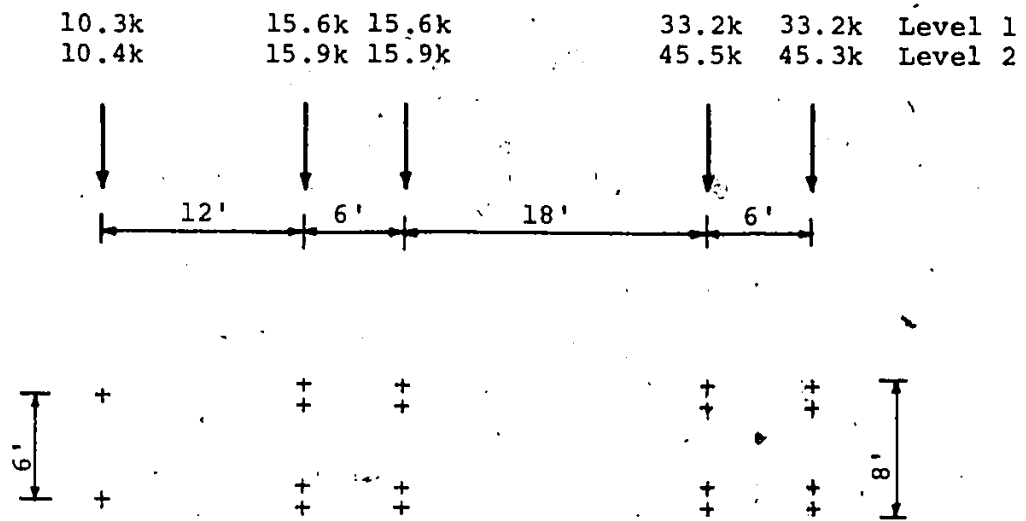


Fig. 4.6. Details of one of the testing vehicles.

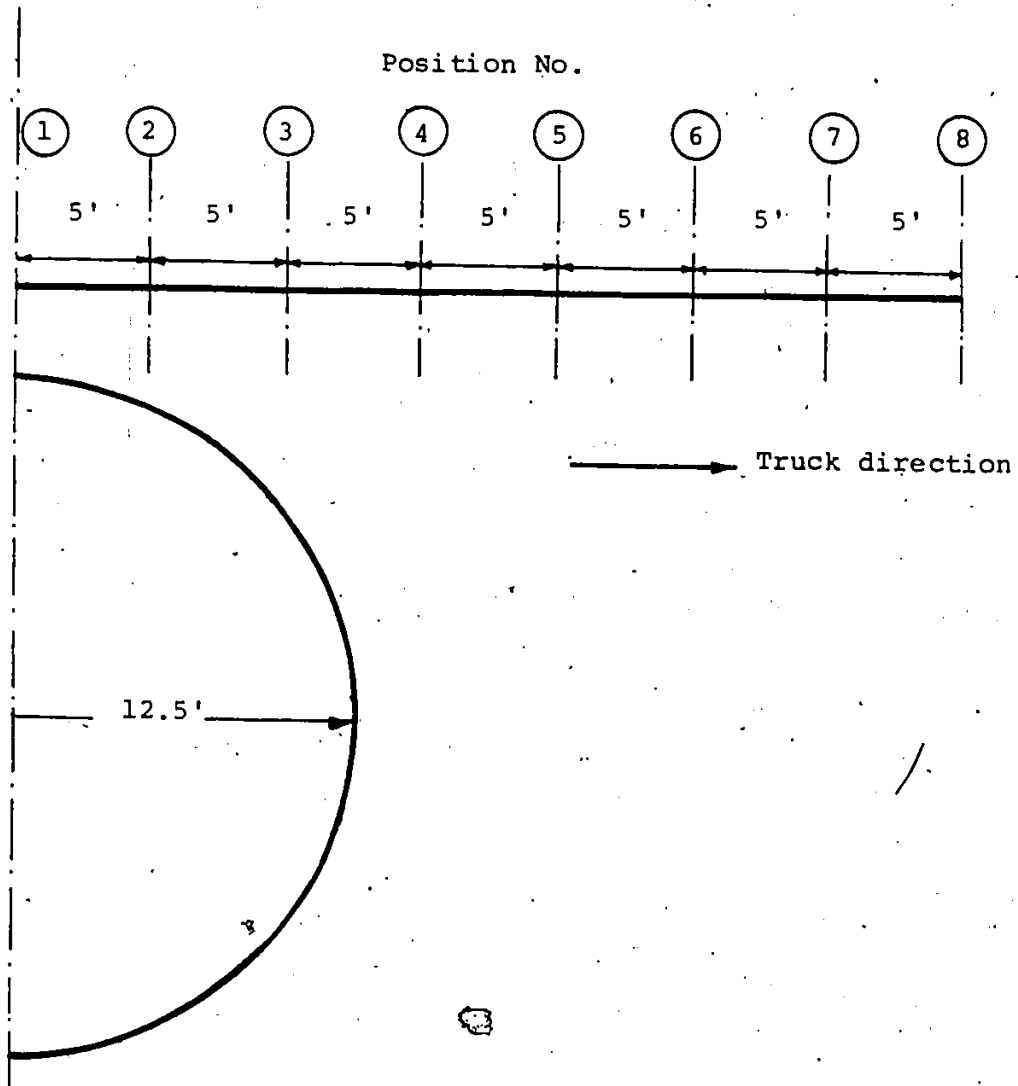
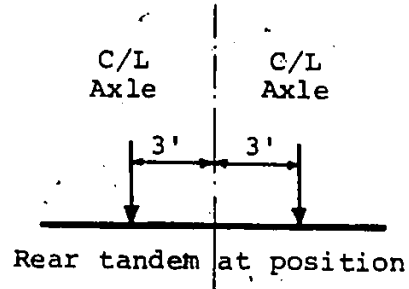


Fig. 4.7. Rear tandem positions during testing.

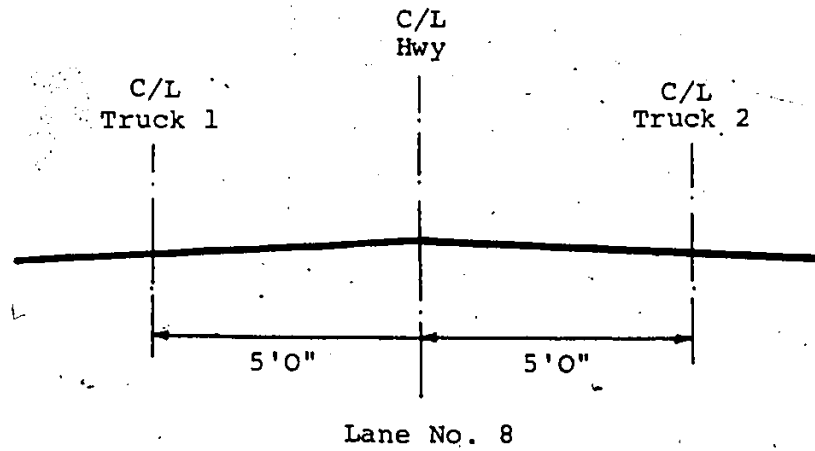
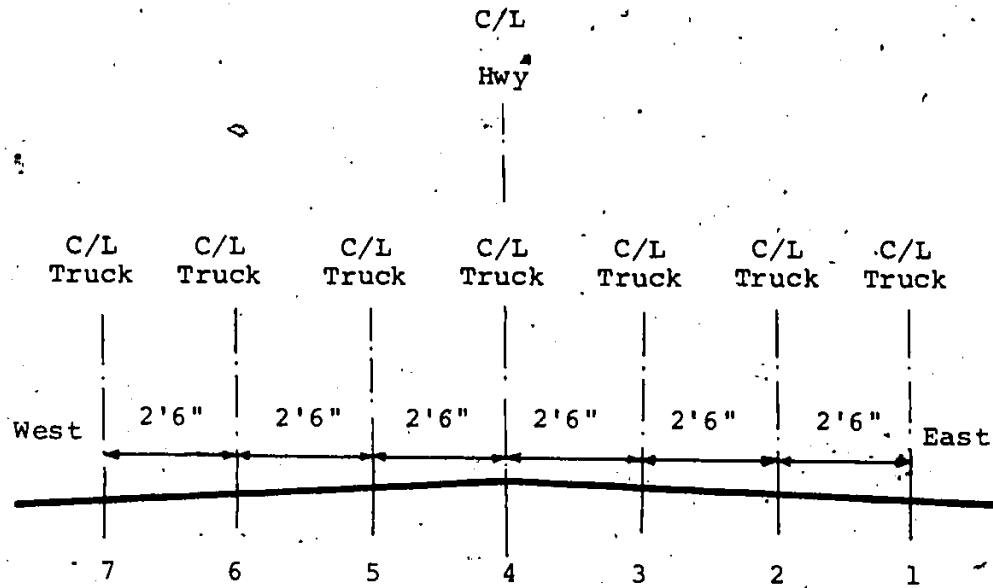


Fig. 4.8., Different vehicle lanes during testing.

167

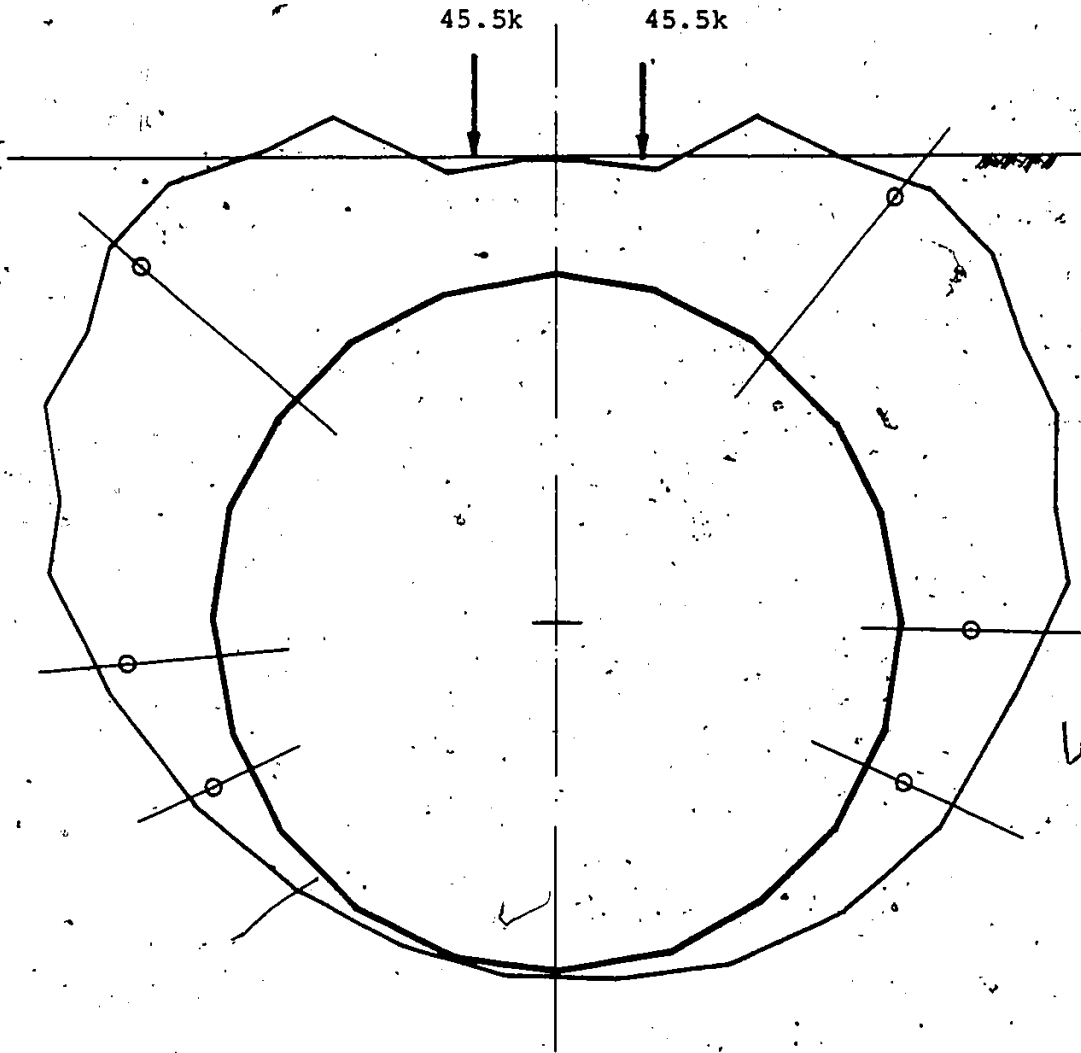


Fig. 4.9. Experimental and analytical live load thrust in White Ash Creek due to Load Level 2, Lane 4 and Position 1.

Scale: 0 \longleftarrow 100 lb/in.

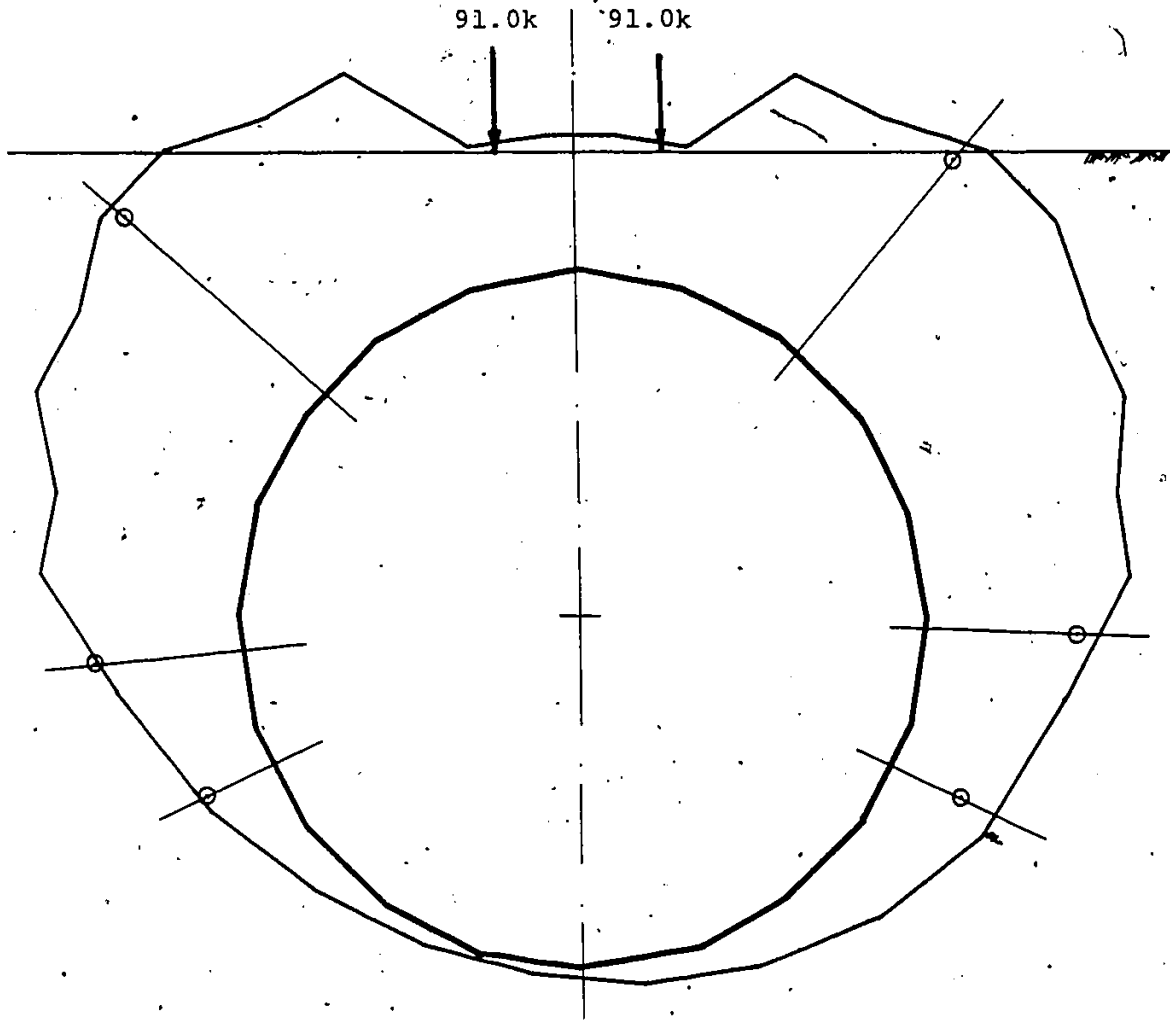


Fig. 4.10. / Experimental and analytical live load thrust in White Ash Creek due to Load Level 2, Lane 8 and Position I.

Scale: 0 \longleftarrow 100 lb/in.

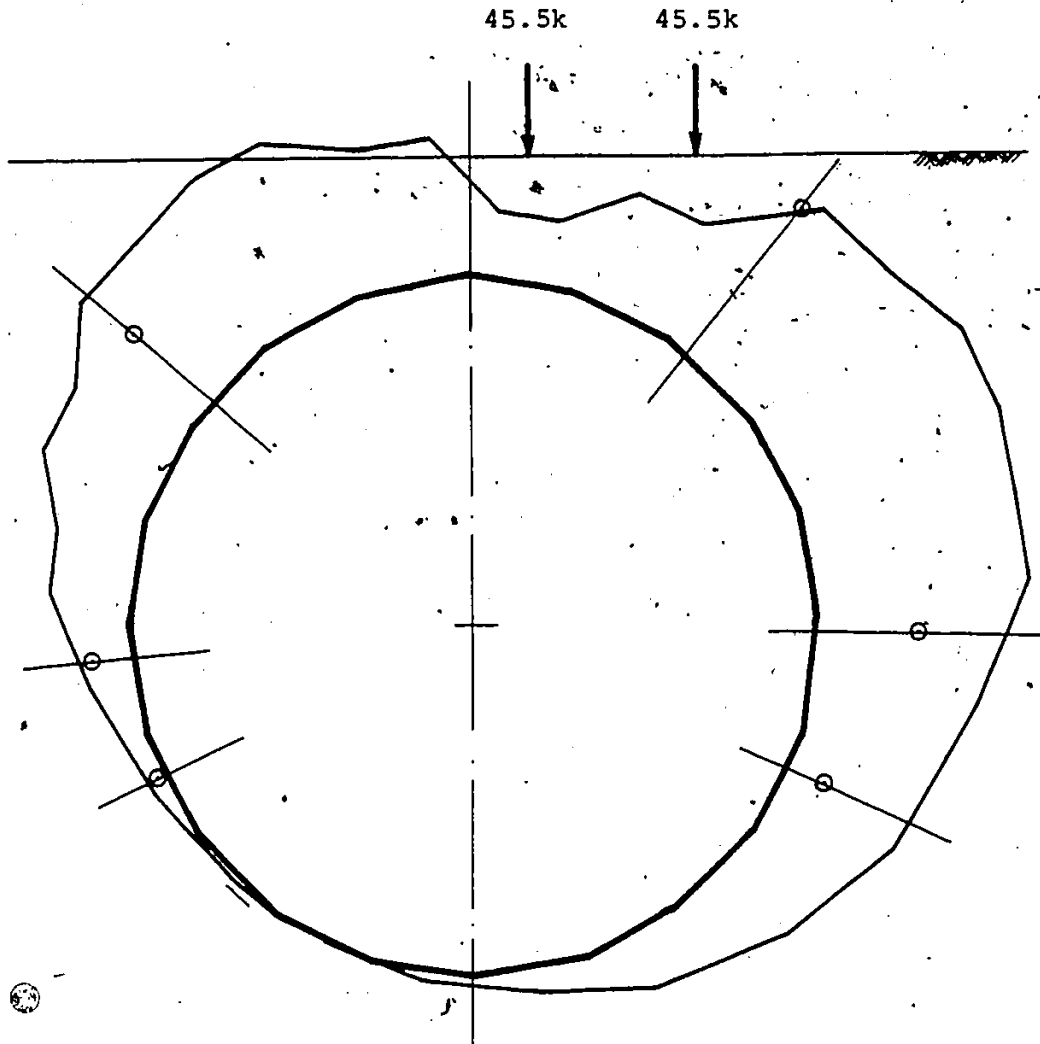


Fig. 4.11. Experimental and analytical live load thrust in White Ash Creek due to Load Level 2, Lane 4 and Position 2.

Scale: 0 — 100 lb/in.

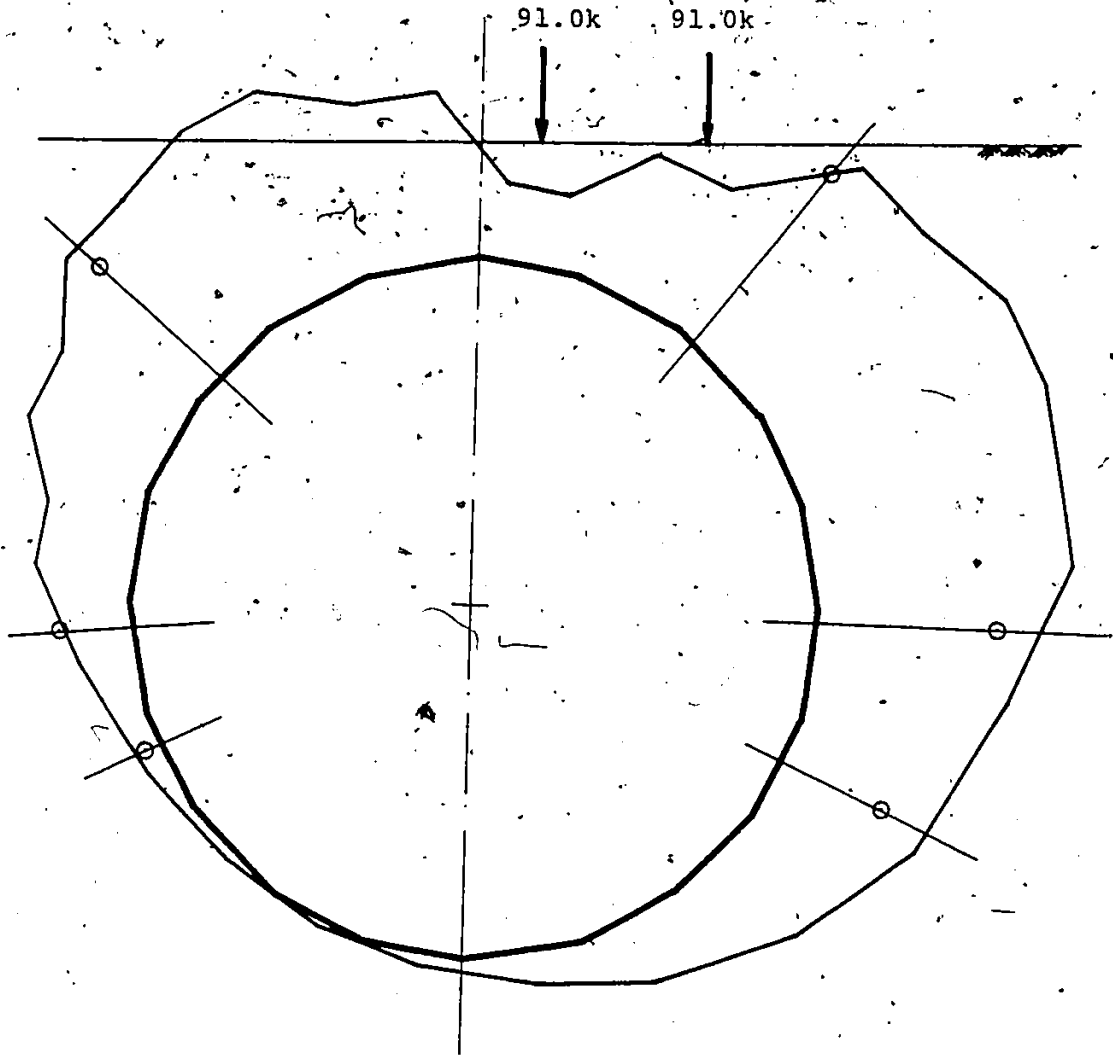


Fig. 4.12 Experimental and analytical live load thrust in White Ash Creek due to Load Level 2, Line 8 and Position 2.

Scale: 0 \longleftarrow 100 lb/in.

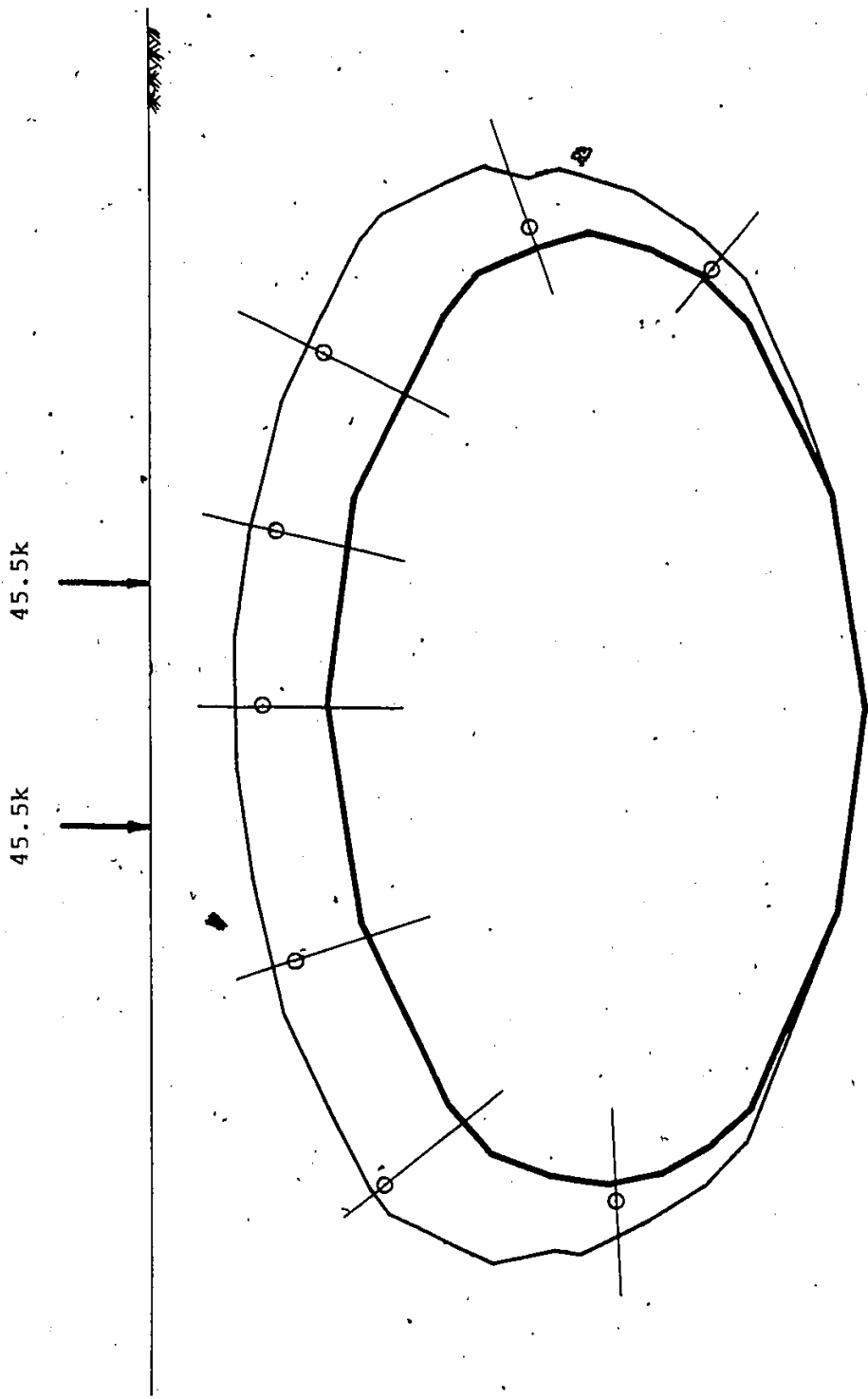


Fig. 4.13. Experimental and analytical live load thrust in Adelaide Creek Load Level 2, Lane 4, and Position 1.

Scale: 0 |---| 200 lb/in.

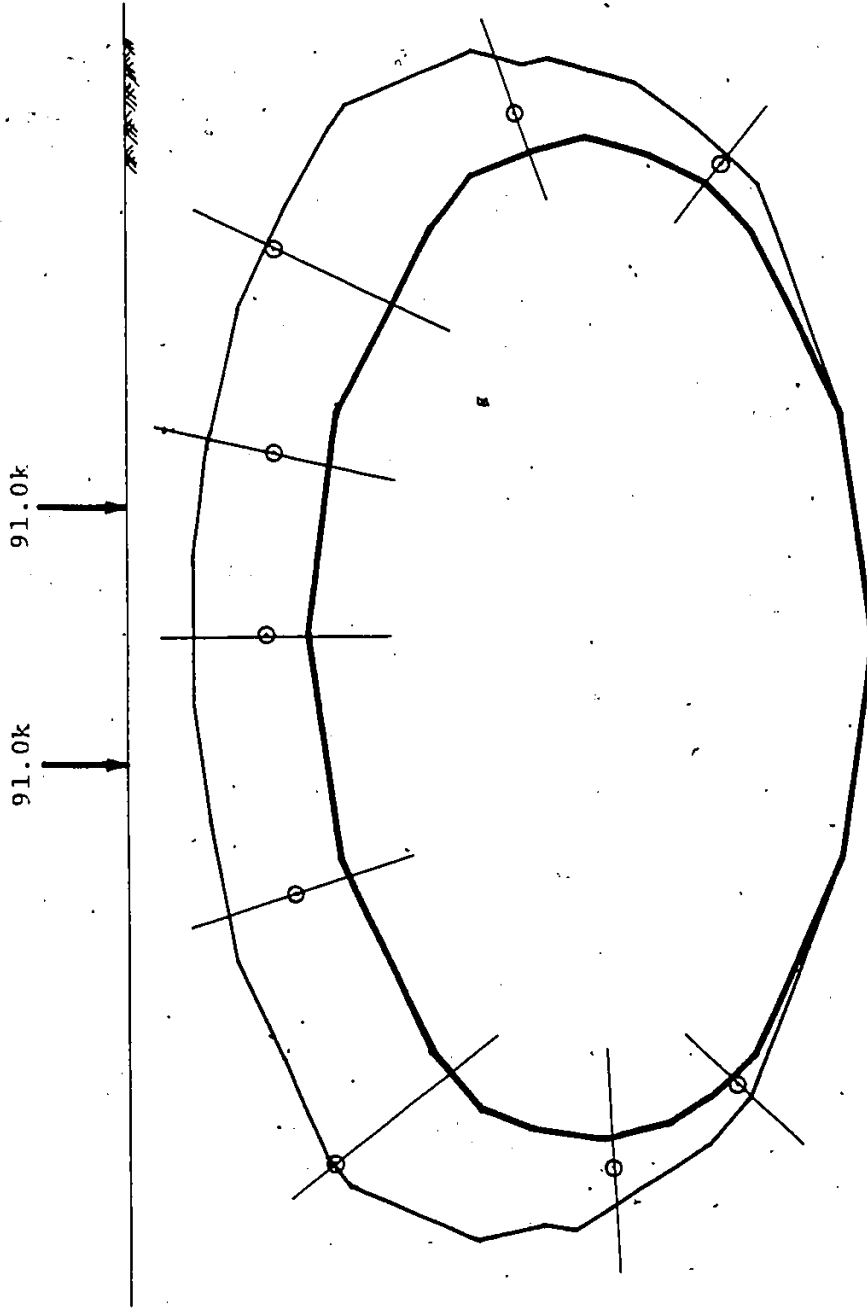


Fig. 4.14. Experimental and analytical live load thrust in Adelaide Creek due to Load Level 2, Lane 8 and Position 1.

Scale: 0  200 lb/in.

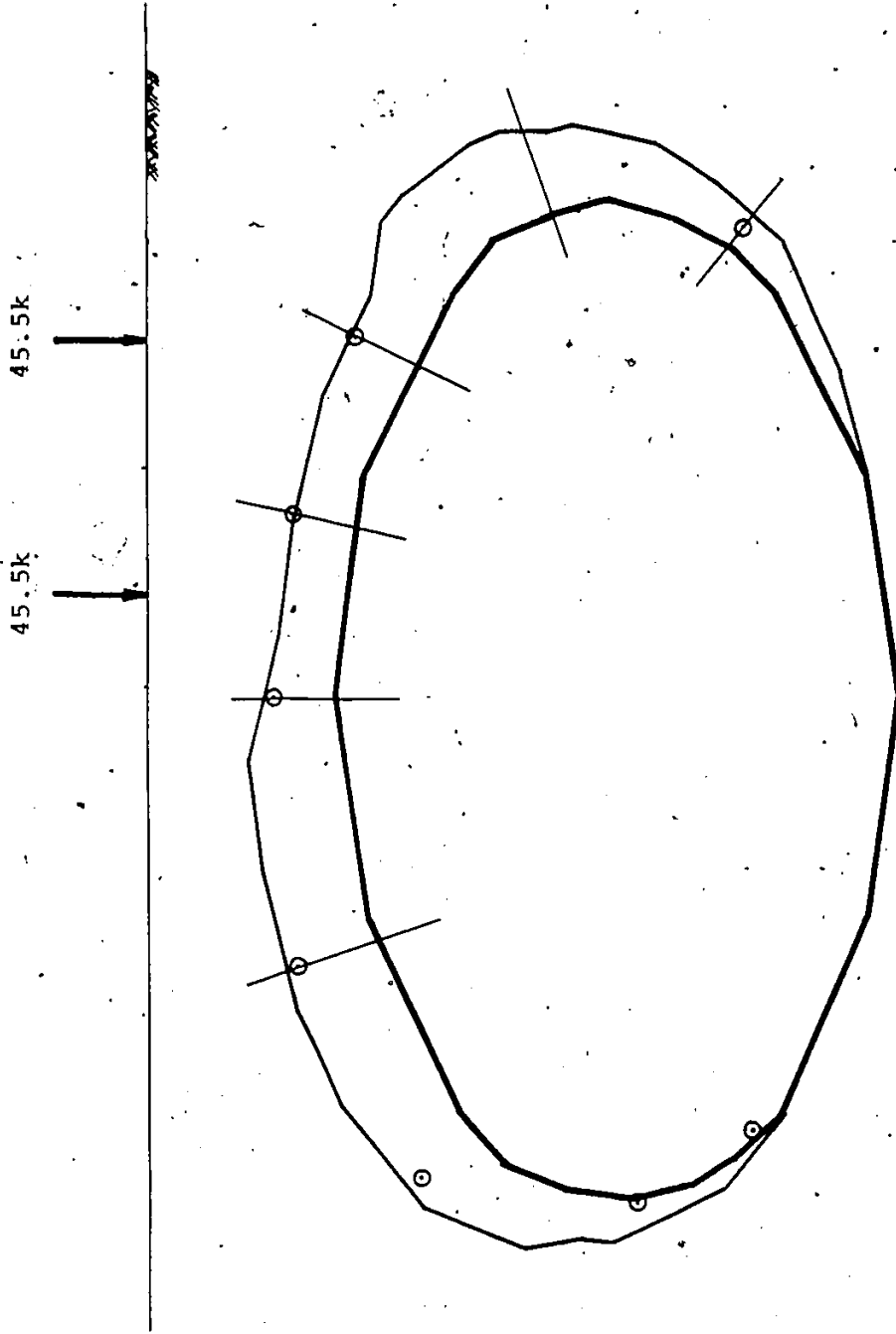


Fig. 4.15. Experimental and analytical live load thrust in Adelaide Creek due to Load Level 2, Lane 4 and Position 2.

Scale: 0 — 200 lb/in.

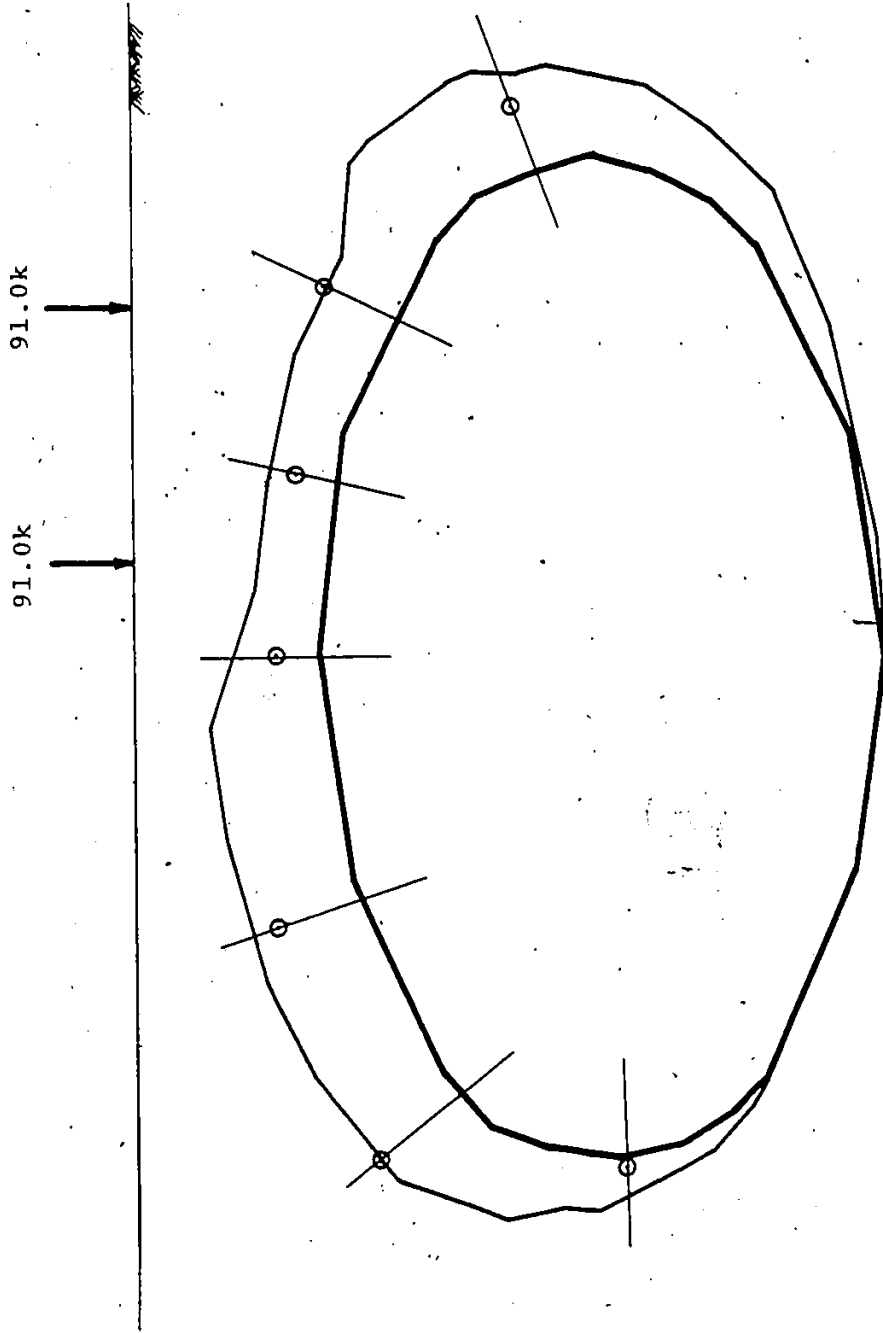


Fig. 4.16. Experimental and analytical live load thrust in Adelaide Creek due to Load Level 2, Lane 8 and Position 2.

Scale: 0 ——— 200 lb/in.

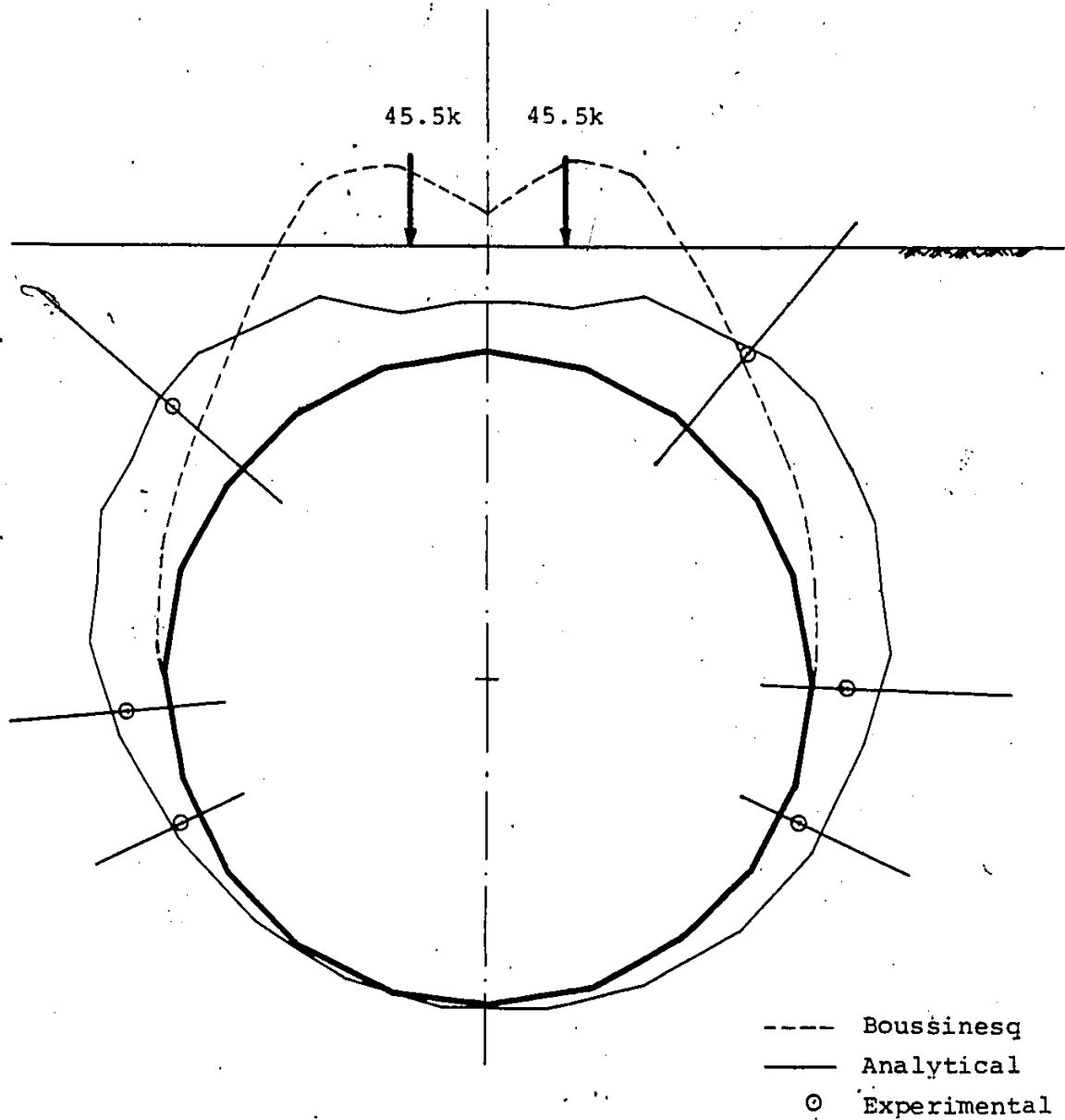


Fig. 4.17. Live load pressure distribution in White Ash Creek due to Load Level 2, Lane 4, Position 1.

Scale: 0 ——— 2 psi

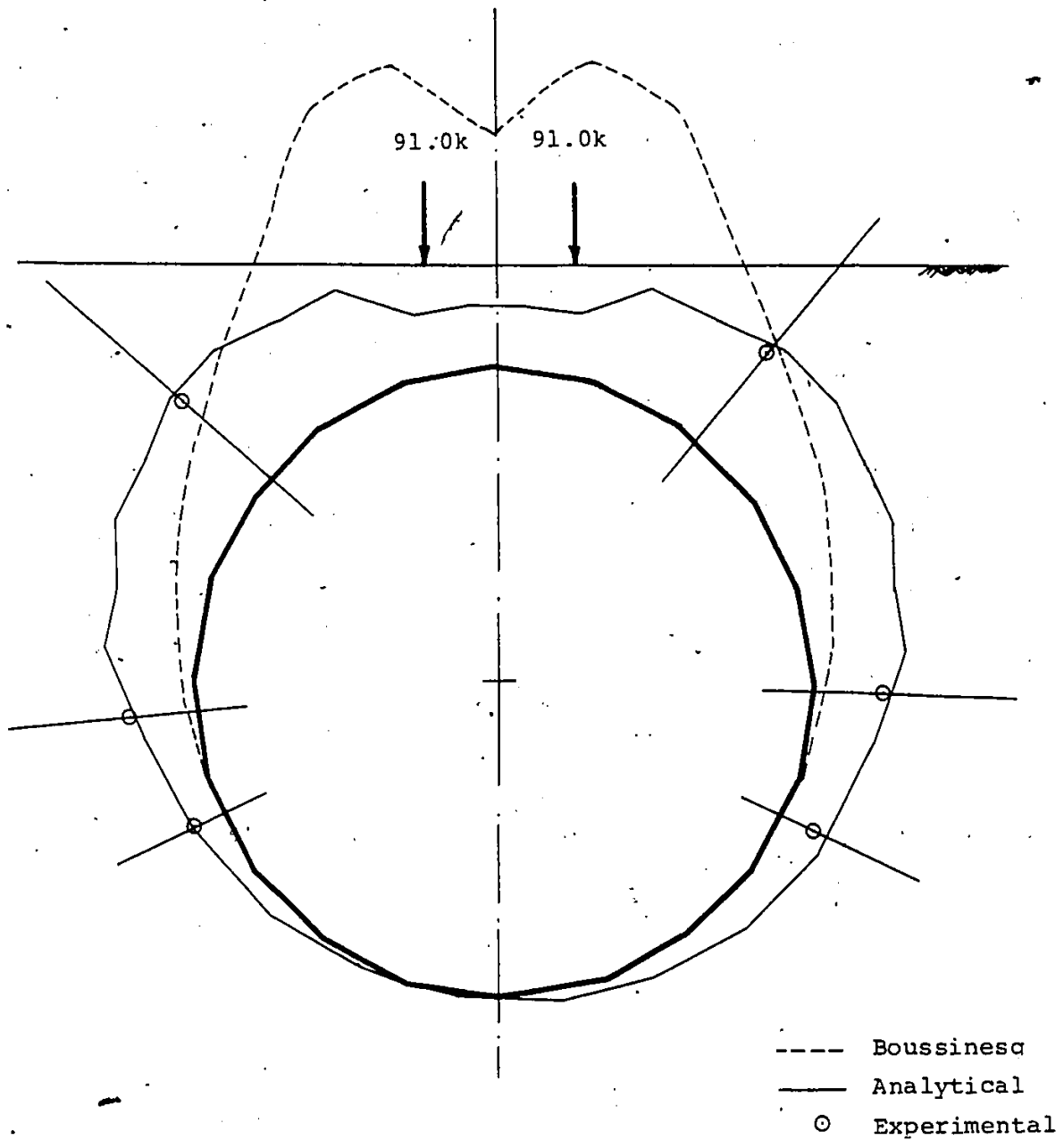


Fig. 4.18. Live load pressure distribution in White Ash Creek due to Load Level 2, Lane 8, Position 1.

Scale: 0 ——— 2 psi

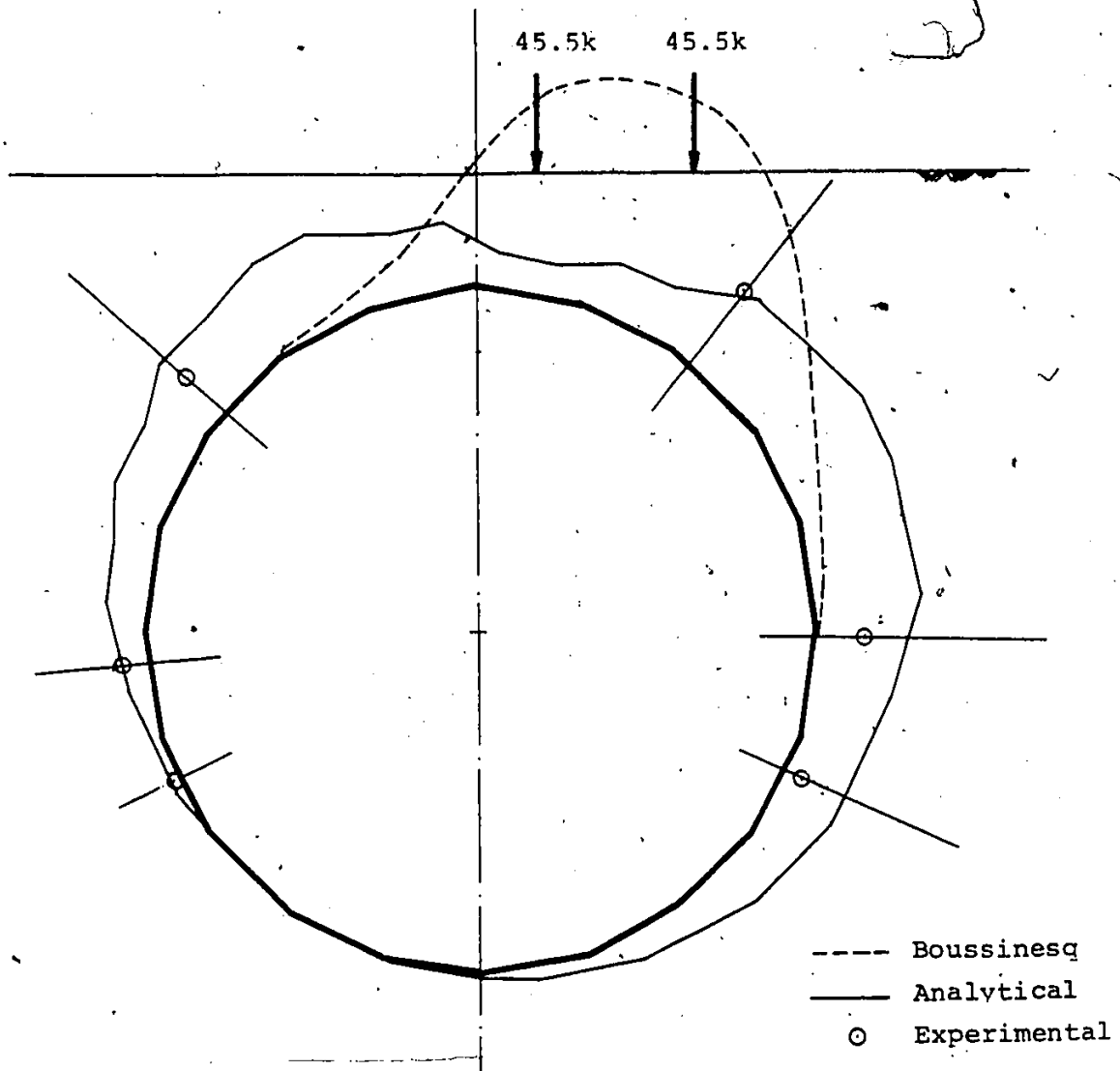


Fig. 4.19. Live load pressure distribution in White Ash Creek due to Load Level₂, Lane 4, Position 2.

Scale: 0 2 psi

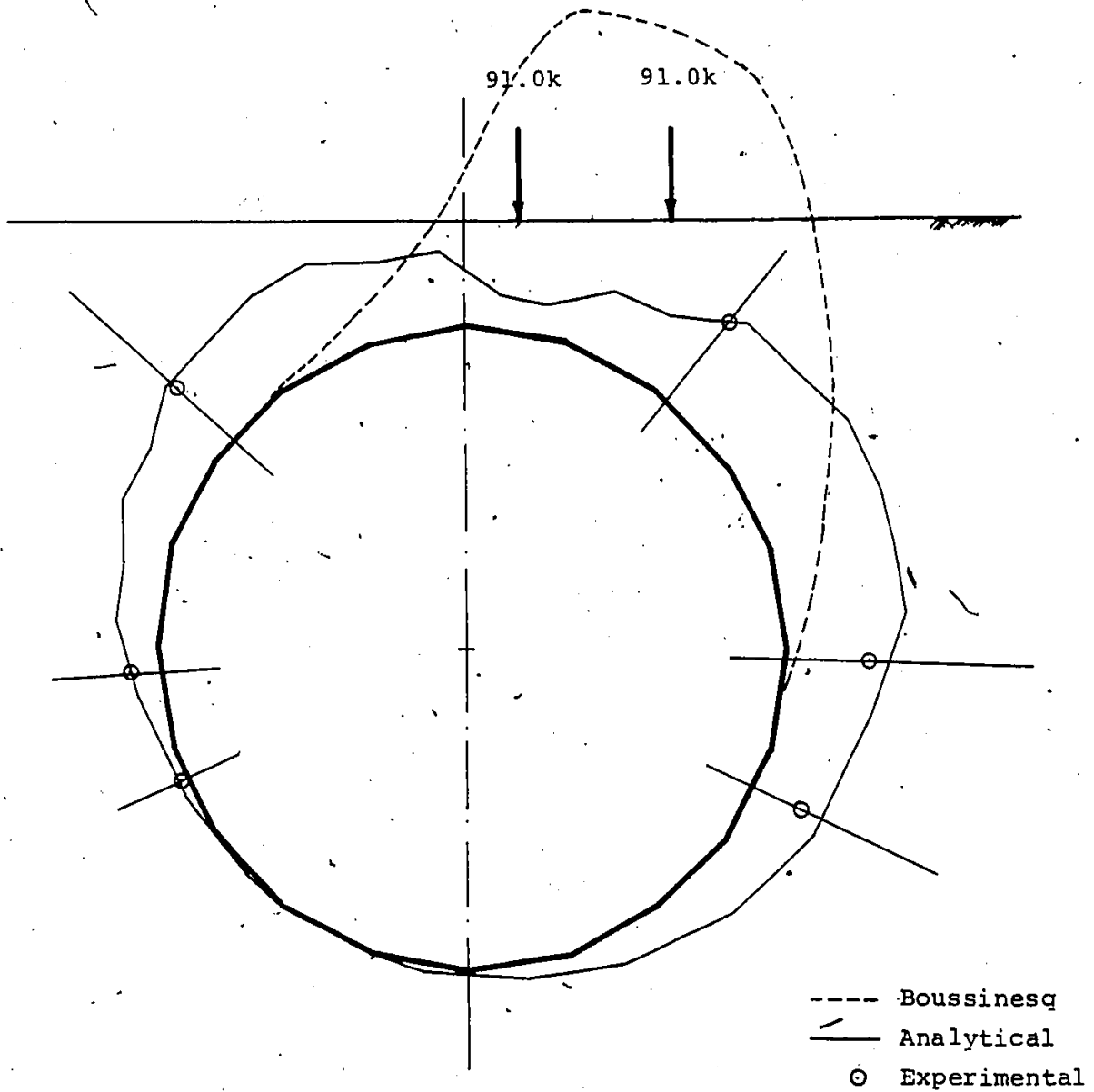


Fig. 4.20. Live load pressure distribution in White Ash Creek due to Load Level 2, Lane 8, Position 2.

Scale: 0 ——— 2 psi

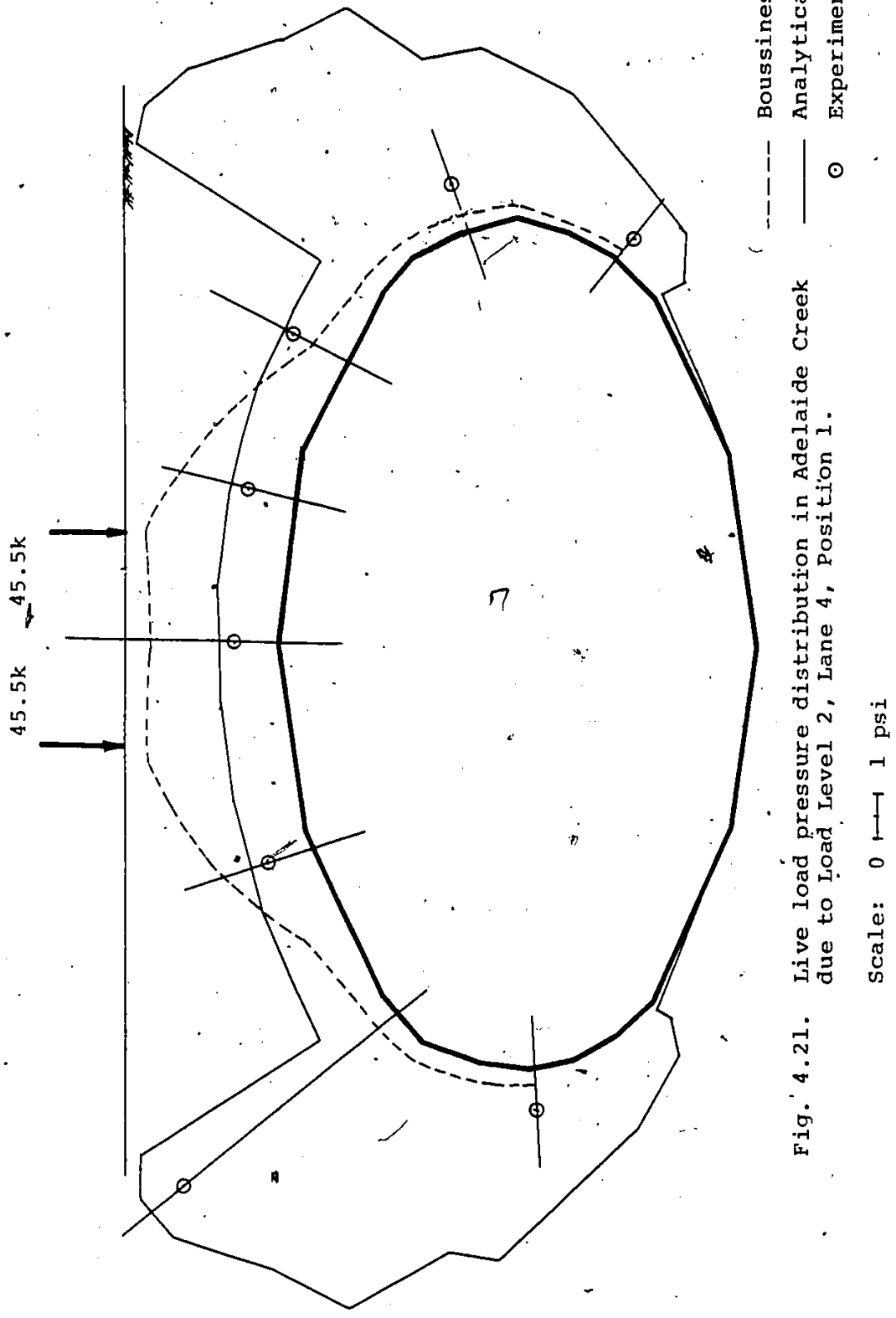
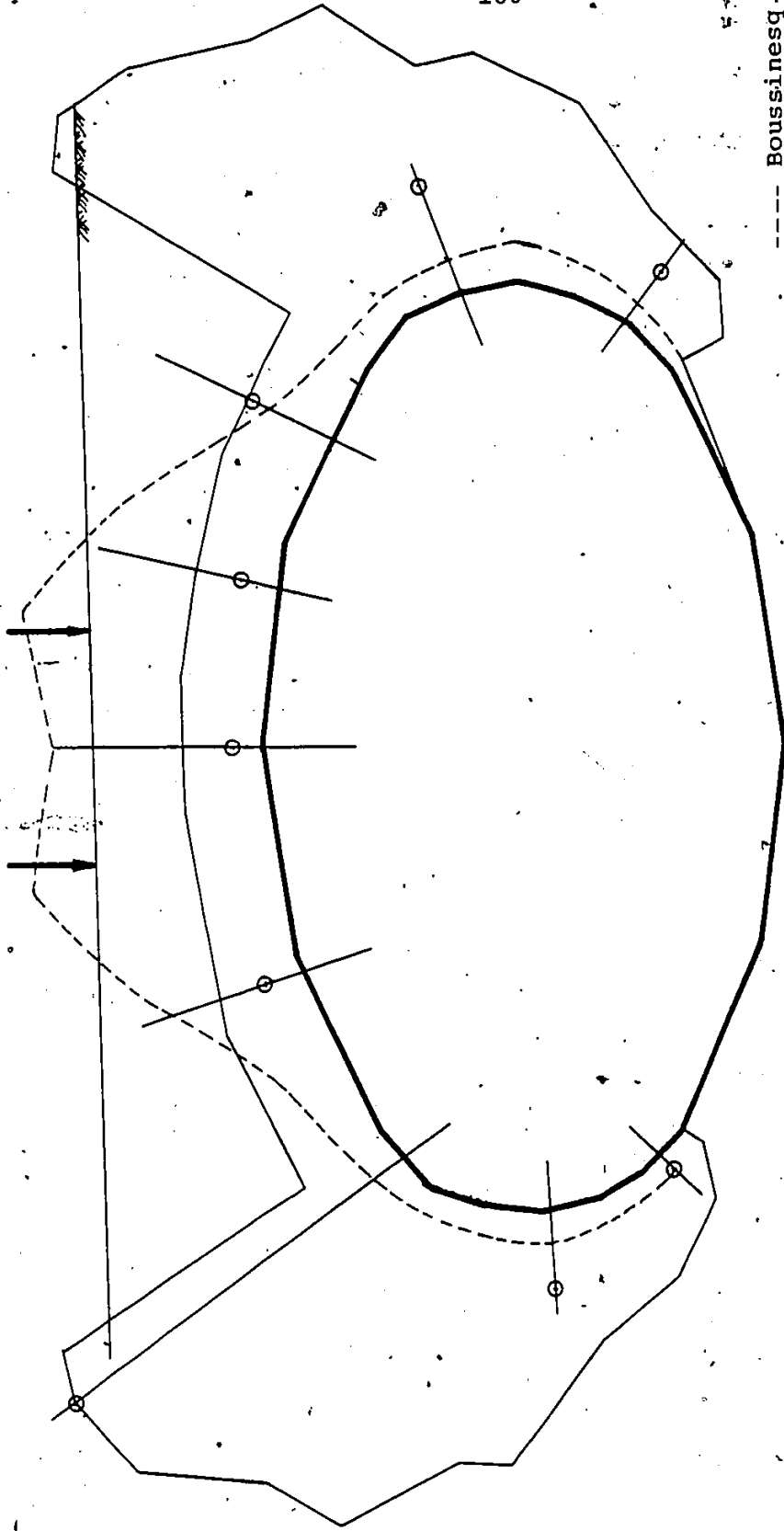


Fig. 4.21. Live load pressure distribution in Adelaide Creek due to Load Level 2, Lane 4, Position 1.

Scale: 0 to 1 psi

91.0k, 91.0k



180

----- Boussinesq
—— Analytical
○ Experimental

Fig. 4.22. Live load pressure distribution in Adelaide Creek due to Load Level 2, Lane 8, Position 1.

Scale: 0 — 1 psi

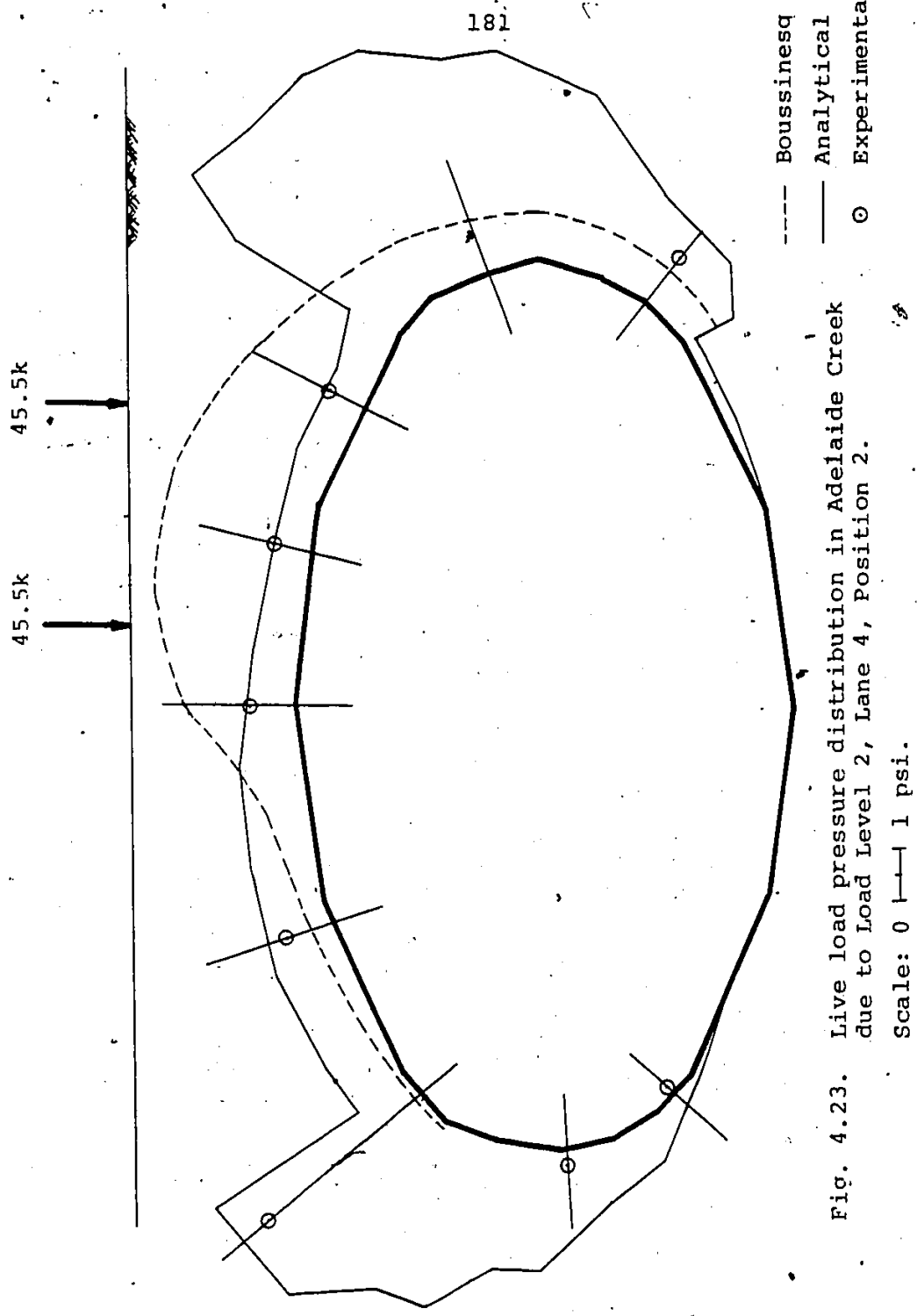
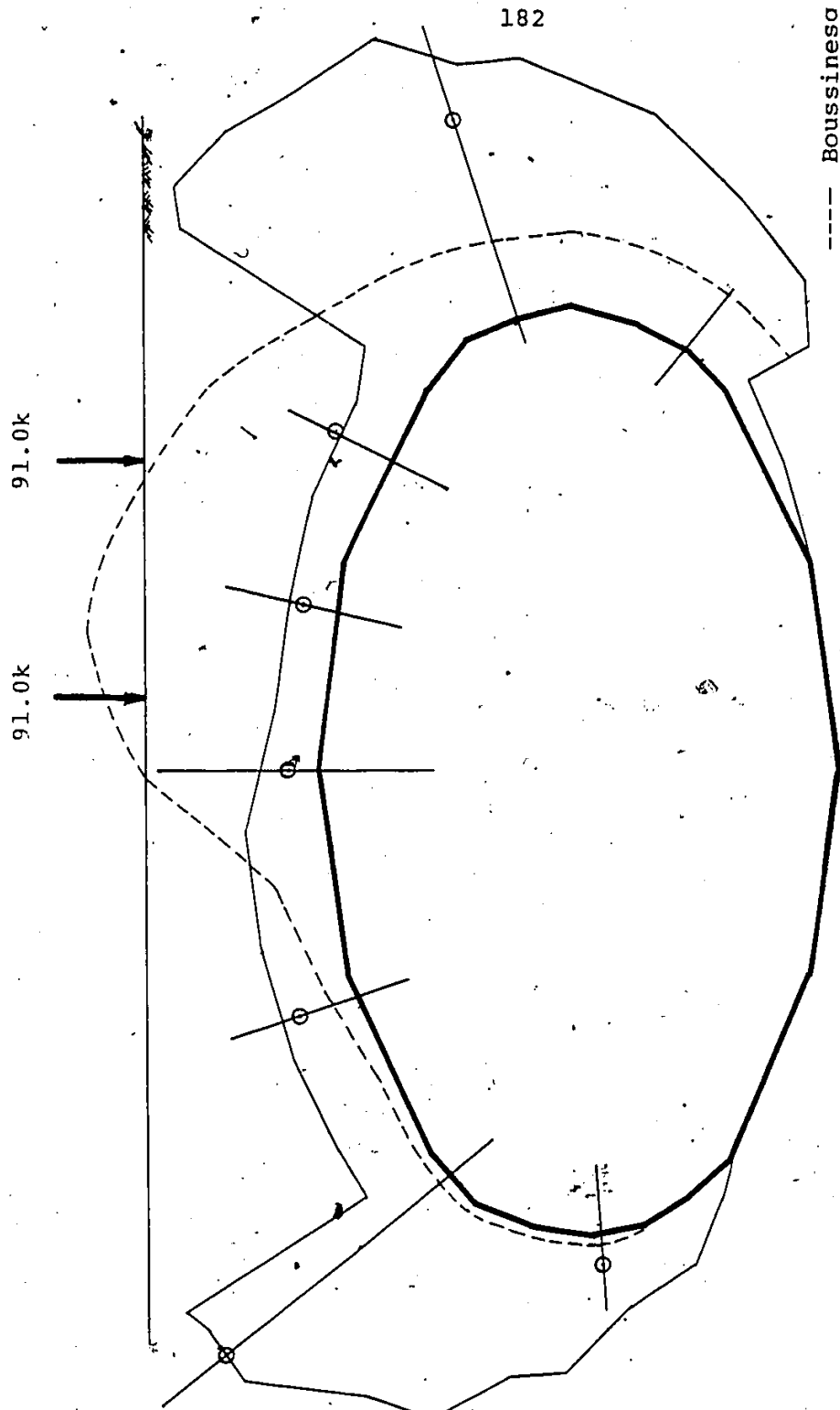


Fig. 4.23. Live load pressure distribution in Adelaide Creek due to Load Level 2, Lane 4, Position 2.



- - - Boussinesq
 — Analytical
 ○ Experimental

Fig. 4.24. Live Load pressure distribution in Adelaide Creek due to Load Level 2, Jane 8, Position 2.

Scale: 0 — 1 psi

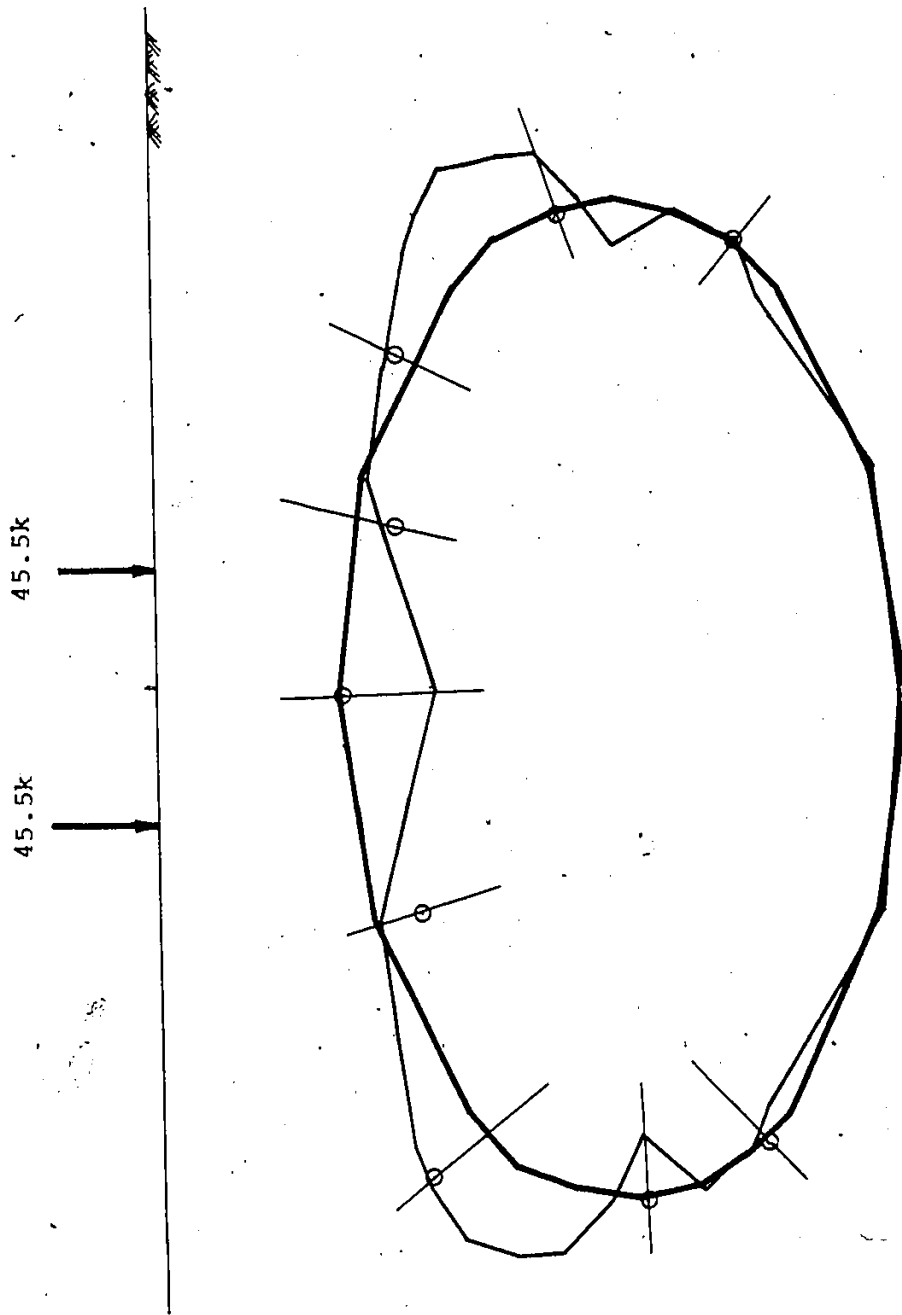


Fig. 4.25. Experimental and analytical live load moment in Adelaide Creek due to Load Level 2, Lane 4 and Position 1.

Scale: 0  100 lb.in/in.

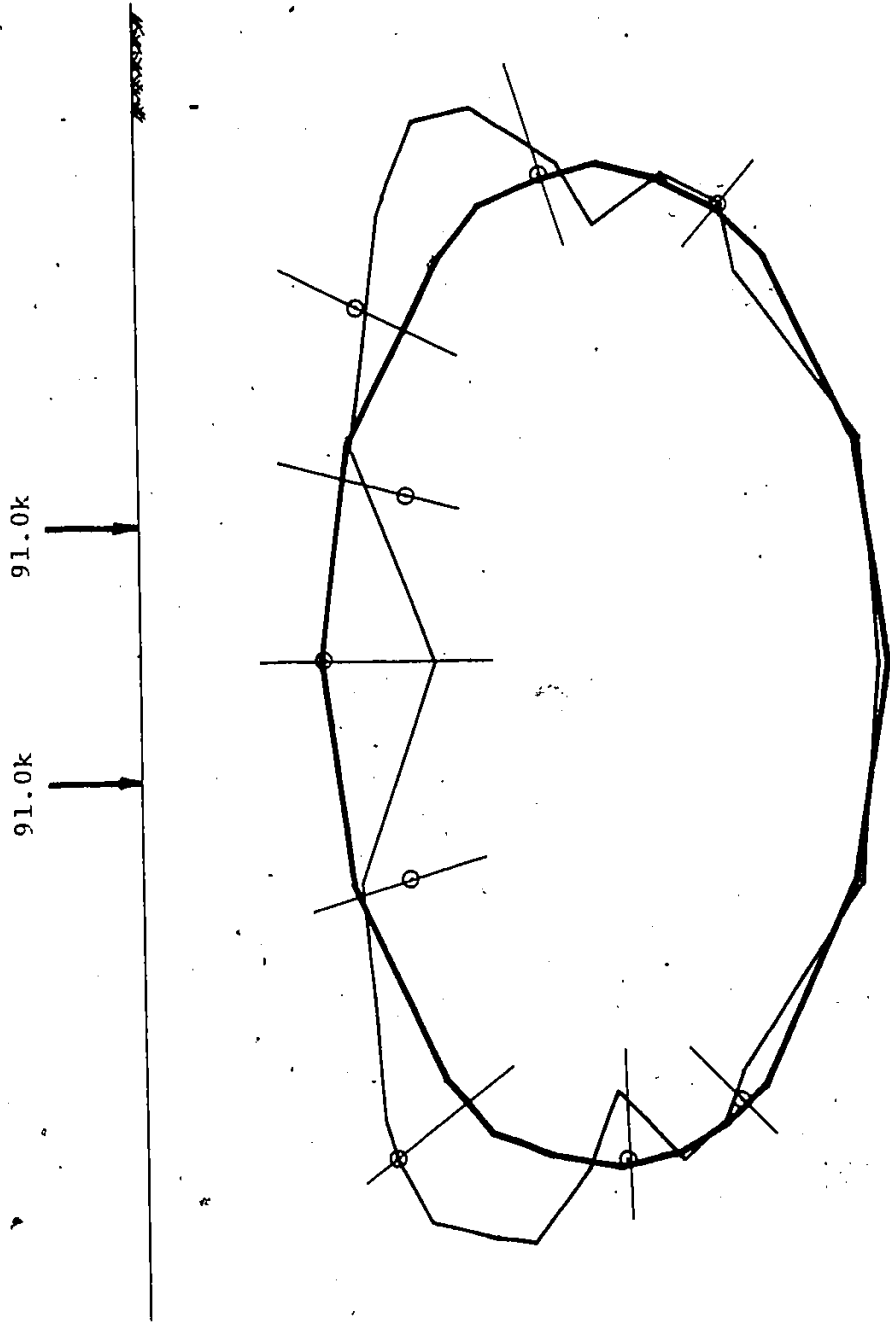


Fig. 4.26. Experimental and analytical live moment in Adelaide Creek due to Load Level 2, Lane 8 and Position 1.

Scale: 0 |---| 100 lb.in/in.

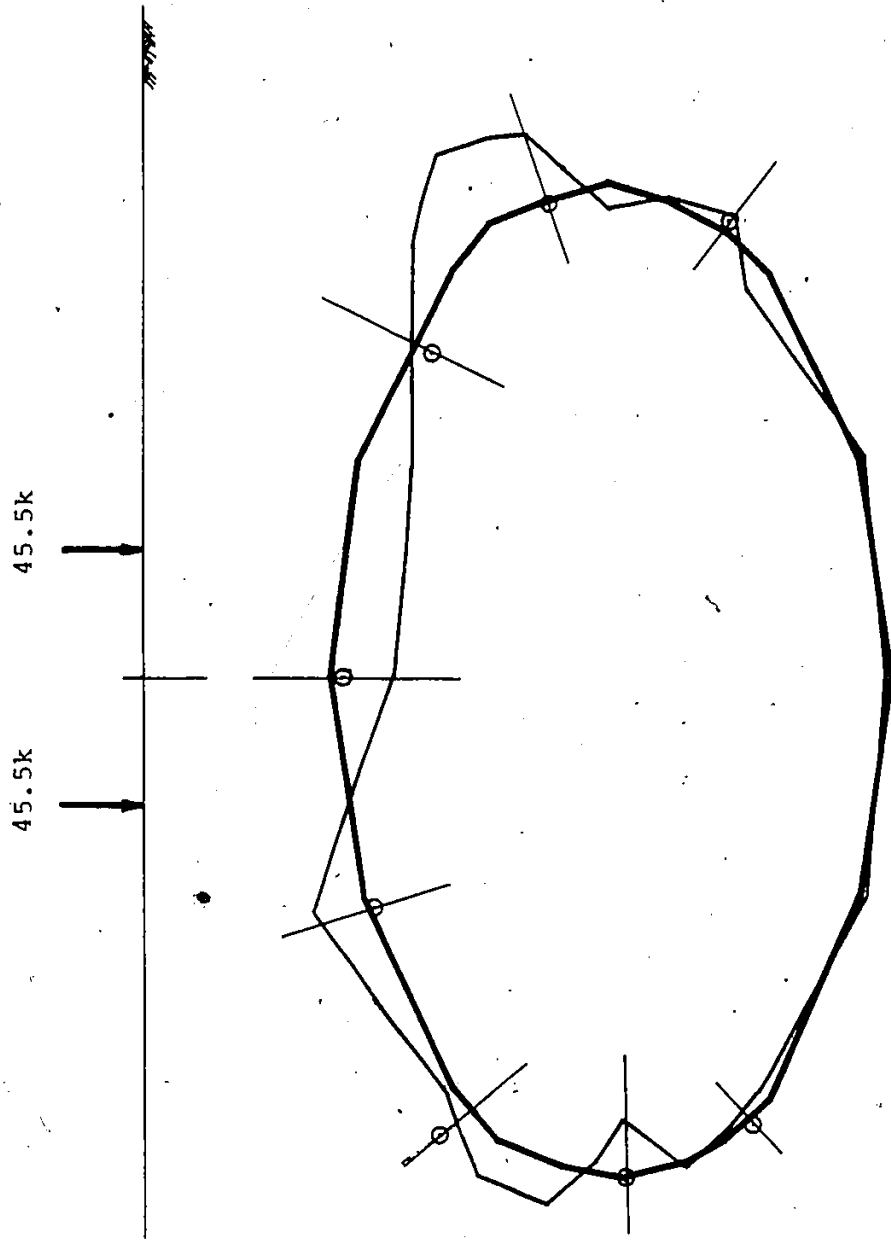


Fig. 4.27. Experimental and analytical live load moment in Adelaide Creek due to Load Level 2, Lane 4 and Position 1.

Scale: 0 [line] 100 lb.in/in.

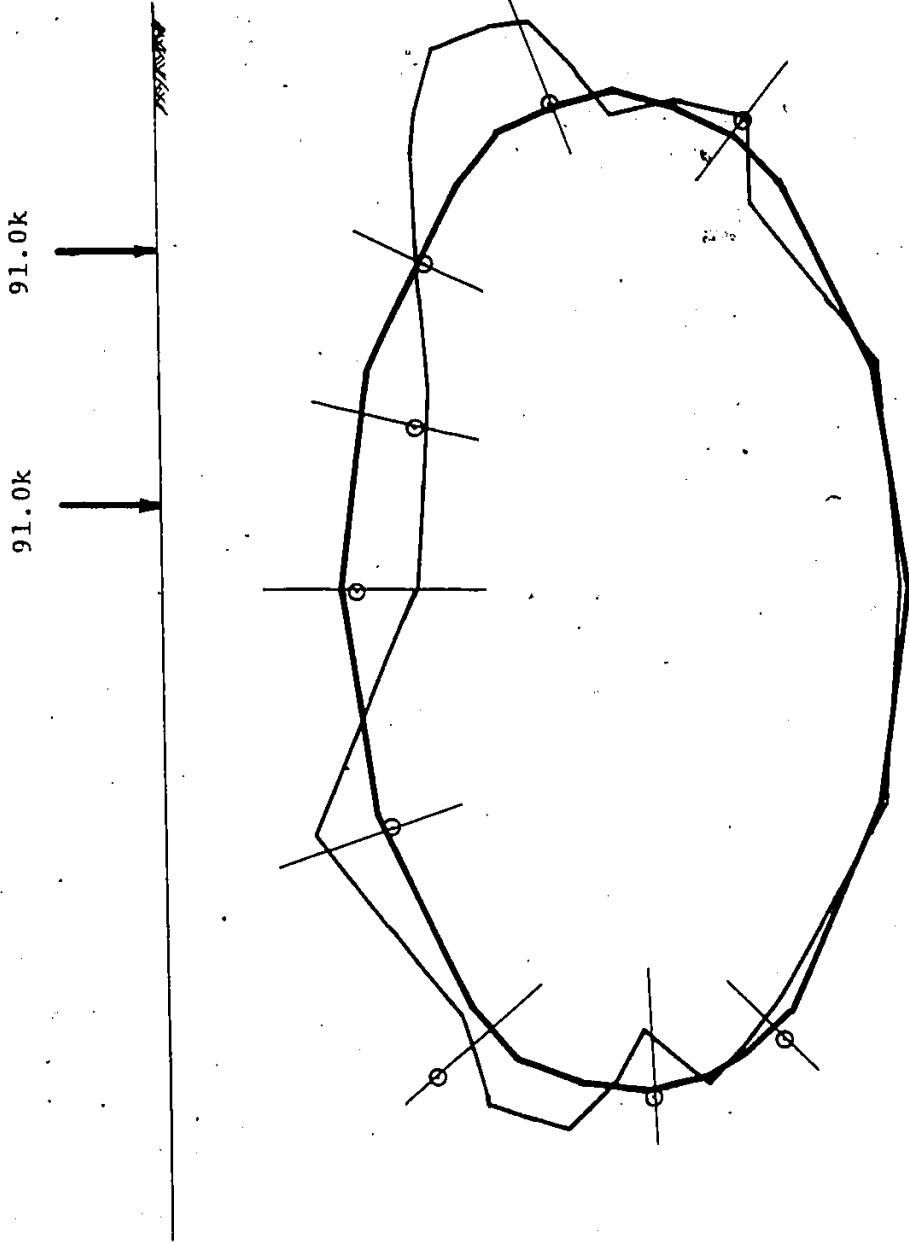


Fig. 4.28. Experimental and analytical live load moment in Adelaide Creek due to Load Level 2, Lane 8 and Position 2.

Scale: 0 $\overline{\text{---}}$ 100 lb.in/in.

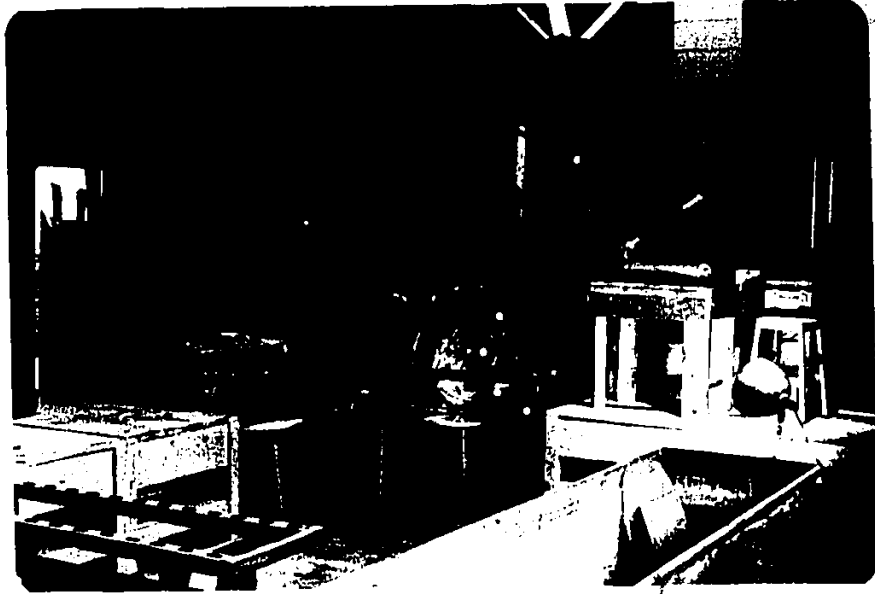


Fig. 4.29. Experimental Set-Up.

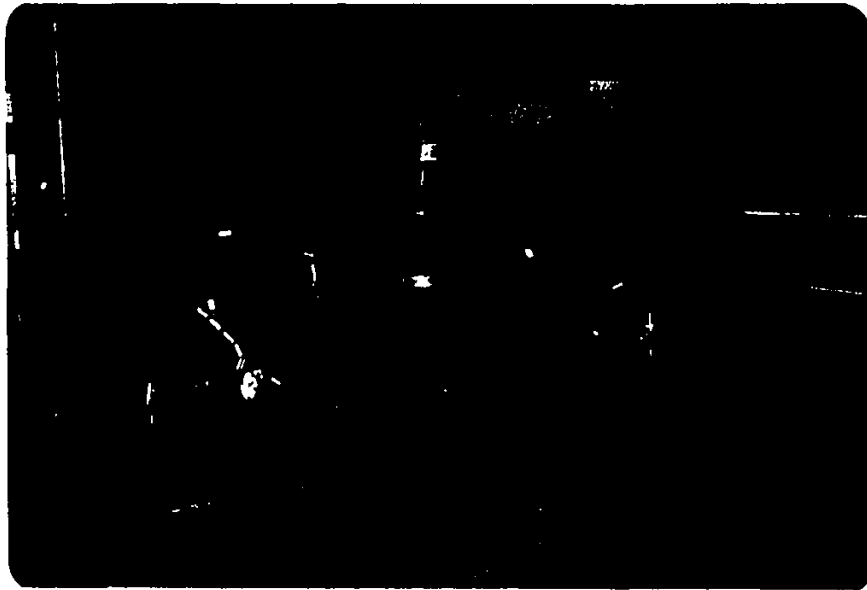


Fig. 4.30. Dial Gauge Locations on Loading Beams

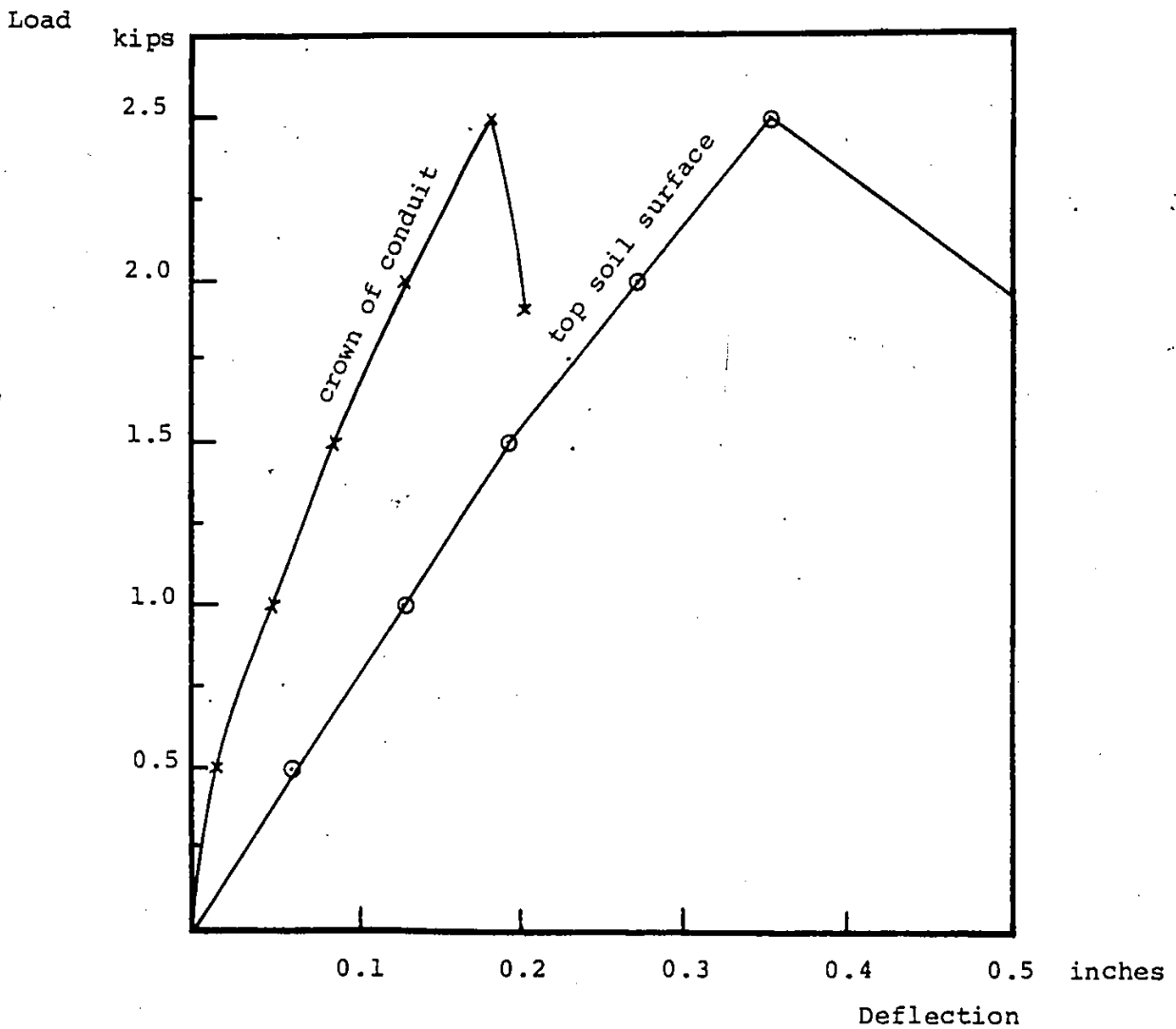


Fig. 4.31. Load deflection curves for the first cycle of loading in Test 1.

Analytical failure load = 3.22 kips

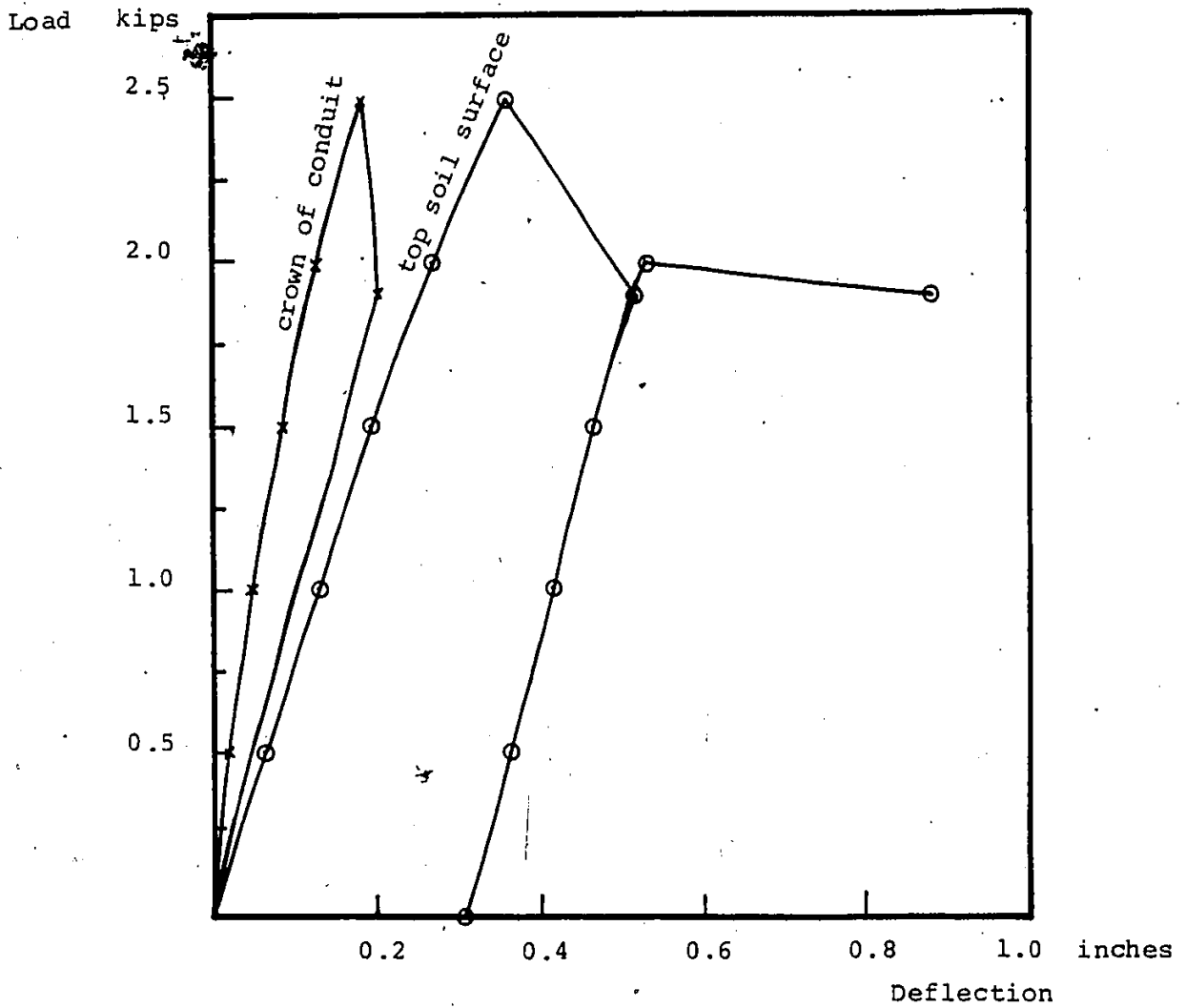


Fig. 4.32. Load-deflection curves for two cycles of loading in Test 1.

Analytical failure load = 3.22 kips

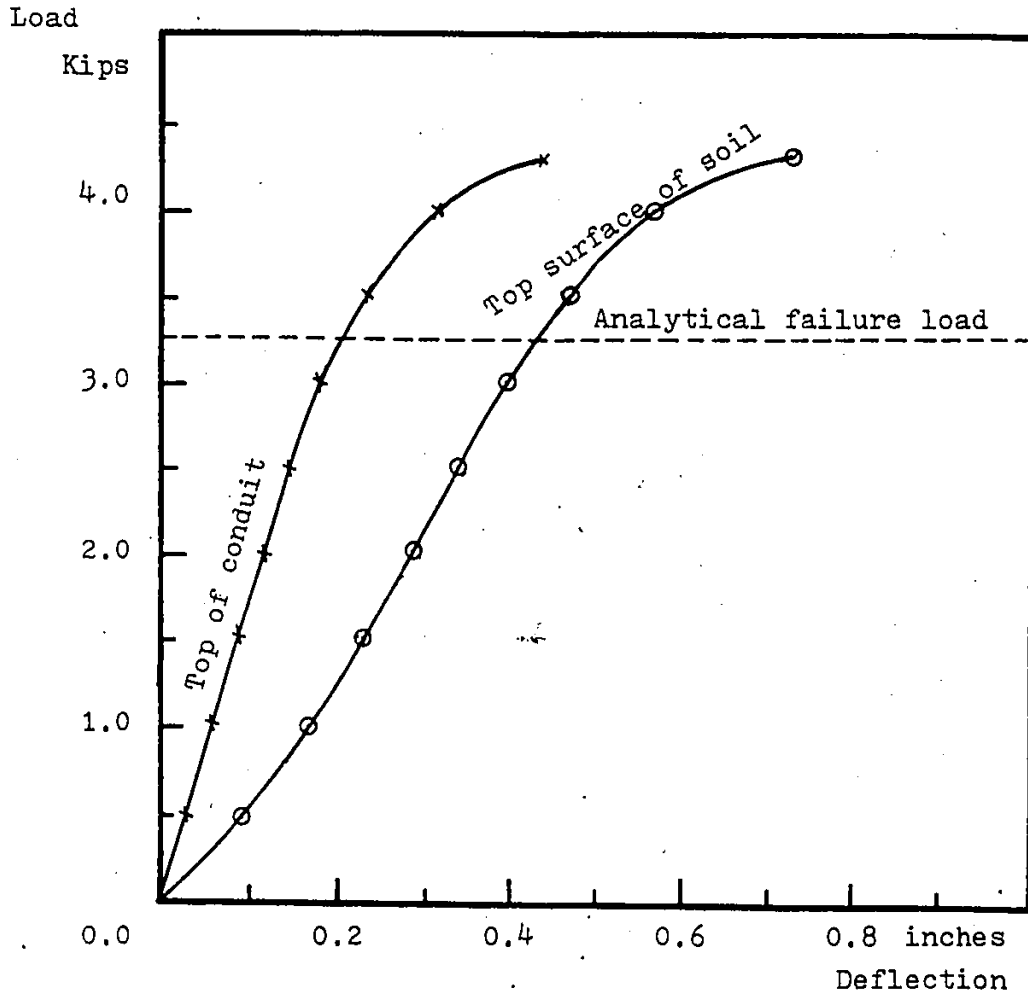


Fig. 4.33. Load-Deflection curves for laboratory Test No. 2.

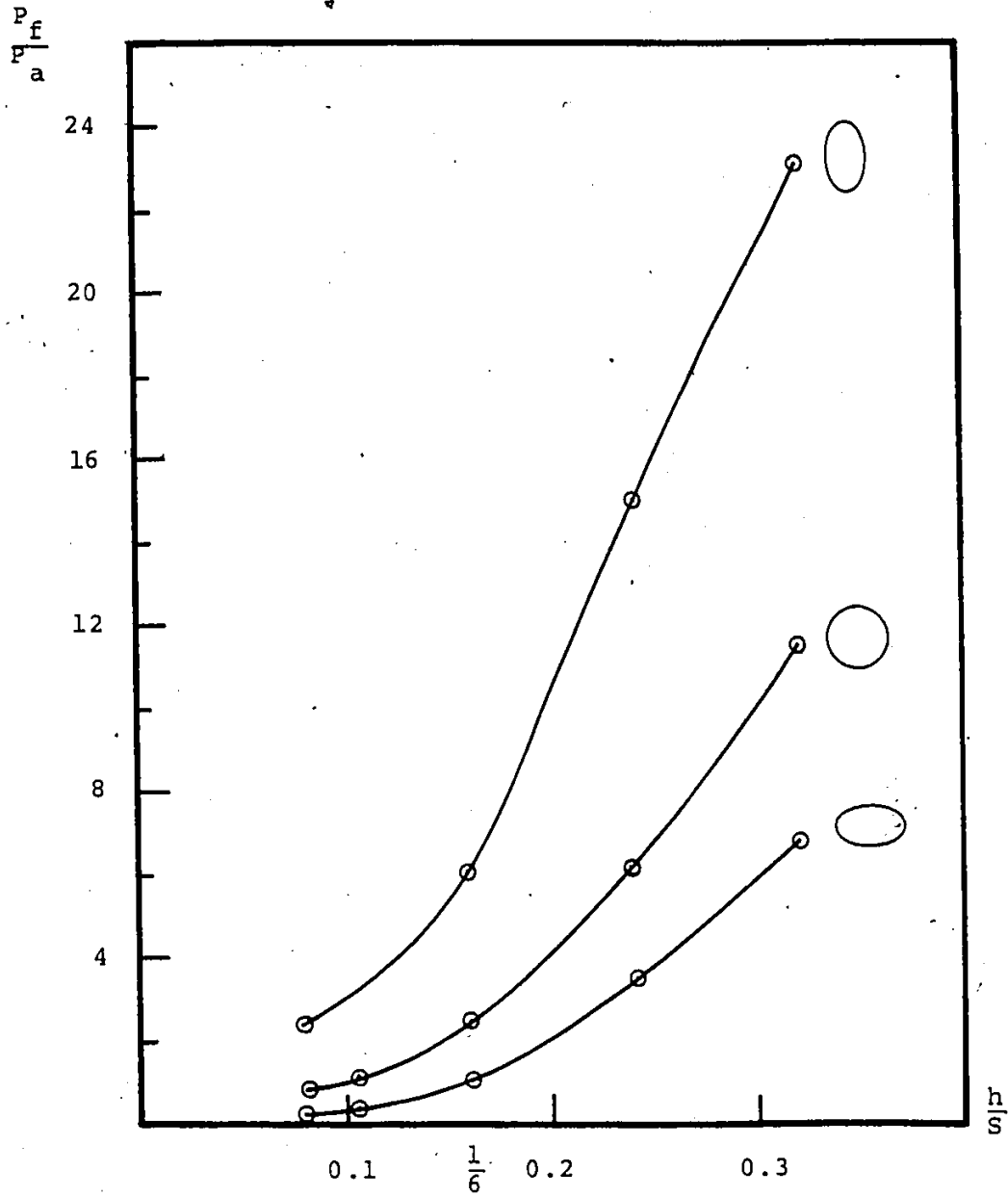


Fig. 5.1. Effect of height of cover on soil failure under centric axle load.

$$\gamma = 0.069 \text{ lbs./in}^3$$

$$\phi_o = 45^\circ$$

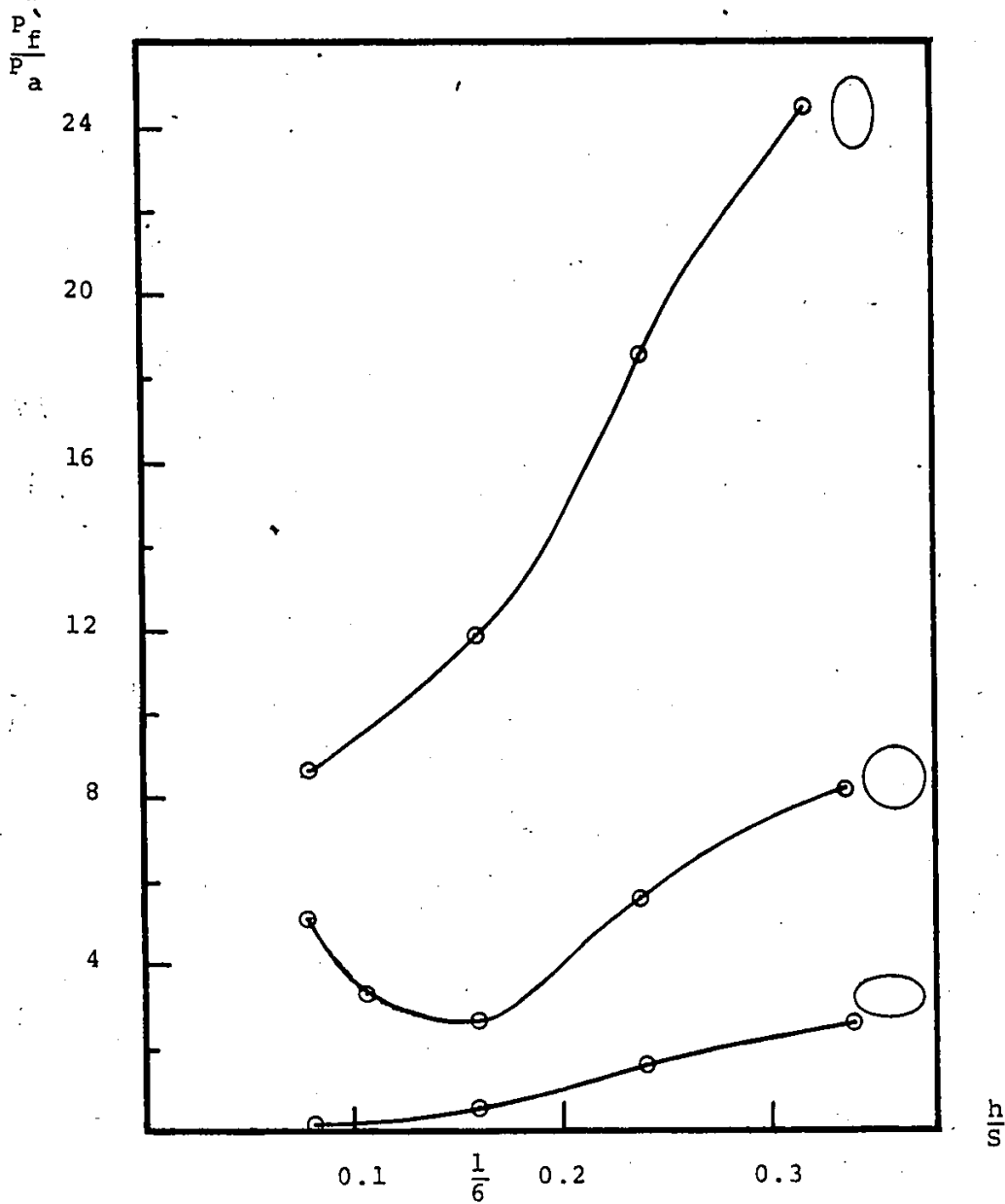


Fig. 5.2. Effect of height of cover on soil failure under multi-axle truck loading.

$$\gamma = 0.069 \text{ lbs./in}^3$$

$$\phi_o = 45^\circ$$

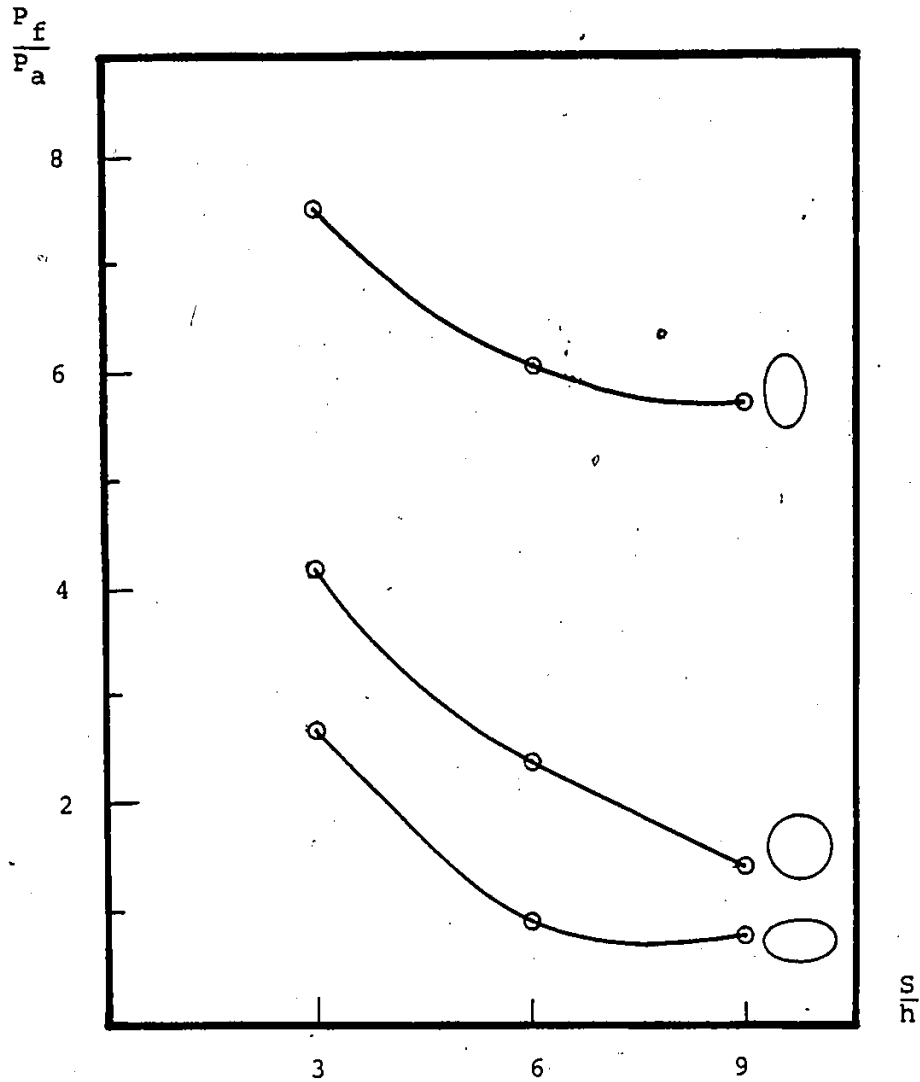


Fig. 5.3. Effect of conduit size on soil failure under centric axle load.

$$\gamma = 0.069 \text{ lbs./in}^3$$

$$\phi_0 = 45^\circ$$

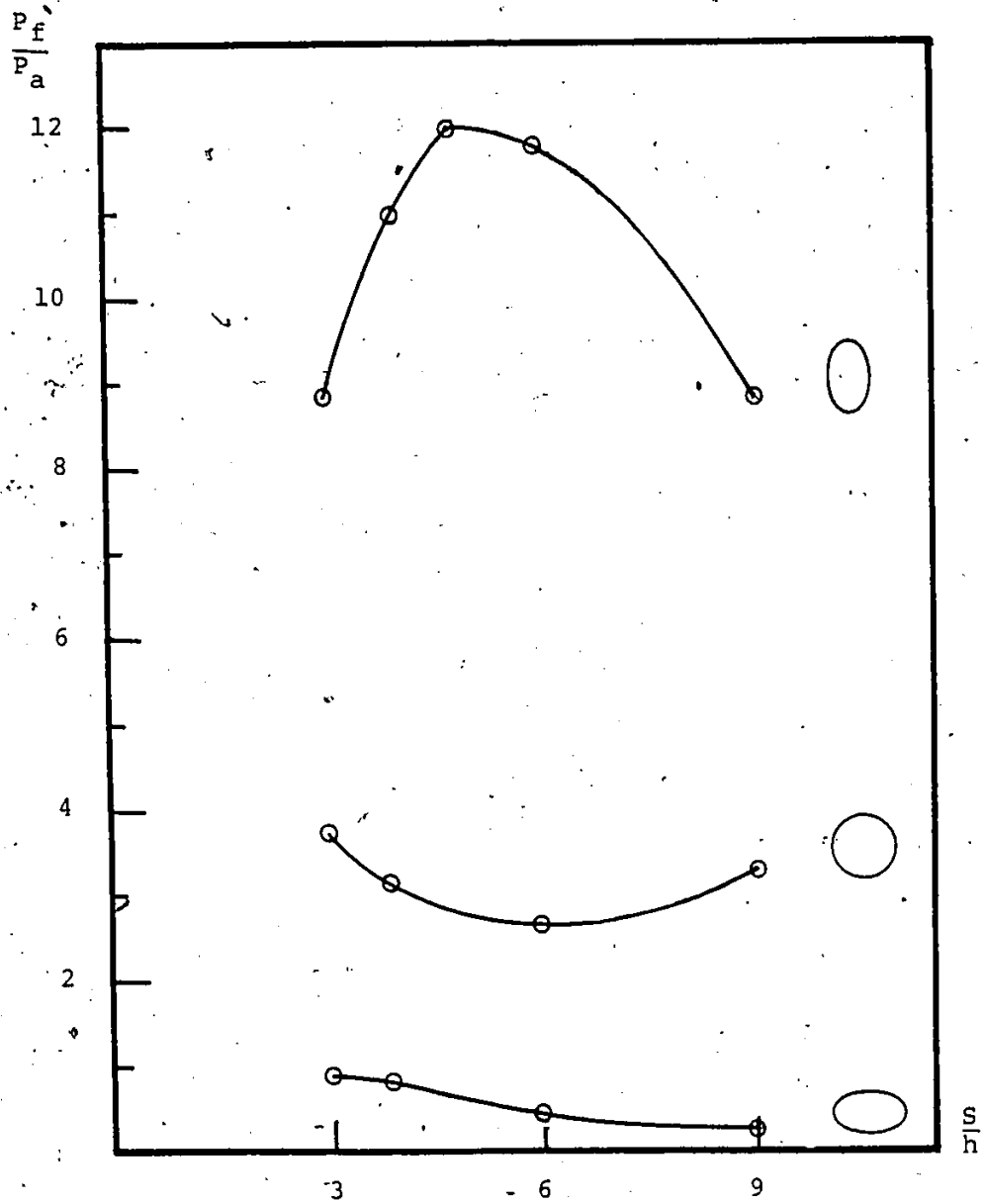


Fig. 5.4. Effect of conduit size on soil failure under multi-axle truck loading.

$\gamma = 0.069 \text{ lbs./in}^3$

$\phi_o = 45^\circ$

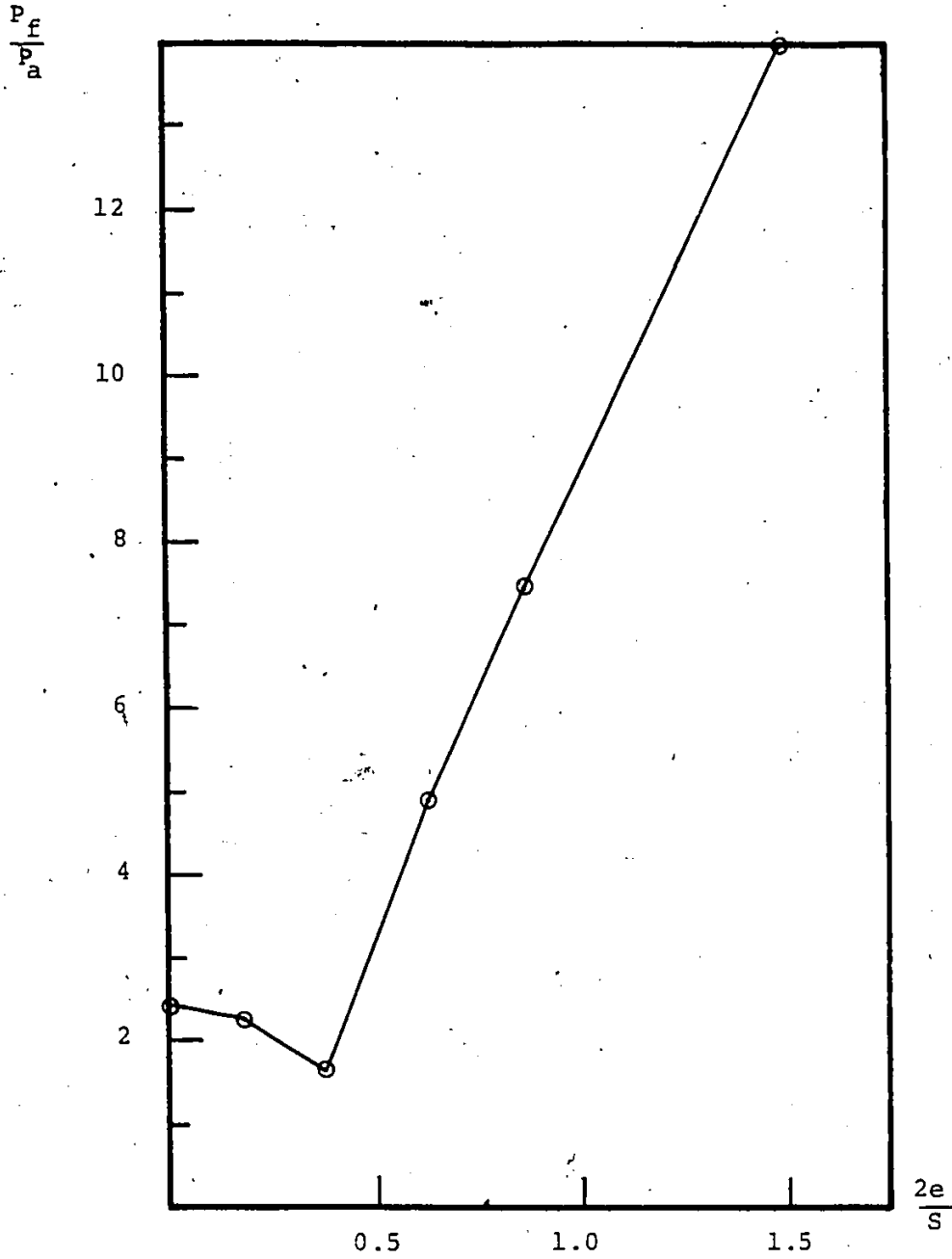


Fig. 5.5. Effect of eccentricity of an axle load.

$$\gamma = 0.069 \text{ lbs./in}^3$$

$$\phi_0 = 45^\circ$$

APPENDIX A

STIFFNESS MATRICES FOR FINITE ELEMENTS

APPENDIX A

STIFFNESS MATRICES FOR FINITE ELEMENTS

The stiffness matrices for the finite elements used in this study are given in this appendix in the same order of their appearance in the dissertation.

A.1 Derivation of Constant Strain Triangular Element Stiffness Matrix

The constant strain triangular element shown in Figure 3.6 is considered directly with respect to the global axes. The polynomial functions for displacements at any point within the triangular element are given in Equations 3.10a and 3.10b. In matrix form, they are written as:

$$\{u\} = [\Phi] \{\alpha\} \quad (A.1)$$

where,

$$\{u\}^T = \{u \ v\} \quad (A.2)$$

$$[\Phi] = \begin{bmatrix} 1 & x & y & 0 & 0 & 0 \\ 0 & 0 & 0 & 1 & x & y \end{bmatrix} \quad (A.3)$$

$$\{\alpha\}^T = \{\alpha_1 \ \alpha_2 \ \alpha_3 \ \alpha_4 \ \alpha_5 \ \alpha_6\} \quad (A.4)$$

The vector of interpolation coefficients $\{\alpha\}$ is related to the vector of nodal displacements $\{q\}$ through Equation 3.2:

$$\{q\} = [A] \{\alpha\} \quad (\text{A.5})$$

where,

$$\{q\}^T = \{u_1 \ v_1 \ u_2 \ v_2 \ u_3 \ v_3\} \quad (\text{A.6})$$

$$[A] = \begin{bmatrix} 1 & x_1 & y_1 & 0 & 0 & 0 \\ 0 & 0 & 0 & 1 & x_1 & y_1 \\ 1 & x_2 & y_2 & 0 & 0 & 0 \\ 0 & 0 & 0 & 1 & x_2 & y_2 \\ 1 & x_3 & y_3 & 0 & 0 & 0 \\ 0 & 0 & 0 & 1 & x_3 & y_3 \end{bmatrix} \quad (\text{A.7})$$

(x_1, y_1) , (x_2, y_2) and (x_3, y_3) are the nodal coordinates for the triangular element in the counterclockwise direction.

Solving Equation A.5 for $\{\alpha\}$, yields:

$$\{\alpha\} = [A]^{-1} \{q\} \quad (\text{A.8})$$

where,

$$[A]^{-1} = \frac{1}{2A_t}$$

$$\begin{bmatrix} x_2 y_3^{-x_3 y_2} & 0 & x_3 y_1^{-x_1 y_3} & 0 & x_1 y_2^{-x_2 y_1} & 0 \\ y_2^{-y_3} & 0 & y_3^{-y_1} & 0 & y_1^{-y_2} & 0 \\ x_3^{-x_2} & 0 & x_1^{-x_3} & 0 & x_2^{-y_1} & 0 \\ 0 & x_2 y_3^{-x_3 y_2} & 0 & x_3 y_1^{-x_1 y_3} & 0 & x_1 y_2^{-x_2 y_1} \\ 0 & y_2^{-y_3} & 0 & y_3^{-y_1} & 0 & y_1^{-y_2} \\ 0 & x_3^{-x_2} & 0 & x_1^{-x_3} & 0 & x_2^{-y_1} \end{bmatrix}$$

200

(A.9)

A_t is the area of the triangular element given by:

$$A_t = \frac{1}{2} [x_1(y_2 - y_3) + x_2(y_3 - y_1) + x_3(y_1 - y_2)] \quad (\text{A.10})$$

The strains at any point within the element are given by Equations 3.11a, 3.11b and 3.11c. In matrix form, the strain vector may be written as:

$$\{\epsilon\} = [B] \{\alpha\} \quad (\text{A.11})$$

where,

$$\{\epsilon\} = \{\epsilon_x \quad \epsilon_y \quad \epsilon_{xy}\} \quad (\text{A.12})$$

$$[B] = \begin{bmatrix} 0 & 1 & 0 & 0 & 0 & 0 \\ 0 & 0 & 0 & 0 & 0 & 1 \\ 0 & 0 & 1 & 0 & 1 & 0 \end{bmatrix} \quad (\text{A.13})$$

For plane strain condition, the stress-strain relationships given by Equations 3.12a, 3.12b and 3.12c can be represented in the form:

$$\{\sigma\} = [D] \{\epsilon\} \quad (\text{A.14})$$

where,

$$\{\sigma\}^T = \{\sigma_x \quad \sigma_y \quad \tau_{xy}\} \quad (\text{A.15})$$

and

$$[D] = \frac{E}{(1+\nu)(1-2\nu)} \begin{bmatrix} 1-\nu & \nu & 0 \\ \nu & 1-\nu & 0 \\ 0 & 0 & \frac{1-2\nu}{2} \end{bmatrix} \quad (\text{A.16})$$

Substituting the matrices [A] from Equation A.9, [B] from Equation A.13 and [D] from Equation A.16 into Equation 3.8, and performing the integration over the volume of the element, the element stiffness matrix is generated. It is given by:

$$[k]_c = \frac{Et}{4A_t(1+\nu)(1-2\nu)} \begin{bmatrix} k_{11} & k_{12} & k_{13} & k_{14} & k_{15} & k_{16} \\ k_{21} & k_{22} & k_{23} & k_{24} & k_{25} & k_{26} \\ k_{31} & k_{32} & k_{33} & k_{34} & k_{35} & k_{36} \\ k_{41} & k_{42} & k_{43} & k_{44} & k_{46} & k_{47} \\ k_{51} & k_{52} & k_{53} & k_{54} & k_{55} & k_{56} \\ k_{61} & k_{62} & k_{63} & k_{64} & k_{65} & k_{66} \end{bmatrix} \quad (\text{A.17})$$

where,

t is the thickness of the element taken as unity,

$$k_{11} = (1-\nu)(y_2-y_3)^2 + \frac{1-2\nu}{2}(x_3-x_2)^2$$

$$k_{12} = \nu(x_3-x_2)(y_2-y_3) + \frac{1-2\nu}{2}(x_3-x_2)(y_2-y_3)$$

$$k_{13} = (1-\nu)(y_2-y_3)(y_3-y_1) + \frac{1-2\nu}{2}(x_3-x_2)(x_1-x_3)$$

$$k_{14} = \nu(x_1-x_3)(y_2-y_3) + \frac{1-2\nu}{2}(x_3-x_2)(y_3-y_1)$$

$$k_{15} = (1-v)(y_1-y_2)(y_2-y_3) + \frac{1-2v}{2}(x_3-x_2)(x_2-x_1)$$

$$k_{16} = v(x_2-x_1)(y_2-y_3) + \frac{1-2v}{2}(x_3-x_2)(y_1-y_2)$$

$$k_{22} = (1-v)(x_3-x_2)^2 + \frac{1-2v}{2}(y_2-y_3)^2$$

$$k_{23} = v(x_3-x_2)(y_3-y_1) + \frac{1-2v}{2}(x_1-x_3)(y_2-y_3)$$

$$k_{24} = (1-v)(x_1-x_3)(x_3-x_2) + \frac{1-2v}{2}(y_2-y_3)(y_3-y_1)$$

$$k_{25} = v(x_3-x_2)(y_1-y_2) + \frac{1-2v}{2}(x_2-x_1)(y_2-y_3)$$

$$k_{26} = (1-v)(x_2-x_1)(x_3-x_2) + \frac{1-2v}{2}(y_1-y_2)(y_2-y_3)$$

$$k_{33} = (1-v)(y_3-y_1)^2 + \frac{1-2v}{2}(x_1-x_3)^2$$

$$k_{34} = v(x_1-x_3)(y_3-y_1) + \frac{1-2v}{2}(x_1-x_3)(y_3-y_1)$$

$$k_{35} = (1-v)(y_1-y_2)(y_3-y_1) + \frac{1-2v}{2}(x_1-x_3)(x_2-x_1)$$

$$k_{36} = v(x_2-x_1)(y_3-y_1) + \frac{1-2v}{2}(x_1-x_3)(y_1-y_2)$$

$$k_{44} = (1-v)(x_1-x_3)^2 + \frac{1-2v}{2}(y_3-y_1)^2$$

$$k_{45} = v(x_1-x_3)(y_1-y_2) + \frac{1-2v}{2}(x_2-x_1)(y_3-y_1)$$

$$k_{46} = (1-v)(x_2-x_1)(x_1-x_3) + \frac{1-2v}{2}(y_1-y_2)(y_3-y_1)$$

$$k_{55} = (1-v)(y_1-y_2)^2 + \frac{1-2v}{2}(x_2-x_1)^2$$

$$k_{56} = v(x_2-x_1)(y_1-y_2) + \frac{1-2v}{2}(x_2-x_1)(y_1-y_2)$$

$$k_{66} = (1-v)(x_2-x_1)^2 + \frac{1-2v}{2}(y_1-y_2)^2$$

Remaining terms are obtained by symmetry.

A.2 Derivation of Linear Strain Triangular Element Stiffness Matrix

The linear strain triangular element shown in Figure 3.7 is first considered with respect to its local axes. The assumed displacement functions at any point within the triangular element are given in Equations 3.13a and 3.13b. In matrix form, they are expressed as in Equations A.1 and A.2; however, here the interpolation matrix reads as follows:

$$[\phi] = \begin{bmatrix} 1 & x & y & x^2 & y^2 & xy & 0 & 0 & 0 & 0 & 0 & 0 \\ 0 & 0 & 0 & 0 & 0 & 0 & 1 & x & y & x^2 & y^2 & xy \end{bmatrix} \quad (\text{A.18})$$

and the vector of interpolation coefficients is given by:

$$\{\alpha\}^T = \{\alpha_1 \quad \alpha_2 \quad \alpha_3 \quad \alpha_4 \quad \alpha_5 \quad \alpha_6 \quad \alpha_7 \quad \alpha_8 \quad \alpha_9 \quad \alpha_{10} \quad \alpha_{11} \quad \alpha_{12}\} \quad (\text{A.19})$$

Accordingly, the vector of nodal displacements and matrix [A], in Equation A.5, take the form:

$$\{q\} = \{u_1 \quad v_1 \quad u_2 \quad v_2 \quad u_3 \quad v_3 \quad u_4 \quad v_4 \quad u_5 \quad v_5 \quad u_6 \quad v_6\} \quad (\text{A.20})$$

$$[A] = \begin{bmatrix}
 1 & 0 & 0 & 0 & 0 & 0 & 0 & 0 & 0 & 0 & 0 & 0 & 0 \\
 0 & 0 & 0 & 0 & 0 & 1 & 0 & 0 & 0 & 0 & 0 & 0 & 0 \\
 1 & x_2 & 0 & x_2^2 & 0 & 0 & 0 & 0 & 0 & 0 & 0 & 0 & 0 \\
 0 & 0 & 0 & 0 & 0 & 1 & x_2 & 0 & 0 & x_2^2 & 0 & 0 & 0 \\
 1 & x_3 & y_3 & x_3^2 & y_3^2 & x_3 y_3 & 0 & 0 & 0 & 0 & 0 & 0 & 0 \\
 0 & 0 & 0 & 0 & 0 & 0 & 1 & x_3 & y_3 & x_3^2 & y_3^2 & x_3 y_3 & 0 \\
 1 & \frac{1}{2}(x_2+x_3) & \frac{y_3}{2} & \frac{1}{4}(x_2+x_3)^2 & \frac{y_3^2}{4} & \frac{1}{2}y_3(x_2+x_3) & 0 & 0 & 0 & 0 & 0 & 0 & 0 \\
 0 & 0 & 0 & 0 & 0 & 1 & \frac{1}{2}(x_2+x_3) & \frac{y_3}{2} & \frac{1}{2}(x_2+x_3)^2 & \frac{y_3^2}{4} & \frac{1}{2}y_3(x_2+x_3) & 0 & 0 \\
 1 & \frac{1}{2}x_3 & \frac{1}{2}y_3 & \frac{1}{4}x_3^2 & \frac{1}{4}y_3^2 & \frac{1}{2}x_3 y_3 & 0 & 0 & 0 & 0 & 0 & 0 & 0 \\
 0 & 0 & 0 & 0 & 0 & 0 & 1 & \frac{1}{2}x_3 & \frac{1}{2}y_3 & \frac{1}{4}x_3^2 & \frac{1}{4}y_3^2 & \frac{1}{2}x_3 y_3 & 0 \\
 1 & \frac{1}{2}x_2 & 0 & \frac{1}{4}x_2^2 & 0 & 0 & 0 & 0 & 0 & 0 & 0 & 0 & 0 \\
 0 & 0 & 0 & 0 & 0 & 0 & 1 & \frac{1}{2}x_2 & 0 & \frac{1}{4}x_2^2 & 0 & 0 & 0
 \end{bmatrix}$$

(A.21)

(0,0), (0,x₂) and (x₃, y₃) are the local coordinates of the corner nodes of the element in the anticlockwise direction. The mid side nodal coordinates, in terms of corner node coordinates, are $(\frac{x_2+x_3}{2}, \frac{y_3}{2})$, $(\frac{x_3}{2}, \frac{y_3}{2})$ and $(\frac{x_2}{2}, 0)$.

In Equation A.8, the inverse of matrix [A] is obtained as:

$$[A]^{-1} = \begin{bmatrix} A_{11} & A_{12} \\ \text{---} & \text{---} \\ A_{21} & A_{22} \end{bmatrix} \quad (A.22)$$

where the submatrices in $[A]^{-1}$ are given as follows:

$$A_{11} = \begin{bmatrix} 1 & 0 & 0 & 0 & 0 & 0 \\ \frac{-3}{x_2} & 0 & \frac{-1}{x_2} & 0 & 0 & 0 \\ \frac{-3}{y_3}(1 - \frac{x_3}{x_2}) & 0 & \frac{x_3}{y_3 x_2} & 0 & \frac{-1}{y_3} & 0 \\ \frac{2}{x_2} & 0 & \frac{2}{x_2} & 0 & 0 & 0 \\ \frac{2}{y_3} [1 - \frac{x_3}{x_2} (2 - \frac{x_3}{x_2})] & 0 & \frac{2}{y_3} (\frac{x_3}{x_2})^2 & 0 & \frac{2}{y_3} & 0 \\ \frac{4}{x_2 y_3} (1 - \frac{x_3}{x_2}) & 0 & \frac{-4}{y_3} \frac{x_3}{x_2} & 0 & 0 & 0 \end{bmatrix} \quad (A.23)$$

$$A_{12} = \begin{bmatrix} 0 & 0 & 0 & 0 & 0 & 0 \\ 0 & 0 & 0 & 0 & \frac{4}{x_2} & 0 \\ 0 & 0 & \frac{4}{y_3} & 0 & \frac{-4x_3}{y_3 x_2} & 0 \\ 0 & 0 & 0 & 0 & \frac{-4}{x_2^2} & 0 \\ \frac{-4}{y_3} \frac{x_3}{x_2} & 0 & \frac{-4}{y_3} \left(1 - \frac{x_3}{x_2}\right) & 0 & \frac{4x_3}{y_3 x_2} \left(1 - \frac{x_3}{x_2}\right) & 0 \\ \frac{4}{x_2 y_3} & 0 & \frac{-4}{x_2 y_3} & 0 & \frac{-4}{x_2 y_3} \left(1 - \frac{2x_3}{x_2}\right) & 0 \end{bmatrix}$$

(A.24)

$$A_{21} = \begin{bmatrix} 0 & 1 & 0 & 0 & 0 & 0 \\ 0 & \frac{-3}{x_2} & 0 & \frac{-1}{x_2} & 0 & 0 \\ 0 & \frac{-3}{Y_3} \left(1 - \frac{x_3}{x_2}\right) & 0 & \frac{x_3}{x_2 Y_3} & 0 & \frac{-1}{Y_3} \\ 0 & \frac{2}{x_2} & 0 & \frac{2}{x_2} & 0 & 0 \\ 0 & \frac{2}{Y_3} \left[1 - \frac{x_3}{x_2} \left(2 - \frac{x_3}{x_2}\right)\right] & 0 & \frac{2}{Y_3} \left(\frac{x_3}{x_2}\right)^2 & 0 & \frac{2}{Y_3} \\ 0 & \frac{4}{x_2 Y_3} \left(1 - \frac{x_3}{x_2}\right) & 0 & \frac{-4}{Y_3} \left(\frac{x_3}{x_2}\right) & 0 & 0 \end{bmatrix}$$

(A.25)

and

$$A_{22} = \begin{bmatrix} 0 & 0 & 0 & 0 & 0 & 0 \\ 0 & 0 & 0 & 0 & 0 & \frac{4}{x_2} \\ 0 & 0 & 0 & \frac{4}{y_3} & 0 & \frac{-4x_3}{x_2 y_3} \\ 0 & 0 & 0 & 0 & 0 & \frac{4}{x_2} \\ 0 & \frac{-4}{y_3} \left(\frac{x_3}{x_2} \right) & 0 & \frac{4}{y_3} \left(1 - \frac{x_3}{x_2} \right) & 0 & \frac{4}{y_3} \frac{x_3}{x_2} \left(1 - \frac{x_3}{x_2} \right) \\ 0 & \frac{4}{x_2 y_3} & 0 & \frac{-4}{x_2 y_3} & 0 & \frac{-4}{x_2 y_3} \left(1 - \frac{2x_3}{x_2} \right) \end{bmatrix}$$

(A.26)

By applying Equations 3.11a, 3.11b and 3.11c the strain vector $\{\epsilon\}$ in Equation A.11 remains as given in Equation A.12. However, the matrix $[B]$, relating the strain vector to coefficients vector, becomes:

$$[B] = \begin{bmatrix} 0 & 1 & 0 & 2x & 0 & y & 0 & 0 & 0 & 0 & 0 & 0 \\ 0 & 0 & 0 & 0 & 0 & 0 & 0 & 0 & 1 & 0 & 2y & x \\ 0 & 0 & 1 & 0 & 2y & x & 0 & 1 & 0 & 2x & 0 & y \end{bmatrix} \quad (A.27)$$

The vectors and matrix of the stress-strain relationship for plane strain conditions are given by Equations A.14, A.15 and A.16.

By substituting the matrices $[A]^{-1}$ from Equation A.22, $[B]$ from Equation A.27, and $[D]$ from Equation A.16, into Equation 3.8, and performing the integration over the volume of the triangular element, the element stiffness matrix is obtained as follows:

$$[k_e]_1 = \frac{t}{2} \begin{bmatrix} k_{1-1} & k_{1-2} & \dots & \dots & \dots & k_{1-11} & k_{1-12} \\ k_{2-1} & k_{2-2} & \dots & \dots & \dots & k_{2-11} & k_{2-12} \\ k_{3-1} & k_{3-2} & \dots & \dots & \dots & k_{3-11} & k_{3-12} \\ k_{4-1} & k_{4-2} & \dots & \dots & \dots & k_{4-11} & k_{3-12} \\ k_{5-1} & k_{5-2} & \dots & \dots & \dots & k_{5-11} & k_{5-12} \\ k_{6-1} & k_{6-2} & \dots & \dots & \dots & k_{6-11} & k_{6-12} \end{bmatrix}$$

$$\begin{array}{cccccc}
 k_{7-1} & k_{7-2} & \dots & \dots & k_{7-11} & k_{7-12} \\
 k_{8-1} & k_{8-2} & \dots & \dots & k_{8-11} & k_{8-12} \\
 k_{9-1} & k_{9-2} & \dots & \dots & k_{9-11} & k_{9-12} \\
 k_{10-1} & k_{10-2} & \dots & \dots & k_{10-11} & k_{10-12} \\
 k_{11-1} & k_{11-2} & \dots & \dots & k_{11-11} & k_{11-12} \\
 k_{12-1} & k_{12-2} & \dots & \dots & k_{12-11} & k_{12-12}
 \end{array}$$

(A.28)

where,

$$k_{1-1} = \frac{d_{11}}{\alpha} + d_{33} \left(1 - \frac{x_3}{x_2}\right)^2 \frac{x_2}{y_3}$$

$$k_{1-2} = (d_{12} + d_{33}) \left(1 - \frac{x_3}{x_2}\right)$$

$$k_{1-3} = \frac{1}{3} \left[d_{11} \frac{y_3}{x_2} - d_{33} \left(1 - \frac{x_3}{x_2}\right) \frac{x_3}{y_3} \right]$$

$$k_{1-4} = \frac{1}{3} \left[-d_{12} \frac{x_3}{x_2} + d_{33} \left(1 - \frac{x_3}{x_2}\right) \right]$$

$$k_{1-5} = \frac{1}{3} d_{33} \left(1 - \frac{x_3}{x_2}\right) \frac{x_2}{y_3}$$

$$k_{1-6} = \frac{1}{3} d_{12}$$

$$k_{1-7} = 0$$

$$k_{1-8} = 0$$

$$k_{1-9} = \frac{-4}{3} d_{33} \left(1 - \frac{x_3}{x_2}\right) \frac{x_2}{y_3}$$

$$k_{1-10} = \frac{-4}{3} d_{12}$$

$$k_{1-11} = \frac{4}{3} \left[-d_{11} \frac{y_3}{x_2} + d_{33} \left(1 - \frac{x_3}{x_2}\right) \frac{x_3}{y_3}\right]$$

$$k_{1-12} = \frac{4}{3} \left[d_{12} \frac{x_3}{x_2} - d_{33} \left(1 - \frac{x_3}{x_2}\right)\right]$$

$$k_{2-2} = d_{22} \left(1 - \frac{x_3}{x_2}\right)^2 \frac{x_2}{x_3} + d_{33} \frac{y_3}{x_2}$$

$$k_{2-3} = \frac{1}{3} \left[d_{12} \left(1 - \frac{x_3}{x_2}\right) - d_{33} \frac{x_3}{x_2}\right]$$

$$k_{2-4} = \frac{1}{3} \left[-d_{22} \left(1 - \frac{x_3}{x_2}\right) \frac{x_3}{y_3} + d_{33} \frac{y_3}{x_2}\right]$$

$$k_{2-5} = \frac{1}{3} d_{33}$$

$$k_{2-6} = \frac{1}{3} d_{22} \left(1 - \frac{x_3}{x_2}\right) \frac{x_2}{y_3}$$

$$k_{2-7} = 0$$

$$k_{2-8} = 0$$

$$k_{2-9} = \frac{-4}{3} d_{33}$$

$$k_{2-10} = \frac{-4}{3} d_{22} \left(1 - \frac{x_3}{x_2}\right) \frac{x_2}{y_3}$$

$$k_{2-11} = \frac{4}{3} \left[-d_{12} \left(1 - \frac{x_3}{x_2}\right) + d_{33} \frac{x_3}{x_2}\right]$$

$$k_{2-12} = \frac{4}{3} \left[d_{22} \left(1 - \frac{x_3}{x_2}\right) \frac{x_3}{y_3} - d_{33} \frac{y_3}{x_2}\right]$$

$$k_{3-3} = d_{11} \frac{x_2}{y_3} + d_{33} \left(\frac{x_3}{x_2}\right)^2 \frac{x_2}{y_3}$$

$$k_{3-4} = -\frac{x_3}{x_2} (d_{12} + d_{33})$$

$$k_{3-5} = \frac{1}{3} d_{33} \frac{x_3}{y_3}$$

$$k_{3-6} = \frac{1}{3} d_{12}$$

$$k_{3-7} = -\frac{4}{3} d_{33} \frac{x_3}{y_3}$$

$$k_{3-8} = \frac{4}{3} d_{12}$$

$$k_{3-9} = 0$$

$$k_{3-10} = 0$$

$$k_{3-11} = \frac{4}{3} \left[-d_{11} \frac{y_3}{x_2} + d_{33} \left(1 - \frac{x_3}{x_2} \right) \frac{x_3}{y_3} \right]$$

$$k_{3-12} = \frac{4}{3} \left[-d_{12} \left(1 - \frac{x_3}{x_2} \right) + d_{33} \frac{x_3}{x_2} \right]$$

$$k_{4-4} = d_{22} \left(\frac{x_3}{x_2} \right)^2 \frac{x_2}{y_3} + d_{33} \frac{y_3}{x_2}$$

$$k_{4-5} = -\frac{1}{3} d_{33}$$

$$k_{4-6} = \frac{1}{3} d_{22} \frac{x_3}{y_3}$$

$$k_{4-7} = \frac{4}{3} d_{33}$$

$$k_{4-8} = -\frac{4}{3} d_{22} \frac{x_3}{y_3}$$

$$k_{4-9} = 0$$

$$k_{4-10} = 0$$

$$k_{4-11} = \frac{4}{3} \left[d_{12} \frac{x_3}{x_2} - d_{33} \left(1 - \frac{x_3}{x_2} \right) \right]$$

$$k_{4-12} = \frac{4}{3} \left[d_{22} \left(1 - \frac{x_3}{x_2} \right) \frac{x_3}{y_3} - d_{33} \frac{y_3}{x_2} \right]$$

$$k_{5-5} = d_{33} \frac{x_2}{y_3}$$

$$k_{5-6} = 0$$

$$k_{5-7} = \frac{-4}{3} d_{33} \frac{x_3}{y_3}$$

$$k_{5-8} = \frac{4}{3} d_{33}$$

$$k_{5-9} = \frac{-4}{3} d_{33} \left(1 - \frac{x_3}{x_2}\right) \frac{x_2}{y_3}$$

$$k_{5-10} = \frac{-4}{3} d_{33}$$

$$k_{5-11} = 0$$

$$k_{5-12} = 0$$

$$k_{6-6} = d_{22} \frac{x_2}{y_3}$$

$$k_{6-7} = \frac{4}{3} d_{12}$$

$$k_{6-8} = \frac{-4}{3} d_{22} \frac{x_3}{y_3}$$

$$k_{6-9} = \frac{-4}{3} d_{12}$$

$$k_{6-10} = \frac{-4}{3} d_{22} \left(1 - \frac{x_3}{x_2}\right) \frac{x_2}{y_3}$$

$$k_{6-11} = 0$$

$$k_{6-12} = 0$$

$$k_{7-7} = \frac{8}{3} d_{33} \frac{x_2}{y_3} \left[1 - \frac{x_3}{x_2} - \left(\frac{x_3}{x_2} \right)^2 \right] + \frac{8}{3} d_{11} \frac{y_3}{x_2}$$

$$k_{7-8} = \frac{4}{3} \left(1 - 2 \frac{x_3}{x_2} \right) (d_{12} - d_{33})$$

$$k_{7-9} = \frac{8}{3} \left[-d_{11} \frac{y_3}{x_2} + d_{33} \left(1 - \frac{x_3}{x_2} \right) \frac{x_3}{y_3} \right]$$

$$k_{7-10} = \frac{-4}{3} \left(1 - 2 \frac{x_3}{x_2} \right) (d_{12} + d_{33})$$

$$k_{7-11} = \frac{-8}{3} d_{33} \left(1 - \frac{x_3}{x_2} \right) \frac{x_2}{y_3}$$

$$k_{7-12} = \frac{-4}{3} (d_{33} + d_{12})$$

$$k_{8-8} = \frac{8}{3} \left\{ d_{22} \frac{x_2}{y_3} \left[1 - \frac{x_3}{x_2} + \left(\frac{x_3}{x_2} \right)^2 \right] + d_{33} \frac{y_3}{x_2} \right\}$$

$$k_{8-9} = \frac{-4}{3} (d_{12} + d_{33}) \left(1 - 2 \frac{x_3}{x_2} \right)$$

$$k_{8-10} = \frac{8}{3} \left[d_{22} \left(1 - \frac{x_3}{x_2} \right) \frac{x_3}{y_3} - d_{33} \frac{x_3}{y_3} \right]$$

$$k_{8-11} = \frac{-4}{3} (d_{33} + d_{12})$$

$$k_{8-12} = \frac{-8}{3} d_{22} \left(1 - \frac{x_3}{x_2} \right) \frac{x_2}{y_3}$$

$$k_{9-9} = \frac{8}{3} \left\{ d_{11} \frac{y_3}{x_2} + \frac{x_2}{y_3} d_{33} \left[1 - \frac{x_3}{x_2} - \left(\frac{x_3}{x_2} \right)^2 \right] \right\}$$

$$k_{9-10} = \frac{4}{3} (d_{12} + d_{33}) \left(1 - 2 \frac{x_3}{x_2}\right)$$

$$k_{9-11} = \frac{-8}{3} d_{33} \frac{x_3}{y_3}$$

$$k_{9-12} = \frac{4}{3} (d_{33} + d_{12})$$

$$k_{10-10} = \frac{8}{3} \left\{ d_{22} \frac{x_2}{y_3} \left[1 - \frac{x_3}{x_2} - \left(\frac{x_3}{x_2}\right)^2\right] + d_{33} \frac{y_3}{x_2} \right\}$$

$$k_{10-11} = \frac{4}{3} (d_{33} + d_{12})$$

$$k_{10-12} = \frac{-8}{3} d_{22} \frac{x_3}{y_3}$$

$$k_{11-11} = \frac{8}{3} \left\{ d_{11} \frac{y_3}{x_2} + d_{33} \frac{x_2}{y_3} \left[1 - \frac{x_3}{x_2} + \left(\frac{x_3}{x_2}\right)^2\right] \right\}$$

$$k_{11-12} = \frac{4}{3} (d_{12} + d_{33}) \left(1 - 2 \frac{x_3}{x_2}\right)$$

$$k_{12-12} = \frac{8}{3} \left\{ d_{22} \frac{x_2}{y_3} \left[1 - \frac{x_3}{x_2} - \left(\frac{x_3}{x_2}\right)^2\right] + d_{33} \frac{y_3}{x_2} \right\}$$

d_{11} , d_{12} , d_{22} and d_{33} are the components of the constitutive matrix. For plane strain, these components are given by:

$$d_{11} = d_{22} = \frac{E(1-\nu)}{(1+\nu)(1-2\nu)} \quad (\text{A.29})$$

$$d_{12} = \frac{\nu E}{(1+\nu)(1-2\nu)} \quad (\text{A.30})$$

$$d_{33} = \frac{E}{2(1+\nu)} \quad (\text{A.31})$$

The above local element stiffness matrix is transformed into the global system using the following transformation matrix:

$$[T]_e = \begin{bmatrix} \cos\theta & \sin\theta & 0 & 0 & 0 & 0 & 0 & 0 & 0 & 0 & 0 \\ -\sin\theta & \cos\theta & 0 & 0 & 0 & 0 & 0 & 0 & 0 & 0 & 0 \\ 0 & 0 & \cos\theta & \sin\theta & 0 & 0 & 0 & 0 & 0 & 0 & 0 \\ 0 & 0 & -\sin\theta & \cos\theta & 0 & 0 & 0 & 0 & 0 & 0 & 0 \\ 0 & 0 & 0 & 0 & \cos\theta & \sin\theta & 0 & 0 & 0 & 0 & 0 \\ 0 & 0 & 0 & 0 & -\sin\theta & \cos\theta & 0 & 0 & 0 & 0 & 0 \\ 0 & 0 & 0 & 0 & 0 & 0 & \cos\theta & \sin\theta & 0 & 0 & 0 \\ 0 & 0 & 0 & 0 & 0 & 0 & -\sin\theta & \cos\theta & 0 & 0 & 0 \\ 0 & 0 & 0 & 0 & 0 & 0 & 0 & 0 & \cos\theta & \sin\theta & 0 \\ 0 & 0 & 0 & 0 & 0 & 0 & 0 & 0 & -\sin\theta & \cos\theta & 0 \\ 0 & 0 & 0 & 0 & 0 & 0 & 0 & 0 & 0 & 0 & \cos\theta \\ 0 & 0 & 0 & 0 & 0 & 0 & 0 & 0 & 0 & 0 & \sin\theta \\ 0 & 0 & 0 & 0 & 0 & 0 & 0 & 0 & 0 & -\sin\theta & \cos\theta \end{bmatrix}$$

(A.32)

where θ is the angle between the global and local axes.

A.3 Local Stiffness Matrix for Nine-noded Linear Strain Quadrilateral Element

The nine-noded linear strain quadrilateral element is shown in Fig. 3.8. Following the steps described in Section 3.5.3, the local stiffness matrix is given by:

$$[k]_n = \frac{t}{2} \begin{bmatrix} k_{1-1} & k_{1-2} & \dots & \dots & \dots & k_{1-17} & k_{1-18} \\ k_{2-1} & k_{2-2} & \dots & \dots & \dots & k_{2-17} & k_{2-18} \\ k_{3-1} & k_{3-2} & \dots & \dots & \dots & k_{2-17} & k_{2-18} \\ k_{4-1} & k_{4-2} & \dots & \dots & \dots & k_{4-17} & k_{4-18} \\ k_{5-1} & k_{5-2} & \dots & \dots & \dots & k_{5-17} & k_{5-18} \\ k_{6-1} & k_{6-2} & \dots & \dots & \dots & k_{6-17} & k_{6-18} \\ \dots & \dots & \dots & \dots & \dots & \dots & \dots \\ \dots & \dots & \dots & \dots & \dots & \dots & \dots \\ k_{17-1} & k_{17-2} & \dots & \dots & \dots & k_{17-17} & k_{17-18} \\ k_{18-1} & k_{18-2} & \dots & \dots & \dots & k_{18-17} & k_{18-18} \end{bmatrix}$$

(A.33)

where,

$$k_{1-1} = d_{11} \left(\frac{y_4}{x_3} - \frac{y_2}{x_3} \right) + d_{33} \left[\left(1 - \frac{x_4}{x_3} \right)^2 \frac{x_3}{y_4} - \left(1 - \frac{x_2}{x_3} \right)^2 \frac{x_3}{y_2} \right]$$

$$k_{1-2} = (d_{12} + d_{33}) \left(\frac{x_2}{x_3} - \frac{x_4}{x_3} \right)$$

$$k_{1-3} = -\frac{1}{3} d_{33} \left(1 - \frac{x_2}{x_3} \right) \frac{x_3}{y_2}$$

$$k_{1-4} = -\frac{1}{3} d_{12}$$

$$k_{1-5} = \frac{1}{3} \left\{ d_{11} \left(\frac{y_4}{x_3} - \frac{y_2}{x_3} \right) - d_{33} \left[\left(1 - \frac{x_4}{x_3} \right) \frac{x_4}{y_4} - \left(1 - \frac{x_2}{x_3} \right) \frac{x_2}{y_2} \right] \right\}$$

$$k_{1-6} = \frac{1}{3} (d_{33} + d_{12}) \left(\frac{x_2}{x_3} - \frac{x_4}{x_3} \right)$$

$$k_{1-7} = \frac{1}{3} d_{33} \left(1 - \frac{x_4}{x_3} \right) \frac{x_3}{y_4}$$

$$k_{1-8} = \frac{1}{3} d_{12}$$

$$k_{1-9} = -\frac{4}{3} d_{33} \left(-\frac{x_3}{y_2} + \frac{x_2}{y_2} \right)$$

$$k_{1-10} = \frac{4}{3} d_{12}$$

$$k_{1-11} = 0$$

$$k_{1-12} = 0$$

$$k_{1-13} = 0$$

$$k_{1-14} = 0$$

$$k_{1-15} = -\frac{4}{3} d_{33} \left(\frac{x_3}{y_4} - \frac{x_4}{y_4} \right)$$

$$k_{1-16} = -\frac{4}{3} d_{12}$$

$$k_{1-17} = \frac{4}{3} \left\{ d_{33} \left[\frac{x_4}{y_4} - \frac{x_4^2}{x_3 y_4} + \frac{x_2^2}{x_3 y_2} \right] \right\}$$

$$k_{1-18} = -\frac{4}{3} (d_{12} + d_{33}) \left(\frac{x_2}{x_3} - \frac{x_4}{x_3} \right)$$

$$k_{2-2} = d_{22} \left[\left(-\frac{x_4}{x_3} \right)^2 \frac{x_3}{y_4} - \left(1 - \frac{x_2}{x_3} \right)^2 \frac{x_3}{y_2} \right] d_{33} \left(\frac{y_4}{x_3} - \frac{y_2}{x_3} \right)$$

$$k_{2-3} = -\frac{1}{3} d_{33}$$

$$k_{2-4} = -\frac{1}{3} d_{22} \left(1 - \frac{x_2}{x_3} \right) \frac{x_3}{y_2}$$

$$k_{2-5} = \frac{1}{3} (d_{12} + d_{33}) \left(\frac{x_2}{x_3} - \frac{x_4}{x_3} \right)$$

$$k_{2-6} = \frac{1}{3} \left\{ d_{33} \left(\frac{y_4}{x_3} - \frac{y_2}{x_3} \right) - d_{22} \left[\left(1 - \frac{x_4}{x_3} \right) \frac{x_4}{y_4} - \left(1 - \frac{x_2}{x_3} \right) \frac{x_2}{y_2} \right] \right\}$$

$$k_{2-7} = \frac{1}{3} d_{33}$$

$$k_{2-8} = \frac{1}{3} d_{22} \left(\frac{x_3}{y_4} - \frac{x_4}{y_4} \right)$$

$$k_{2-9} = \frac{4}{3} d_{33}$$

$$k_{2-10} = \frac{-4}{3} d_{22} \left(-\frac{x_3}{y_2} + \frac{x_2}{y_2} \right)$$

$$k_{2-11} = 0$$

$$k_{2-12} = 0$$

$$k_{2-13} = 0$$

$$k_{2-14} = 0$$

$$k_{2-15} = -\frac{4}{3} d_{33}$$

$$k_{2-16} = -\frac{4}{3} d_{22} \left(\frac{x_3}{y_4} - \frac{x_4}{y_4} \right)$$

$$k_{2-17} = -\frac{4}{3} (d_{12} + d_{33}) \left(\frac{x_2}{x_3} - \frac{x_4}{x_3} \right)$$

$$k_{2-18} = \frac{4}{3} \left[d_{22} \left(\frac{x_4}{y_4} - \frac{x_4^2}{x_3 y_4} - \frac{x_2}{y_2} + \frac{x_2^2}{x_3 y_2} \right) - d_{33} \left(\frac{y_4}{x_3} - \frac{y_2}{x_3} \right) \right]$$

$$k_{3-3} = -d_{33} \frac{x_3}{y_2}$$

$$k_{3-4} = 0$$

$$k_{3-5} = -\frac{1}{3} d_{33} \frac{x_2}{y_2}$$

$$k_{3-6} = \frac{1}{3} d_{33}$$

$$k_{3-7} = 0$$

$$k_{3-8} = 0$$

$$k_{3-9} = -\frac{4}{3} d_{33} \left(-\frac{x_3}{y_2} + \frac{x_2}{y_2} \right)$$

$$k_{3-10} = -\frac{4}{3} d_{22} \left(-\frac{x_3}{y_2} + \frac{x_2}{y_3} \right)$$

$$k_{3-11} = \frac{4}{3} d_{33} \frac{x_2}{y_2}$$

$$k_{3-12} = -\frac{4}{3} d_{33}$$

$$k_{3-13} = 0$$

$$k_{3-14} = 0$$

$$k_{3-15} = 0$$

$$k_{3-16} = 0$$

$$k_{3-17} = 0$$

$$k_{3-18} = 0$$

$$k_{4-4} = -d_{22} \frac{x_3}{y_2}$$

$$k_{4-5} = \frac{1}{3} d_{12}$$

$$k_{4-6} = -\frac{1}{3} d_{22} \frac{x_2}{y_2}$$

$$k_{4-7} = 0$$

$$k_{4-8} = 0$$

$$k_{4-9} = \frac{4}{3} d_{12}$$

$$k_{4-10} = \frac{-4}{3} d_{22} \left(-\frac{x_3}{y_2} + \frac{x_2}{y_2} \right)$$

$$k_{4-11} = \frac{-4}{3} d_{12}$$

$$k_{4-12} = \frac{4}{3} d_{22} \frac{x_2}{y_2}$$

$$k_{4-13} = 0$$

$$k_{4-14} = 0$$

$$k_{4-15} = 0$$

$$k_{4-16} = 0$$

$$k_{4-17} = 0$$

$$k_{4-18} = 0$$

$$k_{5-5} = d_{11} \left(\frac{y_4}{x_3} - \frac{y_2}{x_3} \right) + d_{33} \left(\frac{x_4^2}{x_3 y_4} - \frac{x_2^2}{x_3 y_2} \right)$$

$$k_{5-6} = (d_{12} + d_{33}) \left(\frac{x_2}{x_3} - \frac{x_4}{x_3} \right)$$

$$k_{5-7} = \frac{1}{3} d_{33} \frac{x_2}{y_2}$$

$$k_{5-8} = -\frac{1}{3} d_{12}$$

$$k_{5-9} = 0$$

$$k_{5-10} = 0$$

$$k_{5-11} = \frac{4}{3} d_{33} \frac{x_2}{y_2}$$

$$k_{5-12} = -\frac{4}{3} d_{12}$$

$$k_{5-13} = -\frac{4}{3} d_{33} \frac{x_4}{y_4}$$

$$k_{5-14} = 0$$

$$k_{5-15} = 0$$

$$k_{5-16} = 0$$

$$k_{5-17} = \frac{4}{3} \left[d_{33} \left(\frac{x_4}{y_4} - \frac{x_4^2}{x_3 y_4} - \frac{x_2}{y_2} + \frac{x_2^2}{x_3 y_2} \right) - d_{11} \left(\frac{y_4}{x_3} - \frac{y_2}{x_3} \right) \right]$$

$$k_{5-18} = -\frac{4}{3} (d_{12} + d_{33}) \left(\frac{x_2}{x_3} - \frac{x_4}{x_3} \right)$$

$$k_{6-6} = d_{33} \left(\frac{y_4}{x_3} - \frac{y_2}{x_3} \right) + d_{22} \left(\frac{x_4^2}{x_3 y_4} - \frac{x_2^2}{x_3 y_2} \right)$$

$$k_{6-7} = -\frac{1}{3} d_{33}$$

$$k_{6-8} = \frac{1}{3} d_{22} \frac{x_4}{y_4}$$

$$k_{6-9} = 0$$

$$k_{6-10} = 0$$

$$k_{6-11} = -\frac{4}{3} d_{33}$$

$$k_{6-12} = \frac{4}{3} d_{22} \frac{x_2}{y_2}$$

$$k_{6-13} = \frac{4}{3} d_{33}$$

$$k_{6-14} = -\frac{4}{3} d_{22} \frac{x_4}{y_4}$$

$$k_{6-15} = 0$$

$$k_{6-16} = 0$$

$$k_{6-17} = -\frac{4}{3} (d_{12} + d_{33}) \left(\frac{x_2}{x_3} - \frac{x_4}{x_3} \right)$$

$$k_{6-18} = \frac{4}{3} \left[d_{22} \left(\frac{x_4}{y_4} - \frac{x_4^2}{x_3 y_4} - \frac{x_2}{y_2} + \frac{x_2^2}{x_3 y_2} \right) - d_{33} \left(\frac{y_4}{x_3} - \frac{y_2}{x_3} \right) \right]$$

$$k_{7-7} = d_{33} \frac{x_3}{y_4}$$

$$k_{7-8} = 0$$

$$k_{7-9} = 0$$

$$k_{7-10} = 0$$

$$k_{7-11} = 0$$

$$k_{7-12} = 0$$

$$k_{7-13} = -\frac{4}{3} d_{33} \frac{x_4}{y_4}$$

$$k_{7-14} = \frac{4}{3} d_{33}$$

$$k_{7-15} = -\frac{4}{3} d_{33} \left(\frac{x_3}{y_4} - \frac{x_4}{y_4} \right)$$

$$k_{7-16} = -\frac{4}{3} d_{33}$$

$$k_{7-17} = 0$$

$$k_{7-18} = 0$$

$$k_{8-8} = d_{22} \frac{x_3}{y_4}$$

$$k_{8-9} = 0$$

$$k_{8-10} = 0$$

$$k_{8-11} = 0$$

$$k_{8-12} = 0$$

$$k_{8-13} = \frac{4}{3} d_{12}$$

$$k_{8-14} = -\frac{4}{3} d_{22} \frac{x_4}{y_4}$$

$$k_{8-15} = -\frac{4}{3} d_{12}$$

$$k_{8-16} = -\frac{4}{3} d_{22} \left(\frac{x_3}{y_4} - \frac{x_4}{y_4} \right)$$

$$k_{8-17} = 0$$

$$k_{8-18} = 0$$

$$k_{9-9} = \frac{8}{3} \left[-d_{11} \frac{y_2}{x_3} + d_{33} \left(-\frac{x_3}{y_2} + \frac{x_2}{y_2} - \frac{x_2^2}{x_3 y_2} \right) \right]$$

$$k_{9-10} = -\frac{4}{3} (d_{12} + d_{33}) \left(1 - 2 \frac{x_2}{x_3} \right)$$

$$k_{9-11} = \frac{8}{3} \left[d_{33} \left(-\frac{x_2}{y_2} + \frac{x_2^2}{x_3 y_2} \right) + d_{11} \frac{y_2}{x_3} \right]$$

$$k_{9-12} = \frac{4}{3} (d_{12} + d_{33}) \left(1 - 2 \frac{x_2}{x_3} \right)$$

$$k_{9-13} = 0$$

$$k_{9-14} = 0$$

$$k_{9-15} = 0$$

$$k_{9-16} = 0$$

$$k_{9-17} = \frac{8}{3} d_{33} \frac{x_2}{y_2}$$

$$k_{9-18} = -\frac{4}{3} (d_{12} + d_{33})$$

$$k_{10-10} = \frac{8}{3} [d_{22} \left(-\frac{x_3}{y_2} + \frac{x_2}{y_2} - \frac{x_2^2}{x_3 y_2} \right) - d_{33} \frac{y_2}{x_3}]$$

$$k_{10-11} = \frac{4}{3} (d_{12} + d_{33}) \left(1 - 2 \frac{x_2}{x_3} \right)$$

$$k_{10-12} = \frac{8}{3} [d_{22} \left(-\frac{x_2}{y_2} + \frac{x_2^2}{x_3 y_2} \right) + d_{33} \frac{y_2}{x_3}]$$

$$k_{10-13} = 0$$

$$k_{10-14} = 0$$

$$k_{10-15} = 0$$

$$k_{10-16} = 0$$

$$k_{10-17} = -\frac{4}{3} (d_{33} + d_{12})$$

$$k_{10-18} = \frac{8}{3} d_{22} \frac{x_2}{y_2}$$

$$k_{11-11} = \frac{8}{3} [d_{33} \left(-\frac{x_3}{y_2} + \frac{x_2}{y_2} - \frac{x_2^2}{x_3 y_2} \right) - d_{11} \frac{y_2}{x_3}]$$

$$k_{11-12} = -\frac{4}{3} (d_{33} + d_{12}) \left(1 - 2 \frac{x_2}{x_3} \right)$$

$$k_{11-13} = 0$$

$$k_{11-14} = 0$$

$$k_{11-15} = 0$$

$$k_{11-16} = 0$$

$$k_{11-17} = -\frac{8}{3} d_{33} \left(-\frac{x_3}{y_2} + \frac{x_2}{y_2} \right)$$

$$k_{11-18} = \frac{4}{3} (d_{12} + d_{33})$$

$$k_{12-12} = \frac{8}{3} d_{22} \left(-\frac{x_3}{y_2} + \frac{x_2}{y_2} - \frac{x_2^2}{x_3 y_2} \right) - d_{33} \frac{y_2}{x_3}$$

$$k_{12-13} = 0$$

$$k_{12-14} = 0$$

$$k_{12-15} = 0$$

$$k_{12-16} = 0$$

$$k_{12-17} = \frac{4}{3} (d_{33} + d_{12})$$

$$k_{12-18} = -\frac{8}{3} d_{22} \left(-\frac{x_3}{y_2} + \frac{x_2}{y_2} \right)$$

$$k_{13-13} = \frac{8}{3} \left[d_{33} \left(\frac{x_3}{y_4} - \frac{x_4}{y_4} + \frac{x_4^2}{x_3 y_4} \right) + d_{11} \frac{y_4}{x_3} \right]$$

$$k_{13-14} = \frac{4}{3} (d_{12} + d_{33}) \left(1 - 2 \frac{x_4}{x_3} \right)$$

$$k_{13-15} = \frac{8}{3} \left[d_{33} \left(\frac{x_4}{y_4} - \frac{x_4^2}{x_3 y_4} \right) - d_{11} \frac{y_4}{x_3} \right]$$

$$k_{13-16} = -\frac{4}{3} (d_{12} + d_{33}) \left(1 - 2 \frac{x_4}{x_3} \right)$$

$$k_{13-17} = -\frac{8}{3} d_{33} \left(\frac{x_3}{y_4} - \frac{x_4}{y_4} \right)$$

$$k_{13-18} = -\frac{4}{3} (d_{12} + d_{13})$$

$$k_{14-14} = \frac{8}{3} \left[d_{22} \left(\frac{x_3}{y_4} - \frac{x_4}{y_4} + \frac{x_4^2}{x_3 y_4} \right) + d_{33} \frac{y_4}{x_3} \right]$$

$$k_{14-15} = -\frac{4}{3} (d_{12} + d_{33}) \left(1 - 2 \frac{x_4}{x_3} \right)$$

$$k_{14-16} = \frac{8}{3} \left[d_{22} \left(\frac{x_4}{y_4} - \frac{x_4^2}{x_3 y_4} \right) - d_{33} \frac{y_4}{x_3} \right]$$

$$k_{14-17} = -\frac{4}{3} (d_{33} + d_{12})$$

$$k_{14-18} = -\frac{8}{3} d_{22} \left(\frac{x_3}{y_4} - \frac{x_4}{y_4} \right)$$

$$k_{15-15} = \frac{8}{3} \left[d_{11} \frac{y_4}{x_3} + d_{33} \left(\frac{x_3}{y_4} - \frac{x_4}{y_4} + \frac{x_4^2}{x_3 y_4} \right) \right]$$

$$k_{15-16} = \frac{4}{3} (d_{12} + d_{33}) \left(1 - 2 \frac{x_4}{x_3} \right)$$

$$k_{15-17} = -\frac{8}{3} d_{33} \frac{x_4}{y_4}$$

$$k_{15-18} = \frac{4}{3} (d_{12} + d_{33})$$

$$k_{16-16} = \frac{8}{3} \left[d_{22} \left(\frac{x_3}{y_4} - \frac{x_4}{y_4} + \frac{x_4^2}{x_3 y_3} \right) + d_{33} \frac{y_4}{x_3} \right]$$

$$k_{16-17} = \frac{4}{3} (d_{33} + d_{12})$$

$$k_{16-18} = -\frac{8}{3} d_{22} \frac{x_4}{y_4}$$

$$k_{17-17} = \frac{8}{3} \left[d_{11} \left(\frac{y_4}{x_3} - \frac{y_2}{x_3} \right) + d_{33} \left(\frac{x_3}{y_4} - \frac{x_4}{y_4} + \frac{x_4^2}{x_3 y_4} - \frac{x_3}{y_2} + \frac{x_2}{y_2} - \frac{x_2^2}{x_3 y_2} \right) \right]$$

$$k_{17-18} = \frac{8}{3} (d_{12} + d_{33}) \left(\frac{x_2}{x_3} - \frac{x_4}{x_3} \right)$$

$$k_{18-18} = \frac{8}{3} \left[d_{33} \left(\frac{y_4}{x_3} - \frac{y_2}{x_3} \right) + d_{22} \left(\frac{x_3}{y_4} - \frac{x_4}{y_4} + \frac{x_4^2}{x_3 y_4} - \frac{x_3}{y_2} + \frac{x_2}{y_2} - \frac{x_2^2}{x_3 y_2} \right) \right]$$

where d_{11} , d_{12} , d_{22} and d_{33} are given in Equations A.29, A.30, and A.31.

A. 4 Transformation matrix for the Eight-noded Quadrilateral Element

The following transformation matrix is used to transform the local stiffness matrix of the eight-noded linear strain quadrilateral element into the global axes:

A.5 Beam Element Stiffness Matrix

The element stiffness matrix of the beam element in its local co ordination is given by:

$$[k_e]_b = E_e \begin{bmatrix} \frac{A}{L} & 0 & 0 & -\frac{A}{L} & 0 & 0 \\ 0 & \frac{12I}{L^3} & \frac{6I}{L^2} & 0 & -\frac{12I}{L^3} & \frac{6I}{L^2} \\ 0 & \frac{6I}{L^2} & \frac{4I}{L} & 0 & -\frac{6I}{L^2} & \frac{2I}{L} \\ -\frac{A}{L} & 0 & 0 & \frac{A}{L} & 0 & 0 \\ 0 & -\frac{12I}{L^3} & -\frac{6I}{L^2} & 0 & \frac{12I}{L^3} & -\frac{6I}{L^2} \\ 0 & \frac{6I}{L^2} & \frac{2I}{L} & 0 & -\frac{6I}{L^2} & \frac{4I}{L} \end{bmatrix}$$

(A.35)

where,

$$E_e = \frac{E}{1-\nu^2} \quad (A.36)$$

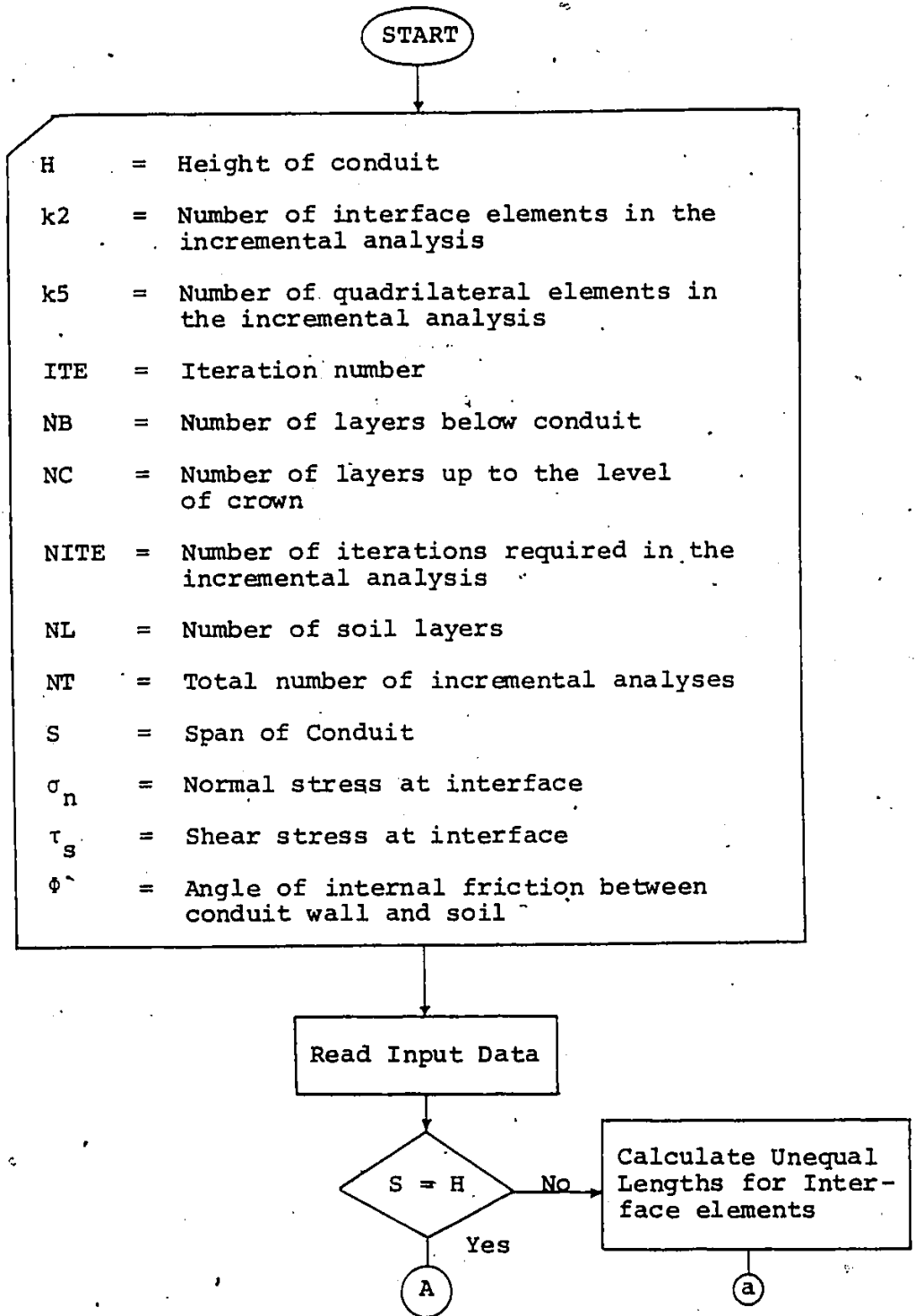
and A and I are the cross-sectional area and the moment of inertia per unit length, respectively. The transformation matrix may be written as:

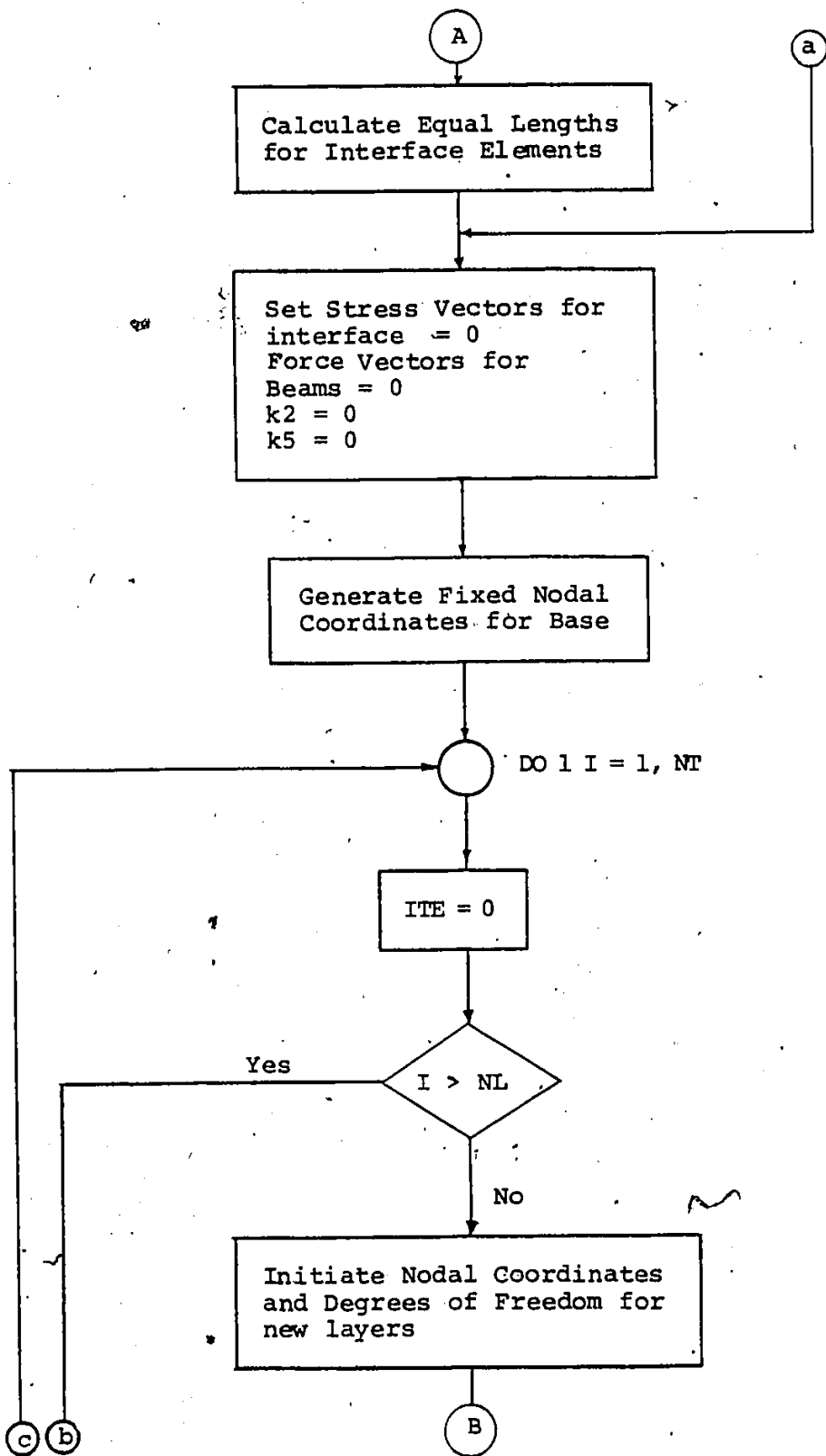
$$[T]_6 = \begin{bmatrix} \cos\theta & \sin\theta & 0 & 0 & 0 & 0 \\ -\sin\theta & \cos\theta & 0 & 0 & 0 & 0 \\ 0 & 0 & 1 & 0 & 0 & 0 \\ 0 & 0 & 0 & \cos\theta & \sin\theta & 0 \\ 0 & 0 & 0 & -\sin\theta & \cos\theta & 0 \\ 0 & 0 & 0 & 0 & 0 & 1 \end{bmatrix}$$

(A.37)

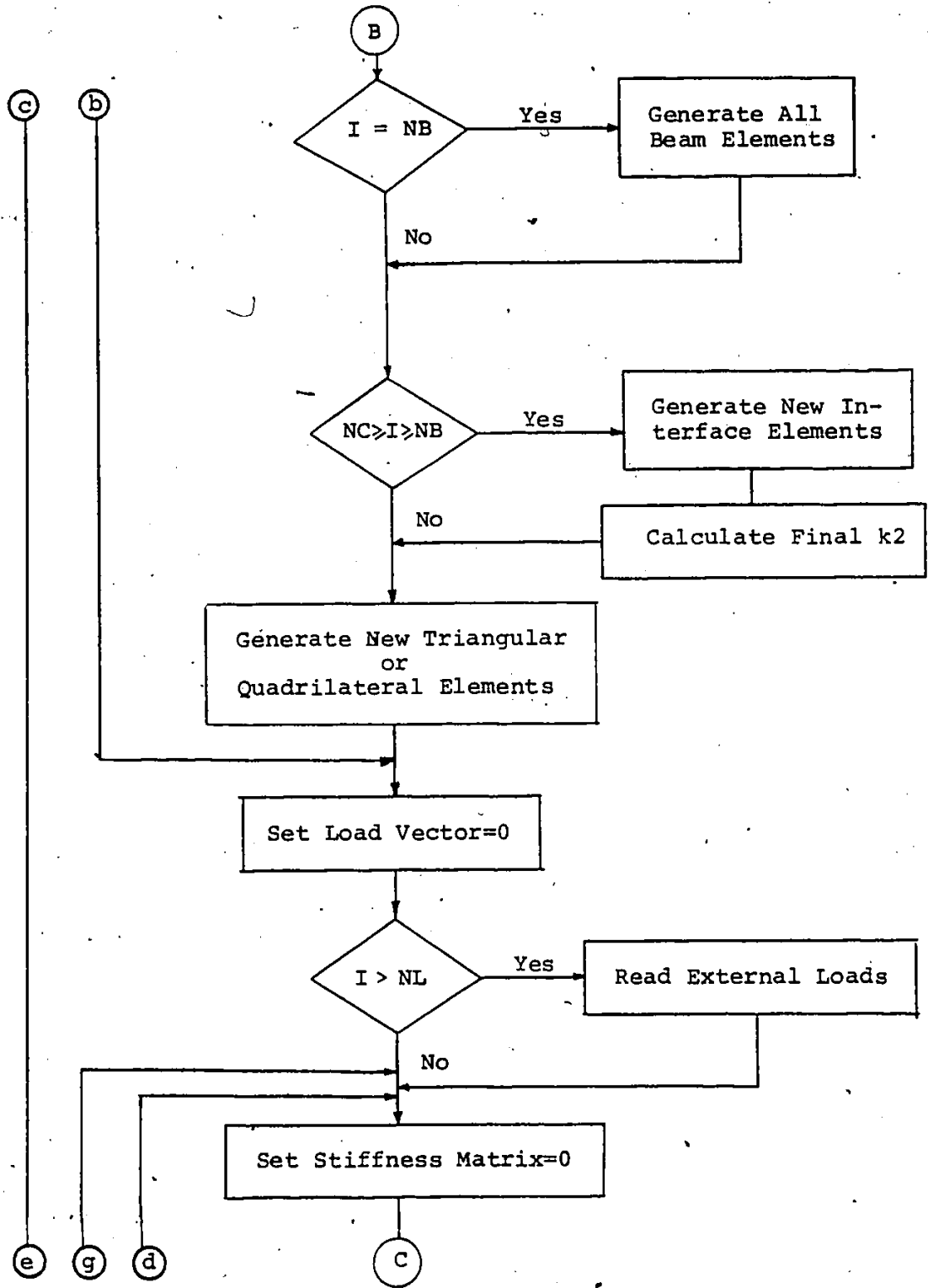
APPENDIX B

FLOW CHART

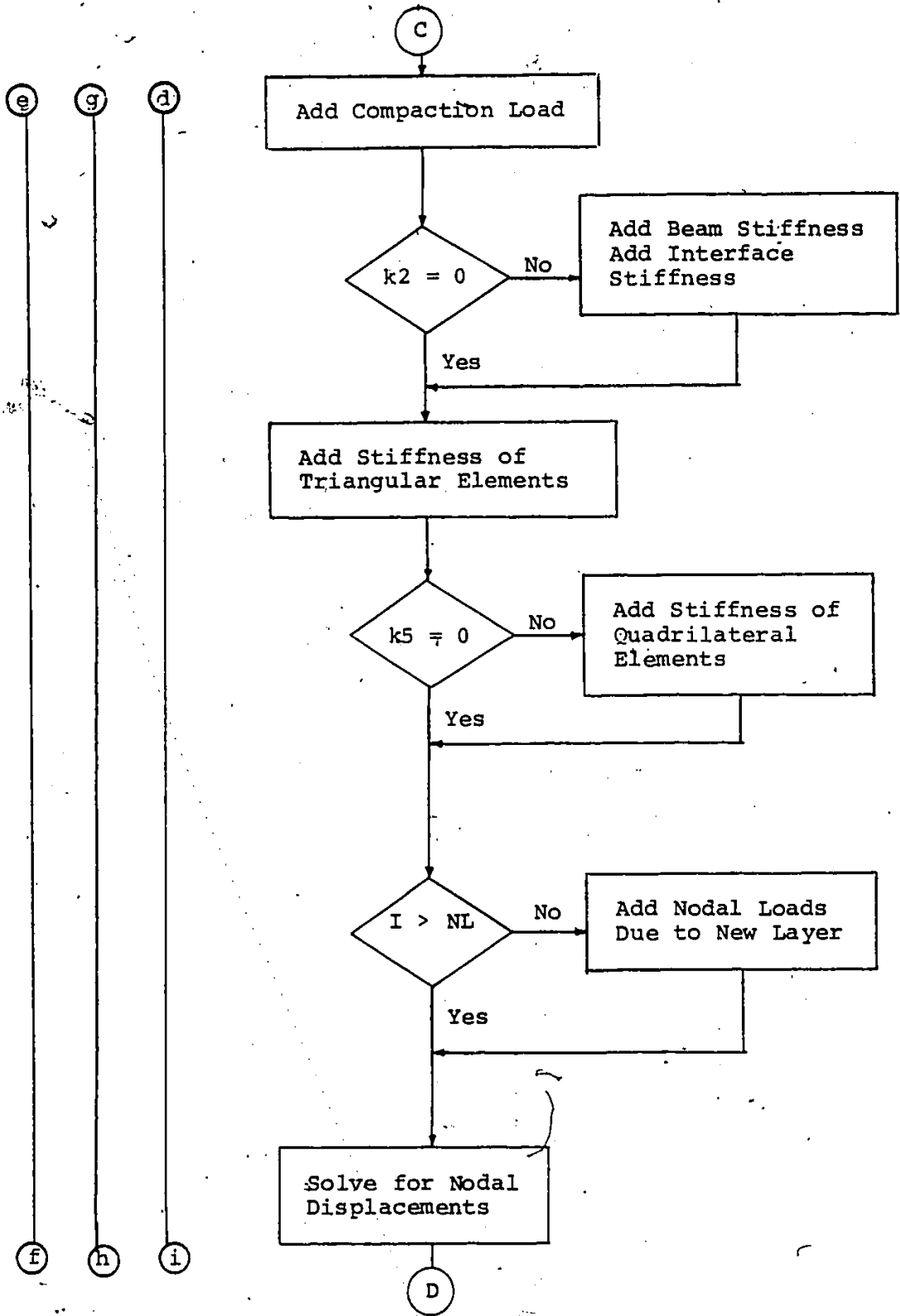


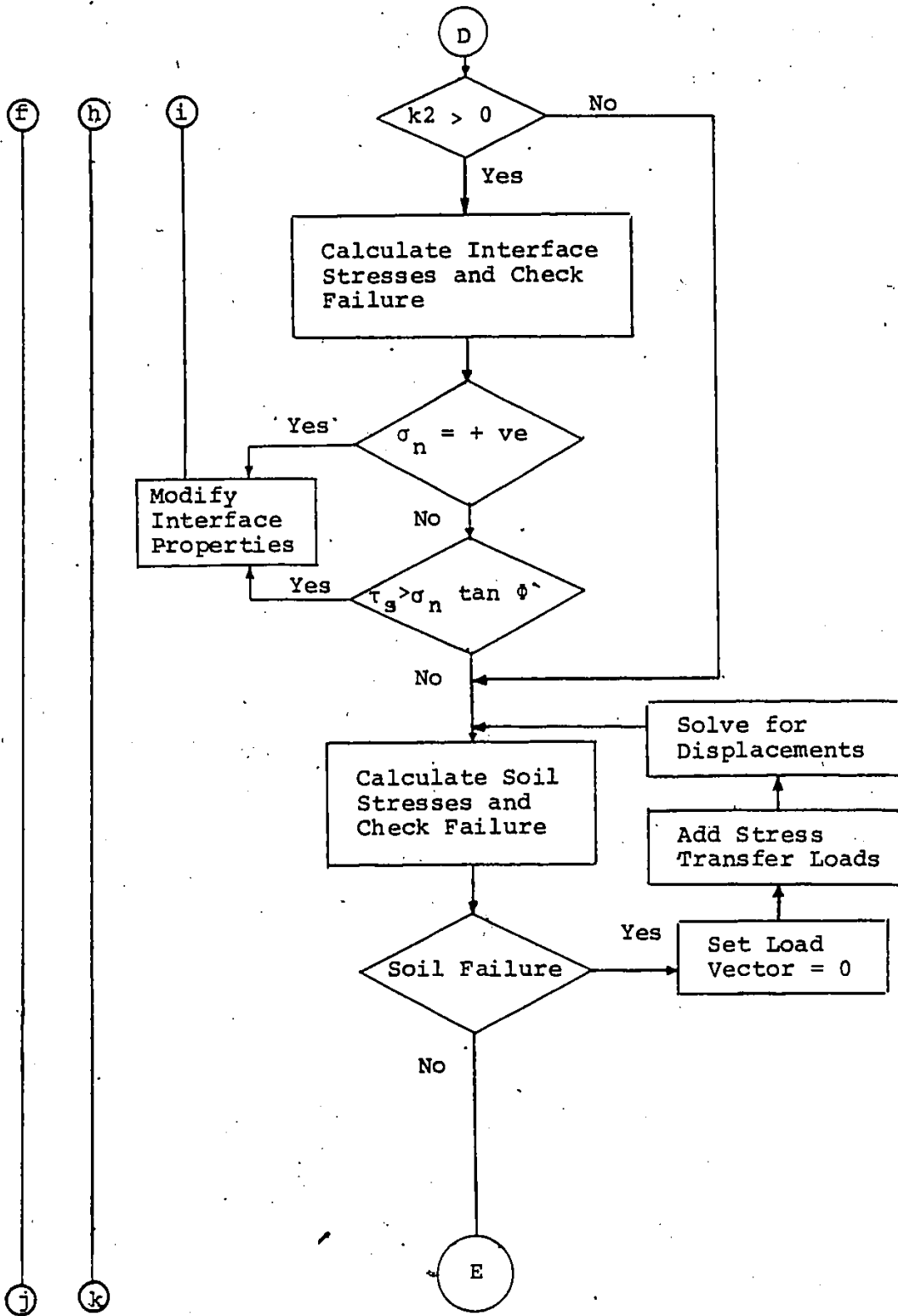


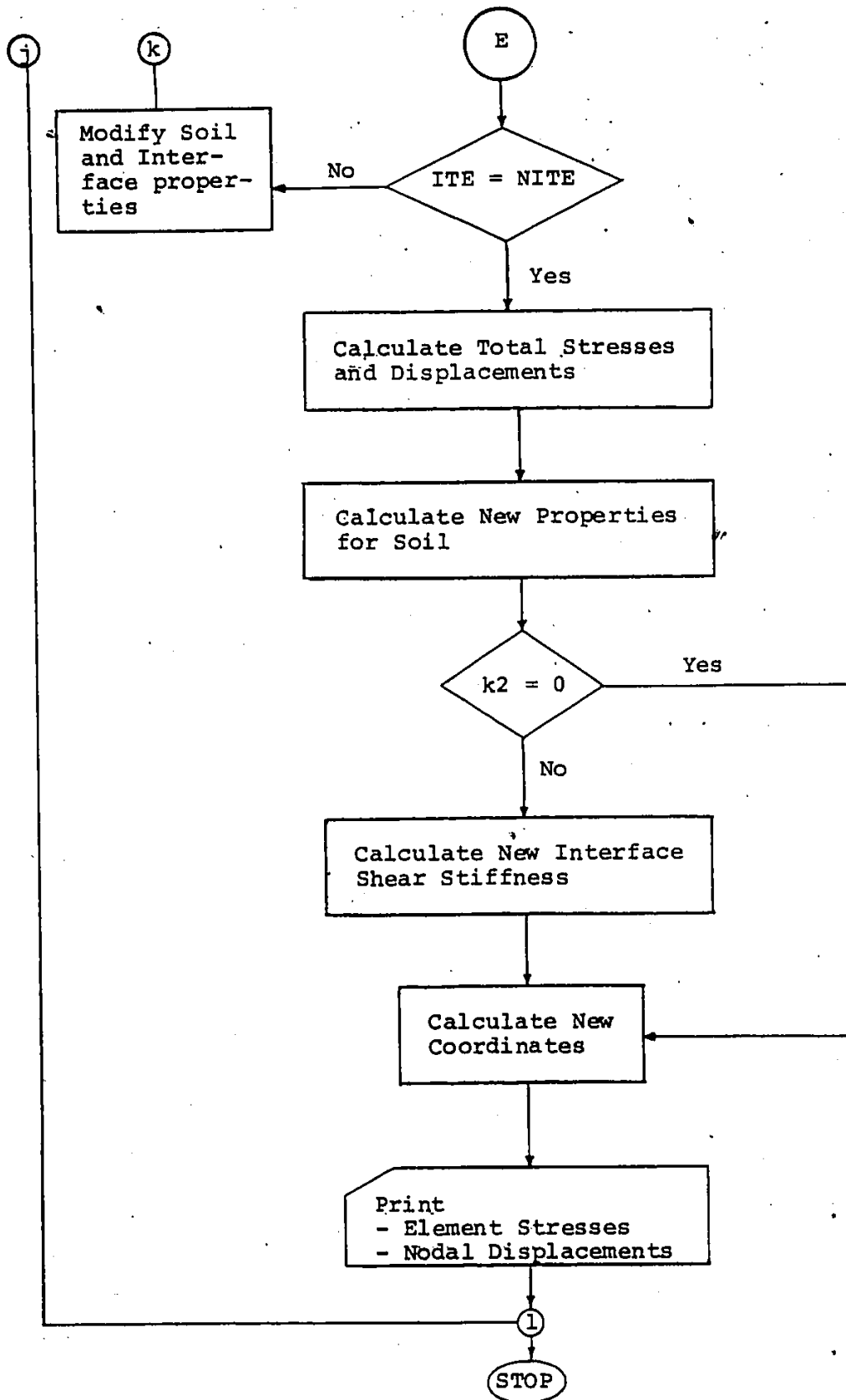
242



24.3







APPENDIX C

TABLES

Table C.1 Comparison between analytical results using method 1 and method 2 for representing live load.

Beam Element No.	Thrust (lb/in)				Moment (lb/in)	
	White Ash		Adelaide		Adelaide	
	P_d	$P_{d'}$	P_d	$P_{d'}$	P_d	$P_{d'}$
1	-16.6	-11.5	10.8	14.5	5.9	6.0
2	-31.8	-23.2	2.6	8.4	-1.7	-1.9
3	-19.0	-16.2	-19.9	-19.0	1.0	1.3
4	-65.1	-52.7	-39.1	-32.1	26.0	26.7
5	-41.2	-41.1	-59.0	-59.8	-26.0	-26.6
6	-86.7	-72.8	-48.8	-41.9	6.5	6.3
7	-87.5	-89.7	-77.5	-79.0	6.5	5.2
8	-150.9	-136.6	-62.8	-56.3	-21.4	-22.5
9	-156.7	-161.1	-84.8	-86.6	1.8	0.6
10	-225.6	-217.3	-203.1	-203.3	96.0	99.0
11	-239.3	-246.0	-235.3	-242.3	-60.3	-65.5
12	-254.1	-249.8	-227.2	-228.8	2.3	2.5
13	-239.3	-246.0	-235.2	-242.2	4.9	3.9
14	-254.1	-249.8	-227.5	-228.7	-90.8	-93.3
15	-298.9	-307.8	-321.6	-332.1	69.4	72.9
16	-297.7	-303.5	-315.8	-324.6	-96.2	-97.5
17	-299.0	-307.8	-321.7	-332.2	84.1	87.1
18	-297.7	-303.5	-315.7	-324.5	-100.3	-100.4

Table C.1 continued

Beam Element No.	Thrust (lb/in)				Moment (lb/in)	
	White Ash		Adelaide		Adelaide	
	P_d	$P_{d'}$	P_d	$P_{d'}$	P_d	$P_{d'}$
19	-337.2	-350.1	-385.9	-400.6	97.3	100.0
20	-327.4	-341.8	-370.0	-384.6	-94.3	-96.4
21	-337.2	-350.2	-385.9	-400.6	90.0	93.6
22	-327.5	-341.8	-370.0	-384.6	-88.3	-92.4
23	-289.7	-307.0	-399.9	-420.5	82.4	86.9
24	-281.5	-300.7	-387.8	-409.9	-42.1	-44.9
25	-289.6	-307.0	-399.8	-420.3	41.6	45.0
26	-281.5	-300.7	-387.6	-409.7	1.4	-3.1
27	-150.7	-167.1	-201.2	-218.6	4.6	7.1
28	-151.17	-168.5	-202.9	-221.3	69.2	72.8
29	-149.7	-166.1	-200.5	-217.8	-67.2	-70.4
30	-150.3	-167.7	-202.2	-220.6	138.0	146.9

Table C.2 Analytical and Measured Relative Vertical Displacements at Crown of the Tested Conduits (in inches):

Structure	Lane No.	Position No.	Measured Value	Analytical Value
White Ash	4	1	0.024	0.08280
White Ash	8	1	0.044	0.10370
White Ash	4	2	0.027	0.06118
White Ash	8	2	0.050	0.07277
Adelaide	4	1	0.000	0.12508
Adelaide	8	1	0.000	0.15179
Adelaide	4	2	0.010	0.09496
Adelaide	8	2	0.010	0.11652

Table C.3 Measured displacements at dial gauge locations
G1 to G9 in Test No. 1. (In inches $\times 10^{-3}$)

Load (Kips)	G ₁ [*]	G ₂ [*]	G ₃ ^{**}	G ₄ ^{**}	G ₅ ^{**}	G ₆ ^{**}	G ₇ ^{***}	G ₈ ^{***}	G ₉ ^{***}
0.50	56	63	17	24	27	10	21	19	17
1.00	132	130	69	71	79	60	52	52	47
1.50	191	189	128	127	139	95	90	91	79
2.00	277	265	197	181	209	155	132	135	119
2.50	369	344	290	256	300	217	187	191	168
1.90	562	473	492	356	523	300	-	-	185
0.00	335	269	337	230	369	180	9	11	5
0.50	399	325	369	254	395	205	34	36	26
1.00	451	378	407	283	441	220	62	66	53
1.50	509	427	456	321	495	260	95	97	81
2.00	578	488	522	371	565	300	128	133	123
1.92	933	830	884	703	926	630	141	147	136

- * G1 and G2 are loading frame displacements
 ** G3 to G6 are I-Beam displacements
 *** G7 to G9 are conduit crown displacements

Table C.4 Measured displacements at dial gauge locations
G₁ to G₉ in Test No. 2. (In inches x 10⁻³)

Load (Kips)	G ₁ *	G ₂ *	G ₃ **	G ₄ **	G ₅ **	G ₆ **	G ₇ **	G ₈ ***	G ₉ ***
0.50	87	100	71	85	71	70	23	23	23
1.00	162	221	139	125	139	136	54	52	46
1.50	237	262	194	179	198	192	86	83	72
2.00	296	311	248	237	256	255	118	115	100
2.50	351	363	299	295	311	314	151	150	128
3.00	408	412	353	351	366	371	189	188	162
3.50	479	546	422	395	436	408	242	245	213
3.75	524	571	465	425	486	454	277	282	240
4.00	564	611	513	460	526	492	319	324	278
4.30	694	736	641	570	666	590	433	449	383
0.00	31	284	291	235	307	295	100	104	90

- * G₁ and G₂ are loading frame displacements
 ** G₃ to G₆ are I-Beam displacements
 *** G₇ to G₉ are conduit crown displacements

BIBLIOGRAPHY

1. AASHTO, "Standard Specifications for Highway Bridges," American Association of State Highway and Transportation Officials, Washington, D.C., 1977.
2. Abdel-Sayed, G., "Stability of Flexible Conduits Embedded in Soil," Canadian Journal of Civil Engineering, Vol. 5, No. 3, September, 1978.
3. Abdel-Sayed, G., and Bakht, B., "Soil-Steel Structure Design by the Ontario Code: Part 2, Structural Considerations," Canadian Journal of Civil Engineering, Vol. 8, No. 3, September, 1981.
4. Abel, J. F., Mark, R., and Richards, R., "Stresses Around Flexible Elliptic Pipes," Journal of the Soil Mechanics and Foundations Division, ASCE, Vol. 99, No. SM7, July, 1973.
5. Abel, J. F., "Nonlinear Finite Element Analysis of Large Flexible Pipes," Dayton Symposium on Lateral Pressures Generated by Pipes, Piles, Tunnels and Caissons, Dayton, Ohio Section, ASCE, February, 1975.
6. Abel, J. F., Nasir, G. A., and Mark, R., "Stresses and Deflections in Soil-Structure Systems Formed by Long-Span Elliptic Pipe," Report to Armco Steel Corporation, Civil Engineering Department, Princeton University, July, 1977.
7. AISI, "Handbook of Steel Drainage and Highway Construction Products," American Iron and Steel Institution, Washington, D.C., 1971.
8. Al-Hussaini, M. M., and Radhakrishnan, N., "Analysis of Plane Strain Tests Using the Finite Element Method," Proceedings, Symposium on Applications of the Finite Element Method in Geotechnical Engineering, Waterways Experiment Station, Vicksburg, Mississippi, May, 1972.
9. Alizadeh, A., "Evaluation of the Computer Program for the Analysis and Design of Culverts (CANDE)," Report for the Ontario Ministry of Transportation and Communications, H. G. Engineering Ltd., March, 1977.
10. Allgood, J.R., "The Behaviour of Shallow-Buried Cylinders," Proceedings of the Symposium on Soil-Structure Interaction, Univ. of Arizona, Tucson, Arizona, 1964.

11. Allgood, J. R., and Ciani, J. B., "The Influence of Soil Modulus on the Behaviour of Cylinders in Sand," Highway Research Record No. 249, Highway Research Board, National Academy of Sciences, Washington, D.C., 1968.
12. Allgood, J. R., "Structures in Soil under High Loads," Journal of the Soil Mechanics and Foundations Division, ASCE, Vol. 97, No. SM3, March, 1971.
13. Allgood, J. R., and Takahashi, S. K., "Balanced Design and Finite Element Analysis of Culverts," Highway Research Record No. 413, Highway Research Board, National Academy of Sciences, Washington, D.C., 1972.
14. Allgood, J. R., "Summary of Soil-Structure Interaction," Naval Civil Engineering Lab., Port Huenene, California, NCEL-TR-771, July, 1972.
15. Allgood, J. R., Discussion of "Buckling of Soil-Surrounded Tubes," Journal of the Soil Mechanics and Foundations Division, ASCE, Vol. 93, No. SM5, September 1967.
16. Baikie, L. D., "Strength of Corrugated Steel Arches Under Compacted Sand Backfill," Ph.D. Thesis presented to the Civil Engineering Department, Nova Scotia Technical College, 1966.
17. Bakht, B., "Live Load Testing of Soil-Steel Structures," Report to the Ontario Ministry of Transportation and Communications, SRR-80-4, August, 1980.
18. Bartkus, E. A., and Vey, E., "Granular Earth Pressures on Steel Tunnel Lining," Bulletin 141, Highway Research Board, National Academy of Sciences, Washington, D.C., 1956.
19. Booy, C., "Flexible Conduit Studies," Prairie Farm Rehabilitation Administration, Canada Department of Agriculture, Saskatoon, 1957.
20. Bowles, J. E., "Foundation Analysis and Design," McGraw Hill Book Company, Second Edition, 1977.
21. Breth, H., Schuster, E., and Pise, P., "Axial Stress-Strain Characteristics of Sand," Journal of the Soil Mechanics and Foundations Division, ASCE, Vol. 99, No. SM8, August, 1973.

22. Brown, C. B., Green, D. R., and Pawsey, S., "Flexible Culverts Under High Fills," Journal of the Structural Division, ASCE, Vol. 94, No. ST4, April, 1968.
23. Burns, J. Q., and Richard, R. M., "Attenuation of Stresses for Buried Cylinders," Proceedings, Symposium on Soil-Structure Interaction, University of Arizona, Tucson, Arizona, 1964.
24. Burns, J. Q., "An Analysis of Circular Cylindrical Shells Embedded in Elastic Media," Ph.D. Thesis presented to the Engineering Mechanics Department, University of Arizona, Tucson, Arizona, 1965.
25. Chan, S. K., and Tuba, I. S., "A Finite Element Method for Contact Problems of Solid Bodies, Part I Theory and Validation," International Journal of Mechanical Science, Volume 13, 1971.
26. Chang C. Y., and Duncan, J. M., "Analysis of Soil Movements Around a Deep Excavation," Journal of the Soil Mechanics and Foundations Division, ASCE, Vol. 96, No. SM5, September, 1970.
27. Clough, G. W., and Duncan, J. M., "Finite Element Analysis of Retaining Wall Behaviour," Journal of the Soil Mechanics and Foundations Division, ASCE, Vol. 97, No. SM12, December, 1971.
28. Clough, G. W., "Application of the Finite Element Method to Earth-Structure Interaction," State-of-the-Art Report," Proceedings, Symposium on Applications of the Finite Element Method in Geotechnical Engineering, Waterways Experiment Station, Vicksburg, Mississippi, May, 1972.
29. Clough, R. W., and Woodward, R. J., "Analysis of Embankment Stresses and Deformations," Journal of the Soil Mechanics and Foundations Division, ASCE, Vol. 93, No. SM4, July, 1967.
30. Conry, T. F., and Seires, A., "A Mathematical Programming Method for Design of Elastic Bodies in Contact," Journal of Applied Mechanics, Vol. 38, 1971.
31. Coon, M. D., and Evans, R. J., "Recoverable Deformation of Cohesionless Soils," Journal of the Soil Mechanics and Foundations Division, ASCE, Vol. 97, No. SM2, February, 1971.

32. CSPI, "CSP Technical Manual," Corrugated Steel Pipe Institute, Mississauga, Ontario, 1972.
33. CSPI, "Composite Design of Soil-Steel Structures," Corrugated Steel Pipe Institute, Mississauga, Ontario, 1972.
34. CSPI, "Soil-Steel Bridge Structures," Corrugated Steel Pipe Institute, Mississauga, 1978.
35. Dar, S. M., and Bates, R. C., "Stress Analysis of Hollow Cylindrical Inclusions," Journal of the Geotechnical Engineering Division, ASCE, Vol. 100, No. GT2, February, 1974.
36. Davis, R. E., and Bacher, A. E., "California's Culvert Research Program - Description, Current Status, and Observed Peripheral Pressures," Highway Research Record No. 249, Highway Research Board, National Academy of Sciences, Washington, D. C., 1968.
37. Demin, J., "Field Verification of Ring Compression Conduit Design," Highway Research Record, No. 166, National Academy of Sciences, Washington, D.C., January, 1965.
38. Desai, C. S., and Abel, J. F., "Introduction to the Finite Element Method, A Numerical Method for Engineering Analysis," Van Nostrand Reinhold Company, New York, 1972.
39. Desai, C. S., and Holloway, D. M., Discussion of "Nonlinear Analysis of Stress and Strain in Soils," Journal of the Soil Mechanics and Foundations Division, ASCE, Vol. 97, No. SM5, May, 1971.
40. Desai, C. S., "Nonlinear Analysis Using Spline Functions," Journal of the Soil Mechanics and Foundations Division, ASCE, Vol. 97, No. SM10, October, 1971.
41. Desai, C. S., "Overview, Trends and Projections: Theory, and Applications of the Finite Element Method in Geotechnical Engineering," Proceedings, Symposium on Applications of the Finite Element Method in Geotechnical Engineering, Waterways Experiment Station, Vicksburg, Mississippi, May, 1972.
42. Desai, C. S., and Holloway, D. M., "Load-Deformation Analysis of Deep Pile Foundations," Proceedings,

Symposium on Applications of the Finite Element Method in Geotechnical Engineering, Waterways Experiment Station, Vicksburg, Mississippi, May, 1972.

- 43. Desai, C. S., "Numerical Design-Analysis of Piles in Sands," Journal of the Geotechnical Engineering Division, ASCE, Vol. 100, No. ST6, June 1974.
- 44. Desai, C. S., and Wu, T. H., "A General Function for Stress-Strain Curves," Proceedings, 2nd International Conference on Numerical Methods in Geomechanics, Blacksburg, Virginia, June, 1976.
- 45. Desai, C. S., and Christian, J. T., "Numerical Methods in Geotechnical Engineering," McGraw Hill Book Company, 1977.
- 46. Dimassio, F. L., and Sandler, I. S., "Material Model for Granular Soils," Journal of Engineering Mechanics Division, ASCE, Vol. 97, No. EM3, June 1971.
- 47. Domaschuk, L., and Wade, N. H., "A Study of Bulk and Shear Moduli of Sand," Journal of the Soil Mechanics and Foundations Division, ASCE, Vol. 95, No. SM2, March, 1969.
- 48. Drawsky, R., "An Accurate Design Method for Buried Flexible Conduit Structures," HRB Circ. 34, July, 1966.
- 49. Drnevish, V. P., "Constrained and Shear Moduli for Finite Elements," Journal of the Geotechnical Engineering Division, ASCE, Vol. 101, No. GT 5, May, 1975.
- 50. Duffy, J., and Mindlin, R. D., "Stress-Strain relation of Granular Media," Journal of Applied Mechanics, ASME, Vol. 24, 1957.
- 51. Duncan, J. M., and Chans, C. Y., "Nonlinear Analysis of Stress and Strain in Soils," Journal of the Soil Mechanics and Foundations Division, ASCE, Vol. 96, No. SM5, September, 1970.
- 52. Duncan, J. M., and Clough, G. W., "Finite Element Analyses of Port Allen Lock," Journal of the Soil Mechanics and Foundations Division, ASCE, Vol. 97, No. SM8, August, 1971.

53. Duncan, J. M., "Finite Element Analyses of Stresses and Movements in Dams, Excavations and Slopes," Proceedings, Symposium on Applications of the Finite Element Method in Geotechnical Engineering, Waterways Experiment Station, Vicksburg, Mississippi, May, 1972.
54. Duncan, J. M., and Lefebvre, G., "Earth Pressures on Structures due to Fault Movement," Journal of the Soil Mechanics and Foundations Division, ASCE, Vol. 99, No. SM12, December, 1973.
55. Duncan, J. M., "Design Studies for a 35-ft. Span Aluminum Culvert for Greenbrier County, West Virginia," Report to Highway Products Division, Kaiser Aluminum and Chemical Sales, Inc., Oakland, California, July, 1975.
56. Duncan, J. M., "Finite Element Analysis of Buried Flexible Metal Culvert Structures," Laurits Bjerrum Memorial Volume, Norwegian Geotechnical Institute, Oslo, Norway, 1976.
57. Duncan, J. M., "Behavior and Design of Long Span Metal Culverts," Journal of the Geotechnical Engineering Division, ASCE, Vol. 105, No. GT3, March, 1979.
58. Duncan, J. M., Wong, K. S., and Ozawa, Y. "FEADAM: A Computer Program for Finite Element Analysis of Dams," Report No. UCB/GT/80-02, University of California, Berkeley, California, 1980.
59. Dunlop, P., and Duncan, J. M., "Development of Failure around Excavated Slopes," Journal of the Soil Mechanics and Foundations Division, ASCE, Vol. 96, No. SM2, March, 1970.
60. Ekhande, S. G., "Effect of Live Load on the Soil-Steel Structure under Shallow Cover," M.A.Sc. Thesis presented to the Civil Engineering Department, University of Windsor, 1981.
61. Ellison, R. D., "Load Deformation Mechanism for Bored Piles," Journal of the Soil Mechanics and Foundations Division, ASCE, Vol. 97, No. SM4, April, 1971.
62. El-Sohby, M.A., "Elastic Behaviour of Sand," Journal of the Soil Mechanics and Foundations Division, ASCE, Vol. 95, No. SM11, November, 1969.

63. Fenner, R. T., "Finite Element Methods for Engineers," The MacMillan Press Ltd., London, Great Britain, 1975.
64. Fitzhardinge, C., "Economical Highway Bridge Designs • Using Earth and Steel," Paper presented at IRF, International Road Federation, Australian Road Conference, Melbourne, April, 1978.
65. Gallagher, R. H., "Finite Element Analysis Fundamentals," Prentice-Hall, Inc., 1975.
66. Ghaboussi, J., Wilson, E. L., and Isenberg, "Finite Element for Rock Joints and Interfaces," Journal of Soil Mechanics and Foundations Division, ASCE, Vol. 99, No. SM10, October, 1973.
67. Girijavanallabhan, C. G., and Reese, L. C., "Finite Element Method for Problems in Soil Mechanics," Journal of the Soil Mechanics and Foundations Division, ASCE, Vol. 94, No. SM2, March, 1968.
68. Goodman, R. E., and Brown, C. B., "Dead Load Stresses and the Instability of Slopes," Journal of the Soil Mechanics and Foundations Division, ASCE, Vol. 89, No. SM3, May, 1963.
69. Goodman, R. E., and Taylor, R. L., "A Model for the Mechanics of Jointed Rock," Journal of the Soil Mechanics and Foundations Division, ASCE, Vol. 94, No. SM3, May, 1968.
70. Gudehus, G., "Finite Elements in Geomechanics," John Wiley & Sons, Inc., 1977.
71. Hafez, H. H., Abdel-Sayed, G., "Long Span Soil-Steel Structures: An Economical Alternative to Short Span Bridges," Proceedings, AMSE Annual Convention, Plainfield, Indiana, September, 1981.
72. Hansen, T. B., Discussion of "Hyperbolic Stress-Strain Response: Cohesive Soils," Journal of the Soil Mechanics and Foundations Division, ASCE, Vol. 89, No. SM4, July, 1963.
73. Hardin, B. O., "Constitutive Relations for Air Field Subgrade and Base Course Materials," Technical Report UKY 32-71 CE5, University of Kentucky, College of Engineering, Soil Mechanics Series No. 4, Lexington, Kentucky, 1970.

74. Hasnain, M., "Shear Strength Characteristics of A Crushed Quartz Sand," Master Thesis submitted to Civil Engineering Department, University of Ottawa, 1974.
75. Holubec, I., "Elastic Behaviour of Cohesionless Soil," Journal of the Soil Mechanics and Foundations Division, ASCE, Vol. 94, No. SM6, November, 1968.
76. Heuze, F. E., Goodman, R. E., and Bornstein, A., "Numerical Analyses of Deformability Tests in Jointed Rock - 'Joint Perturbation' and 'No Tension' Finite Element Solutions," Rock Mechanics, Vol. 3, 1971.
77. Hoeg, K., "Pressure Distribution on Underground Structural Cylinders," Technical Report No. AFWL TR-65-98, Air Force Weapons Laboratory, Kirkland Air Force Base, New Mexico, April, 1966.
78. Hoeg, K., "Stresses Against Underground Structural Cylinders," Journal of the Soil Mechanics and Foundations Division, ASCE, Vol. 94, No. SM4, July, 1968.
79. Howard, A. K., "Laboratory Load Tests on Buried Flexible Pipes," Proceedings, 92nd Annual Conference of the AWWA, Chicago, Illinois, 1972.
80. Howard, A. K., and Selander, C. E., "Laboratory Load Tests on Buried Reinforced Thermosetting, Thermoplastic and Steel Pipes," Proceedings, 28th Annual Technical Conference, Reinforced Plastics/Composites Institute, the Society of the Plastics Industry, Inc., 1973.
81. Howard, A. K., "Modulus of Soil Reaction (E') Values for Buried Flexible Pipes," Transportation Research Board Meeting, Washington, D. C., January, 1976.
82. Howard, A. K., "Modulus of Soil Reaction Values for Buried Flexible Pipes," Journal of the Geotechnical Engineering Division, ASCE, Vol. 103, No. GT1, January, 1977.
83. Janbu, N., "Soil Compressibility as Determined by and Triaxial Tests," Proceedings, European Conference on Soil Mechanics and Foundation Engineering, Weisbaden, Vol. 1, Germany, 1963.

84. Katona, M. G., Smith, J. M., Odello, R. J., and Allgood, J. R., "CANDE: Engineering Manual - A Modern Approach for the Structural Design of Buried Culverts," FHWA/RD-77-5, Navy Civil Engineering Laboratory, Port Hueneme, California, October, 1976.
85. Katona, M. G., and Smith, J. M., "CANDE: Users Manual," FHWA/RD-77-6, Navy Civil Engineering Laboratory, Port Hueneme, California, October, 1976.
86. Katona, M. G., and Smith, J. M., "CANDE: Systems Manual," FHWA/RD-77-7, Navy Civil Engineering Laboratory, Port Hueneme, California, October, 1976.
87. Kay, J. N., and Krizek, R. J., "Adaptation of Elastic Theory to the Design of Circular Conduits," Civil Engineering Transactions, Institution of Engineers, Australia, 1970.
88. Khosla, V. K., and Wu, T. H., "Stress-Strain Behaviour of Sand," Journal of the Geotechnical Engineering Division, ASCE, Vol. 102, No. GT4, April, 1976.
89. Kirkland, J. L., and Walker, R. E., "Fundamental Studies of Medium-Structure Interaction: Finite Element Analysis of Buried Cylinders," Waterways Experiment Station Report N-72-7, June, 1972.
90. Kloeppe, K., and Glock, D., "Theoretische und Experimentelle Untersuchungen zu den Traslast-Problemen Beiseweicher, in die Erde Eingebetteter Rohre," Report No. 10, Institut fur Statik and Stahlbau Technische Hochschule Darmstadt, Darmstadt, Germany, 1970.
91. Ko, H. Y., and Scott, R. F., "Deformation of Sand in Shear," Journal of the Soil Mechanics and Foundations Division, ASCE, Vol. 93, No. SM5, September, 1967.
92. Ko, H. Y., and Masson, R. M., "Nonlinear Characterization and Analysis of Sand," Proceedings, 2nd International Conference on Numerical Methods in Geomechanics, Blacksburg, Virginia, June, 1976.
93. Kondner, R. L., "Hyperbolic Stress-Strain Response: Cohesive Soils," Journal of Soil Mechanics and Foundations Division, ASCE, Vol. 89, No. SMI, February, 1963.

94. Kondner, R. L., and Zelasko, J. S., "A Hyperbolic Stress-Strain Formulation for Sands," Proceedings, 2nd Pan-American Conference on Soil Mechanics and Foundation Engineering, Vol. I, Brazil, 1963.
95. Kondner, R. L., and Zelasko, J. S., "Void Ratio Effects on the Hyperbolic Stress-Strain Response of Sand," Laboratory Shear Testing of Soils, ASTM, STP No. 361, Ottawa, 1963.
96. Kraft, L. M., and Krishnamurthy, N., "Analytical Model for Evaluation Stress-Strain Response of Soils," Journal of Materials, ASTM, Vol. 6, No. 4, December, 1971.
97. Krizek, R. J., Parmelee, R. A., Kay, J. N., and Elnaggar, H. A., "Structural Analysis and Design of Pipe Culverts," National Cooperative Highway Research Program, Report No. 116, Highway Research Board, National Academy of Sciences, Washington, D.C., 1971.
98. Kulhawy, F. H., Duncan, J. M., and Seed, H. B., "Finite Element Analysis of Stresses and Movements in Embankments during Construction." Report No. TE69-4, University of California, Berkley, Ca., 1969.
99. Lade, P. V., and Duncan, J. M., "Elastoplastic Stress-Strain Theory for Cohesionless Soil," Journal of the Geotechnical Engineering Division, ASCE, Vol. 101, No. GT10, October, 1975.
100. Lade, P. V., and Duncan, J. M., "Stress-Path Dependent Behaviour of Cohesionless Soil," Journal of the Geotechnical Engineering Division, ASCE, Vol. 102, No. GT1, January 1976.
101. Lee, K. L., and Seed, H. B., "Drained Strength Characteristics of Sands," Journal of the Soil Mechanics and Foundations Division, ASCE, Vol. 93, No. SM6, November, 1967.
102. Lee, K. L., "Co-parison of Plane Strain and Triaxial Tests on Sand," Journal of the Soil Mechanics and Foundations Division, ASCE, Vol. 96, No. SM3, May, 1970.
103. Lefebvre, G., Laliberte, M., Lefebvre, L. M., Lafleur, J., and Fisher, C. L., "Measurement of Soil Arching Above a Large Diameter Flexible Culvert," Canadian Geotechnical Journal, Vol. 13, No. 1, 1976.

104. Leonards, G. A., "Foundation Engineering," McGraw-Hill Book Company, 1962.
105. Leussink, H., and Wittke, W., "Difference in Triaxial and Plane Strain Shear Strength," Symposium on Laboratory Shear Testing of Soils, ASTM, Special Technical Publication No. 361, 1964.
106. Luscher, U., and Hoeg, K., "The Beneficial Action of the Surrounding Soil on the Load Carrying Capacity of Buried Tubes," Proceedings of the Symposium on Soil-Structure Interaction, University of Arizona, Tucson, Arizona, 1964.
107. Luscher, U., and Hoeg, K., "The Action of Soil Around Buried Tubes," Proceedings of the 6th International Conference on Soil Mechanics and Foundations Engineering, Montreal, Canada, Vol. II, 1965.
108. Luscher, U., "Buckling of Soil-Surrounded Tubes," Journal of the Soil Mechanics and Foundations Division, ASCE, Vol. 92, No. SM6, November, 1966.
109. Madsen, J. H., "Development of Super Span Design," Paper presented at the 32nd Canadian Geotechnical Conference, Quebec; Quebec, September, 1979.
110. Mahmoud, A. A., "Shallow Flexible Cylindrical Grain Bins," Ph.D. Thesis presented to the Civil Engineering Department, University of Windsor, 1979.
111. Marston A., "The Theory of External Loads on Closed Conduits in the Light of the Latest Experiments," Bulletin No. 96, Iowa Engineering Experiment Station, Ames, Iowa, 1930.
112. Melosh, R. J., and Bamford, R. M., "Efficient Solution of Load Deflection Equations," Journal of the Structural Division, ASCE, Vol. 95, No. ST4, April, 1969.
113. Meyerhoff, G. G., and Baikie, L. D., "Strength of Steel Culvert Sheets Bearing against Compacted Sand Backfill," Highway Research Record No. 30, Highway Research Board, National Academy of Sciences, Washington, D. C., 1963.
114. Meyerhoff, G. G., and Fisher, C. J., "Composite Design of Underground Steel Structures," Engineering Journal, Engineering Institute of Canada, Vol. 46, No. 9, September, 1963.

115. Meyerhoff, G. G., "Composite Design of Shallow Buried Steel Structures," Annual Convention of the Canadian Good Roads Association, Corrugated Metal Pipe Institute, Halifax, September, 1966.
116. Meyerhoff, G. G., "Some Problems in the Design of Shallow-Buried Steel Structures," Proceedings, Canadian Structural Engineering Conference, Toronto, Ontario, February, 1968.
117. Meyerhoff, G. G., "Some Research on Underground Flexible Arches," Proceedings, Conference on Subway Construction, Budapest, September, 1970.
118. Miyahara, F., and Ergatoudis, J. G., "Matrix Analysis of Structure-Foundation Interaction," Journal of the Structural Division, ASCE, Vol. 102, No. ST1, January, 1976.
119. Nataraja, M. S., "Finite Element Solution of Stresses and Displacements in Soil-Culvert Systems" Ph.D. Thesis presented to the Civil Engineering Department, University of Pittsburg, 1973.
120. Ngo, D., and Scordelis, A. C., "Finite Element Analysis of Reinforced Concrete Beams," Journal of American Concrete Institute, Vol. 64, No. 3, March, 1967.
121. Nielson, F. D., "Soil-Structure Arching Analysis of Buried Flexible Structures," Highway Research Record No. 185, Highway Research Board, National Academy of Sciences, Washington, D. C., 1967.
122. Nielson, F. D., "Design of Circular Soil-Culvert Systems," Highway Research Record No. 413, Highway Research Board, National Academy of Sciences, Washington, D. C., 1972.
123. Nielson, F. D., "Experimental Studies in Soil-Structure Interaction," Highway Research Record No. 413, Highway Research Board, National Academy of Sciences, Washington, D. C., 1972.
124. OMTC, "Ontario Highway Bridge Design Code," Ontario Ministry of Transportation and Communications, 1979.
125. Ozawa, Y., and Duncan, J. M., "ISBILD: A Computer Program for Analysis of Static Stresses and Movements in Embankments," Geotechnical Engineering Report, University of California, Berkely, California, 1973.

126. Ozawa, Y., and Duncan, J. M., "Elasto-Plastic Finite Element Analyses of Sand Deformations," Proceedings, 2nd International Conference on Numerical Methods in Geomechanics, Blacksburg, Virginia, June, 1976.

127. Palmerton, J. B., "Application of Three-Dimensional Finite Element Analysis," Proceedings, Symposium on Applications of the Finite Element Method in Geotechnical Engineering, Waterways Experiment Station, Vicksburg, Mississippi, May, 1972.

128. Pedersen, P., "Some Properties of Linear Strain Triangles and Optimal Finite Element Models," International Journal for Numerical Methods in Engineering, Vol. 7, 1973.

129. Poorooshasb, H. B., Holubec, I., and Sherbourne, A. N., "Yielding and Flow of Sand in Triaxial Compression," Part I, Canadian Geotechnical Journal, Vol. III, No. 4, November, 1966.

130. Poorooshasb, H. B., Holubec, I., and Sherbourne, A. N., "Yielding and Flow of Sand in Triaxial Compression," Part II, Canadian Geotechnical Journal, Vol. IV, No. 4, November, 1967.

131. Potyondy, J. G., "Skin Friction Between Various Soils and Construction Materials," Geotechnique, London, Vol. II, 1961.

132. Poulos, H. G., and Davis, E. H., "Elastic Solutions for Soil and Rock Mechanics," John Wiley & Sons, Inc., New York, N. Y., 1974.

133. Prakash, S., Nayak, G. C., and Gupta, R., "Analysis of Buried Pipe under Embankment," Proceedings, 2nd International Conference on Numerical Methods in Geomechanics, Blacksburg, Virginia, June, 1976.

134. Ramberg, W., and Osgood, W. R., "Description of Stress-Strain Curves by Three Parameters," Technical Note No. 902, National Advisory Committee for Aeronautics, Washington, D.C., 1943.

135. Richards, R. M., and Abbott, B. J., "Versatile Elastic Plastic Stress-Strain Formula," Technical Note, Journal of the Engineering Mechanics Division, ASCE, Vol. 101, No. EM4, August, 1975.

136. Rockey, K. C., Evans, H. R., Griffiths, D. W., and Nethercot, D. A., "The Finite Element Method: A Basic Introduction," Crosby Lockwood Staples, London, Great Britain, 1975.
137. Salencon, J., "Application of the Theory of Plasticity in Soil Mechanics," John Wiley & Sons, Inc., 1977.
138. Savin, G. N., "Stress Concentration Around Holes Which Are Strengthened by Elastic Rings," International Series of Monographs in Aeronautics and Astronautics, Vol. I, Div. I, Chapter V, 1961.
139. Schofield, A., and Wroth, P., "Critical State Soil Mechanics," McGraw Hill Book Company, New York, 1968.
140. Selig, E. T., "Subsurface Soil-Structure Interaction: A Synopsis," Highway Research Record No. 413, Highway Research Board, National Academy of Sciences, Washington, D.C., 1972.
141. Selig, E. T., "Stresses and Deflections Around Large Corrugated-Metal, Buried Structures," Dayton Symposium on Lateral Pressures Generated by Pipes, Piles, Tunnels and Caissons, Dayton, Ohio Section, ASCE, February, 1975.
142. Selig, E. T., "Instrumentation of Large Buried Culverts," Performance Monitoring for Geotechnical Construction, ASTM STP 584, American Society for Testing and Materials, Philadelphia, Pa., August, 1975.
143. Selig, E. T., and Calabrese, S. J., "Performance of a Large Corrugated Steel Culvert," Transportation Research Record No. 548, Washington, D.C., 1975.
144. Selig, E. T., Abel, J. F., Kulhawy, F. H., and Falby, W. E., "Review of the Design and Construction of Long-Span, Corrugated-Metal, Buried Conduits," FHWA/RD-77-131, Federal Highway Administration, Washington, D.C., August, 1977.
145. Selig, E. T., Abel, J. F., Kulhawy, F. H., and Falby, W. E., "Long-Span Buried Structure: Design and Construction Journal of the Geotechnical Engineering Division, ASCE, Vol. 104, No. GT7, July, 1978.
146. Smith, I. M., "A Finite Element Approach to Elastic Soil

Structure Interaction," Canadian Geotechnical Journal, Vol. 2, No. 7, May, 1970.

147. Spangler, M. G., "The Structural Design of Flexible Pipe Culverts," Iowa State College, Engineering Experimental Station, Bulletin No. 153, 1941.
148. Spangler, M. G., and Handy, R. L., "Soil Engineering," Intext Educational Publishers, Third Edition, 1973.
149. Szechy, K., "The Art of Tunnelling," Akademiai Kiado, Budapest, 1973.
150. Terzaghi, K., and Peck, R. B., "Soil Mechanics in Engineering Practice," John Wiley & Sons, Inc., New York, Second Edition, 1967.
151. Timoshenko, S. P., and Gere, J. M., "Theory of Elastic Stability," McGraw Hill Book Company, New York, N.Y., 1961.
152. Van Leeuwen, H. J., "A Product Designer Looks at Highway Overpasses," EIC-68, BR x STR G, AGM Preprint, Halifax, N.S., May 28-31, 1968.
153. Watkins, R. K., "Failure Conditions of Flexible Culverts Embedded in Soil," Highway Research Board, Vol. 39, National Academy of Sciences, Washington, D.C., 1960.
154. Watkins, R. K., "Structural Design of Buried Circular Conduits," Highway Research Record No. 145, Highway Research Board, National Academy of Sciences, Washington, D.C., 1966.
155. Watkins, R. K., and Ghavimi, M., and Longhurst, G. R., "Minimum Cover for Buried Flexible Conduits," ASCE, Vol. 94, No. P11, October, 1968.
156. Weidler, J. B., and Paslaw, P. R., "Constitutive Relations for Inelastic Granular Medium," Journal of Engineering Mechanics Division, ASCE, Vol. 96, No. EM4, August, 1970.
157. White, H. L., and Layer, J. P., "The Corrugated Metal Conduit as a Compression Ring," Proceedings, Highway Research Board, Vol. 39, National Academy of Sciences, Washington, D. C., 1960.

158. White, H. L., "Largest Metal Culvert Designed by Ring Compression Theory," Civil Engineering, ASCE, Vol. 31, No. 1, January, 1961.
159. Winterkorn, H. F., and Fang, H. Y., "Foundation Engineering Handbook," Van Nostrand Reinhold Company, New York, 1975.
160. Wong, K. S., and Duncan, J. M., "Hyperbolic Stress-Strain Parameters for Nonlinear Finite Element Analyses of Stresses and Movements in Earth Masses," Geotechnical Engineering Report, TE 74-3, University of California, Berkeley, California, 1974.
161. Wong, K.S., and Duncan, J. M., "Summary of Field Instrumentation Study on a 35 ft. Span Aluminum Culvert in Greenbrier County, West Virginia," Report to Highway Products Division, Kaiser Aluminum and Chemical Sales, Inc., Oakland, California, 1976.
162. Wroth, C. P., and Basset, R. E., "A Stress-Strain Relationship for the Shearing Behaviour," Geotechnique, Vol. XV, No. 1, 1965.
163. Zienkiewicz, O. C., Valliapan, S., and King, I. P., "Stress-Analysis of Rock as a 'No Tension' Material," Geotechnique, Vol. XVIII, No. 1, March, 1968.
164. Zienkiewicz, O. C., Best, B., Dullase, C., and Stass, K. G., "Analysis of Nonlinear Problems in Rock Mechanics with Particular Reference to Jointed Rock Systems," Proceedings, 2nd International Congress on Rock Mechanics, Belgrad, 1970.
165. Zienkiewicz, O. C., "The Finite Element Method in Engineering Science," McGraw Hill Book Company, New York, N.Y., 1971.

VITA AUCTORIS

Hisham Hussein Hafez

The author was born on February 10, 1951 in Cairo, Egypt. In 1968, he completed his secondary school education at "College des Frères, De La Salle," Cairo, Egypt. Then he joined the Faculty of Engineering, Cairo University, where he was granted undergraduate scholarships for five consecutive years. In 1973, he graduated from Cairo University with a degree of Bachelor of Science in Civil Engineering (Distinction with Honours). Then, he was appointed as Teaching and Research Assistant at the Civil Engineering Department, Cairo University.

In 1975, he joined the Civil Engineering Department at The University of Windsor, Windsor, Ontario, Canada, as a teaching and research assistant. In 1977, the author obtained a Master of Science Degree in Civil Engineering from The University of Windsor. The author prepared this dissertation in partial fulfillment of the requirements for the Degree of Doctor of Philosophy.